Constrained Sintering of Patterned Ceramic Films on Stiff Substrates

TECHNISCHE UNIVERSITÄT DARMSTADT

Vom Fachbereich Material- und Geowissenschaften
der Technischen Universität Darmstadt

zur Erlangung des akademischen Grades
Doktor – Ingenieur
(Dr.-Ing.)

genehmigte Dissertation von

Dipl.-Ing. Christine Cornelia Jamin
aus Speyer

Referent:	Prof. Dr.-Ing. Jürgen Rödel
Koreferent:	Prof. Dr.-Ing. Olivier Guillon
Tag der Einreichung:	27.03.2014
Tag der Prüfung:	09.05.2014

Darmstadt 2014

D17

Acknowledgements

First I wish to thank Prof. Dr. Olivier Guillon (Friedrich-Schiller-Universität Jena) for thinking up this chef-d'oeuvre, supervising my scientific debut during his time at TU Darmstadt and boosting morale whenever, to my chagrin, I encountered an impasse. I am especially grateful for his patience when my family-induced ennuis resulted in temporary slowdowns.

I also wish to thank Prof. Dr. Jürgen Rödel for giving me the opportunity to work in his group and accepting to be the examiner of this thesis. I am particularly grateful for his readiness to accommodate my impromptu visits whenever I had scientific or administrative queries.

I also wish to acknowledge the contributions of Dr. Torsten Kraft, Tobias Rasp and Dr. Andreas Wonisch from Fraunhofer Institut für Werkstoffmechanik in Freiburg. With patience and understanding for the hardships we experimentalists sometimes face, they have provided simulations that truly improved our understanding of my data. Many thanks for the fruitful discussions in our project meetings and comments on this manuscript.

Furthermore I would like to thank Prof. Paula Vilarinho, Prof. Ana Senos and Dr. Luis Amaral for welcoming me in their workgroup at Universidade de Aveiro. Our collaboration and interesting discussions helped me to see beyond my own research field. Muito obrigada pela sua ajuda!

Prof. PhD Kyle Webber and Dr. Eric Patterson have greatly contributed to this work by reading the first thesis draft. Thus, they have made valuable comments that were subsequently incorporated into this work. Hence, this draft has become a lot more readable due to their help. Consequently, I wish to express my thanks for this help.

More thanks go to our technical and administrative specialists in the NAW group: Michael Heyse for his help with grinding and polishing, Gundel Fliß and Roswita Geier for putting up with the copious amounts of paperwork I generated and Irene Mieskes and Gila Völzke for our woman-to-woman pep talks.

I would like to thank Thomas Dirsch for his support during the in-situ ESEM experiments. The pictures would not be half as cool without you.

I also wish to thank Dr. Jesus Gonzalez from the Mechanics of Functional Materials Group of Universität Jena for measuring some of the free sintering curves.

I would also like to acknowledge the contribution of my Diploma student Britta Lilge as well as my bachelor students Peter Keil and Fabian Grimm. Further thanks go to Sravan Vadlamani, Raschid Baraki, Sascha Seils and Marc Adamiak whom I had the pleasure to supervise during their advanced research lab courses.

Raschid Baraki, Sascha Seils, Peter Keil and Marcus Schmitt also contributed to my work as student helpers and excelled by using their both their brains and muscles during stamp casting, interferometry measurements and slurry preparation. I still feel guilty for making you crush all that glass frit.

Many thanks go to my colleagues from NAW group (in no particular order): Eva A., Gerrit, Jami, Eric, Julia, Silke, Markus K., Torsten, Thorsten, Klaus, Robert, Daniel, Jochen, Mie, Yohan, Wook, Raschid, Debbi, Claudia, Martin, Markus J., Florian, Eva S., Matias, Azatuhi, Jiadong, Philipp, Hairui, Jaemyung and Raju. I wish to apologize to everyone that I forced to switch on my computer on my homeoffice days or switch off my furnace. You lightened up more than just one dreary polishing session!

I definitely wish to thank my husband Daniel for doing the lion's share of the family work during the final phase of this thesis and putting up with my ill humor.

Further thanks go to my parents and parents-in-law for their emotional and practical support, especially the free high-quality child care they provided. I probably would not have eaten a decent meal during the past couple of years if it wasn't for you.

1. Introduction

Patterned ceramics or metallic films are the basis of many devices in electronics [1], microfluidics [2] and sensor technology [3]. Examples range from well-established industrial applications such as integrated circuit boards or low temperature co-fired ceramic (LTCC) modules to more recent academic developments, including micro-hotplates for gas sensing [4] and micro-reactors found in "lab-on-a-chip" – assemblies [5]. Many of these devices are fabricated by a deposition or etching process that is followed by a sintering step. The latter controls the microstructure of the materials and is therefore crucial for the mechanical properties of the finished component. In the case of films, the geometrical constraint created by the substrate plays an important role since the stresses it generates may compromise the mechanical stability of the product and result in cracking [6]. Constrained sintering is hence the subject of extensive research with multilayer structures, rigid inclusions or continuous films on rigid substrates being the center of attention [7]. In recent years, the ongoing miniaturization process has created new challenges both on the theoretical and practical side since the finite lateral film dimensions must be incorporated into constrained sintering models and new techniques are needed to fabricate the ever smaller structures.

Traditional subtractive patterning techniques used for most microelectronic devices consist of the preparation of a continuous film by dip or spin coating followed by lithographic patterning and a selective etching step to bring out the desired features. The lithographic step tends to be especially costly. In addition, etching is limited to a small number of materials such as photoresists [8]. One alternative set of techniques is soft lithography [9], which includes a variety of additive patterning techniques that use a soft elastomer stamp. Soft lithographic techniques such as replica molding, embossing and micro-molding in capillaries are currently the subject of academic research with auspicious prospects of making the transition to industrial mass fabrication. In micro-molding in capillaries (MIMIC), the stamp patterns include channel structures that draw the precursor solution from its reservoir into the cavities designed to yield the desired features. Channel widths of several micrometers are state of the art [10] and current research is focused on decreasing the channel size into the submicron range. This method remedies some of the shortcomings of subtractive patterning since the lithographic step is limited to the fabrication of a patterned silicon wafer used as a negative for repeated stamp fabrication.

On the industrial scale, soft lithography is already in use to pattern special surfaces that are inaccessible by conventional lithography, *e.g.* very large or curved surfaces [11]. However, patterned films deposited by MIMIC experience topographical deviations from the channel shape during deposition, drying and sintering. The constraint imposed by the channel walls during drying and by the substrate during sintering can result in deformation, cracking or delamination [12]. In practice, this may lead to broken interconnect structures, thus compromising the functionality of the components. The film edges are particularly sensitive to these effects and their contribution to the overall behavior

of the film is thought to become quite substantial when the feature size is small enough [13]. Thus, the in-plane constraint that governs the sintering behavior of continuous films may be relieved in narrow film patterns, leading to an intermediate state between free and fully constrained sintering. In order to quantify the deviation of patterned film sintering from perfect constraint, the degree of constraint is defined as the ratio of vertical to lateral strain components and studied for various film-substrate systems. This work aims to remedy the lack of experimental data on densification and shrinkage of discontinuous films. The role of the film-substrate interface is investigated with special focus in the verification of existing mathematical models and simulation results. The obtained data are placed at the disposal of simulation researchers to develop further codes to predict the shape, densification and microstructure of sintering ceramic patterns.

This work is divided into five sections:

Chapter two summarizes the most important theoretical concepts of constrained sintering, cracking and creep, provides a literature review on MIMIC technology as well as simulation results on patterned films.

In chapter three, the experimental methods are explained. The custom pattern used is described and the film deposition methods as well as characterization techniques are presented.

Chapter four presents the results of this work and is split into four sections. First, the drying behavior is characterized. Then, an exhaustive study of densification, shrinkage, microstructural anisotropy and delamination of pure alumina stripe patterns is presented in the second section. The aim is to elucidate the influence of edge effects on the overall sintering behavior with declining feature size. These experiments are carried out using smooth, rough and platinum coated sapphire substrates. Some of these experiments are repeated with additions of a liquid phase in section three. To quantify the influence of the film-substrate interface, an interface friction coefficient is calculated for the different systems. In the fourth section, cracking around intentionally introduced cavities is related to the geometry and interface effects studied in section one. Shrinkage of annular films is then further investigated as a function of the interface friction coefficient.

A general discussion is given in chapter five. The data from chapter four are used to assess the validity of the predictions of various mathematical methods and simulation results available in the literature. The influence of the friction coefficient on constrained sintering is discussed. Simulation results fitted to the experimental data have been contributed by researchers at Fraunhofer Institut für Werkstoffmechanik in Freiburg who collaborate in a joint research project funded by Deutsche Forschungsgemeinschaft; they are reviewed in order to understand the influence of the stress state on densification, cracking and microstructure development.

The dissertation is concluded by a brief summary and outlook.

2. Theory

2.1. Soft micro-molding in capillaries

In recent years, micro-patterning techniques have become the focus of research designed to improve the fabrication process of micro-devices used in fluidics, sensor technology, electronic packaging, optical components and micro-electromechanical systems (MEMS). Since conventional optical lithography is only suited for a narrow range of photoresist materials, alternative techniques are needed to pattern ceramic materials [8] [10]. One solution to this problem is the use of flexible elastomeric stamps for ceramic patterning. Methods based on this principle are subsumed under the term soft lithography. Both printing and molding techniques are available, the latter including a variety of working principles [14]. Apart from traditional replica molding, micro-transfer molding works by filling the voids in an elastomeric mold with a precursor solution which is then placed on a substrate after the removal of excess material. This method is particularly suited for layer-by-layer printing and allows control of feature thickness by mechanical deformation [9].

Whenever clearly separated stripes on a smooth substrate are required, micro-molding in capillaries (MIMIC) is the method of choice [15]. Here, the filling of capillaries is achieved by wetting and spreading of a liquid precursor or suspension from a reservoir. Contact between the substrate and the stamp is made before the filling process, thus forming closed channels that are filled with solution while the substrate area in between the structures ideally remains uncoated. Thus, MIMIC is particularly suited for the study of the lateral shrinkage during the sintering of clearly separated ceramic stripes. Currently, MIMIC is being used to deposit line structures of sensor materials like SnO_2 or ZnO_2 [3] [16] [17], actuator materials such as PZT [12] [18] [19], semiconductor materials including SiC [20] [21] or indium tin oxide (ITO) used as transparent electrode material [22]. Free standing structures such as ceramic sieves, Fresnel zone plates and micro-contact switches can be fabricated by MIMIC of alumina slurry onto glassy carbon substrates since the low adhesion of both materials facilitates layer detachment after sintering [23]. These structures are shown in Figure 2-1.

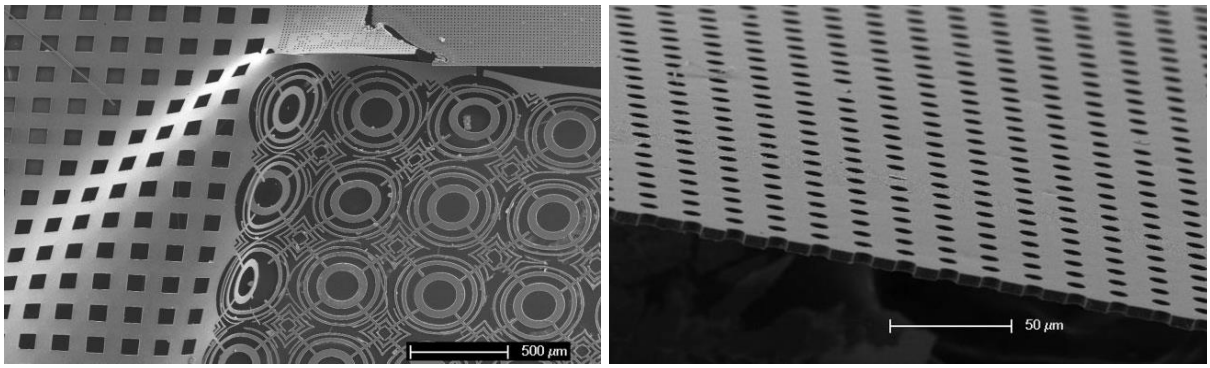

Figure 2-1. Free standing alumina structures. Left: Rectangular sieve structure and Fresnel zone plates. Right: Alumina sieve with circular holes [23].

A mathematical description of the filling process of a square channel from a droplet-shaped slurry reservoir with radius r is given schematically in Figure 2-2. When liquid from the droplet reservoir fills a rectangular channel with side length x up to a distance of z, a minimization of the free surface energies of the channels brings about the following change in total free energy:

$$\Delta G = \gamma_{LV}\Delta A_{drop} - f(\gamma_{SV}\,\gamma_{SL}\,\gamma_{SV'}\,\gamma_{SL'})\Delta A_{channel} \quad (1)$$

$$\Delta G = \frac{x^2 \Delta z\,\gamma_{LV}}{r} - [3x\Delta z(\gamma_{SV} - \gamma_{SL}) + x\Delta z(\gamma_{SV'} - \gamma_{SL'})] \quad (2)$$

Where γ_{LV} is the interfacial free energy of the liquid-vapor interface, $\gamma_{SL}$and γ_{SV} the interfacial free energies of the solid-liquid and the solid-vapor interfaces of the stamp material and $\gamma_{SL'}$ and $\gamma_{SV'}$ the interfacial free energies of the solid-liquid and the solid-vapor interfaces of the substrate. When the change in interfacial free energy due the reduction of droplet surface area is very small ($r \gg x$), the following approximation applies:

$$\Delta G \cong -[3x\Delta z(\gamma_{SV} - \gamma_{SL}) + x\Delta z(\gamma_{SV'} - \gamma_{SL'})] \quad (3)$$

This can be expressed in terms of the contact angles of the liquid with the stamp surface θ and the substrate θ':

$$\Delta G \cong -x\Delta z\gamma_{LV}(3\cos\theta + \cos\theta') \quad (4)$$

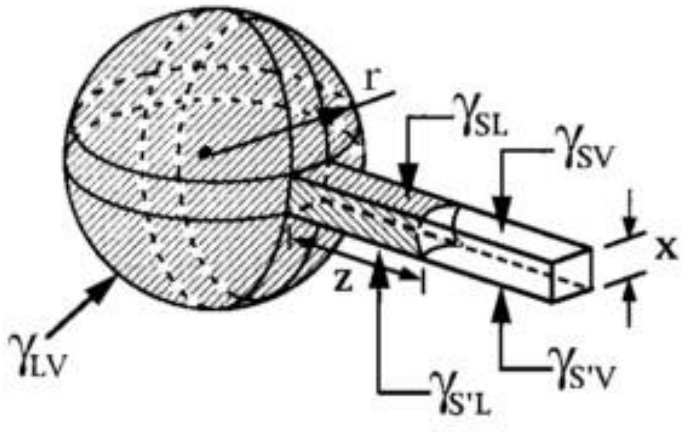

Figure 2-2. Model for channel filling from a spherical drop during the MIMIC process. γ_{SV}, γ_{SL} and γ_{LV}, refer to the solid-vapor, solid-liquid and liquid-vapor interfaces, respectively [15].

Filling of the channel is determined by the minimization of the interfacial free energies of the four surfaces, three of which are made of PDMS and one of the substrate material. Due to the relatively high interfacial free energy of PDMS compared to typical substrate materials such as sapphire (21.6 mJ/m^2 [15] compared to 5.3 mJ/m^2 [24]), the liquids typically wet the stamp rather than the support in order to minimize the free surface energy. Thus, the stamp shape is maintained during deposition. Organic solvents with low surface tension and low viscosity have the best channel filling properties. When it comes to ceramic suspensions, this means that low solid contents up to 10wt% are usually applied [16].

However, when fine ceramic stripes with high green density and low distortion during drying are desired, aqueous slurries with high solid loading and a small particle size are required [25]. To compensate for the resulting high viscosity, channel filling can be enhanced by vacuum assisted methods [26] or by an additional wetting liquid [27]. Furthermore, since PDMS is hydrophobic, oxygen plasma treatment is necessary to exchange surface methyl groups by hydroxide groups and thus render the stamp hydrophilic [28].

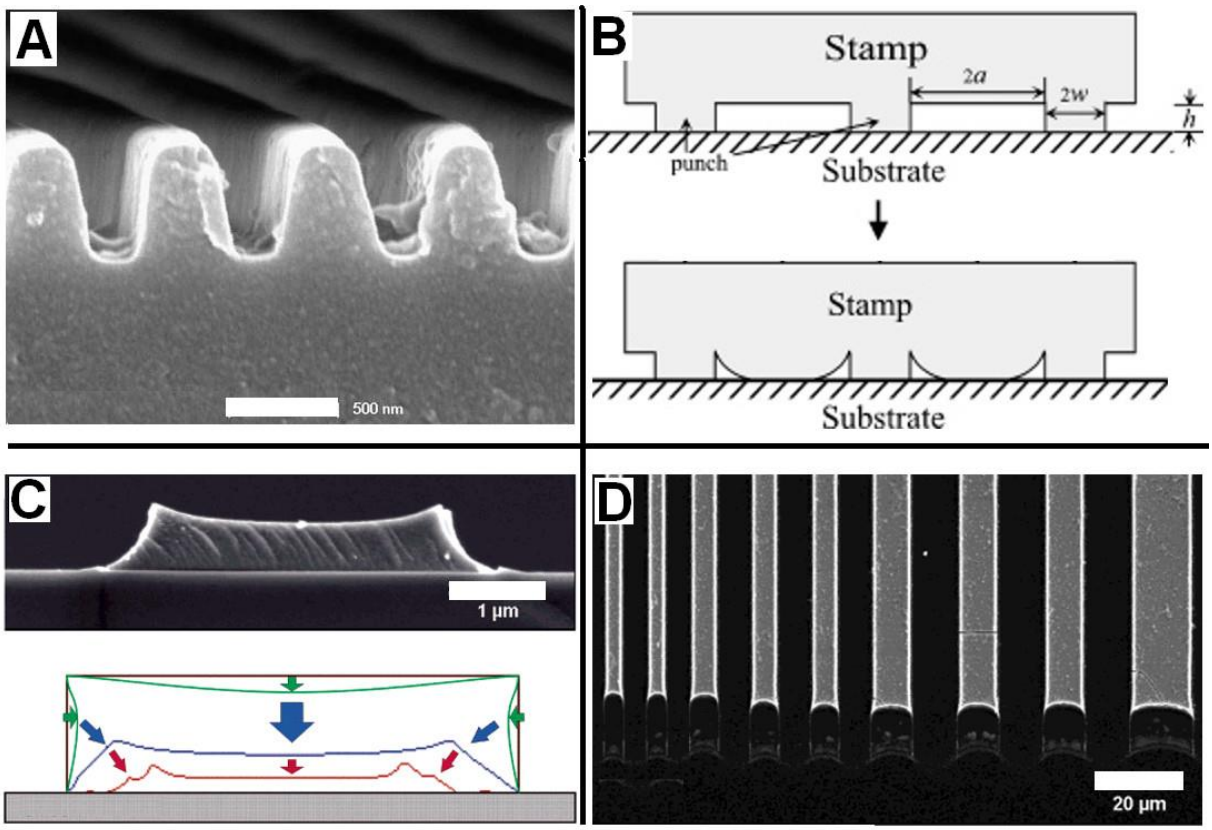

Figure 2-3. Shape distortion effects during MIMIC. A: Trapezoidal distortion of photoresist channel in the master pattern [29]. B: Surface tapering during roof collapse in the stamp [30]. C: double-peak formation due to preferential wetting of the stamp corners [12]. D: Edge effects at the meniscus [12].

During the molding process of stripes with rectangular cross sections, deviation from the ideal shape of the master pattern is usually observed. This is due to four effects:

- Trapezoidal distortion of the master channels
- Roof collapse during deposition
- Double-peak formation during drying
- Meniscus shape

Shape distortion may arise already during master fabrication. Channel cross sections in the master pattern can become trapezoidal during X-ray lithography due to a decrease in cure width with increasing cure depth [29] [31]. An example of this effect is given in Figure 2-3 A, where the cross section of a nano-fluidic channel system is shown. The distorted shape of the master is then emulated in the PDMS stamps.

In addition, deformation of the channel roof during deposition can lead to surface tapering in the stripes, thus reducing their thickness. This effect, known as roof collapse, is caused by the adhesion between PDMS stamp and substrate that leads to a downward curvature of the channel roof. Wide stripes separated by narrow punches are most affected by this phenomenon [30]. A schematic of roof collapse is shown in Figure 2-3 B.

During the molding process, preferential wetting of the PDMS stamp by the suspension occurs at the upper channel corners since they are the points of maximum curvature. In case of channel with a low thickness-to-width ratio, the suspension can detach from the center of the channel ceiling whilst remaining attached to the corners. This results in the so-called double-peak shape of deposited stripes that consist of two maxima at the edges separated by a trough. Distortion is enhanced during drying and sintering or curing as illustrated by the blue and red height profiles shown in Figure 2-3 C. The trough depth can be minimized by ensuring slow drying [12]. Drying speed can be controlled by adjusting the temperature and ambient humidity [28].

Finally, a meniscus is formed at the suspension front during capillary movement. This causes a rounded shape at the channel end (see Figure 2-3 D). All of these effects must be taken into consideration when studying the constrained drying and sintering of ceramic stripes.

Microstructural anisotropy in MIMIC

Microstructural anisotropy is a common feature of sintered films attached to rigid substrates [7]. However, green films can already present anisotropy to a degree that depends on the fabrication method. During dry uniaxial pressing, for instance, the friction between the powder and the walls of the mold leads to a low packing density and non-uniform green density in the green body [32].

To date, no literature on the initial microstructure of MIMIC structures is available. However, since MIMIC is a microfluidic process that involves the flow of ceramic slurry along a substrate, a comparison with tape casting or dip coating processes is adequate. In tape casting, the slurry is distributed over the substrate using a doctor blade. The substrate usually moves while the doctor blade remains stationary. Studies of Raj et al. [33] on the sintering behavior of tape cast and injection molded alumina green bodies found enhanced shrinkage perpendicular to the casting direction. This was related to the preferential orientation of the particles along the casting direction that results in denser packing along the flow direction. Furthermore, pore orientation is not random in the green body; pore analysis after free sintering of laminated alumina tapes revealed a preferential orientation of pores parallel to the casting plane [34].

2.2. Theory of Sintering

The term sintering designates the consolidation of a porous body that is usually accompanied by densification and macroscopic shrinkage. The underlying driving force is energy minimization, with interfacial and surface free energy entering the balance. Reduction of interfacial area in powder compacts as well as pore elimination is achieved via atomistic transport. Depending on the material system in question, viscous flow, evaporation – condensation, transport through a liquid phase or solid state diffusion can occur. Three different sintering schemes are described in the literature. Accordingly, we differentiate between viscous sintering, liquid phase sintering and solid state sintering. Sintering is generally activated by exposing the material to elevated temperatures beneath the melting point of the main material and can be aided by an external pressure. During solid state sintering, different material transport paths are possible: Diffusion can occur at the grain boundaries, through the lattice or along the free surfaces. However, only the first two can result in densification. In liquid phase sintering, an additional diffusion path is provided by the liquid phase [32].

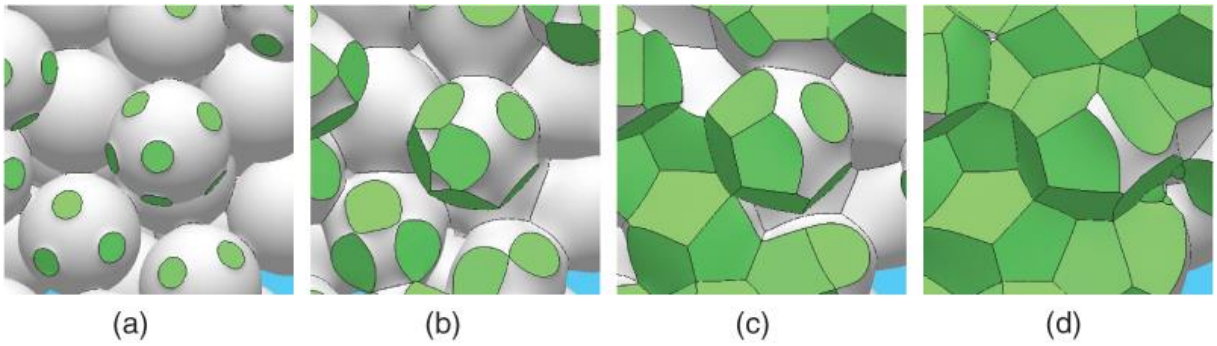

Figure 2-4. Evolution of the microstructure during sintering. a) Initial stage, b) intermediate stage (open porosity), c) intermediate stage (onset of pore closure), d) final stage. Picture taken from [35].

The sintering process is divided in three stages: Initial, intermediate and final stage. In viscous and solid state sintering, these stages are defined with respect to density and pore configuration: The first stage is characterized by neck formation at the contact points of the particles and brings about cohesion and a slight density increase of ca. 3%. This is shown in Figure 2-4 a). Neck formation occurs via diffusion of atoms from the center of the grain boundary to the neck as a consequence of the gradient in chemical potential. The three sintering stages are preceded by a phase of adhesion, rearrangement and repacking due to the orientation dependent grain boundary energy [32]. During the intermediate stage a drastic increase in density is observed. The pore structure of the sintering body resembles a skeletal structure with interconnected pores stretching throughout the compact (Figure 2-4 b); the channels break up, leading to closed porosity (Figure 2-4 c). At densities above 92% the final stage begins that is characterized by porosity closure, shrinkage and grain growth that result in a merely incremental increase in density. This is illustrated in Figure 2-4 d.

The three stages that compose the liquid phase sintering process are somewhat different. Here, the initial stage includes the rearrangement of solid particles in the liquid phase and is accompanied by a steep increase in density. In the intermediate stage, a solution-precipitation process usually follows. Here, the solid main component dissolves in the liquid phase to be subsequently precipitated at locations with a lower chemical potential. The final stage is referred to as final pore removal by pore filling and solid state sintering. It may involve transport of matter along solid-solid contact points. As in solid state sintering, only a small increase in density is observed during the final stages of sintering [36]. In the following sections, the individual sintering mechanisms are described. The focus is placed on the solid state sintering of polycrystalline materials and liquid phase sintering with focus on densification during the individual sintering stages.

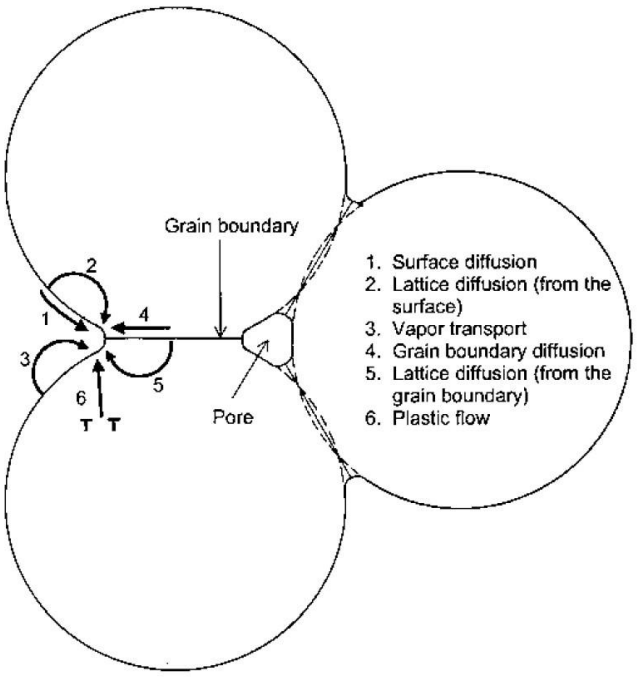

Figure 2-5. Mass transport mechanisms in solid state and viscous sintering [32].

2.2.1. Solid state sintering

Mass transport paths

Mass flow during solid state sintering can occur by surface and bulk transport mechanisms, each of the two classes consisting of various actual mass flow paths. This is illustrated in Figure 2-5, where an assembly of three grains located around a pore is schematically depicted. Mass transport can occur as follows:

- Along the surface (surface diffusion)
- Through pore space (vapor transport)
- Along grain boundaries (grain boundary diffusion)
- Through the lattice (volume diffusion or plastic flow)

The first two paths do not cause the particle centers to approach, thus no densification is achieved. Whenever mass from the particle interior is deposited at the neck, densification follows. This is the case for bulk and grain boundary diffusion of atoms from the grain boundary to the neck. Plastic flow is most often observed in metals; in ceramics, high pressure is usually necessary to induce it [32].

The sintering stress

A basic quantity that determines the sintering process is the sintering stress, or sintering potential. It is defined as an equivalent externally applied stress that would cause a densification rate equal to that resulting from free sintering [32]. The sintering stress Σ is related to pore surface curvature and interfacial energy [37]:

$$\Sigma = \frac{\gamma_{SV}}{r} + \frac{\gamma_{GB}}{G} \tag{5}$$

Here, γ_{GB} and γ_{SV} are the free energies of the grain boundary and the solid-vapor interface, respectively. r is the radius of curvature of the pore and G the grain size.

Initial stage neck growth

The description of neck growth during the initial stage is based on the two sphere model [38]. Figure 2-6 shows an assembly of two spherical grains of radius D that form a neck of radius X and under an angle θ. The gradient in curvature along the surface of the connected spheres results in a gradient in chemical potential which in turn acts as the driving force for mass flow. Assuming that the change in energy due to the reduction of surface area equals the energy dissipated by mass flow, the following relation of neck size ratio as a function of sintering time can be derived [38]:

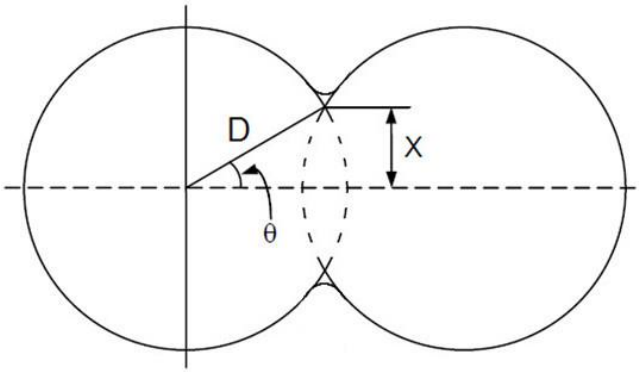

Figure 2-6. Schematic representation of Frenkel's two sphere model. Picture from Ref. [39].

$$\left(\frac{X}{D}\right)^n = \frac{Bt}{D^m} \tag{6}$$

Where t is the sintering time and B a term that includes a variety of parameters such as the diffusion coefficient, atomic volume and and surface tension. B, n and m take different values for volume, surface and grain boundary diffusion. In the early stages of sintering, surface diffusion is usually dominant since its activation energy is lowest.

Macroscopic shrinkage can be used as an estimate for the neck size using the following relation [38]:

$$\left(\frac{X}{2D}\right)^2 = \frac{\Delta L}{L_0} \tag{7}$$

With $\frac{\Delta L}{L_0}$ representing the change in specimen length.

Intermediate stage

During the intermediate sintering stage, necks are no longer independent but part of a network of pores and grains. Pore rounding, densification and grain growth are concurrent phenomena taking place at this stage. In addition to local neck curvature, the driving force is now reduction of pore surface area. The pore structure is modeled as a fully interconnected network of cylindrical pores located at the grain edges. This can be visualized using a simplified model based on the tetrakaidecahedron configuration [38]. In this model, the sintering body is described as a space filling array of tetrakaidecahedral grains. The pores form open channels and will remain attached to the grain boundaries since pore-boundary separation requires high energies when dihedral angles are below 120°. Atoms will therefore diffuse from the center of the grain boundary to the pore surface. From these assumptions, the densification rates due to lattice or grain boundary diffusion in the intermediate stage can be approximated as follows [32]:

$$\frac{\dot{\rho}}{\rho} = \frac{AD_l\gamma_{SV}\Omega}{\rho kTG^m} \tag{8a}$$

$$\frac{\dot{\rho}}{\rho} = \frac{B\delta_{gb}D_{gb}\gamma_{SV}\Omega}{\rho(1-p)^{1/2}kTG^m} \tag{8b}$$

Here, $\dot{\rho}$ is the change in fractional density with time, G the grain size, γ_{SV} the solid-vapor interfacial energy, D_l and D_{gb} the diffusion coefficients for lattice and grain boundary diffusion, respectively; Ω the atomic volume, A a constant, δ_{gb} the grain boundary diffusion length and m an exponent that takes the value of 3 in case of lattice diffusion and 4 in the case of grain boundary diffusion.
Grain growth during the intermediate stage results in a time-dependent increase in grain size in agreement with [32]

$$G^m = G_0^m + Kt \tag{9}$$

Where the temperature dependent parameter K depends on parameters such as grain boundary mobility, grain boundary energy and grain boundary shape. The exponent m takes values between 2 and 4. Grain growth accelerates towards the end of the intermediate stage as the pores shrink and their pinning effect vanishes [38].

Final stage

The final stage is characterized by closed porosity and densities above 92%. Densification is slow as grain growth occurs. At the beginning of the final stage, closed pores are still attached to the corners of the grains. In the simplistic view of the tetrakeidecahedral model, continuous shrinkage of closed pores leads to complete removal. Shrinkage of pores far away from the grain boundaries, however, in reality is slow since vacancy diffusion paths are long. When pore shrinkage occurs via lattice diffusion, the densification rate is as follows:

$$\frac{\dot{\rho}}{\rho} = \frac{12D_v\Omega}{\rho kTG^3}\left(\frac{4\gamma_{SV}}{d_P} - P_g\right) \tag{10}$$

Where d_P is the pore radius and P_g the gas pressure inside the pore [38].
Grain growth occurs through atom diffusion across curved grain boundaries as a consequence of the difference in chemical potential between atoms on the concave and convex side. The driving force for

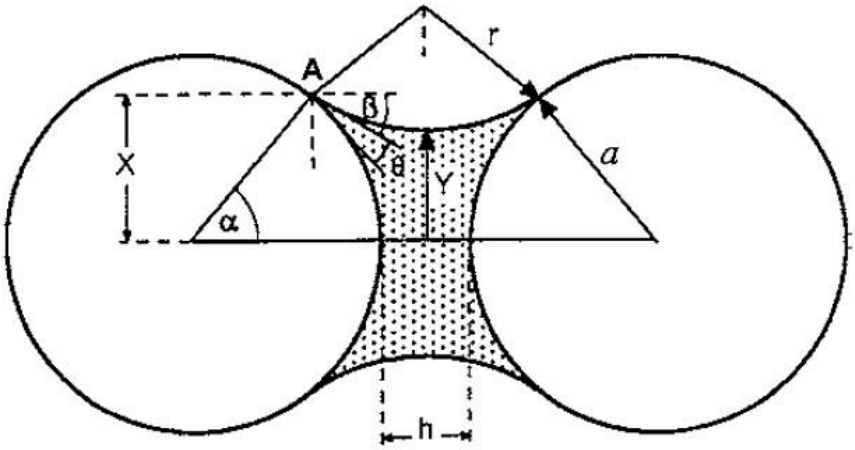

Figure 2-7. Two sphere model for liquid phase sintering [32]. A liquid pocket has formed in between adjacent particles.

this process is again the minimization of the total free energy of the system via reduction of grain boundary area since the latter is associated with a free energy. Two types of grain growth are commonly distinguished: Normal grain growth involves a narrow grain size range as well as uniform pore growth; abnormal grain growth, by contrast, is characterized by growth of some large grains at the expense of smaller ones.

2.2.2. Liquid phase sintering

The sintering of engineering materials that do not densify sufficiently at a given temperature can be enhanced by the addition of a small amount of liquid phase. This liquid phase can be a glassy additive with a lower melting point than the main material, such as the sintering of alumina with a silicate glass [40] or a material that forms a eutectic with the main component, as in the sintering zinc oxide with bismuth oxide [41]. The liquid phase can remain unchanged throughout the firing process (persistent liquid) or vanish by crystallization or incorporation into the solid phase (transient liquid). The microstructure is characterized by large, spherical or polyhedral grains surrounded by pockets of liquid phase [38].

In Figure 2-7, the idealized two-sphere model for liquid phase sintering is given [32]. A liquid bridge has formed between the two grains whose thickness greatly exceeds the grain boundary thickness in solid state sintering materials. The driving force for densification is the removal of pores in the liquid phase, thus reducing the interfacial area between liquid and vapor phases. The pressure Δp exerted on the surface a spherical pore of radius *r* inside a liquid pocket is given by the Laplace equation [32]:

$$\Delta p = -\frac{2\gamma_{LV}}{r} \tag{11}$$

Where γ_{LV} is the interfacial free energy of the liquid-vapour interface. Pressure values can be in the order of magnitude of several MPa, thus greatly enhancing densification. Furthermore, particle rearrangement is aided by reducing interparticle friction and matter transport is enhanced due to the higher diffusivity of solid atoms through the liquid than through the solid bulk. Prior to the first sintering stage, the liquid must form, wet the particles and spread through along grain boundaries by capillary forces. The wetting of the solid phase requires low surface tension of the liquid and a small contact angle θ, given by Young's equation [32]:

$$\gamma_{SV} = \gamma_{SL} + \gamma_{LV} \cos\theta \tag{12}$$

where γ_{LV}, γ_{SV} and γ_{SL} are the interfacial free energies of the liquid-vapor, solid-vapor and solid-liquid interfaces of a drop of liquid deposited onto a flat surface.

Complete wetting occurs at $\theta = 0°$. Spreading takes place when the specific energy of two solid-liquid interfaces is less than the energy of one solid-liquid interface. Liquid penetration of the grain boundary is controlled by the dihedral angle which is the angle ψ between the solid-liquid interfacial free energies as shown in Figure 2-8 [32]:

$$\cos\frac{\psi}{2} = \frac{\gamma_{SS}}{2\gamma_{SL}} \tag{13}$$

Complete penetration occurs when the dihedral angle is greater or equal 180°. Once the liquid has penetrated the grain boundaries, capillary forces are exerted on the grains. This force is given by

$$F = -\pi X^2 \Delta p + 2\pi X \gamma_{LV} \cos\beta \tag{14}$$

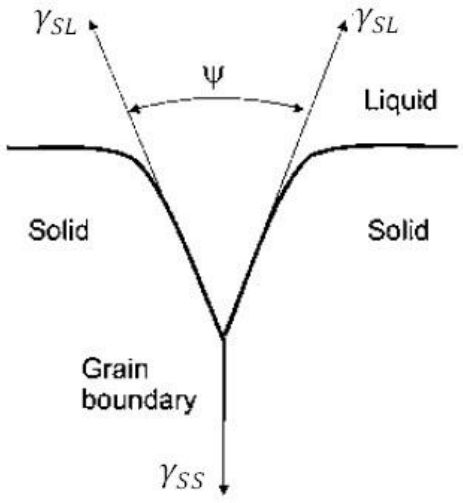

Figure 2-8. Dihedral angle at a two-grain juncture wetted by a liquid phase [32].

X is the size of the neck, β the angle formed by liquid meniscus and grain and $\Delta p = \gamma_{LV}\left(\frac{1}{h} - \frac{1}{r}\right)$ the pressure difference over the different radii of curvature. Small ψ result in a compressive force [32].

Initial stage – particle rearrangement

Once wetting has occurred, solid particles will rearrange into higher density packings due to the forces exerted by the liquid. Primary particle rearrangement takes place shortly after the formation of the liquid phase due to the surface tension force of the liquid film. At low contact angles, shrinkage occurs by approach of adjacent particles. Secondary rearrangement occurs in the case of liquid penetration of the grain boundaries leading to fragmented particles. Since dissolution of grain boundaries takes time, secondary rearrangement happens more slowly. Contact points of solid particles and sharp edges tend to dissolve due to their high chemical potential, thus smoothing the particles and enhancing rearrangement. In addition, liquid rearrangement by capillary action and sequential pore filling take place, small pores being filled first. Inhomogeneous particle packings may densify locally via solid state diffusion, while leaving large pores elsewhere that remain unfilled after firing [32].

Intermediate stage – solution-precipitation

The solution-precipitation stage is characterized by densification, coarsening and in some cases changes in grain shape. Small solid particles or contact points of particles dissolve due to their high chemical potential and reprecipitation occurs at locations of minimum chemical potential. Kingery's contact flattening model and densification accompanied by Ostwald ripening are used to describe the processes taking place in the intermediate stage [36]. Coarsening is observed towards the end of the stage.

Contact flattening is driven by the capillary force of the interparticle liquid film and results in dissolution of contact points. The flattening contact points approach, thus leading to densification. The rate of matter transport can be determined by diffusion through the melt or by the speed of the interface solution and reprecipitation reaction. In the first case, shrinkage scales with time t and particle radius D as follows [36]:

$$-\frac{\Delta L}{L_0} = \left(\frac{A\delta_L}{kT}\right)^{1/3}\left(\frac{t^{1/3}}{D^{4/3}}\right) \tag{15}$$

Here, δ_L represents the thickness of the liquid film, A a parameter that includes geometrical and physical constants such as the diffusion coefficient of solid through the liquid, the solubility of the solid in the liquid, the solid-liquid interfacial free energy and the atomic volume. kT is the product of Boltzmann constant and temperature.

For phase boundary reaction controlled densification, shrinkage is proportional to the square root of sintering time and the inverse of the particle radius [36]:

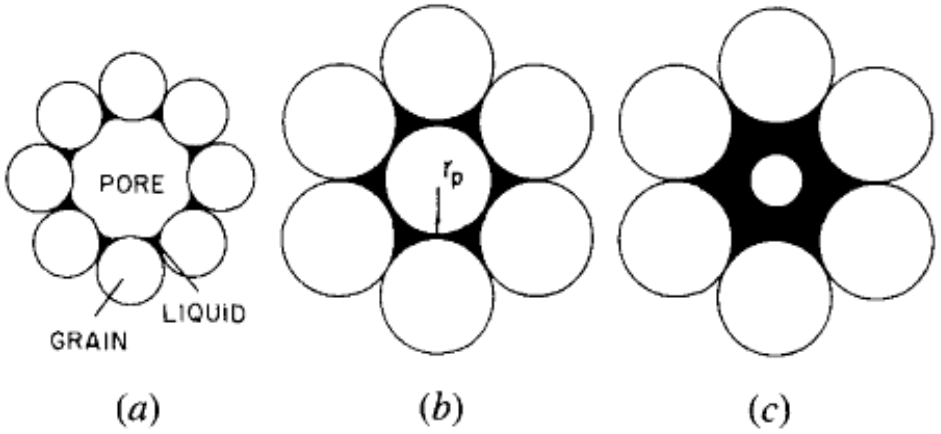

Figure 2-9. Evolution of liquid meniscus and pore filling during liquid phase sintering. (a) Initial meniscus shape prior to coarsening, (b) critical meniscus radius equal to pore radius (c) pore filling. Picture taken from [42].

$$-\frac{\Delta L}{L_0} = \left(\frac{B}{kT}\right)^{1/2}\left(\frac{t^{1/2}}{D}\right) \tag{16}$$

Where the parameter B again includes physical and geometrical constants.

Densification accompanied by Ostwald ripening involves the dissolution of smaller grains and their subsequent reprecipitation onto large grains. Since precipitation can only take place at locations unobstructed by neighboring grains, coarsening is accompanied by shape accommodation [36].

Final stage – pore removal

In the final stage, the above mentioned coarsening becomes dominant. A rigid network of solid-solid contacts forms, allowing solid state diffusion to take place. In addition, the filling of large pores results in the growth of adjacent grains into the newly formed liquid pockets [32]. Densification in this manner is slow; entrapped gases cause a pressure that reduces densification.

Pore filling model

Experiments do not support some of the assumptions made in the contact flattening model, such as approximately constant number and size of pores. It was therefore suggested that densification is driven by the filling of pores with the melt. This was later expanded into Kang's theory of pore filling driven by grain growth [43]. The pore filling model defines three stages according to the behavior of the liquid: The first stage includes liquid coagulation to minimize the liquid-vapor interfacial area; during stage two, liquid redistribution takes place followed by pore filling in the third stage. The latter stage is the slowest and thus governs liquid phase sintering kinetics.

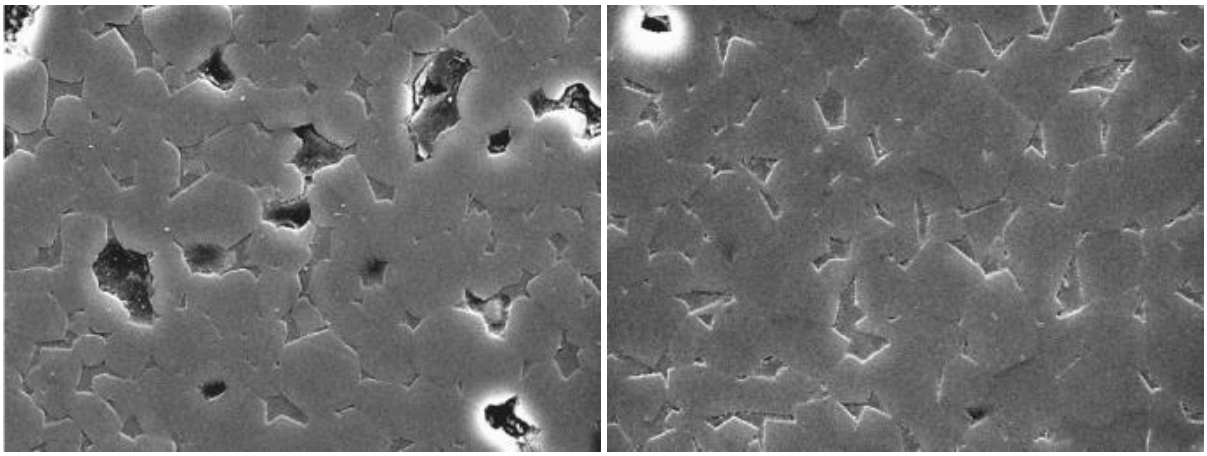

Figure 2-10. Microstructure of liquid phase sintered alumina during the intermediate (left) and final stage (right) exhibiting filled an unfilled pores [44].

Pore filling is driven by the difference in liquid pressure. The radius of the liquid meniscus at the pore surface increases during coarsening, as shown in Figure 2-9. Wetting and subsequent instantaneous pore filling occurs when the pore radius becomes equal to the liquid meniscus radius.

Liquid phase sintering of alumina with additions of CaO – Si_2O_3 – Al_2O_3

Dong et al. [44] have found that alumina sintered with 10vol% CaO – Si_2O_3 – Al_2O_3 (CAS) glass shows contact flattening of initially spheroidal grains. While the number of pores decreases with time, only a small increase in grain size was found. In contrast to the pore filling theory, small unfilled pores coexisted with larger filled pores, as shown in Figure 2-10, resulting in an unaltered pore size distribution during the intermediate stage. Trapped gases inside closed pores were found to be the reason for the reduced densification [45] [46].

2.3. Continuum mechanical description of sintering

The continuum mechanical description of sintering is commonly applied since it allows the consideration of macroscopic factors and their influence on densification [47]. The sintering body is viewed as a viscoelastic material whose response to an applied stress is described using a Maxwell element (combination of a spring and a dashpot). The viscoelastic response to an applied strain is the superposition of an instantaneous elastic strain and a time dependent deformation by viscous flow or creep [48]. However, Bordia and Scherer [49] [50] argued that the elastic strain component is negligible, thus allowing the description of the sintering body as a purely viscous solid. Hence, application of the elastic-viscous analogy [51] to the constitutive equations for a linear, elastic solid yields the constitutive equations for sintering of a linear, isotropic viscous material:

$$\dot{\varepsilon}_i^c = \dot{\epsilon}^f + \frac{1}{E^P}\left[\sigma_i - \nu^P(\sigma_j + \sigma_k)\right] \tag{17}$$

Here, the indexes $i \neq j \neq k$ take the values of 1, 2 or 3 representing the three principal axes. $\dot{\varepsilon}_i^c$ and $\dot{\epsilon}^f$ are the constrained and free strain rates, respectively; σ represents the stress. $\nu^P$and E^P represent the viscous Poisson's ratio and the uniaxial viscosity. The latter two parameters depend on the microstructure of the material, which in turn depends on the sintering stage. Thus, the evolution of the microstructure must be accounted for by changing values of $\nu^P$and E^P; in addition, $E^P$is a function of temperature [52]. The bulk and shear viscosities are related to $\nu^P$and E^P as follows [32]:

$$K_P = \frac{E^P}{3\,(1 - 2\nu^P)} \tag{18}$$

$$G_P = \frac{E^P}{2\,(1 + 2\nu^P)} \tag{19}$$

A different formulation of the constitutive equation for isotropic sintering that includes the sintering stress is given in eq. 20:

$$\dot{\varepsilon_{ij}} = \frac{\sigma'_{ij}}{2G_P} + \delta_{ij}\frac{\sigma_m - \sigma_s - \Delta p}{3K_P} \tag{20}$$

Here, σ_m and σ'_{ij} are the mean and deviatoric component of the external stress, δ_{ij} the Kronecker symbol, Δp the gas overpressure inside closed pores and σ_s the sintering stress.
In uniaxial load-assisted sintering, the following assumptions can be made: and $\sigma_j = \sigma_k = 0$ and when $\dot{\varepsilon}_i^c = 0$, $\sigma_i = \sigma_s$ .The uniaxial sintering pressure σ_s can thus be calculated using eq. 21:

$$\sigma_s = E^P\,\dot{\epsilon}^f \tag{21}$$

The viscous Poisson's ratio is related to the bulk and shear modulus in the following manner [53]:

$$\nu^P = \frac{3\,\frac{K_P}{G_P} - 2}{6\,\frac{K_P}{G_P} + 2} \tag{22}$$

The viscous parameters can be determined by sinter forging [54], cyclic loading dilatometry [55] or the bending creep test [56]. Determination of the viscous parameters by sinter forging requires a set of uniaxial load-assisted sintering experiments with different applied pressures. Axial and radial sintering

strains are recorded in-situ using laser-equipment. In order to avoid the formation of microstructural anisotropy due to the load, discontinuous experiments are carried out during which the load is only applied over a limited density range during the sintering cycle. The envelope of different sets of experiments is then plotted to generate stress and viscosity curves [57] [58]. Cyclic loading dilatometry is based on a similar principle; here, the load is applied for short times followed by periods of free sintering in order to remedy the microstructural anisotropy. Strains are recorded in-situ [55]. Finally, the bending creep test involves the application of a load onto a bending bar that is supported on both ends. The deflection rate in the specimen center is then measured and used to compute the uniaxial viscosity. Additional free sintering experiments are performed to obtain $\dot{\epsilon}^f$ [56].

In Table 2-1, values for the viscous Poisson's ratio for several sintering materials are summarized. Independent of the sintering mechanism, ν^Ptends to start at low values around 0.1 to 0.2 when density is low. At relative densities close 100%, ν^P approaches 0.5 which represents the values for an incompressible, isotropic viscous liquid. Values higher than 0.5 obtained from experiments are due to microstructural anisotropy that may arise during load-assisted methods for the determination of ν^P.

2.3.1. Sintering models

Since the viscous parameters included in eq. 17 depend on the microstructure of the sintering material, the uniaxial viscosity as well as the Poisson's ratio must be measured for a large number of points during the sintering cycle. Since this procedure is time-consuming, sintering models are applied in order to calculate the viscous parameters as a function of a variety of parameters, such as temperature, density or grain size. In the review of Green et al. [7], sintering models are categorized as micromechanical and phenomenological models.

Micromechanical models are based on the definition of an elementary cell including single or multiple particle contacts or an isolated pore. In case of solid state sintering, the dominant diffusion path is specified and the shrinkage of the cell is predicted. The sintering stress is then calculated using the techniques as described by Wakai et al. [59]. The sintering stress can be associated with the total energy of the pore volume, the pore curvature or the surface tension of the pores.

Early models were usually aimed at predicting viscous sintering. The most important micromechanical models valid for solid state sintering include the work of Ashby [60], who constructed sintering diagrams including a variety of sintering mechanisms. Each mechanism is assigned a field in the plane of neck/particle size ratio vs. temperature. The diagrams are constructed using neck growth equations based on simple geometric models as well as material constants such as diffusion coefficients.

Svoboda et al. [61] and Riedel et al. [62] started from the assumption that pores during intermediate and final stage sintering are in equilibrium and have uniformly curved surfaces with minimum energy. The sintering stress is assumed to be proportional to the pore surface curvature and the total pore volume. Here, grain boundary diffusion was set as dominant transport mechanism.

Table 2-1. Poisson's ratio of different materials.

Material	Sintering mechanism	Density range	ν_P	References
Alumina	Solid state	65% - 96%	0.20 – 0.43	[53]
Gd doped Ceria	Solid state	80% - 92%	0.34 – 0.44	[63]
Ca-aluminosilicate glass + alumina filler	Viscous	76% - 97%	0.10 – 0.60	[39]
Pb-borosilicate glass + alumina filler	Viscous	74% - 93%	0.25 – 0.45	[64]
WC-Co (experiment)	Liquid phase	55% - 100%	0.10 – 0.70	[65]
WC-Co (simulation)	Liquid phase	65% - 100%	0.15 – 0.50	[66]

McMeeking and Kuhn [67] have modelled diffusional creep of polycrystalline sintering materials. They as well started from the assumption that grain boundary diffusion is the dominant transport mechanism. This allows the derivation of shear and bulk viscosities that depend on the relative density and particle size. The model by Du and Cocks [68] also allows the prediction of creep deformation of sintering ceramics bodies and includes grain growth as well. Phenomenological models based on sinter forging experiments have been proposed by many researchers. Venkatachari and Raj's [69] findings have later been validated by Zuo et al. [53] in a discontinuous sinter forging experiment with alumina.

2.3.2. Sintering under geometric constraint

In the presence of a geometric constraint, internal tensile stresses may arise in the sintering body that cause significant differences from free sintering behavior. Among these effects, reduced densification kinetics and damage such as cracking, localized porosity maxima or shape distortion have been reported.

Several scenarios that bring about differential densification have been reported: Composites involving rigid particles inside a sintering matrix, sintering films attached to a rigid substrate, multilayer systems of two or more different materials and green bodies with density variations [7]. In addition, an external compressive stress can be applied to a sintering body. This stress enhances densification as compared to densification resulting solely from sintering stress [32].

2.3.3. Sintering of constrained films

Continuous sintering films attached to rigid substrates are the basis of many engineering applications such as solid oxide fuel cells [70] or thermal barrier coatings [71]. In Figure 2-11, a schematic of such

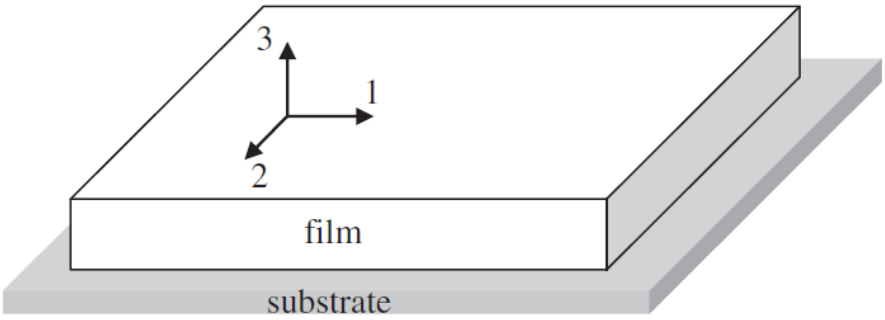

Figure 2-11. Schematic of sintering film on a rigid substrate [72].

a film is presented. The study of constrained film sintering using the continuum mechanical approach is based on the assumption of perfect adhesion of the film to the non-densifying substrate resulting in perfect constraint; *e. g.* the complete inhibition of in-plane shrinkage of the film. This inhibition results in tensile in-plane stresses that counteract densification as well as retarded sintering kinetics typical for constrained sintering. In addition, strain rate in the stress-free direction perpendicular to the substrate is enhanced compared to the free sintering strain rate since all shrinkage takes place in this direction.

Constitutive equation

The continuum mechanical description of continuous sintering films on rigid substrates dates back to the works of Scherer and Garino [73] as well as Garino and Bowen [52] who have introduced the assumptions of perfect constraint ($\dot{\varepsilon}_1^c = \dot{\varepsilon}_2^c = 0$), zero out-of-plane stress ($\sigma_3 = 0$) and non-zero in-plane stress components ($\sigma_1 = \sigma_2 \neq 0$), into eq. 17, thus obtaining the following relationships for the in-plane stress and out-of-plane strain rate:

$$\sigma = -\frac{\dot{\epsilon}^f E_p}{1-\nu^P} \tag{23}$$

$$\dot{\varepsilon}_3^c = \frac{(1+\nu^P)}{(1-\nu^P)}\dot{\epsilon}^f \tag{24}$$

Substituting the isotropic, free densification rate $\left(\frac{\dot{\rho}}{\rho}\right)_f = -3\dot{\epsilon}^f$ into eq. 24 yields the following equation for the constrained film densification rate:

$$-\dot{\varepsilon}_3^c = \left(\frac{\dot{\rho}}{\rho}\right)_c = \frac{1}{3}\frac{(1+\nu^P)}{(1-\nu^P)}\left(\frac{\dot{\rho}}{\rho}\right)_f \tag{25}$$

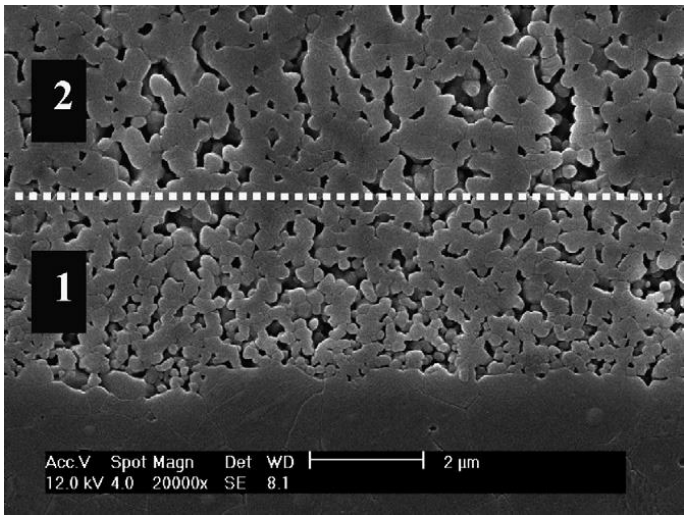

Figure 2-12. Example for a transverse isotropic microstructure in a sintered alumina film including elongated pores along the out-of-plane axis. Picture taken from [34].

According to [52], eq. 25 is well suited to describe the reduced densification kinetics of viscous sintering films. In the case of solid state sintering films, eq. 25 strongly overestimates the densification of many systems, especially in technically relevant systems such as alumina [74] or yttria stabilized zirconia [75]. Thus, it was concluded that the assumption of an isotropic material is not valid. Since the deviation from the isotropic model occurs after a certain sintering time, the development of an anisotropic microstructure was held responsible. This conclusion is supported by gradients in density and porosity along the vertical direction that have been observed in sintered alumina [34] [76] and zirconia films [77]. In both systems, preferential pore orientation was observed along the thickness direction with elliptical elongation that is severe near the substrate and then declines with increasing thickness. An example for such a microstructure is provided in the micrograph in Figure 2-12.

Two reasons are put forward to explain this behavior: Firstly, particle rearrangement is supposed to be hindered at the substrate. In addition, neck formation and growth is favored in the unstressed direction, *e. g.* in the direction perpendicular to the substrate, whereas necks may break due to the tensile stresses imposed by the substrate. This was validated in discrete element simulations by Martin et al. [78] who observed the behavior of particle contacts in different orientations. A similar anisotropy was found in pressure-assisted sintering of alumina specimens that is thought to develop as a consequence of the preferential growth of necks perpendicular to the loading direction [79].

As a consequence, anisotropic constitutive laws for sintering bodies were established by Bordia et al. [80]. Here, the special case of a transversely isotropic material was treated. Such materials display an isotropic microstructure in two dimensions that differs from the microstructure along the third direction. This kind of anisotropy is found in sintering films, where the in-plane directions are equal in terms of microstructure but elongated pores are aligned along the out-of-plane dimension. The analysis starts from the constitutive equations for the principal stresses of a viscous body:

$$\dot{\varepsilon}_1^c = \dot{\epsilon}_1^f + \frac{\sigma_1}{E_1^P} - \frac{\nu_{21}^P \sigma_2}{E_2^P} - \frac{\nu_{31}^P \sigma_3}{E_3^P} \tag{26a}$$

$$\dot{\varepsilon}_2^c = \dot{\epsilon}_2^f + \frac{\sigma_2}{E_2^P} - \frac{\nu_{12}^P \sigma_1}{E_1^P} - \frac{\nu_{32}^P \sigma_3}{E_3^P} \tag{26b}$$

$$\dot{\varepsilon}_3^c = \dot{\epsilon}_3^f + \frac{\sigma_3}{E_3^P} - \frac{\nu_{23}^P \sigma_2}{E_2^P} - \frac{\nu_{13}^P \sigma_1}{E_1^P} \tag{26c}$$

In the case of a transversely isotropic sintering film, the in-plane viscous coefficients are bound to be equal while the out-of-plane stress and in-plane strain rates are zero. Thus, insertion of $\dot{\epsilon}_1^f = \dot{\epsilon}_2^f$, $E_1^P = E_2^P$, $\nu_{12}^P = \nu_{21}^P$, $\nu_{13}^P = \nu_{23}^P$, $\nu_{31}^P = \nu_{32}^P$, $\dot{\epsilon}_1^c = \dot{\epsilon}_2^c = 0$ and $\sigma_3 = 0$, into eqs. 25 yields expressions for the in-plane stress and out-of-plane densification rate analogous to eqs. 22 and 23, but with five different constitutive parameters [80]:

$$\sigma = -\frac{\dot{\epsilon}_1^f E_1^P}{1 - \nu_{12}^P} \tag{27}$$

$$\dot{\varepsilon}_3^c = \dot{\varepsilon}_3^f + \frac{2\nu_{13}^P}{1 - \nu_{12}^P} \dot{\epsilon}_1^f \tag{28}$$

The constrained densification rate then becomes

$$\left(\frac{\dot{\rho}}{\rho}\right)_c = \frac{\nu_{13}^P}{1 - \nu_{12}^P} \left[\left(\frac{\dot{\rho}}{\rho}\right)_f + \dot{\epsilon}_3^f\right] - \dot{\epsilon}_3^f \tag{29}$$

Anisotropic constitutive laws have been successful in reproducing the sintering behavior of alumina films on rigid substrates. Li et al. [72] contrasted their predictions of the anisotropic model for constrained sintering by Cocks with literature results on the densification of alumina films and found a good agreement between experimental and calculated curves.

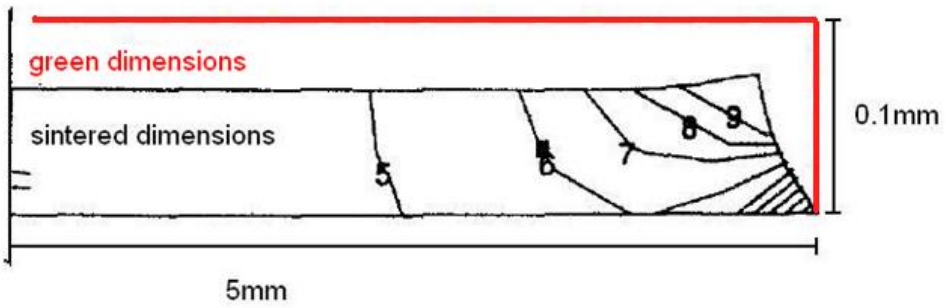

Figure 2-13. Density distribution obtained by viscoelastic finite element modelling [81]. Density is maximal at the free film corner and decreases with increasing distance from the edge.

2.3.4. Simulation of the sintering of patterned films

Simulations of film densification, shape distortion or crack growth are of technical interest in order to ensure reliability and dimensional control in practical applications. Several simulation methods are available. On the particle scale, the discrete element method allows the observation of individual particle contacts. This method is therefore suited for the study of phenomena on the grain scale, such as microstructural development or cracking. In addition, finite element simulations based on different constitutive sintering models are widely used to study phenomena on the macroscopic length scale such as deformation and density distribution in films bonded to rigid substrates.

Finite element simulations

Several simulation approaches are available to predict shape distortion and densification of sintering films. Conventional finite element modelling has been applied to simulate the sintering behavior of films attached to a rigid substrate by implementing constitutive sintering models. Zhao and Dharani [81] have devised a viscoelastic finite element model and simulated the constant heating rate sintering of zinc oxide films. They were successful in reproducing the reduced densification rate observed in experiments. In addition, edge effects such as shape distortion and non-uniform local density (Figure 2-13) were found whilst properties were homogeneous in the uniformly stressed film center. Delamination of the constrained corner from the film edge was not simulated due to the boundary condition of fixed nodes on the substrate. It was, however, predicted since Young's modulus was found to be minimal at this location.

Finite element modelling of sintering films was further improved by Olevsky et al. [82]. Their multiscale approach involves a Monte-Carlo model in order to account for the changing microstructure during sintering, a factor that has not been included by Zhao and Dharani. Here, a similar shape distortion and density distribution as in [81] was predicted; delamination, however, could not be studied.

Kraft and Riedel [83] have developed an FEM simulation approach for solid state sintering that can be applied to thin films. Simulation of the three sintering stages is carried out using a simplified description of rearrangement and neck formation and by describing pore surfaces during the second and third stages as equilibrium surfaces. The main diffusion path is along the grain boundaries; bulk and surface diffusion are also considered. Microstructural development such as grain coarsening is included in the model. Eq. 20 is used as constitutive equation for the macroscopic strain rate. This means that the sintering stress is incorporated into the model. This approach has been applied to the simulation of sintering films on rigid substrates. Here, perfect adhesion to the substrate is not enforced as in other FEM methods; by contrast, failure initiation by a maximum nominal stress criterion is included. This has the advantage of simulating delamination from the substrate [84].

Discrete element simulations

Whenever phenomena at the length scale of the particle size are concerned, the finite element method is not adequate. Thus, particle-based simulation methods have been developed that allow the characterization of individual particle contacts throughout the sintering process. The discrete element method (DEM) is based on the representation of every individual grain as a distinct particle whose interactions with adjacent particles obey certain force laws [85]. Since long computation times are necessary for high numbers of particles, this method is primarily applied to simulate representative volume elements of sintering bodies or thin, patterned films.

The first step in a DEM simulation is the assignment of spatial coordinates to all particles, thus generating the green microstructure. Then, an initial velocity, mass and moment of inertia are assigned to each particle. At this point, distributed properties may be introduced, thus providing an opportunity to generate inhomogeneous microstructures. Unlike in molecular dynamics, particle rotation is also allowed in DEM.

One possible method to generate the initial particle configuration has been used by Henrich et al. [86]. Here, spherical particles with the desired particle size distribution, but half the intended particle radius are placed into a box at random locations. Care has to be taken to avoid overlaps between particles. This procedure is continued until the desired green density is achieved. Then, the particle radius is expanded until its actual value is re-established; overlap is avoided by assigning repulsive forces to each particle. Coordination number is subsequently increased by a DEM simulation including a long-range pair potential that draws particles toward each other.

The simulation algorithm is as follows [86]: During each time interval, the simulation starts by determining the nearest neighbors of each particle within a cut-off radius. Then interparticle forces $\boldsymbol{F}_{ij}$ and torque $\boldsymbol{T}_{ij}$ are determined and velocities $\boldsymbol{v}_i$ calculated via Newton's equations of motion:

$$\frac{d}{dt}\boldsymbol{r}_i = \boldsymbol{v}_i \tag{30a}$$

$$m\frac{d}{dt}\boldsymbol{r}_i = \boldsymbol{F}_i^{tot} = \sum_{j\neq i}\boldsymbol{F}_{ij} \tag{30b}$$

$$I\frac{d}{dt}\boldsymbol{\omega}_i = \boldsymbol{T}_i^{tot} = \sum_{j\neq i}\boldsymbol{T}_{ij} \tag{30c}$$

This is typically followed by the integration of the equations of motion:

$$\boldsymbol{r}_i(t+\Delta t) = \boldsymbol{r}_i(t) + \Delta t\boldsymbol{v}_i(t) + \frac{1}{2m}(\Delta t)^2\boldsymbol{F}_i^{tot} \tag{31a}$$

$$\boldsymbol{v}_i\left(t+\frac{1}{2}\Delta t\right)=\boldsymbol{v}_i(t)+\frac{1}{2m}\Delta t\,\boldsymbol{F}_i\ (t) \tag{31b}$$

$$\boldsymbol{\omega}_i\left(t+\frac{1}{2}\Delta t\right)=\boldsymbol{\omega}_i(t)+\frac{1}{2I}\Delta t\,\boldsymbol{T}_i\ (t) \tag{31c}$$

Then, appropriate constitutive equations for sintering have to be chosen in order to provide the force laws for simulation. DEM simulations based on the models of Riedel et al [62] [87] and Bouvard and McMeeking [88] have been reported in the literature. In the first case, grain boundary diffusion is viewed as the dominant densification mechanism and pore shape is assumed to be in equilibrium. Using these assumptions, expressions for the normal forces between neighboring particles are derived. Furthermore, tangential viscous forces are established to quantify the resistance against sliding [78]:

$$\boldsymbol{T}_\mathrm{s}\sim\eta\,\frac{du}{dt} \tag{32}$$

Here, η is a viscosity parameter that has to be determined experimentally or fitted and that has two components [86]. η_{part} designates the interparticle viscous force. In addition, a viscous drag η_{sub} can also be imposed between particles and a substrate. This has been done by Martin and Bordia [78] as well as Rasp et al. [13] in order to study constrained sintering. The latter have also used a factor λ that scales the normal forces between particles and the substrate in comparison to the forces acting between film particles.

Several constrained sintering problems have been studied using DEM: Martin and Bordia have investigated the sintering of pillar-like structures bonded to rigid substrates [78]. They found porosity gradients along the out-of-plane direction that resulted in rising density with increasing distance from the substrate, as observed in real sintering films. These gradients turned out to be independent of the pillar shape (rectangular or cylindrical). Furthermore, the viscous drag imposed by the substrate greatly influenced the development of microstructural anisotropy, resulting in large density gradients for high values of η_{sub}. In addition, non-zero lateral strains were found at a few microns distance to the substrate; this was ascribed to the limited propagation of substrate drag throughout the film thickness. The same group has studied the evolution of defects during constrained sintering [89] by observing the propagation of an intentionally introduced elliptical crack in a sintering specimen that is constrained in the direction perpendicular to the precrack. Here, crack propagation was found to be enhanced for large values of interparticle friction η_{part}. In addition, an influence of green density on the cracking was found: High-density specimens showed crack propagation to a smaller degree than low density specimens. Both effects were ascribed to the impeded crack healing in specimens where little rearrangement is possible. The toughness of sintering bodies with different green densities was investigated by observing the behavior of individual particle necks ahead of a crack tip by Jauffrès et al. [90].

Rasp et al. [91] have studied the influence of the coordination number in the green body on densification and found reduced sintering kinetics for small initial coordination numbers. The development of microstructural anisotropy during pressure assisted sintering was investigated by Wonisch et al [79]. They found that microstructural anisotropy developed as a consequence of an anisotropic distribution of particle contact area. Large contact area developed in the loading direction that led to low axial strain rates during subsequent free sintering.

2.3.5. Sintering with rigid inclusions

The presence of non-sintering second phase particles interferes with the densification of the matrix material. For solid state sintering materials, densification is significantly reduced and can be completely inhibited at high volume fractions of second phase. In addition, cracks originating from the interface may form. Viscous sintering materials are also prone to reduced densification, but to a lesser extent. Three reasons for this behavior are commonly put forward: First, differential sintering between matrix and rigid particles leads to transient stresses. Second, a rigid network is formed if the volume fraction exceeds the percolation threshold. Third, regions in the immediate vicinity of the particles may present an inhomogeneous microstructure and experience differential densification [32].

Calculation of the transient stresses is based on the composite sphere model. This approach is in turn based on the assumption that a rigid particle acts as the core surrounded by a circular cladding of matrix phase. Once the matrix starts to shrink, the inclusion is subjected to compressive stresses whereas the surrounding matrix experiences tensile stresses that are maximal at the interface and decrease with increasing distance by a factor $1/r^3$ [32]. Both purely viscoelastic models [92] and combined models using the viscoelastic analogy alongside experimentally derived, density dependent moduli [93] have been used to calculate the matrix stress. However, both models predict physically unreasonable stresses up to 100 times higher than the sintering stress that would cause far greater damage than observed in practice. Scherer then proposed two models based on the elastic-viscous analogy. The first approach is a composite sphere model [94] that yields a matrix stress σ_m up to twice as high as the sintering stress:

$$\frac{\sigma_m}{\Sigma} = \frac{\upsilon_i}{\upsilon_i + \frac{3K_m}{4G_m}} \tag{33}$$

Here, K_m and G_m are the moduli of the matrix and υ_i represents the volume fraction of inclusion particles. The reduced strain rate of the composite $\dot{\varepsilon}_c$ is expressed in terms of the free strain rate of the matrix material via eq. 34:

$$\dot{\varepsilon}_c = \frac{(1-v_i)}{1+\frac{3K_m}{4G_m}v_i}\dot{\varepsilon}_{fm} \quad (34)$$

The second approach is a self-consistent model and leads to the same expressions as the composite sphere model with the exception that the shear modulus of the composite G_{cs} is used instead of G_m. Scherer's models succeed in describing viscous sintering matrix materials with inclusion contents up to 15%vol. At higher contents, percolation of the inclusions comes into play. This leads to a continuous network whose rigidity impedes further densification of the matrix. In the absence of wetting of the inclusions by a glass phase, the percolation threshold lies at 16%vol in 3D network [32]. In the case of polycrystalline materials, a noticeable reduction of the sintering rate occurs at inclusion volume fractions as low as 5vol%, far below the percolation threshold. Lange's [95] model states that the premature densification and grain growth between neighboring rigid inclusions leads to a dense annulus that encloses regions of lower density. Thus, even in the absence of actual percolation, a sort of rigid network appears that resists densification. Furthermore, it was found that localized inhomogeneities due to disrupted powder packaging in the vicinity of the particles also contributed to the reduction of the densification rate [32]. This is referred to as desintering.

2.4. Fracture mechanics

In linear elastic fracture mechanics (LEFM), three cracking modes are defined depending on the nature of the applied stress [96]:

Mode I: Crack opening caused by a tensile load normal to the crack plane

Mode II: Sliding of crack faces by in plane shear loading

Mode III: Out-of-plane shear.

The stress field at a crack tip subjected to mode I loading is described by the stress intensity factor K_I [96]:

$$\sigma_{ij} = \frac{K_I}{\sqrt{2\pi r}} f_{ij}(\theta) \quad (35)$$

Where r is the distance to the crack tip and $f_{ij}(\theta)$ a function based on the distance and angle with respect to the crack tip.

When an infinite specimen of an isotropic, elastic material is flawed and subjected to an external load, stress concentration takes place at the flaw endpoints. A stress concentration factor k_t is defined as the ratio of maximum stress at the endpoint of the major axis of the elliptical flaw divided by the applied load:

$$k_t = \frac{\sigma_A}{\sigma} = 1 + \frac{2a}{b} \quad (36)$$

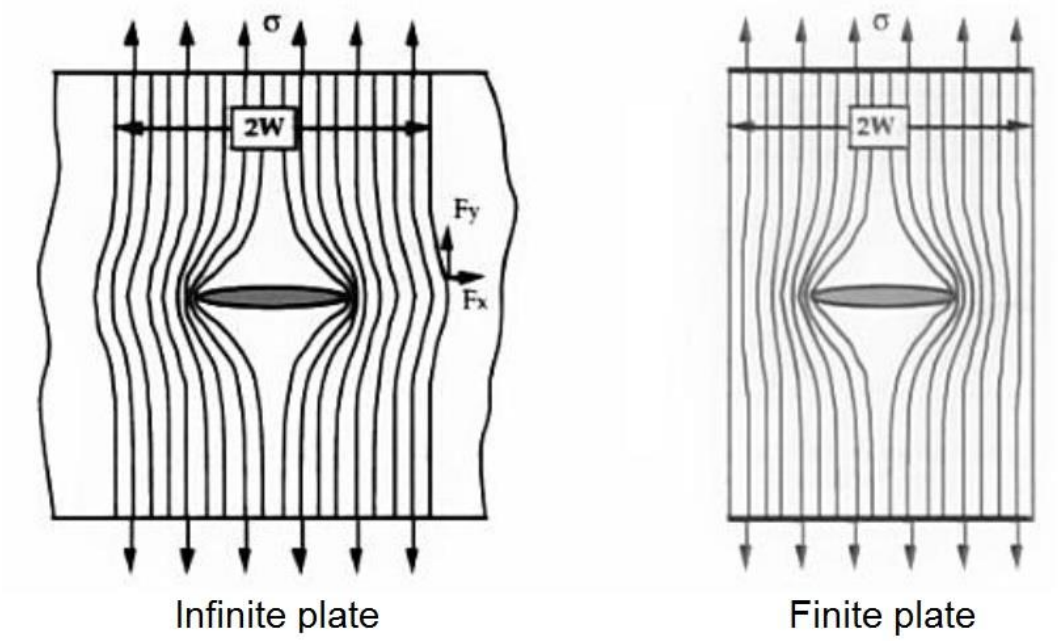

Figure 2-14. Schematic representation of stress buildup due to the proximity of the plate edges to the crack. Picture taken from [96].

Where a and b are the major and minor axis length, respectively. For elliptical flaws, aspect ratio dominates stress intensity. For round flaws, $a = b$ and the stress concentration factor is always 3. Stresses are maximal at the crack tip and then decrease with increasing distance. Cracking occurs when K exceeds a critical value (K_{IC}). In addition the external stress, specimen geometry and finite specimen size influence the stress intensity factor [96]:

$$K_I = \sigma\sqrt{\pi a} f\left(\frac{a}{W}\right) \tag{37}$$

Here, a is the major axis length of the elliptical crack, W the lateral dimension of the specimen and $f\left(\frac{a}{W}\right)$ a correction factor depending on specimen shape. In case of a finite specimen size in the dimension of the crack, several functions are available for $f\left(\frac{a}{W}\right)$; all of them lead to an increase of the stress intensity factor with increasing a-to-W ratio, with K_I tending towards infinity as the ratio approaches unity. The reason for the stress buildup in the direction of finite lateral dimension is given in Figure 2-14. Here, the lines of force are compressed parallel to the edge since boundary conditions require zero force at free edges. Since local stress is proportional to line spacing, a stress buildup occurs perpendicular to the edge.

When studying thin plates of material, stresses in the thickness direction are zero while in-plane stresses are not, as already assumed for sintering thin films. This condition is called plane stress [96].

2.5. Creep fracture

During tertiary creep, microcavities form at grain boundaries and coalesce into microcracks until the formation of a macrocrack leads to catastrophic failure. Creep failure therefore occurs by intergranular cracking. Depending on stress and temperature, different fracture mechanisms predominate. An overview of temperature and stress dependent fracture mechanisms can be found in fracture mechanism maps available for different materials. [97].

Creep fracture in alumina occurs via the formation of two types of voids: Grain boundary cracks and spherical voids on grain boundaries. Cracks are initiated at triple points due to grain boundary sliding. These microcracks subsequently propagate locally along the grain boundaries. Furthermore, pore-like voids form perpendicular to the tensile stress and coalesce by diffusion in pure alumina or viscous flow in case of glassy grain boundary phases. The volume fraction of voids increases linearly with creep strain; the slope increases with grain size [98].

2.6. The film-substrate interface

2.6.1. Film adhesion mechanisms

Surface adhesion is a complex topic that requires knowledge of mechanics, chemistry and materials science. Adhesion is defined as the spontaneous contact between two surfaces brought into a small distance within each other [99]. Well-adhered surfaces cannot be severed without overcoming the work of adhesion. Forces that contribute to film adhesion can be provided by Van-der-Waals forces (dispersive adhesion), mechanical clamping, chemical reactions that result in new interfacial phases, interdiffusion and wetting of the substrate by a liquid.

In case of films made of the same species as the substrate, as in alumina films made of high purity powder attached to smooth sapphire substrates, no chemical compounds form at the interface. Thus, adhesion is mainly determined by dispersive forces; in addition, interdiffusion may take place at elevated temperatures that can lead to growth of the single crystal sapphire substrate into the polycrystalline alumina film [100]. When a rough substrate is employed, film adhesion may be enhanced by mechanical locking of powder particles into the substrate grooves. In addition, contact area is larger in rough substrates, thus enhanced adhesion by Van-der-Waals forces may occur.

When a platinum interlayer is deposited on the sapphire substrate prior to coating with alumina, the different materials may undergo chemical reactions during sintering. Prediction of these reactions is difficult since a suitable Pt-Al-O phase diagram is lacking as of 2014. However, experiments on diffusion bonded platinum-alumina joints used as biocompatible implants did not show any reaction products of platinum and alumina when heated to temperatures up to 1400°C in air and no interdiffusion was observed [101]. Thus, in the absence of a wetting liquid, Van-der-Waals forces and mechanical locking are likely to contribute to the adhesion of the platinum film.

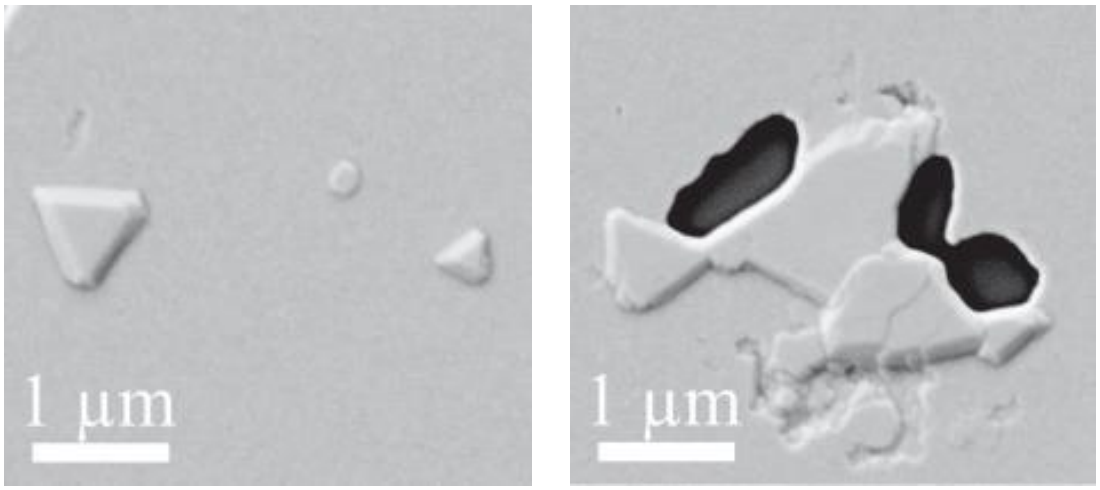

Figure 2-15. Hillock formation on platinum film deposited onto yttria stabilizes zirconia substrate. Left: Isolated hillocks, right: Concurrent formation of holes and hillocks [102].

For example, Floyd ([103] cited in [104]) has shown that a reduction in alumina grain size reduces the bond strength of metal-ceramic seals and surface roughening of ceramic is a common technique substrates in order to enhance film adhesion in the fabrication of microelectronic systems [105].

2.6.2. High temperature stability of alumina-platinum interfaces

Platinum films deposited by sputtering are often subject to in-plane stresses that can be released by prolonged heat treatments. This stress release leads to the disruption of the film structure and has been ascribed to various creep mechanisms [102]. Close to room temperature, strain relaxation occurs via vacancy diffusion from the film surface to the grain boundaries [106]. At higher temperatures, diffusional creep, power law creep, grain boundary gliding or grain rotation have been reported. Starting from 650°C, hillock formation has been observed in sputtered platinum films on zirconia single crystal substrates that was accompanied by film rupture at 700°C [102]. This effect is shown in Figure 2-15 and was ascribed to the concurring minimization of strain energy and surface energy. At 900°C, prolonged thermal treatment of platinum layers can cause complete film breakup into separated islands. This agglomeration process is believed to be driven by the reduction of free surface energy by surface diffusion of platinum. Lifetime of the platinum layers can be increased by adding capping layers or by increasing the film thickness [107]. Furthermore, breakup of very thin platinum films (15nm) into concentric circular arrays of droplets during annealing at 1000°C has been observed. Here, droplet formation due to Rayleigh instability is presented as the underlying mechanism [108].
In addition, the formation of a volatile oxide at temperatures beyond 500°C can lead a significant reduction in film thickness upon heating [109]. With increasing temperature, the formation of PtO_2 becomes faster and lifetime is significantly reduced. At 1250°C, the loss of film thickness is 100nm/h, while at 1500°C, it is 240nm/h [110].

2.6.3. Continuum mechanical analysis of the film substrate interface

Jagota and Hui [111] [112] have provided a description of the film-substrate interface of sintering films and its influence on lateral shrinkage and crack propagation. In their model, the three-dimensional governing equations of viscous materials (eq. 26a-c) are reduced to a two-dimensional form by averaging stresses and velocities through the thickness. Boundary conditions are set based on the assumption that the shear stress τ along the interface is proportional to the in-plane shrinkage velocity v_i via a proportionality factor m that can be expressed in terms of adhesion properties and film thickness:

$$\tau = -m^2 v_i \tag{38}$$

Normalization of the governing equations by the defect size in the film leads to the interface friction coefficient k:

$$k \equiv \frac{m^2(1-(\nu^P)^2)}{E^P} \tag{39}$$

k represents the inverse of the slip distance of the free edge in a sintering film. An experimentally accessible expression for k is given by Bordia and Jagota [113]:

$$k = -\frac{\varepsilon_{free}(1+\nu^P)}{\Delta y} \tag{40}$$

Where Δy is the slip distance of the upper free film corner and ε_{free} represents the sintering strain of a free film with the same starting density after being exposed to the same sintering cycle as the film in question. This expression is valid for small changes in k and ν^P during densification. Small values of k correspond to large slip distances and thus indicate poor adhesion, whereas large values of k describe stiff interfaces. Friction decreases with increasing film thickness. Some properties of sintering films, such as crack growth, can be expressed in terms of the friction coefficient.

Experimental values for the interface friction coefficient are not available in the literature. However, a normalized friction coefficient has been calculated as the inverse slip distance for alumina [113] and YSZ films [114] on smooth sapphire substrates as well as platinum coated sapphire substrates. A summary is given in Table 2-2. Regardless of the film material, sintering films on sapphire substrates presented stiff interfaces whereas platinum interlayers resulted in compliant interfaces. Polycrystalline alumina substrates caused higher friction than their smooth, single crystal counterparts, indicating a possible effect of surface roughness on film adhesion.

The interface friction coefficient depends on film thickness as well as the interface adhesion properties: For well-bonded, stiff interfaces, k is inversely proportional to the film thickness t, whereas in the case of compliant interfaces, it scales inversely with $\sqrt{t}$.

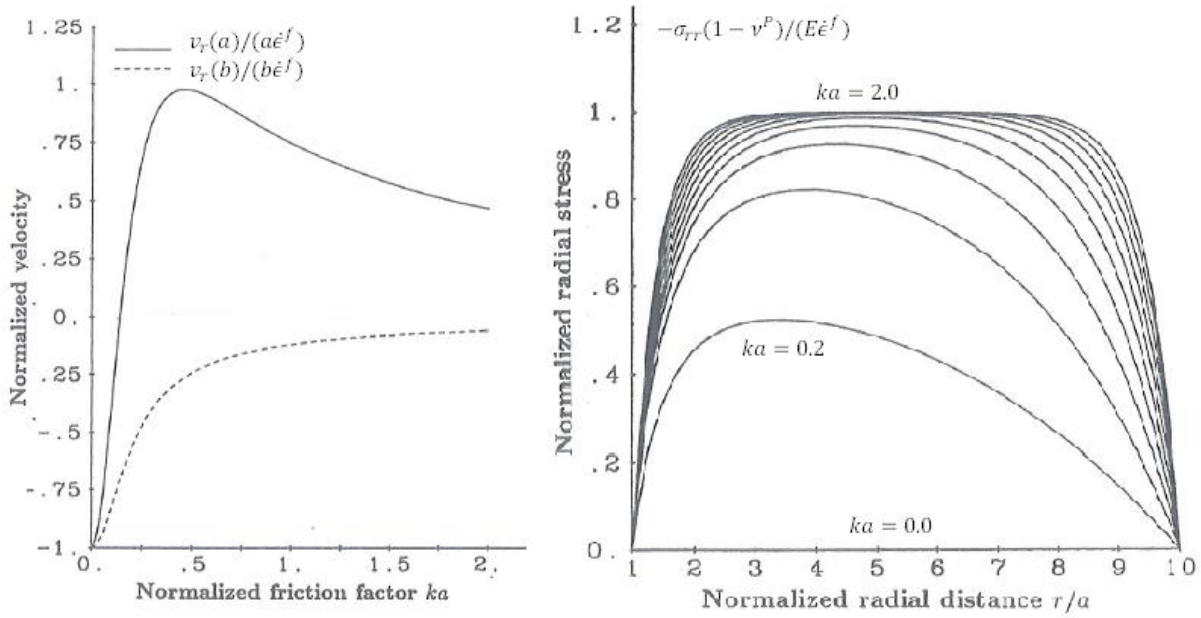

Figure 2-16. Normalized velocity and normalized radial stress for an annulus with a ratio of 10 8outer to inner radius) with increasing distance from the inner free edge. *a* represents the inner radius [111].

2.6.4. Sintering of annular films

The sintering behavior of annular films with inner radius a and outer radius b bonded to rigid substrates can be expressed in terms of the friction coefficient. Parameters such as the lateral shrinkage of the inner and outer free edge as well as tangential and radial stresses in the film are different for compliant and stiff interfaces. As shown in Figure 2-16 (right), high values of k lead to a rapid increase of radial stress starting from the unstressed free edges until a plateau is reached. Small values of k result in a slow stress increase with a maximum in the center of the annulus. This maximum is lower than the plateau values for high k. Consequently, for stiff interfaces, the in-plane velocity of the free edges is dampened in the center of the annulus while lateral shrinkage does occur near the free edges. In the case of compliant interfaces, lateral shrinkage extends throughout the annulus until outer and inner free edges interact, resulting in a positive in-plane velocity at the inner free edge that causes the inner hole to shrink (see Figure 2-16 left).

2.6.5. Crack growth criteria

Within the framework of the interface friction coefficient, predictions on the stability of a precrack in a sintering film can be made. Expressions for the stress intensity factor K_I for a crack in a homogeneous sintering film are derived for the limiting cases of very high and low friction [115]. The

Table 2-2. Normalized friction parameter for different film/substrate material systems.

Film material	Substrate material	Thickness t [µm]	$k_{norm} = -\frac{1}{\Delta y}$ [µm^{-1}]	Interface type	Reference
Alumina	Sapphire	11.8	0.091	Stiff $k \sim \frac{1}{t}$	[113]
		24.7	0.053		
		42.5	0.024		
Alumina	Pt/sapphire	11.8	0.018	Compliant $k \sim \frac{1}{t^2}$	
		24.7	0.015		
		42.5	0.012		
YSZ	Sapphire	10	0.066	Stiff $k \sim \frac{1}{t}$	[114]
		20	0.033		
		40	0.016		
YSZ	Pt/sapphire	10	0.015	Compliant $k \sim \frac{1}{t^2}$	
		20	0.011		
		40	0.007		
YSZ	Alumina	10	0.091	Stiff $k \sim \frac{1}{t}$	
		20	0.045		
		40	0.023		

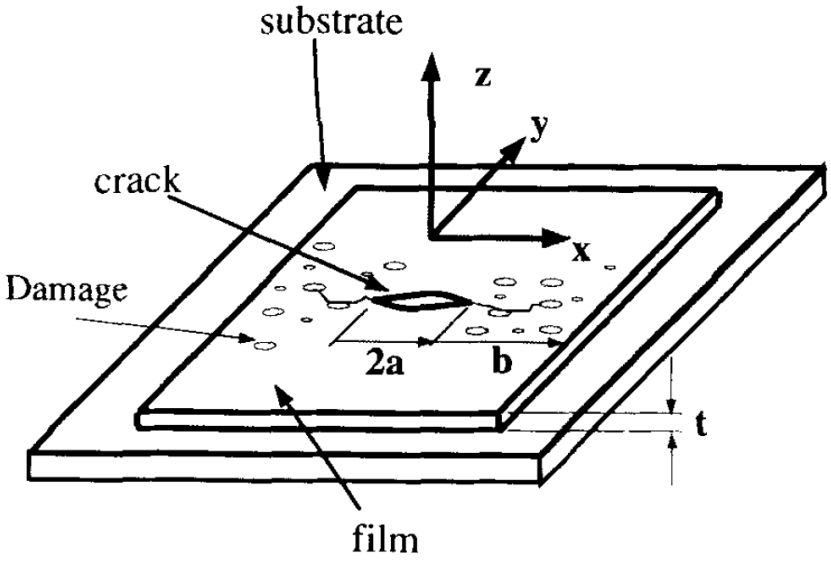

Figure 2-17. Growth and damage formation of an elliptical precrack in a thin, sintering film with finite distance b between precrack front and film edge. Picture taken from Ref [113].

description is valid for an elliptical crack in a thin film of finite dimensions as shown in Figure 2-17.

$$K_I = \sigma\sqrt{\pi a}\, g(ka) \tag{41}$$

With

$$g(ka) = \begin{cases} 1 & (ka \ll 1) \quad (42a) \\ \sqrt{\dfrac{1-\nu^2}{\pi ka}} & (ka \gg 1) \quad (42b) \end{cases}$$

K_I increases as the friction is reduced but does not exceed the limit set for small ka. This means that high friction results in low stress concentration and thus low probability of crack propagation.

The crack is expected to grow by creep crack growth if the contact area ahead of the tip is reduced. Here, two contributions come into play: First, the tensile stresses at the crack tip cause the contact area to decrease, whereas the ongoing sintering process drives neck growth.

Thus, the condition for crack growth is a reduction in contact area right ahead of the crack tip. Based on this condition, criteria for crack growth are developed that can be solved for the limiting cases of very high and low friction:

$$\sqrt{\frac{a}{R'}} > \sqrt{2}\left[\frac{3}{2\pi}\frac{\dot{A}^S}{R^2\dot{\varepsilon}}\frac{(1-\nu)}{(1-2\nu)}\frac{1}{f(\alpha)} + 1\right] = \sqrt{\frac{a_c}{R'}} \qquad (ka \ll 1) \tag{43a}$$

$$\sqrt{\frac{1}{kR'}} > \sqrt{\frac{a_c}{R'}}\sqrt{\frac{\pi}{1-\nu^2}} \qquad (ka \gg 1) \tag{43b}$$

Here, a is the main axis length of the elliptical precrack, R' is the distance between the crack tip and the first particle contact, R the particle radius, a_c the critical crack length, k the interface friction coefficient, $\dot{A}^S$ the rate of increase of the contact area during sintering, ν the viscous Poisson's ratio, $\dot{\varepsilon}$ the linear macroscopic shrinkage rate and $f(\alpha)$ a constant depending on the sintering mechanism. These criteria can be used for the construction of fracture mechanism maps in which fields of crack growth and crack arrest are given in the plane of normalized friction parameter vs. normalized precrack length. Here, the limiting cases of very low crack length and high friction determine the fields of crack arrest; in the intermediate area, crack growth is observed.

3. Experimental procedure

All patterned ceramic layers in this work have been deposited by Micro-molding in Capillaries (MIMIC). The elastomer stamps have been custom made for this work by casting a liquid elastomer onto silicon wafers coated with a patterned photoresist layer. For this purpose, six wafers with spin coated photoresist layer of different thicknesses were patterned. The pattern design and the experimental layout is elucidated in the following section.

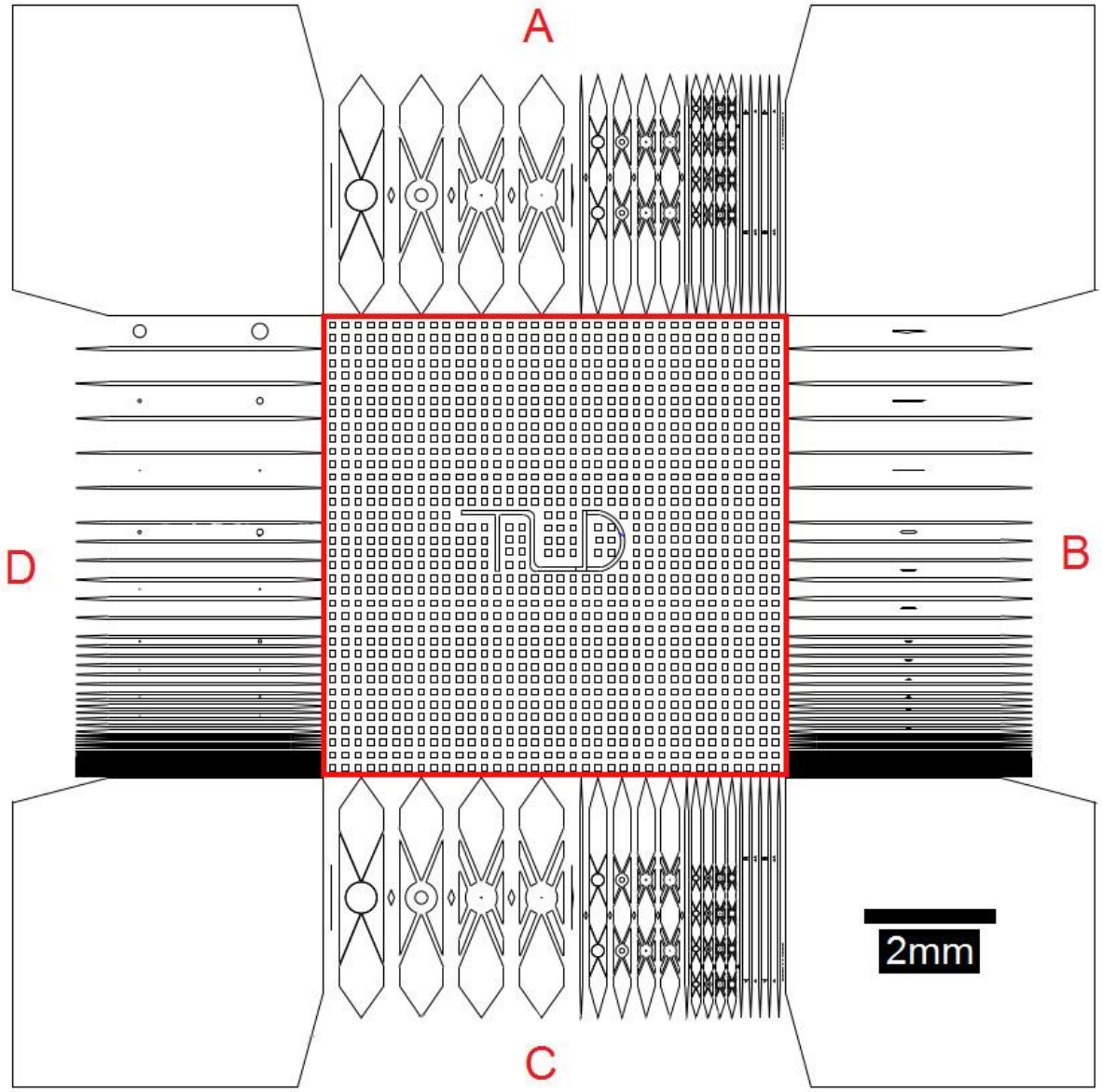

Figure 3-1. Pattern design including rectangular slurry reservoir (red box) and four arrays of ring and stripe structures.

3.1. Pattern design

The stamp pattern was created using Computer Aided Design software (AutoCAD 2009, Autodesk, Germany). An assembly of stripes, elliptical and round stress concentrators and rings is included for the study of constrained densification, crack initiation and growth. This pattern is shown in Figure 3-1. The pattern includes the following structures: The quadratic area inside the red box (7.2mm x 7.2mm) contains a two-dimensional array of squares of 100µm edge length. This section is intended to form the slurry reservoir of the stamps. The four rectangular areas, marked A, B, C and D (3.6mm x 7.2mm), contain the structures to be studied. In all four areas, line patterns connect the slurry reservoir with the structures. Areas A and C are symmetrical and consist of arrays of ring structures in three different sizes as well as an array of four stripes of 100µm width in which different patterns of multiple elongated cavities acting as stress concentrators are located. The total size of the patterned area is therefore 14.4mm x 14.4mm. To facilitate the deposition process, a non-functional edge area is added, thus increasing the stamp area to 18mm x 18mm.

Area B houses arrays of stripes of different widths (5µm, 10µm, 25µm, 50µm, 100µm, 250µm and 500µm). Every array contains at least six stripes of each size. From 50µm to 500µm, every second stripe contains an elliptical cavity whose length is equal to the stripe width. These ellipses are located in the center of the stripes and are oriented parallel to the stripe edges.

Area D is the mirror image of area B with exception of the cavities. Here, two round cavities are introduced into every other stripe instead of ellipses.

3.1.1. Stripe patterns

The stripe features are located in areas B and D. In Figure 3-2, area D is shown. Black and white areas represent uncoated and coated areas in the wafers, respectively. Coated areas in the wafers will form channels in the stamp which in turn produce alumina stripes. Starting from the left, arrays of six stripes of equal width are arranged with declining width from 500µm to 5µm. The arrays are arranged as follows:

1. six stripes of 500µm (red)
2. six stripes of 250µm (green)
3. six stripes of 100µm (yellow)
4. six stripes of 50µm (blue)
5. six stripes of 25µm (not in figure)
6. ten stripes of 10µm (not in figure)
7. 13 stripes of 5µm (not in figure)

5µm wide stripes included in the pattern proved to be too small to be correctly reproduced in the photoresist coating. For the 10µm wide stripes, the same holds true in case of photoresist coatings with a thickness of 16µm or higher.

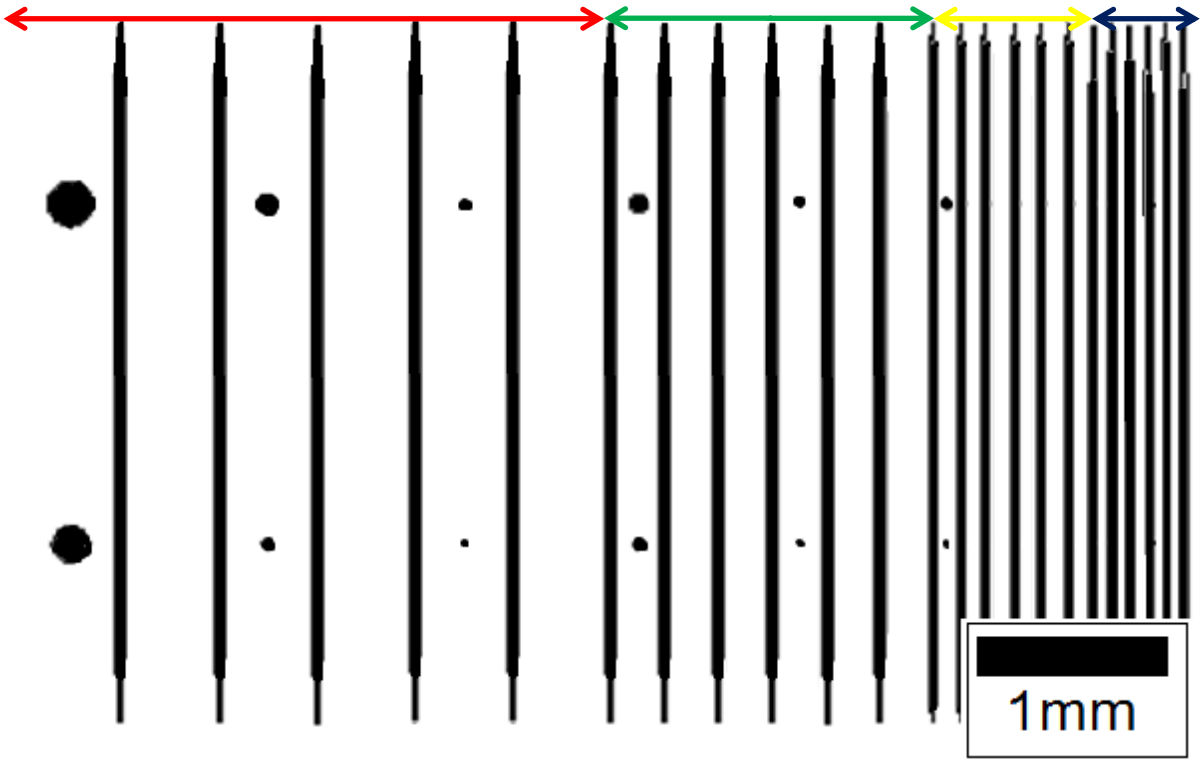

Figure 3-2. Stripe pattern with circular cavities in area D.

To facilitate the flow of the slurry through the stripes, the stripe width directly at the reservoir is larger than the values enumerated above. Along the first 500µm of the stripes, the width decreases continuously until it reaches the desired values. Along the last 500µm of the stripe, its width increases again.

The nomenclature of the stripes includes their thickness and width. A 100µm wide stripe made from a stamp with a thickness of 8.41µm is referred to 8µm x 100µm. For simplicity, the thickness of the elastomer stamps is used to denominate the ceramic samples and rounded to an integer.

3.1.2. Stress concentrators

Round cavities

Round and elliptical stress concentrators have been included into the stripe patterns to study crack initiation and growth in films with limited lateral feature size. The round cavities are introduced into the stripes in area D in Figure 3-1. The center of the hole is always located in the middle of the stripe, as shown in Figure 3-2. Their radii range from 2.5µm to 125µm. In all patterned wafers, even the smallest holes were well formed. Their nomenclature is based on the stripe width and cavity radius: A cavity of 20µm in diameter located in a 50µm wide stripe is referred to as C50-20.

Table 3-1. Single elliptical stress concentrators in Area B.

Feature denomination	Stripe width / major axis [µm]	Stripe N°	Aspect ratio
E500-12.5	500	1	12.5
E500-25	500	3	25
E500-50	500	5	50
E250-6.25	250	1	6.25
E250-12.5	250	3	12.5
E250-25	250	5	25
E100-5	100	1	5
E100-10	100	3	10
E100-20	100	5	20
E50-5	50	1	5
E50-10	50	3	10
E50-25	50	5	25

Elliptical and elongated cavities

Single elliptical cavities are introduced in area B in Figure 3-1 in the same fashion as the round cavities with the exception that only one ellipse was introduced in every other stripe. The major axis always equals half the stripe width; therefore the total ellipse length is identical to the stripe width. There are three ellipses in each length with varying aspect ratios. The elliptical cavities and their sizes are listed in Table 3-1.

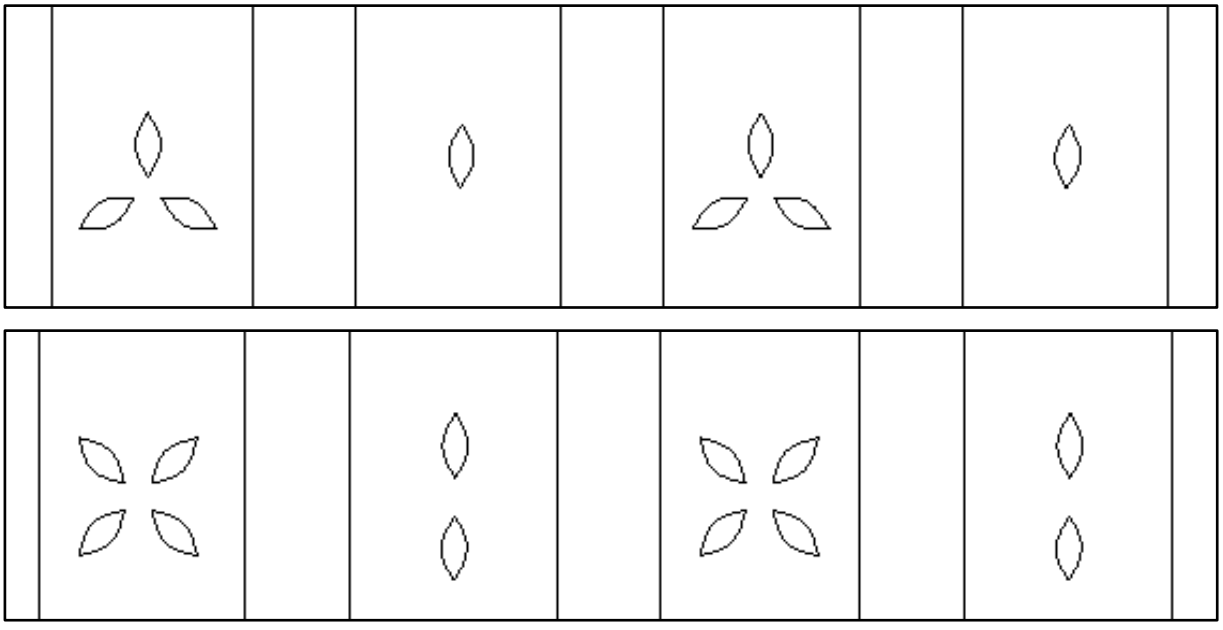

Figure 3-3. Multiple elongated stress concentrators located in Areas A and D.

All elliptical cavities were well formed in the patterned wafers; however, during the first stamp fabrication, the smallest ellipses (type E50-0.04) were ripped off. This occurred in the wafers with the thickest photoresist coating (28µm and 32µm). In all other wafers, the ellipses were well formed.
Multiple elongated cavities were introduced into the 100µm stripes on the right hand side of areas A and C in the pattern for the purpose of studying the crack growth in complex stress fields. Aspect ratio is always 2.5 and the total length is 31µm. They are arranged in single, double, triple and quadruple formation as shown in Figure 3-3.

3.1.3. Ring structures

The ring structures for the experimental validation of Jagota's and Hui's model [111] located in areas A and C are shown in Figure 3-4. The ring structures in the pattern come in three different sizes; the outer radius takes values of R_o = 250µm, R_o = 100µm, and R_o = 50µm. The rings are arranged in arrays of four rings with varying ratios of inner to outer radius. The ratio of the inner to outer radii declines from left to right within each array. For the R_o = 250µm rings, one array is included in the pattern (red box); for the R_o = 100µm rings, two arrays (green boxes); and in case of the R_o = 50µm rings, four arrays are used (yellow boxes). The nomenclature of the rings is based on diameter of the outer ring and the ratio of inner to outer diameter. A ring with outer and inner diameters of 100µm and 40µm, respectively, is referred to as R100-0.40.
Furthermore, channels oriented 45° with respect to the horizontal line are introduced. These channels connect the rings to the slurry reservoir. Before sintering of the patterned films, these channels must be removed prior to sintering to ensure free movement of the outer and inner edges.
All but the thinnest rings (aspect ratio 0.98) were correctly reproduced in all wafers during the patterning process.

3.2. Sample preparation

3.2.1. Wafer fabrication

The pattern designs described above were used to fabricate an intermediate mask with electron beam lithography (Institut für Mikrostrukturtechnik, Karlsruhe Institute of Technology, Germany). The mask contains both a positive and a negative reproduction of the pattern. Via X-ray lithography, six photoresist coated silicon wafers with different thicknesses were irradiated through the mask and developed (see schematic representation in Figure 3-5 left). Three of the wafers were coated with PMMA-950k, a positive photoresist, the other three wafers with SU-8, a negative photoresist.

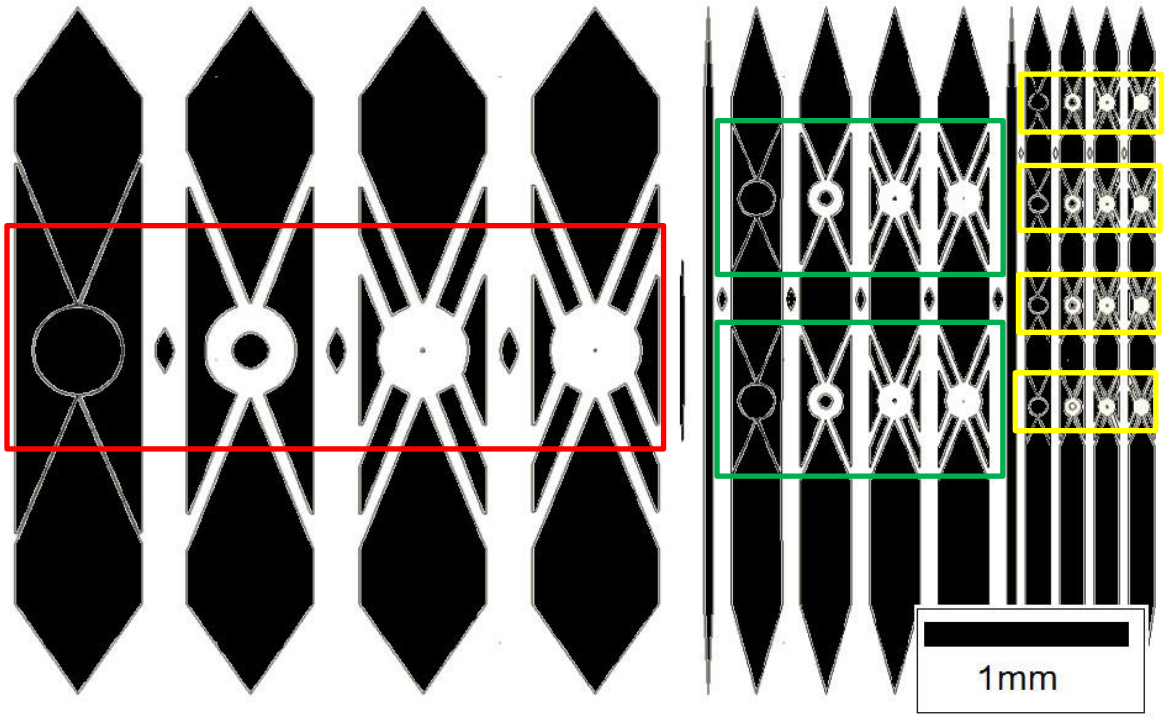

Figure 3-4. Picture of areas A and C with ring structures and multiple stress concentrators.

Therefore, in the SU-8 coated wafers the positive patterns turn into negatives and vice versa. In addition to the custom made wafers, a wafer with a 4.5µm thick photoresist coating containing only stripes was used that has been characterized in a previous work [28]. In Table 3-2 the obtained wafers are listed along with the minimum and maximum profile depths of the corresponding stamps measured by white light interferometry (NV6200, Zygo Lot GmbH, Darmstadt, Germany). The profile depth depended strongly on feature width; wide channels usually had a lower height than thin channels.

3.2.2. Stamp fabrication

Elastomer stamps were produced by casting a liquid mixture of polydimethylsiloxane (PDMS, Sylgard 184, Dow Corning, Midland, USA) with its hardener onto the wafer and subsequent degassing and curing at 80°C for 4h. A schematic representation of the process is given in Figure 3-5 (left). Before the casting step, the wafers were treated with Tridecafluoro-1,1,2,2-tetrahydrooctyltrichlorosilane, ABCR, Karlsruhe, Germany) for 30min in a desiccator to facilitate the separation of the dried stamp. After curing, the stamps were peeled off, cleaned for 3min in isopropanol in an ultrasonic bath and kept in a sealed sample box. The height of the stamp channels was measured by means of white light interferometry (NV6200, ZygoLot GmbH, Darmstadt, Germany). In Figure 3-6, optical micrographs of stamp area A before and after sample preparation are presented. It is shown that the narrowest features have not been successfully reproduced in the patterned wafers.

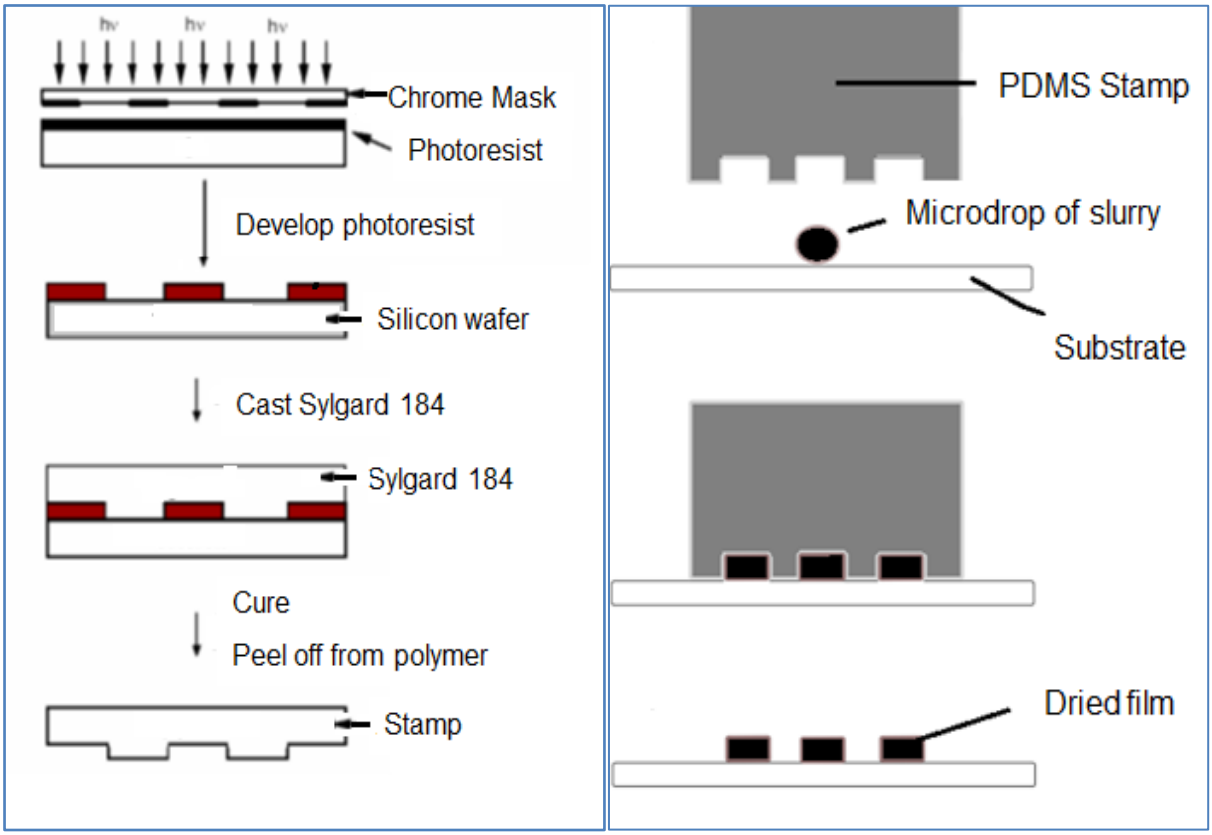

Figure 3-5. Schematic representation of the wafer patterning [9] (left) and the film deposition processes (right).

All the other features were molded without damage, such as irregularities due to air bubbles. Stamp surface was found to be smooth. As a general rule, the patterning process is less successful for the thick photoresist coatings: In case of the stripe patterns, the 5µm wide stripes were damaged in all wafers, whereas the 10µm were damaged in all wafer with profile depths greater or equal 16µm.

Table 3-2. List of wafers with minimum and maximum stamp profile depth.

Profile height	**Photoresist**	**H_{min} [µm]**	**H_{max} [µm]**	**Stripe pattern**
S5	SU-8	4.57	4.57	100µm stripes only
S6	PMMA-950k	6.10	6.35	complete
S16	PMMA-950k	15.54	16.00	complete
S32	PMMA-950k	32.25	32.44	complete
S8	SU-8	8.38	8.45	complete
S12	SU-8	12.15	12.29	complete
S27 - 1	SU-8	25.20	26.07	complete
S27 - 2	SU-8	27.71	28.62	complete

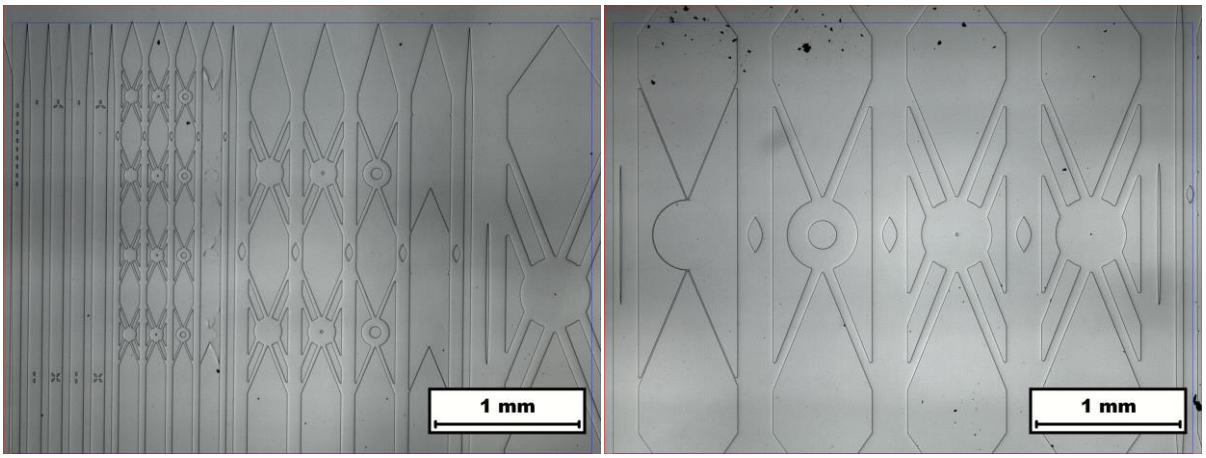

Figure 3-6. Optical micrograph of stamp area A before use (left) and after deposition and cleaning (right).

The narrowest rings could not be reproduced in any of the wafers. Furthermore, some ceramic particles remain attached to the stamp after deposition, despite repeated ultrasonication in isopropanol. Since these impurities can cause cracking, stamps were discarded after use and new stamps were fabricated for every specimen.

3.2.3. Slurry preparation

Solid state sintering

The aqueous slurry used for film preparation was made of 50vol% alumina powder with an average particle size of d_{50}=150nm (TM-DAR, Taimei Chemicals, Japan) dispersed in deionized water. Its pH was set to 10 by adding concentrated ammonium hydroxide and 0.7mg/m² of dispersant (Dolapix CE 64, Zschimmer Schwarz, Germany) per surface area of powder was added to the suspension. The slurry was continuously stirred and cooled in ice during the fabrication process and then deagglomerated for ten minutes in an ultrasonic disperser (UP 200S, Dr Hielscher GmbH, Teltow, Germany). Before use, the slurry was kept on a roll bank for 24h. Each 50mL batch of slurry was used for a maximum period of 4 weeks under constant rolling. The high solid loading was chosen to minimize drying shrinkage and stresses that may lead to cracking around cavities in the green samples.

Liquid phase sintering

For the study of the influence of a transient liquid phase on the constrained densification, liquid phase forming sintering additives ($CaCO_3$ and SiO_2) were added to the alumina powder. These additives form a ternary glass with the alumina matrix during the sintering cycle. A similar coated powder approach has been successfully used in bulk samples [116] where an alumina powder was coated with

CaO and SiO_2 by a co-precipitation method. A liquid phase formed due to the reaction of these additives with the alumina matrix according to the pseudobinary phase diagram in Figure 3-7. This glass formation was achieved by a 30min calcination step at 900°C prior to sintering.

Since bulk samples of the TM-DAR powder used in the solid state sintering experiments of this work show very high densification after 20min at 1400°C even without doping, a slightly coarser alumina powder (AKP-30, Sumitomo Chemical, Tokyo, Japan) with d_{50}=0.3-0.4µm than in the solid state sintering experiments was used. This helps to avoid the formation of a rigid skeleton by solid state sintering at temperatures below the formation of the liquid phase. Coarser powders could not be used as a minimal channel height to particle size ratio of 20 must be maintained to ensure a successful MIMIC process.

The coated powder approach has several drawbacks for the study of constrained liquid phase sintering: Firstly, the amount of liquid phase is not known precisely throughout the sintering cycle; secondly, recrystallization occurs due to the reaction with the alumina matrix, and thirdly, the rather high temperature of 1400°C for the onset of liquid phase sintering that does not allow the use of TM-DAR alumina powder used in the solid state sintering experiments. The use of a ternary Si-Al-Ca glass powder with low glass temperature, no reaction with the alumina matrix and no recrystallization was first intended, but then abandoned as co-stabilization of the studied glass compositions with alumina was not possible due to the different pH values for maximum zeta potential and severe ion leaching of the sub-micron sized glass particles that resulted in a high slurry viscosity. Therefore, the coated powder approach was chosen despite the above mentioned shortcomings.

The coated powder was prepared as follows: 5wt% of the sintering additives was added to the alumina powder in a fashion that the molar ratio of CaO to SiO_2 is 1:1 after precipitation. As CaO cannot be stabilized in an aqueous slurry due to its solubility, $CaCO_3$ nanopowder with d_{50}=90nm (Plasmachem GmbH, Berlin, Germany) was added to the alumina powder. $CaCO_3$ decomposes to CaO and CO_2 when heated to 900°C [117] and can be stabilized in water using Dolapix CE 64 in small amounts [118]. SiO_2 was obtained from the hydrolysis of tetraethylorthosilicate (TEOS, Sigma Aldrich, Germany) onto the mixtures. Batches of Al_2O_3 – $CaCO_3$ – TEOS mixture were dissolved in 200mL semiconductor grade ethanol (Puranal, Sigma Aldrich, Germany) in 500mL PA66 milling crucibles. Ball milling (Pulverisette 5, Fritsch, Idar-Oberstein, Germany) was carried out for the purpose of homogenization for 2h at 150rpm using yttria stabilized zirconia milling beads with 1cm in diameter. Then 200mL of deionized water and 20mL NH_4OH were added to the mixture to speed up the hydrolysis of TEOS. The mixture was again ball milled for 1h and subsequently dried at 90°C for 24h.

An aqueous slurry with a solid content of 40vol% was prepared under constant stirring and ice cooling. The initial pH was set to 9 using NH_4OH. After every addition of 1g, a short ultrasonification cycle (30s) was necessary to disperse the powder. After completion of the powder addition, ten ultrasonification cycles of 1min each were undertaken to deagglomerate the powder.

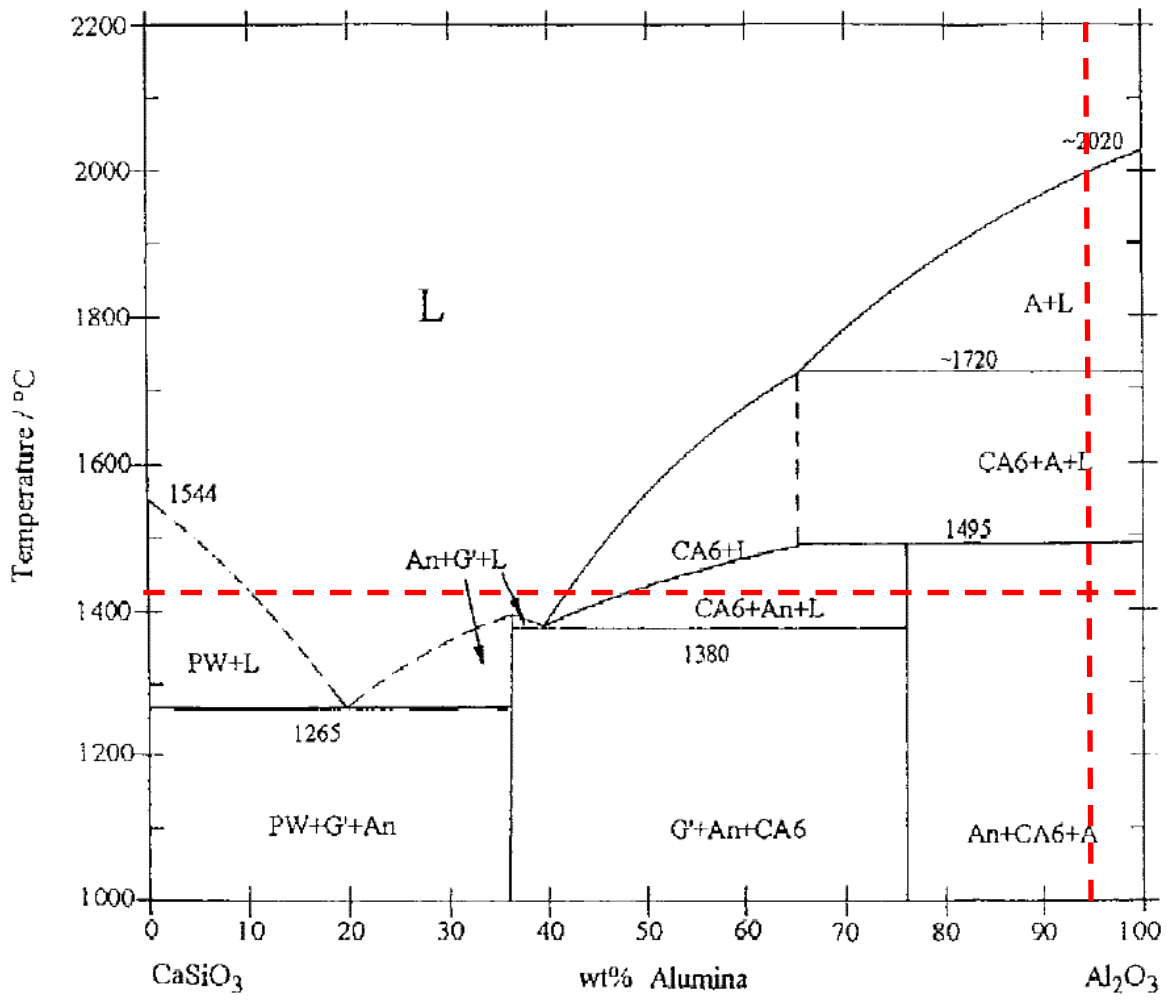

Figure 3-7. Pseudobinary phase diagram of wollastonite – alumina mixtures (section through the tertiary $CaO–SiO_2–Al_2O_3$ phase diagram at a $CaO:SiO_2$ ratio of 1:1. L=Liquid, PW= Pseudowollastonite ($CaO·SiO_2$), An=Anorthite ($CaO·Al_2O_3·2SiO_2$), G'=Gehlenite ($2CaO·Al_2O_3·SiO_2$), A=alumina (Al_2O_3), CA_6=calcium hexaluminate ($CaO·6Al_2O_3$). Taken from Ref. [116].

Between each deagglomeration step, the powder was cooled down to 7°C in a refrigerator. The slurry was then kept at 7°C and continuously stirred prior to deposition. Before every deposition, ultrasonification was repeated. The exact amounts of material are given in Table 3-3. The slurry and some of the 8µm samples used in this work were fabricated by Fabian Grimm within the framework of his bachelor's thesis [119].

As evident from the phase diagram in Figure 3-7, no liquid is present at 1425°C and 5wt% additive concentration. However, since glass formation occurs locally, not all matrix material reacts with the glass formers. Liquid formation is possible over a wide range of concentrations from ca. 10wt% up to 40wt% of alumina.

Table 3-3. Composition of the coated powder and slurry.

Material	Density [g/cm^3]	Molar mass [g/mol]	Amount [g]
Coprecipitation			
Alumina	3.98	101.96	38,0
TEOS	0.94	208.32	3,56
$CaCO_3$	2.73	100.09	1,72
Slurry preparation			
H_2O	1.00	---	24.24
Dolapix CE 64	1.20	---	0.78
Coated alumina	3.87	---	64.64

3.2.4. Substrate preparation

Four different types of substrates were used: Smooth sapphire, rough sapphire and platinum coated smooth sapphire. The smooth sapphire substrates (Crystec GmbH, Berlin, Germany) had a surface roughness of R_a<0.5nm according to the manufacturer. For the study of rough sapphire, the unpolished surface was used whose surface roughness measured using white light interferometry is Ra=0.9 ± 0.3µm.

The samples were soaked for 2h in NaOH, cleaned in isopropanol in an ultrasonic bath for 3min, rinsed with acetone using a paper towel and finally rinsed in ethanol and blown dry with compressed nitrogen. The surface was observed using an optical microscope to ensure that it was free of residue. Substrates that underwent an unsuccessful deposition cycle were cleaned in the same fashion and reused.

For fabrication of platinum coated sapphire substrates, two different coating methods were used. One type of coated samples was prepared by discontinuous sputtering using a sputtering cycle of 4 x 4min at 40mA (Emitech K950X, Quorum Technologies, Ontario, Canada). The samples were annealed at 400°C for 2h directly after sputtering to avoid crack formation due to stress development during the sputtering process. These platinum coatings had an initial thickness of ca. 0.30 ± 0.02µm and could withstand sintering temperatures of up to 1250°C for 4h without complete evaporation of the layer.

A second type of platinum coating able to withstand prolonged exposure to 1350°C was provided by Dr. Shunyi Li (Surface Science group, Department of Materials Science, TU Darmstadt). These samples were coated by continuous DC sputtering that resulted in a layer thickness of 0.36 ± 0.01µm. The surface roughness after sputter coating is supposed to be equal to the uncoated surface, however, during sintering an increase of roughness in the Pt layer due to hillock and hole formation is expected.

Some of the specimens on rough and platinum coated substrates (discontinuously sputtered) were provided by Peter Keil within the framework of his bachelor's thesis [120].

3.2.5. Film deposition

Before deposition, the stamps were subjected to oxygen plasma etching at 40mA for 60s (Polaron PT7100, Quorum Technologies, Sussex, UK). This step renders the stamps hydrophilic for 30min by the exchange of surface methyl groups by hydroxide groups, thus reducing the contact angle with water. This enables the slurry to wet and penetrate the channels [28]. A micro-drop of slurry was then deposited onto the substrate and the stamp was manually placed on top and squeezed gently to ensure contact with the substrate. The drop was placed exactly in the middle of the stamp pattern. The samples were then kept at 7°C under constant spraying of deionized water into the atmosphere during 30min as low temperatures and high ambient humidity help avoid diffusion of water into the stamp during the hydrophilic period. The samples were observed through the transparent stamps to make sure that no detachment of the slurry from the stamp takes place during this period, as this is a sign that drying occurs during the hydrophilic stage. The latter has to be avoided to ensure high green densities and crack-free samples by slow drying. After this period, the samples were placed in a drying cabinet and dried at 40°C in uncontrolled atmosphere for up to 4h depending on the thickness (drying condition I). Some samples were dried at 10°C and 90% ambient humidity in a drying cabinet and during the hydrophilic period and then kept at 40°C and 10% ambient humidity in the same cabinet (drying condition II). Unless stated otherwise, the samples used for evaluation were dried according to drying condition I.

After the drying step, the stamp was peeled off the substrate and discarded. A new stamp was fabricated for every sample to avoid cracking around grooves made by residual particles from prior depositions.

3.2.6. Bulk samples for free sintering experiments

Accompanying free sintering experiments were carried out for the solid state sintered 8µm x 100µm stripes. For this purpose, cylindrical bulk specimens with matching green densities were prepared as follows: ~3.5 ± 0.2g of pure TM-DAR powder were dry pressed for 1min at 13kN in a cylindrical pressing die with 12mm in diameter. Subsequent cold isostatic pressing (KIP 100E, Karl Otto Weber GmbH, Remshalden, Germany) at 250MPa for 1.5min lead to specimens with a height of 13.8mm ± 0.5mm , a diameter of 11.8mm and green densities of 58.6% ± 0.75%.

Free sintering was carried out using the hot forging apparatus described in [121]. Sintering was carried out at 1250°C and 1450°C for 4h using a heating rate of 25°C/min up to 1200°C and 10°C/min up to the isothermal holding time. At 1250°C, the samples were stabilized using a small load of 10N. This corresponds to a pressure of ca. -0.1 MPa and is substantially smaller than the loads used by other researchers (-1.1MPa and higher) on the same powder at the same temperature [53] as well as the sintering stress found in TM-DAR alumina specimens (-2 to -4MPa at 1250°C) [57]. Thus, anisotropy is not expected in the alumina specimen and thus no deviation from free sintering behavior should

occur. Some of the free sintering experiments were carried out by Dr. Jesus Gonzalez (Friedrich Schiller Universität Jena).
Since bulk specimens with green densities matching the 27µm x 100µm stripes could not be prepared using the above mentioned route, free sintering data obtained by DEM simulations were provided by Tobias Rasp (Fraunhofer Intitut für Werkstoffmechanik, Freiburg, Germany).

3.3. Sintering and characterization

3.3.1. Choice of specimens suitable for evaluation

Since MIMIC is a manual process, every specimen has a unique appearance. Thus, all dried specimens were observed under an optical microscope to ensure that all structures to be studied were well formed. As the stamp channels were not always entirely filled with slurry, the length of the stripes varied from 500µm to 3000µm and not all cavities were well formed in most samples. Sample quality and penetration length decreased with increasing thickness.
In case of the solid sintering stripes, a thickness dependent minimum length L_{min} was chosen in a fashion that lateral shrinkage in the direction parallel to the stripe edge was 1% or less during sintering at the maximum isothermal holding time at 1450°C. This minimum length was 500µm for all thicknesses up to 16 µm and 1200µm for 27µm thick specimens. Furthermore, the stripe must be clearly separated from the neighboring stripes along a length that equals at least five times the stripe width. In Figure 3-8, an optical micrograph of a dried 27µm thick specimen is presented with adequate dimensioning.
The quality criteria for the **stripes** are:

- Total pattern length L1 exceeds thickness dependent minimum length L_{min}
- Distance to stripe endpoint L3 exceeds $L_{min}/2$ to avoid edge effects
- Length of clearly separated part of the stripes L2 exceeds fivefold stripe width
- Well-formed edges

In case of the liquid phase sintering stripes, the minimum length was set to 500µm for all thicknesses. During the patterning of rough sapphire substrates, the stamp did not adhere perfectly to the substrates and some of the slurry flowed into the substrate grooves directly adjacent to the channels. Therefore, stripes on rough substrates can never be clearly separated. Thus, the 3rd quality criterion was waived in this case.
The **round, elongated and elliptical cavities** were not always well formed. In case of the thick films, cracking around long elliptical cavities was observed during drying. These cavities were identified under an optical microscope and not used for evaluation. In Figure 3-9, a well formed round cavity is shown. Quality criteria for the **cavities** are:

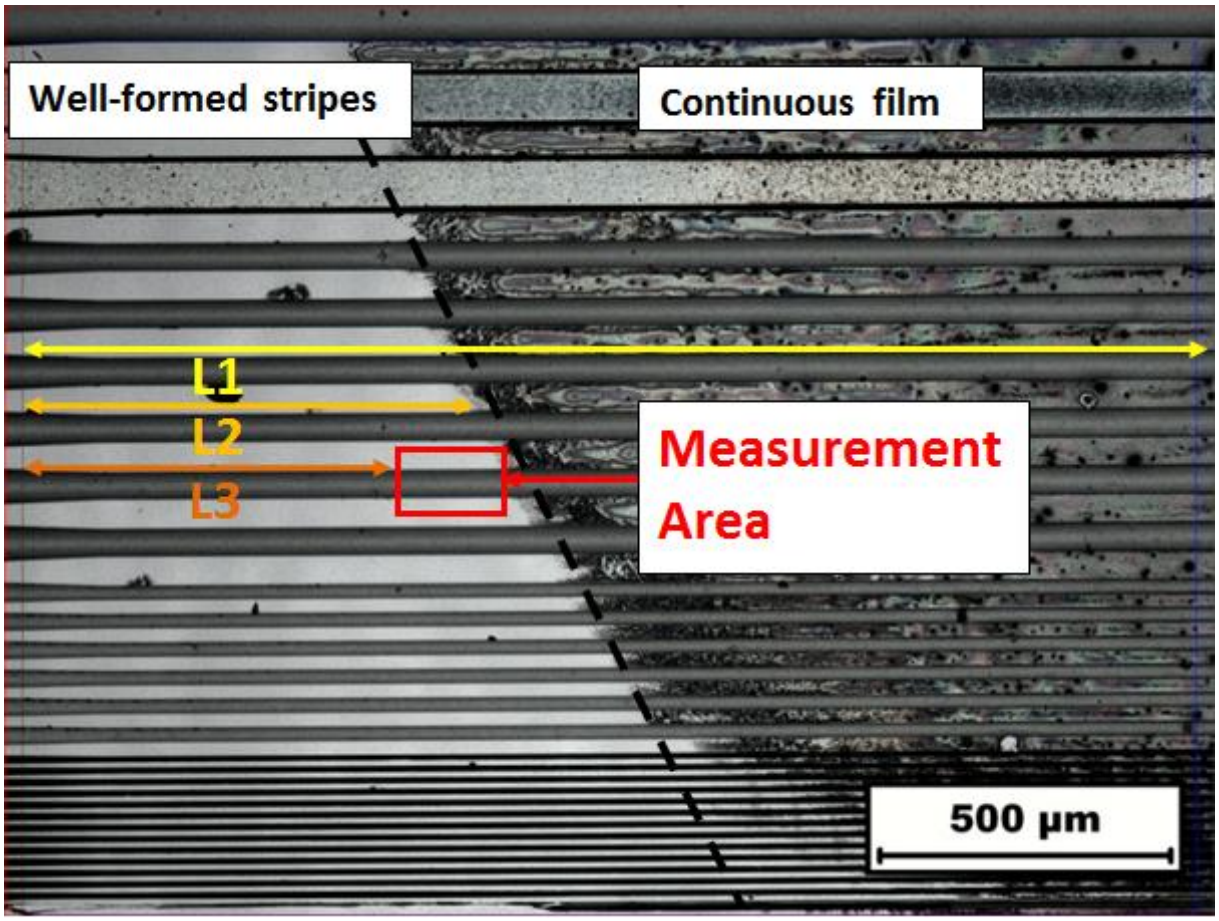

Figure 3-8. Optical micrograph of as-dried 27µm thick alumina stripes on a smooth sapphire substrate.

- No cracking during drying
- Distance from cavity to end of stripe exceeds threefold distance of cavity to edge
- No damage in the immediate vicinity of the cavity

Elliptical cavities were prone to cracking in the green state. This affected all cavities of 100µm length or higher in stripes of thicknesses greater or equal to 16µm. Thus, only ellipses in 8µm thick stripes were studied. In addition, the limitations of the wafer patterning process led to two sharp corners at the endpoint of the major axis instead of the endpoint itself being the point of highest curvature (see Figure 3-9 right). Crack-free multiple **elongated cavities** could be obtained for all stripe thicknesses. An example of the available twofold, triangular and quadruple configurations is presented in Figure 3-10.

The **ring structures** had to be severed from the beams connecting them to the slurry reservoir prior to sintering. This was carried out using a micromanipulator (Model S-926, Signatone, Gilroy, USA). Ring structures must meet the following requirements:

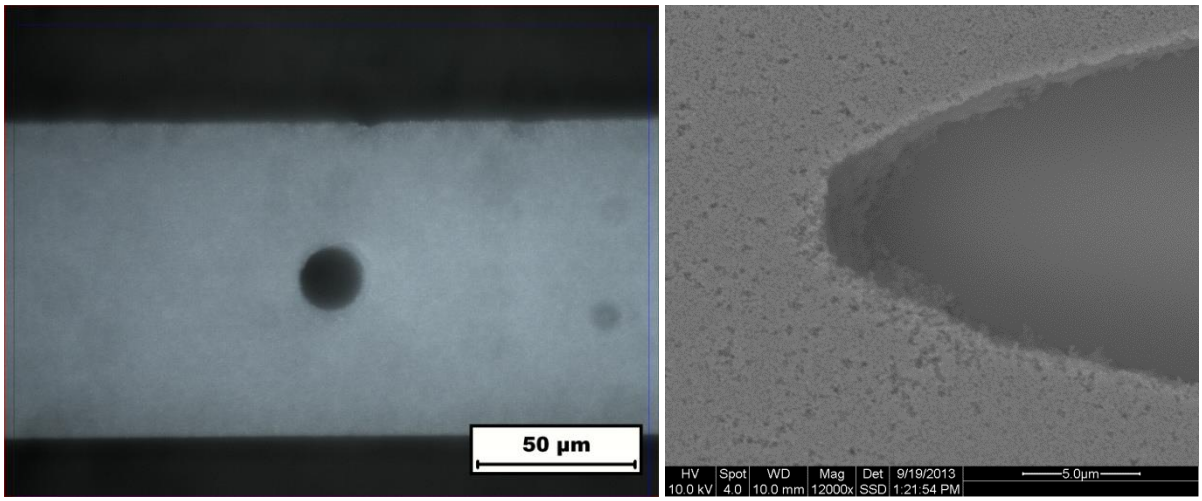

Figure 3-9. Optical micrograph of an as-dried stripe including a crack-free circular cavity (left) and in-situ ESEM micrograph of an endpoint of an elliptical cavity.

- Well-formed edges
- Complete separation of the connecting beams (loose residue may remain)
- Well-formed inner hole

Only the ring systems R200-0.4, R200-0.1, R100-0.4 and R100-0.1 met the standards. Analysis was therefore limited to these geometries.

3.3.2. Sintering conditions

Stripe and bulk samples

Alumina stripe patterns and their cylindrical bulk counterparts were subjected to different sintering cycles depending on the substrate material. In case of the films, a box furnace (Nabertherm, Arnold Schröder Industrieöfen, Flörsheim, Germany) was used; the bulk specimens were freely sintered in the hot forging apparatus with direct laser monitoring of axial and radial strains used in Ref. [121]. Sintering temperatures had to be chosen high enough to yield lateral strain values significantly larger than the measurement error, but low enough to ensure the stability of the platinum coating as well as the absence of mud-cracking in films without stress concentrators. In case of the samples with sintering additives, the lowest temperature at which the formation of liquid phase was observed in top view images by scanning electron microscopy was found to be 1425°C. As this temperature was higher than the stability maximum for platinum coated substrates, liquid phase sintering experiments were only carried out on plain sapphire. Different holding times of up to 4h were applied to obtain isothermal densification and strain curves. In Table 3-4, the sintering conditions are listed.

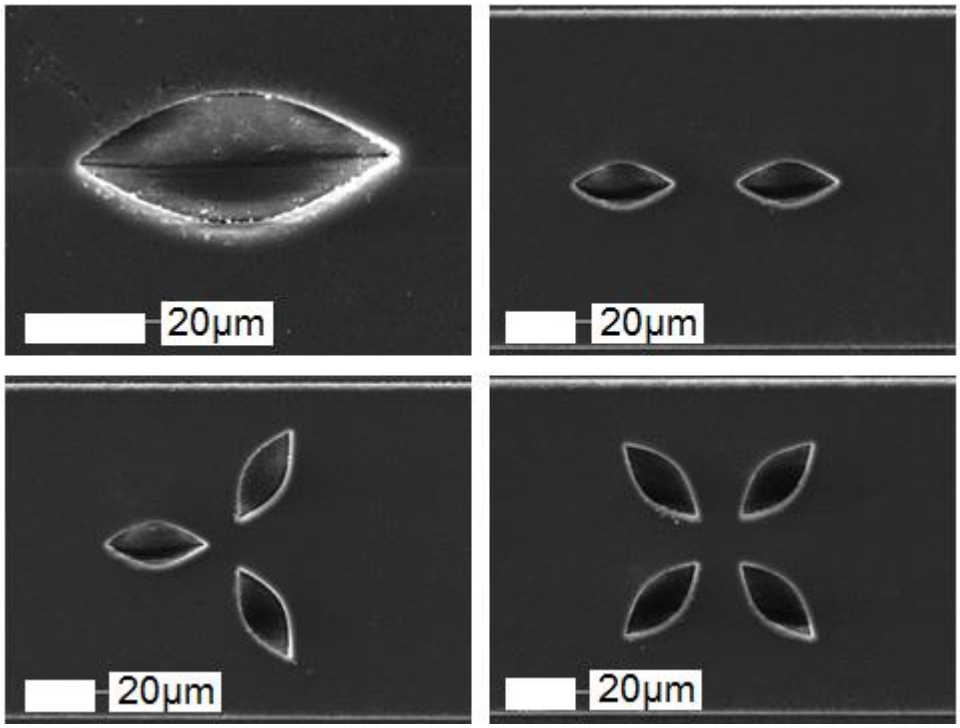

Figure 3-10. Multiple elongated cavities in as-dried stripes of the 27µm x 100µm system.

Crack initiation at cavities

Crack initiation around circular and elliptical cavities was studied at the endpoint of the isothermal holding time. In addition, in-situ environmental scanning electron microscopy (ESEM, Quanta 200F, FEI Company, Eindhoven, Netherlands) experiments were carried out using a hot stage that allows temperatures up to 1500°C inside the ESEM vacuum chamber. As specimens had to be cut into pieces with a maximum size of 3mm x 3mm, the as-deposited films were heated to 1000°C for 15min to provide mechanical stability without densification. Then followed dry cutting by means of a diamond wire saw and subsequent removal of the glue used during cutting at 750°C. The sintering schedule deviates from the one used in the ex-situ experiments; a maximum temperature of 1300°C was chosen for all specimens to increase the lifetime of the hot stage. Furthermore, the heating rate was lowered progressively with increasing temperature since a high image quality at temperatures above 1000°C requires constant adjustment of contrast, brightness and bias fields. The resulting temperature profile is given in Figure 3-11.

Ring structures

Ring structures on discontinuous platinum and smooth sapphire substrates were subjected to two different sintering cycles: I) 5min at the isothermal holding time specified in Table 3-4. and II) 240min at a temperature 100°C below the isothermal sintering time.

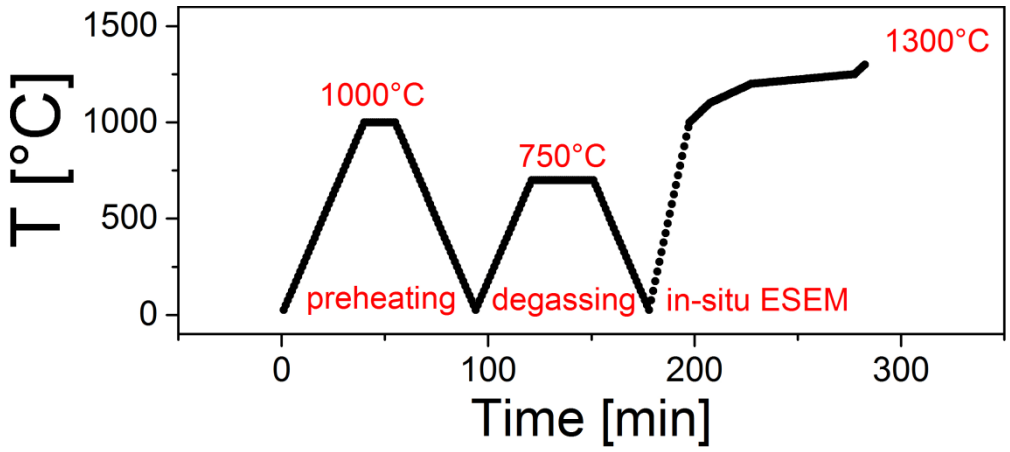

Figure 3-11. Heating schedule used for in-situ ESEM experiments.

3.4. Measurement of shrinkage and densification

3.4.1. Stripe patterns

In order to calculate the sintering shrinkage, the thickness and width of green and sintered stripes were measured. Their lateral dimensions were measured both at the film surface (L2) and at the film-substrate interface (L1, see Figure 3-12) using scanning electron microscopy (SEM; Philips XL3000 FEG, FEI Company, Eindhoven, Netherlands) top view pictures of carbon or gold-palladium coated samples. The minimum was set to 30 measurements on at least 3 different stripes and the standard deviation was used to estimate the measurement error. In case of the 32µm x 250µm and 27µm x 500µm systems, the minimum was lowered to 20 measurements on one stripe since wide stripes in thick stamps could not be produced in large quantities due to difficulties during the deposition process. Height profiles were taken in the green and sintered state using white light interferometry (NV6200, ZygoLot GmbH, Darmstadt, Germany). In this case, the minimum was set to 60 profiles taken from 3

Table 3-4. Sintering conditions of different film/substrate combinations

Film material	Substrate material	Sintering temperature [°C]	Holding time [min]
Pure alumina	Smooth sapphire	1450°C, 1350°C	5 – 240
Pure alumina	Smooth sapphire	1450°C	5 – 240
Pure alumina	Continuously sputtered platinum	1350°C	5 – 240
Pure alumina	Discontinuously sputtered platinum	1250°C	5 – 240
Coated alumina	Smooth sapphire	Annealing: 30min at 900°C Sintering at 1425°C	5 - 20

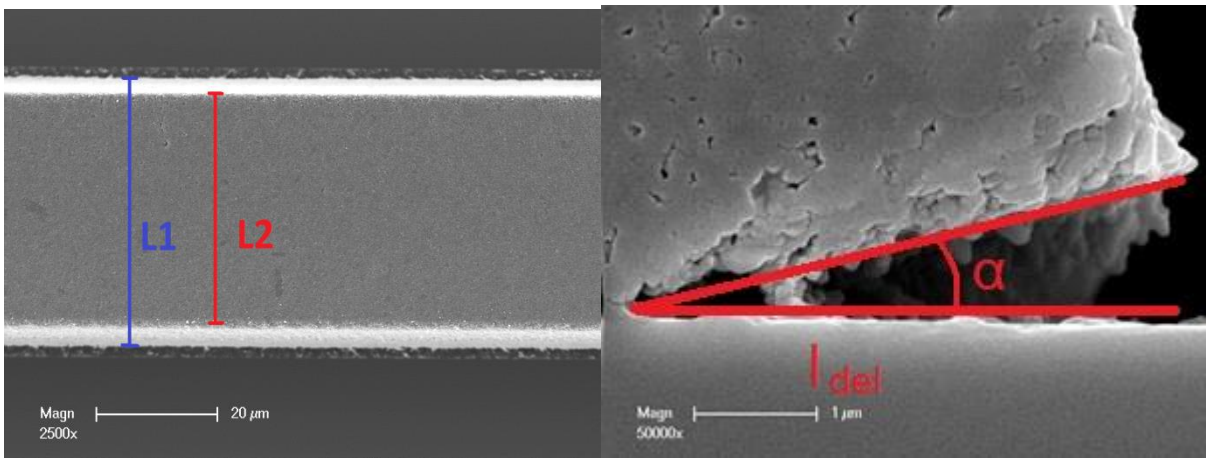

Figure 3-12. Dimensioning of SEM top view pictures (left) and cross sections (right).

or more stripes. Again, the standard deviation was used to estimate the error. Vertical strain in pure alumina films was measured in the center of the films in order to avoid the edge effects such as overshooting during interferometry. Since the 8µm thick liquid phase sintered films had a higher surface roughness than their pure alumina counterparts, a gold-palladium coating was sputtered on top of the samples in order to enhance the reflectivity of each specimen. Consequently, the measurement of green film thickness and sintered thickness could not be carried out on the same specimen. The width and height measurements before and after sintering were used to calculate the true sintering strain according to eq. 44:

$$\epsilon_{true} = \ln\left(\frac{l_i}{l_f}\right) \tag{44}$$

Where l_i is the thickness or width in the green state and l_f the thickness or width after sintering. The dependence of the strain on stripe geometry, substrate material and sintering time was studied.

3.4.2. Microstructural analysis

The delamination, shape and local density of the stripes with widths up to 250µm are investigated using binarised SEM cross sections of epoxide embedded and polished cross sections. For this purpose, the samples used for strain characterization were cut, embedded and polished using the polishing routine given in Table 3-5 after completion of the non-destructive testing (all polishing materials obtained from (ITW Test + Measurement GmbH, Düsseldorf, Germany). Before thermal etching, the excess resin was cut using a rotating diamond blade (Minitom, Struers, Germany) and remaining resin was burnt out at 700°C for 30min. Thermal etching was carried out at 1250°C for 15min on the smooth and rough sapphire substrates as in [34].

Table 3-5. Polishing routine on Phoenix 4000 (Jean Wirtz, Germany).

Polishing cloth	Abrasive type	Lubricant	Speed	Pressure	time
Apex Color Red	75µm	Water	150rpm	1.8 bar	2min
Apex Color Yellow	35µm	Water	300rpm	2.0 bar	2min until free
UltraPad	MetaDi Supreme 9µm	None	150rpm	2.0 bar	3 x 5min
VerduTex	MetaDi Supreme 3µm	None	150rpm	1.8 bar	3 x 5min
ChemoMet	MasterMet 2	MasterMet2	300rpm	1.8 bar	2x 10min
ChemoMet	Clean cloth	Water	150rpm	1.8 bar	10min

Since platinum forms a volatile oxide at temperatures above 500°C [109] evaporation of the platinum interlayer could not be avoided near the cutting edge despite the overall stability of the film. Therefore, the alumina stripes at the cutting edge were not bound to the substrate anymore. Thus, polished cross sections were examined using SEM before resin removal in order to study the morphology of the platinum layer. The binarized cross sections (see Figure 3-13) were evaluated using the software ImageJ (National Institute of Health, Bethesda, USA). For each density data point, a least four stripes have been studied with the exception of the 27µm x 500µm system. Here, the minimum has been lowered to two stripes. The standard deviation of the density values of each binary image was used to estimate the error. For comparison with continuous films, four images from one film of 500µm in width and length were evaluated. Porosity characterization was carried out by applying an elliptical fit of the pore shape. Pore orientation was quantified by using the cumulated weighted length of the Feret's diameter. The pore orientation factor is established as follows:

$$f = \frac{CWL(75°-105°)}{CWL(0-30)+CWL(150°-180°)} \tag{45}$$

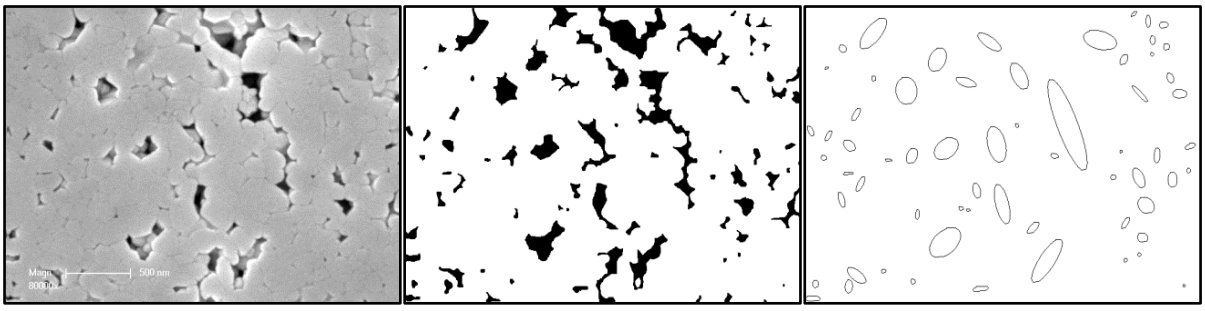

Figure 3-13. SEM micrograph of polished cross section of 27µm x 100µm alumina stripe (left), binarized pictures (middle) and elliptical fit of the pore shape (right).

Where CWL denominates the cumulated weighted length of the pores orientated at the specified angles with respect to the substrate. This length has been weighted by multiplication with the aspect ratio obtained from the elliptical fit of the pore shape.

Delamination angle and length were measured to characterize the film adhesion. The minimum was set to four film edges, including an equal number of data points from the left and right edge.

Cross sections of green specimens suitable for shape characterization only were fabricated by mechanical polishing followed by Broad Ion Beam treatment carried out by Dr. Sören Höhn, Fraunhofer IKTS, Dresden.

3.4.3. Densification curves

Geometric densification curves of 8µm and 27µm thick films on plain sapphire and discontinuously sputtered, platinum coated films were obtained by interrupted sintering experiments of individual specimens for different holding times. The cross section area of the stripes was calculated by integration of a height profile that represents the average height of 60 height profiles. Here, two different assumptions as to the shape of the stripe can be made: In case of the rectangular approximation, only the integrated area (grey part in Figure 3-14) was used. For the trapezoid approximation, however, additional edge area was added (red areas in Figure 3-14). This method was validated for every stripe geometry and substrate by comparing the shape of the interferometer profiles to the shape of polished SEM cross sections for a few points during the sintering cycle.

The limited lateral resolution of white light interferometry was overcome by setting the width of the interferometer curves to the values measured in the scanning electron micrographs. Then the geometric density of each specimen after sintering was calculated using the formula:

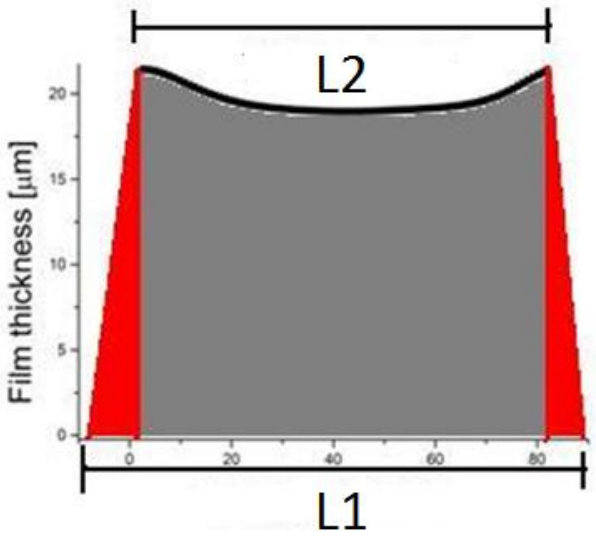

Figure 3-14. Schematic representation of an integrated interferometer profile. Grey area: rectangular approximation, red and grey areas: trapezoid approximation

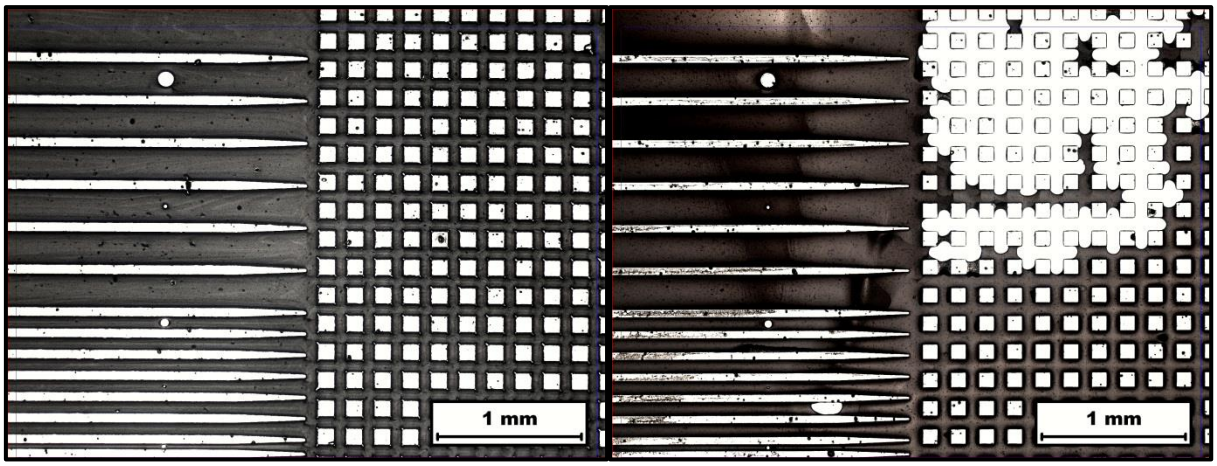

Figure 3-15. Optical micrographs of as-deposited stripes. Left: Stripe thickness 8µm, right: Stripe thickness 16µm.

$$\rho_i = \frac{A_f}{A_i} \cdot \rho_f \tag{46}$$

where ρ_i is the density at every point in the densification curve, ρ_f the final density taken from the SEM cross sections and A_f and A_i the cross section area of the stripe at the end of the densification curve and at the individual isothermal times, respectively. By using the cross section area only, the in-plane shrinkage parallel to the stripe edge was neglected for the density calculation. This is considered valid since the minimum length of the specimens was chosen in a way to ensure that the strain in this dimension was less than 1%.

Green density was calculated by two different methods according to the sample thickness. Samples with thicknesses up to 11µm were found to dry without separation of the stripes from the slurry reservoir and shrinkage only occurred in the thickness and width direction. In stripes with thicknesses greater or equal to 16µm, the connection from stripe to reservoir was severed during drying, as shown in the right graph in Figure 3-15, and an additional drying strain was observed in the length direction. This drying strain is not measureable since the initial stripe length before drying does not correspond to the total pattern length and is therefore different in each sample.

Hence, green density of thick stripes was calculated using eq. 46 as described above as this calculation does not require information about the drying strains. In thin stripes, by contrast, green density was calculated from the solid content of the slurry and the ratio of stamp to green stripe cross section since all drying strain components are accessible for measurement. Here, eq. 46 was also used, with A_f and A_i being the green and stamp cross section area and ρ_f and ρ_i the green density and slurry solid content, respectively.

3.4.4. Interface friction coefficient

The interface friction coefficient was calculated for every solid state sintered film-substrate system using eq. 40. Here, v^P as a function of density for TM-DAR alumina is taken from Zuo et al. [53] who have validated Venkatachari's model data [69] for the viscous Poisson coefficient. The free sintering strain of a bulk specimen with matching green density subjected to the same sintering cycle as the stripe was obtained from free sintering experiments or DEM simulations. The displacement of the upper free edge, Δy, is calculated as half the difference in width of a 100µm wide stripe before and after sintering. The 100µm stripes are chosen for the calculation of k.

3.4.5. Bulk specimens

Densification curves were obtained from the sample volume calculated normalized by the Archimedes density:

$$\rho_i = \frac{V_f}{V_i} \cdot \rho_{Arch} \tag{47}$$

where ρ_i is the density at every point in the densification curve, ρ_{Arch} the Archimedes density determined after sintering and V_f and V_i the cross section area of the stripe at the end of the isothermal holding time and at the individual isothermal times, respectively.

3.4.6. Stress concentrators

The circular cavities were analyzed using SEM top view pictures. Crack length, crack orientation and cavity aspect ratio were measured using the ImageJ software. The green diameter was measured by ESEM since this method requires no metallization. At least two specimens per hole configuration were studied. The influence of the stripe geometry, substrate material and the proximity of the stripe edge on the crack initiation, growth and orientation were studied.

3.6.7. Ring structures

The displacement of the inner and outer edge was calculated by measuring the outer and inner diameters (b and a, respectively; see Figure 3-16) in the green and sintered state using SEM top view pictures. The measurements in the green state were carried out on continuous films prior to the separation of the beams, whereas for sintering only clearly separated structures were used. A minimum of two tructures per configuration was studied. A range of different values for the product of friction coefficient times hole radius was obtained by varying the following parameters:

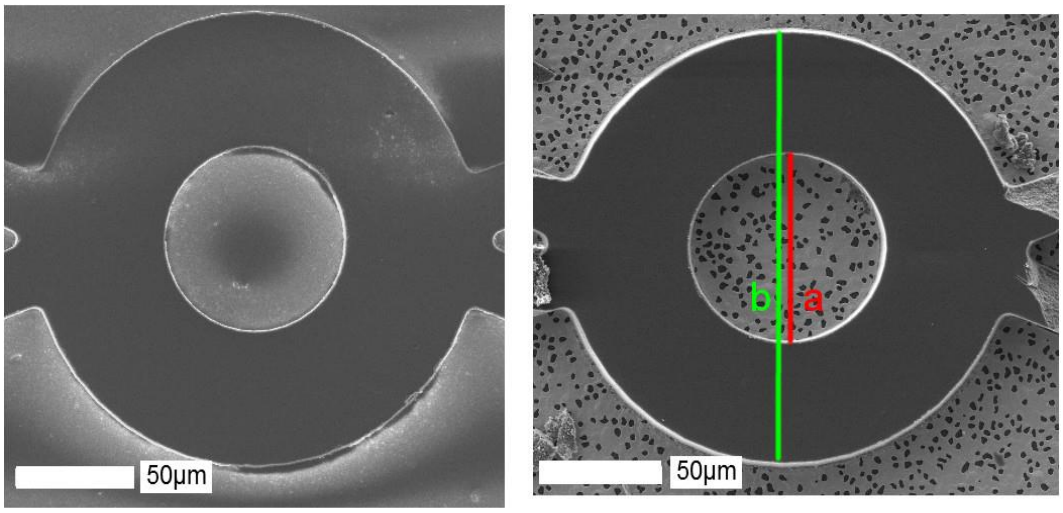

Figure 3-16. Rings of the system R100-0.4. Left: Before channel separation; right: After separation and sintering.

- Substrate material (smooth sapphire / platinum coated sapphire):
  Interface stiffness affects friction coefficient
- Film thickness (8µm / 27µm):
  Thickness dependent edge displacement affects friction coefficient
- Feature size (b=200µm / b=100µm):
  Total feature size affects hole radius

4. Results

4.1. Constrained drying

In Figure 4-1, the vertical drying strains calculated from the stamp and stripe thicknesses measured in the stripe center are plotted as a function of the thickness-to-width ratio of the stripes. The drying strain is found to be strongly dependent on stripe geometry with an increasing tendency from narrow to wide stripes. This is consistent with the preferential dewetting generally observed in MIMIC.

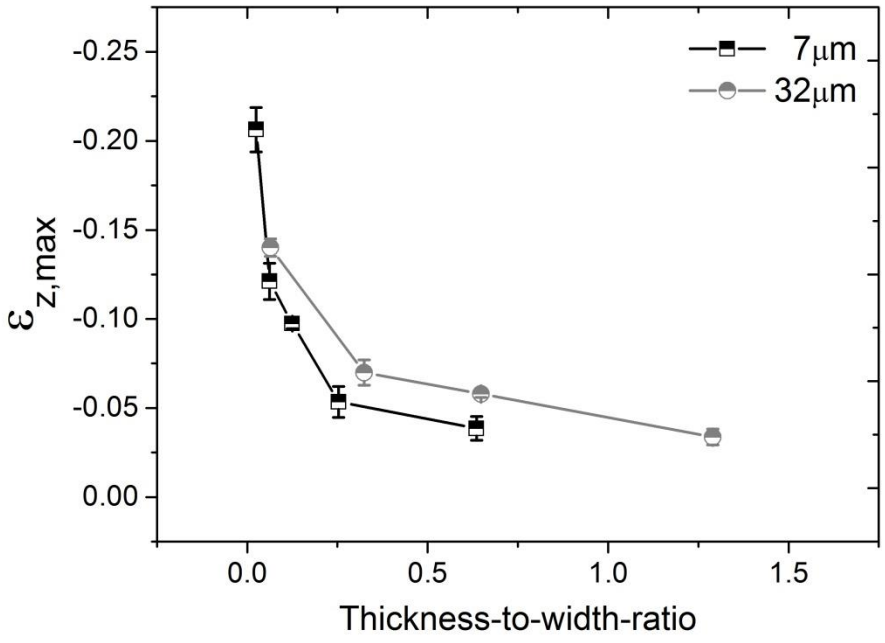

Figure 4-1. True vertical drying strains as a function of aspect ratio for drying condition II samples of different thicknesses.

The geometry dependent drying strains result in a different green density for each stripe. In Table 4-1, green density values directly calculated from the slurry solid content (Method I) are contrasted with the green density from extrapolation of the sintered density (Method II) for the stripe geometries used in this work. It is shown that the extrapolated green density matches the direct calculations from the stamp channel cross section only in case of thin stripes. In case of the thickest specimens, the deviation becomes as high as 14.5%. Hence, constrained drying leads to low densities in thin films while the separation of the channels from the slurry reservoir enable the thick specimens to dry freely and thus attain high densities up to 70% for smooth and rough substrates. Since the vertical drying strains do not differ much in thick and thin specimens with similar thickness-to-width-ratio and strains in the width direction of the stripe tend to be small, this difference in density is related to the additional in-plane strain component in the length direction of the stripes.

Table 4-1. Geometry dependent green densities determined by different methods.

Stamp thickness [µm]	Stamp width [µm]	ρ_{green} [%] smooth substrate		ρ_{green} [%] rough substrate
		Method 1	Method 2	Method 2
5	100	57.9	---	---
8	10	58.7	---	---
8	25	58.6	---	---
8	100	57.0	58.9 ± 2.3	---
11	100	57.0	---	---
16	25	---	65.7 ± 2.0	---
16	50	---	70.3 ± 1.4	---
16	100	56.9	69.6 ± 1.2	---
27	25	---	68.5 ± 1.1	---
27	50	---	68.2 ± 0.8	---
27	100	52.6	67.1 ± 1.0	66.9 ± 2.44
32	100	---	64.6 ± 1.2	---

Despite these substantial drying strains, cracking after drying was not observed in stripes without cavities. The shape of the dried stripes is characterized by a geometry dependent amount of surface tapering and edge inclination already present in the stamp channels. In Figure 4-2, broad ion beam treated cross sections of 7µm and 32µm thick green specimens illustrate these effects.

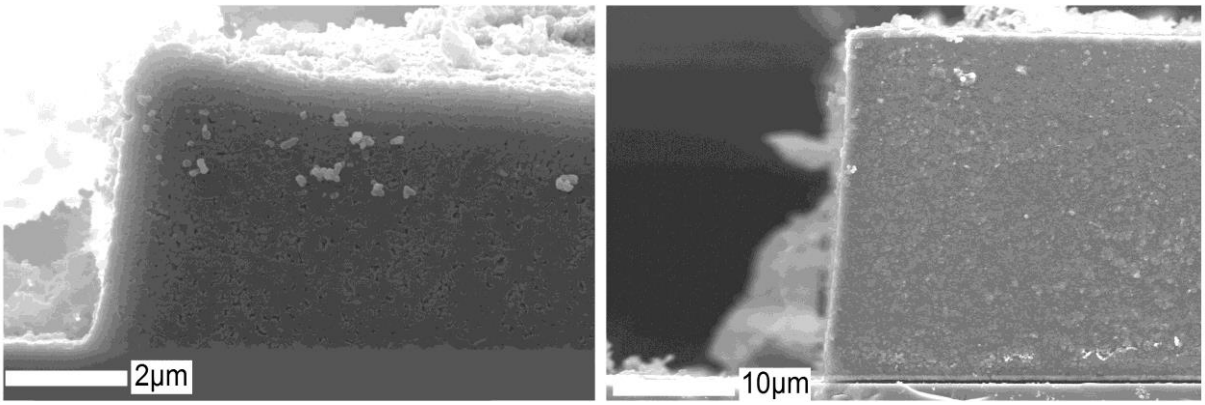

Figure 4-2. SEM cross sections of dried 7µm x 250µm and 32µm x 100µm specimens.

4.2. Constrained sintering

4.2.1. Shape change and delamination

Alumina stripes on plain sapphire

In Figure 4-3, SEM pictures of polished cross sections of 27µm thick stripes on smooth sapphire substrates reveal a geometry dependent sintering deformation. With the exception of the narrow stripe in picture A, the stripes strongly deviate from their initial rectangular shape. Both lateral and vertical shrinkage are non-uniform, thus enhancing both the surface tapering and edge inclination already present to some degree after drying. Near the stripe edges, the height is maximal and decreases towards the stripe middle, where it remains uniform in case of the wide stripes. Hence, wide stripes consist of two distorted edges separated by a mid-section with uniform height. The increased edge inclination bears witness of the enhanced lateral strain near the stripe surface compared to the substrate-bound part of the film. In contrast, the mid-section seems to behave more like a perfectly constrained film. By comparison, the height profile does not reach a plateau in the narrow stripe in Figure 4-3 B, thus giving the impression of two overlapping stripe edges.

Alumina stripes on rough substrates display the same width dependent geometry after sintering. This is shown in Figure 4-4, where polished cross sections of the 27µm thick system with different lateral dimensions are presented for the rough substrate system. Again, narrow stripes remain rectangular while wide stripes experience a separation into deformed edges and constant-height mid-section.

The width of the edge zone of the stripes with a thickness of 27µm, measured from the delaminated corner to the point where the surface curvature reaches zero (in wide stripes) or changes its sign (in narrow stripes), is plotted in Figure 4-5 for smooth and rough substrates. Once a critical stripe width of 100µm is exceeded, the shape of the edge region is identical for all stripes. For smaller widths, the edge zone length is half the stripe width, whereas in case of a 27µm x100µm stripe it makes up around

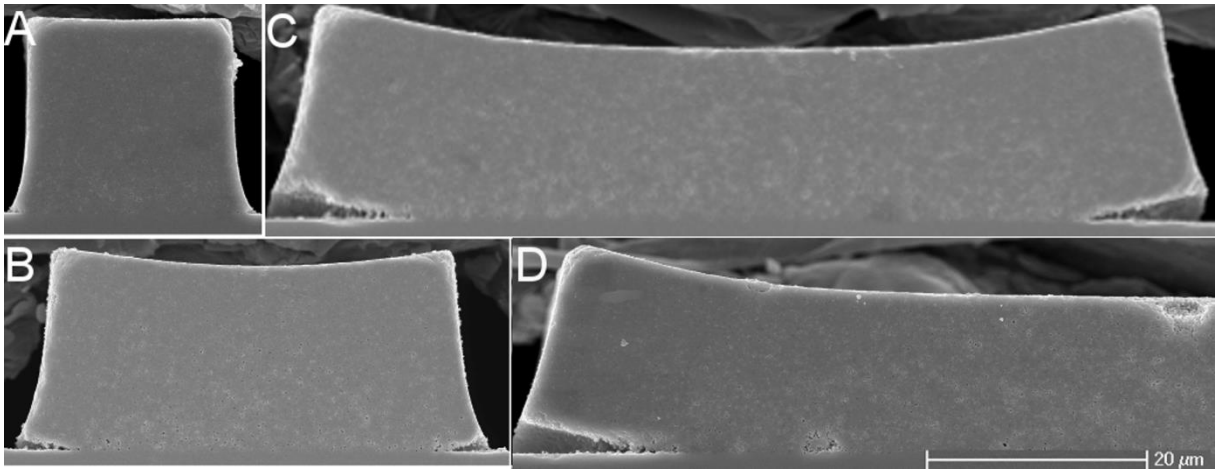

Figure 4-3. SEM cross sections of 27µm thick stripes on smooth sapphire sintered at 1450°C for 4h of different lateral dimensions. A: 25µm, B: 50µm, C: 100µm, D: 500µm.

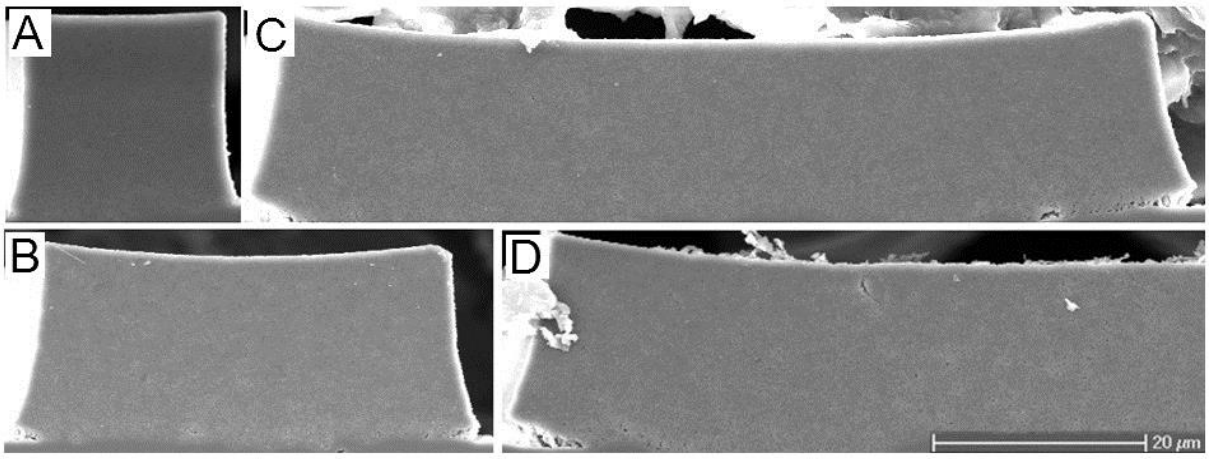

Figure 4-4. SEM cross sections of 27µm stripes on rough sapphire sintered at 1450°C for 4h of different lateral dimensions. A: 25µm, B: 50µm, C: 100µm, D: 500µm.

one third (30-35µm) and remains constant with increasing width. This is illustrated in SEM pictures of the edges of 27µm x 100µm and 27µm x 500µm stripes on smooth substrates (Figure 4-6 A and B) that are similar in extension and shape. Both edges have a higher density near the delaminated and free corners, with increasing porosity towards the center. In thinner stripes, the edge zone is found to be shorter. In Figure 4-6 C, an 8µm x 100µm stripe is depicted whose edge zone extends throughout ca. 10µm, making up about 10% of the stripe width. This hardly exceeds the length of the tapered edge already present in a dried stripe in the left picture in Figure 4-2. Here, the lateral strain near the surface does not seem much greater than near the substrate, indicating a higher influence of the substrate constraint throughout the stripe thickness. In the 8µm system, too, the narrowest stripes (8µm x 10µm) are composed of two overlapping edges. This leads to the assumption that the thickness-to-width-ratio is a crucial parameter for the shape change and edge zone development of sintering stripes.

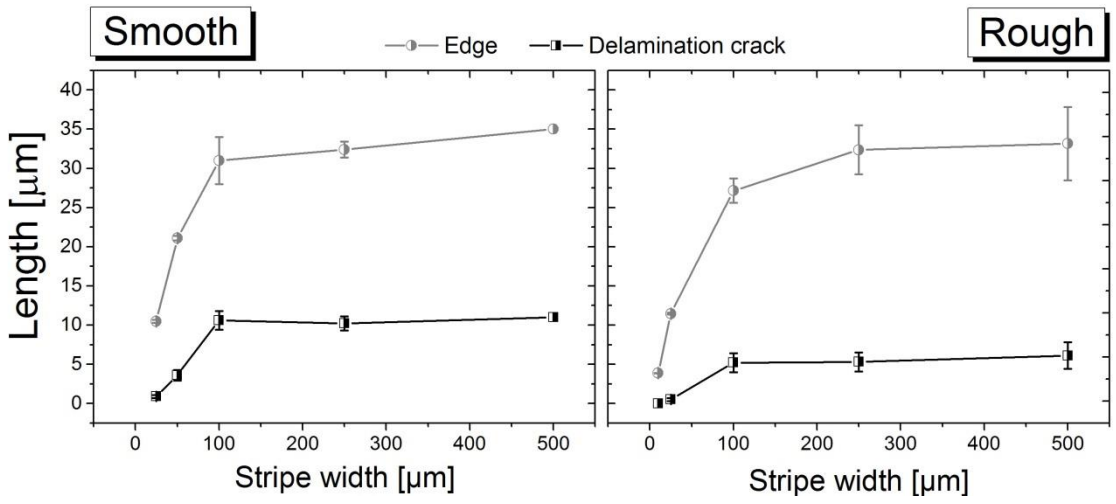

Figure 4-5. Length of edge zone (grey curve) and delamination crack (black curve) of 27µm system as a function of stripe width. Left: smooth sapphire, right: rough sapphire.

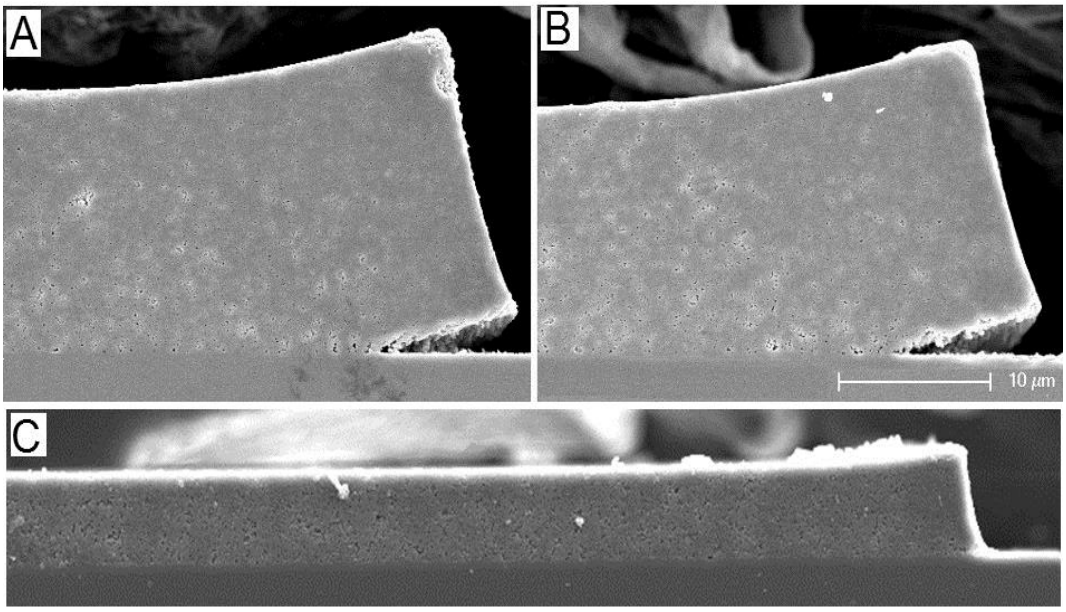

Figure 4-6. Edge zones of 27µm x 100µm (A) and 27µm x 500µm (B) sintered at 1450°C for 4h and 8µm x 100µm (C) sintered at 1450°C for 1h.

In addition, delamination is observed to a varying degree in all specimens with thickness-to-width-ratios of unity or below. In case of the 27µm stripes, the length of the delamination crack increases with stripe width from 0.9µm (27µm x 25µm) up to 10µm (27µm x 100µm) where it reaches a plateau (Figure 4-5 left). The area above the delamination crack shows very low porosity; however, the region right next to it marks the point of maximum porosity. The 8µm stripes show only very short delamination cracks with maximum values below 3µm at high widths, indicating that not only stripe width, but also thickness influences delamination. Thus, delamination is governed by thickness-to-width-ratio, too.

In case of the rough substrate (Figure 4-5 right) the edge zone is similar as in smooth sapphire, with delamination length increasing with stripe width. However, the maximum length of the delamination crack is significantly smaller in rough substrates, only reaching 5µm in the widest stripes. Furthermore, the scattering of the values is greater, reflecting the differences in local substrate properties. Unlike in smooth sapphire, here, 8µm thick stripes of all widths do not show any delamination; however, the compatibility stresses cause enhanced porosity at the constrained edge. The edge zone in the system 8µm is smaller than in the corresponding 27µm stripes (9.2µm for the 8µm x 100µm system vs. 27.2µm in case of the 27µm x 100µm system). This means that in the thin stripes starting from 25µm width, the edge zone always looks the same but is separated by an increasingly large mid-section. Interestingly, the ratio of the 8µm/27µm edge length is similar to their thickness ratio (0.34 vs 0.28).

In order to assess the influence of the enhanced roughness on delamination, 22 SEM pictures of delamination cracks in the systems 27µm x 100µm, 27µm x 250µm and 27µm x 500µm are sorted

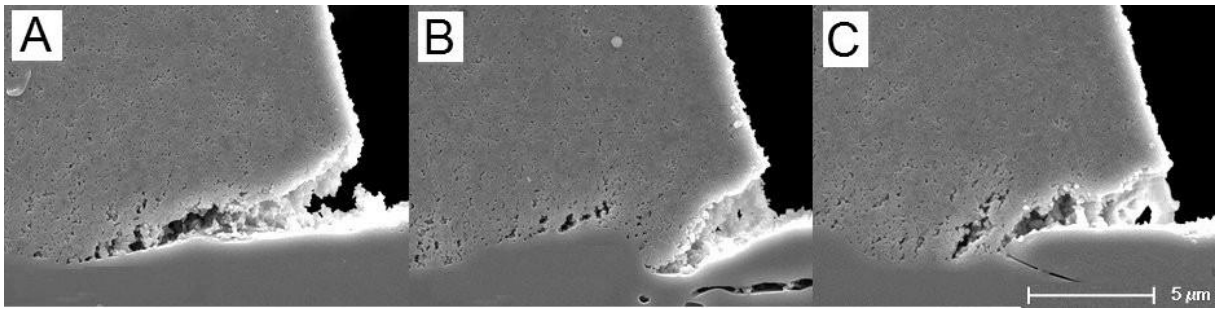

Figure 4-7. Different substrate morphologies present in delaminated stripe edges of wide stripes in the 27µm system. A straight, B positive, C negative slope at the endpoint of the crack.

according to the local morphology of the substrates. Three types of cracks are established (Figure 4-7):

1. Straight substrate or constant downward slope below delamination crack
2. Crack ends at change of slope in substrate (negative/zero to positive)
3. Crack ends at change of slope in substrate (positive/zero to negative)

Cracks that extend over a straight or continually descending substrate (Figure 4-7 A) are found to be longest with an average length of 7.7µm. Individual cracks of this category reach the plateau crack length of smooth sapphire (10µm). In Figure 4-7 B and C, changes in slope act as barriers for the crack, inhibiting further propagation. This results in a shorter cracks; average crack length is 5.1µm in category B and 4.9µm in category C.

Alumina stripes on platinum coated sapphire

When an intermediate layer of platinum is applied, the shape change during sintering differs from the shape change observed in stripes on uncoated sapphire. In Figure 4-8, stripe cross sections on discontinuously sputtered platinum are shown for the 27µm x 50µm and 27µm x 100µm configuration. The development of the edge zones is much less pronounced than in case of the sapphire substrates. Delamination is observed on platinum coated substrates, too, but to a lesser degree than in smooth sapphire. Figure 4-9 illustrates this fact by contrasting the width dependent delamination length for both types of substrates in the 27µm system sintered for 4h at 1350°C. The 27µm x 100µm delamination crack is twice as long without a platinum interlayer.

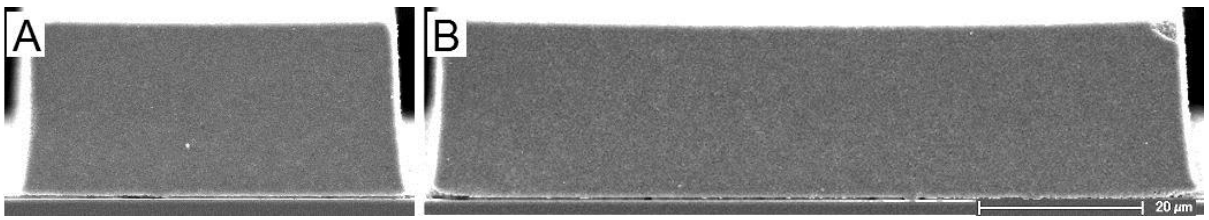

Figure 4-8. SEM cross sections of 27µm stripes on platinum coated sapphire sintered at 1250°C for 4h of different lateral dimensions. A: 27µm x 50µm, B: 27µm x 100µm.

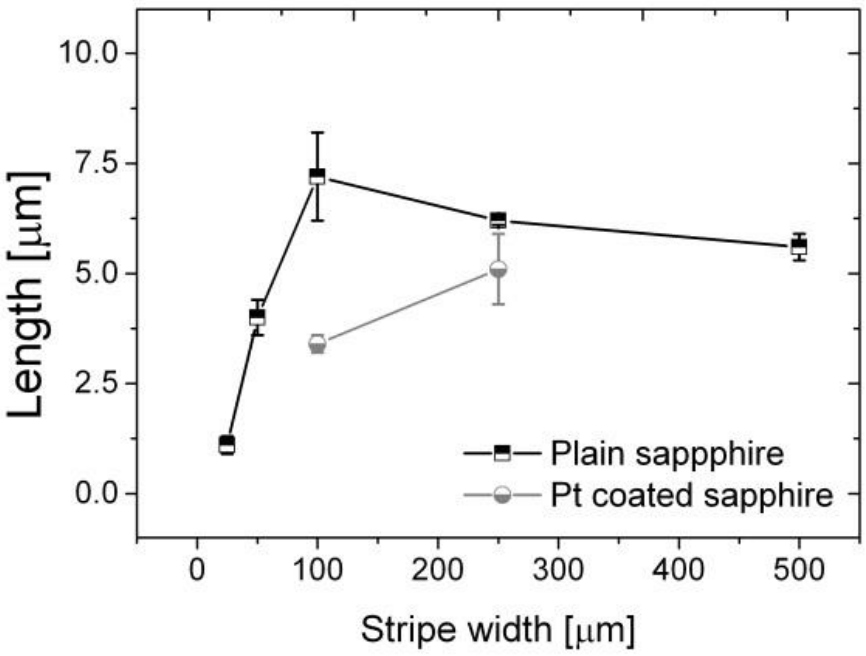

Figure 4-9. Width dependent delamination length for the 27µm system on smooth sapphire (black curve) and platinum coated sapphire (grey curve), both sintered at 1350°C for 4h.

4.2.2. Local density and porosity

Alumina stripes on plain sapphire substrates

The study of **local density** in alumina stripes shows that finite films exhibit not only the out-of-plane density gradient already known from continuous films, but also an additional lateral density gradient. In Figure 4-10 A, density measured in the stripe center on a smooth substrate shows an increasing trend with increasing distance to the substrate. This relationship is observed in all stripe geometries, but the curves are shifted to lower densities for wide stripes. This is consistent with the fact that the high density edge zone dominates the whole 25µm stripe, thus leading to a higher density in the stripe middle and thus to a higher total density. The minimum density at the substrate in 500µm stripes is 9% lower than in the 25µm wide stripe, while the slope of the three curves is similar. Since green density was found to be similar in all studied stripe geometries of the 27µm system, the increase observed differences in final density develop during sintering, not drying. The effect of the proximity of the edge therefore seems to be the same throughout the stripe height and causes an offset in the density vs. height curve.

In Figure 4-10, the local density measured at different locations is plotted as a function of stripe width. Interestingly, the relative density measured at the center of the stripe, both at surface and substrate, decreases with increasing stripe width while the density near the upper free edge remains constant.

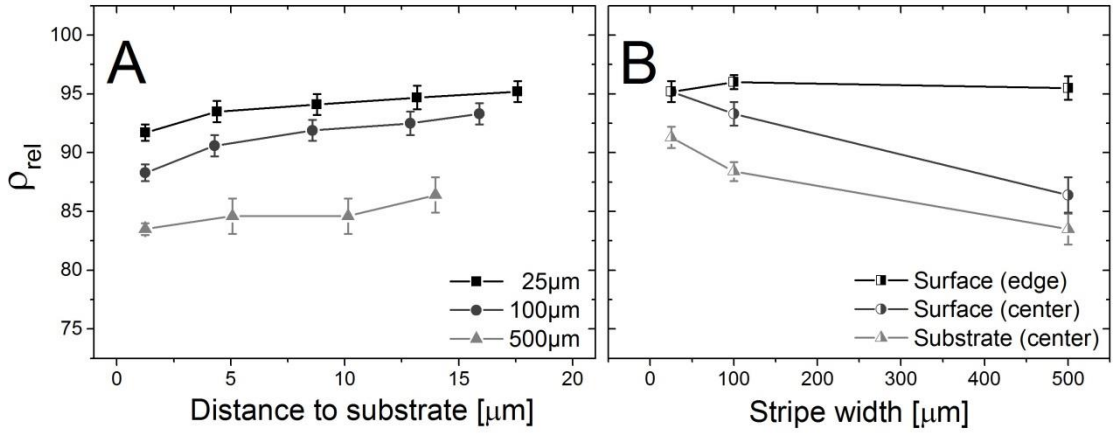

Figure 4-10. Local density of the 27µm stripe system on smooth sapphire sintered at 1450°C for 4h. A: Density in the stripe center as a function of distance to the substrate, B: Density measured at different locations as a function of stripe width. Micrograph size: 3.3µm x 2.5µm

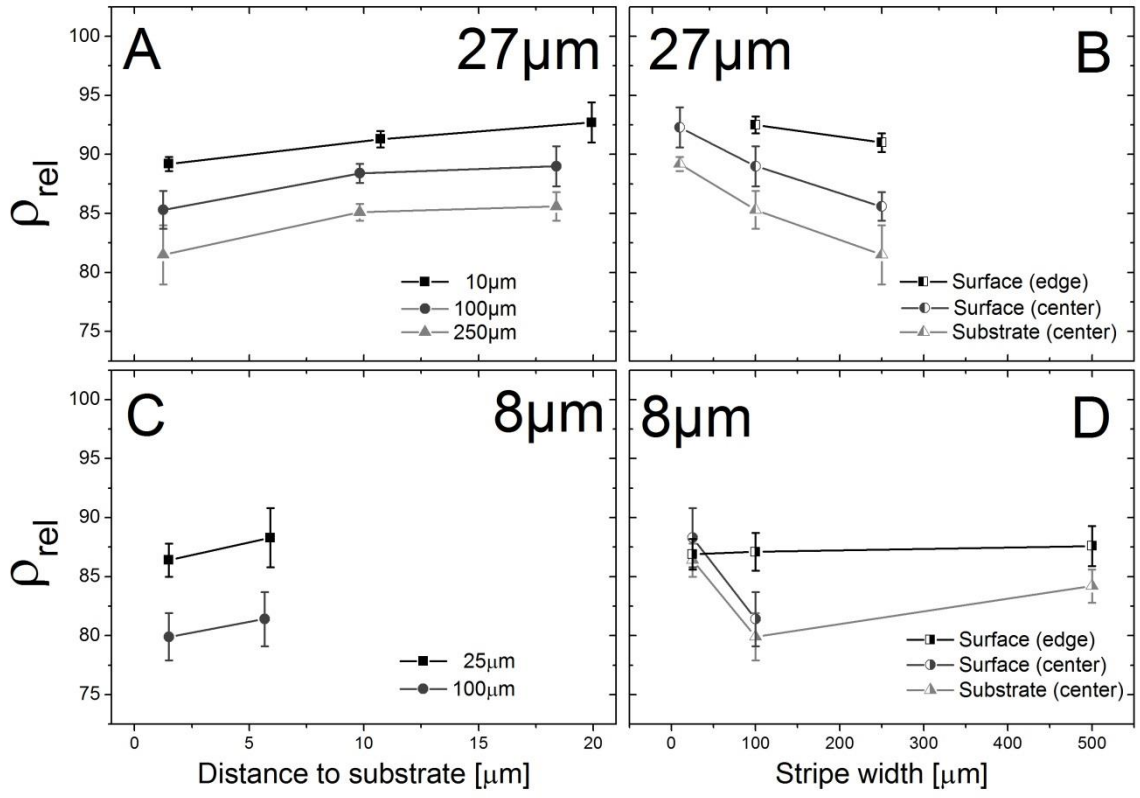

Figure 4-11. Local density on rough sapphire sintered at 1450°C for 4h. A: Density vs. height in 27µm stripes of varying width. B: Density vs. width in 27µm thick stripes at the edge, surface and substrate. C: Density vs. height in 8µm thick stripes of varying width. D: Density vs. width in 8µm stripes at the edge, surface and substrate. Micrograph size: 3.3µm x 2.5µm in the 27µm system and 4µm x 3µm in the 8µm system.

The difference between density at surface and substrate measured in the stripe middle remains constant. In the case of narrow stripes, a skin effect is observed, with high central surface and edge densities of 95%, whereas the central substrate density is 4% lower. Consequently, a low density region near the substrate is enclosed inside a high density skin. In the case of 500µm wide stripes, there is no such skin effect, as the density in the whole film is more homogeneous and significantly lower than the edge density even near the film surface.

Local density of alumina stripes on rough sapphire substrates shows the same trends as in smooth sapphire. In Figure 4-11 A, the density in the stripe center as a function of distance to the substrate exhibits the familiar decrease for all 27µm thick stripes; however, the curves are shifted to slightly lower densities (ca. 2-3%) while maintaining a similar slope as their smooth sapphire counterparts. The width dependent local density values (Figure 4-11 B) show the same trend as in smooth sapphire, with constant density at the free edge and declining central density with increasing stripe width.

In thin films on rough sapphire, such as the 8µm system, there is no detectable thickness dependence of density (Figure 4-11 C). The lateral density gradient, however, is also observed. Furthermore, when comparing the 8µm x 100µm and 27µm x 100µm stripes, a lower density by ca. 5% is observed in all locations for the thinner stripe. Here, the lower green density must be taken into consideration. Stripes of the 8µm x 25µm and 27µm x 100µm systems, however, both show central densities around 85% despite their different starting densities.

In rough sapphire, an additional aspect of local density is studied by taking the local substrate morphology into consideration. Local density in sinusoidal grooves with a typical amplitude of 3.3µm is found to be lower or equal than the mean central density with uncontrolled substrate morphology in 8µm x 100µm stripes. However, the effect is very slight (20.1% porosity in the center and 24.5% in pockets).

Local porosity of the 27µm system on smooth substrates is studied as a function of stripe width. In the 27µm x 100µm stripes, the pore size distribution (see Figure 4-12) is found to be similar near the edge and in the center. In both cases a broad peak is located around 0.1µm, as previously found in freely sintered and continuous TM-DAR films [34]. In case of the 27µm x 25µm system, the size distribution is somewhat narrower but with its peak still located around 0.1µm.

The average pore length is shown in Figure 4-13 as a function of distance to the substrate for the edge and the central 27µm x 100µm film as well as the 27µm x 25µm film. For both stripes, pores in the center are longest at the substrate and become shorter when approaching the surface. In addition, pores are more elongated in the wide stripe throughout the thickness. At the stripe edge, the pores are shorter than in the center and their length remains constant over the thickness. Orientation shows a similar decreasing trend in the 100µm wide stripe, with a maximum of 1.4 near the substrate center that indicates orientation perpendicular to the substrate. With increasing distance to the substrate, the pore orientation factor falls below 1.0; this indicates orientation parallel to the substrate.

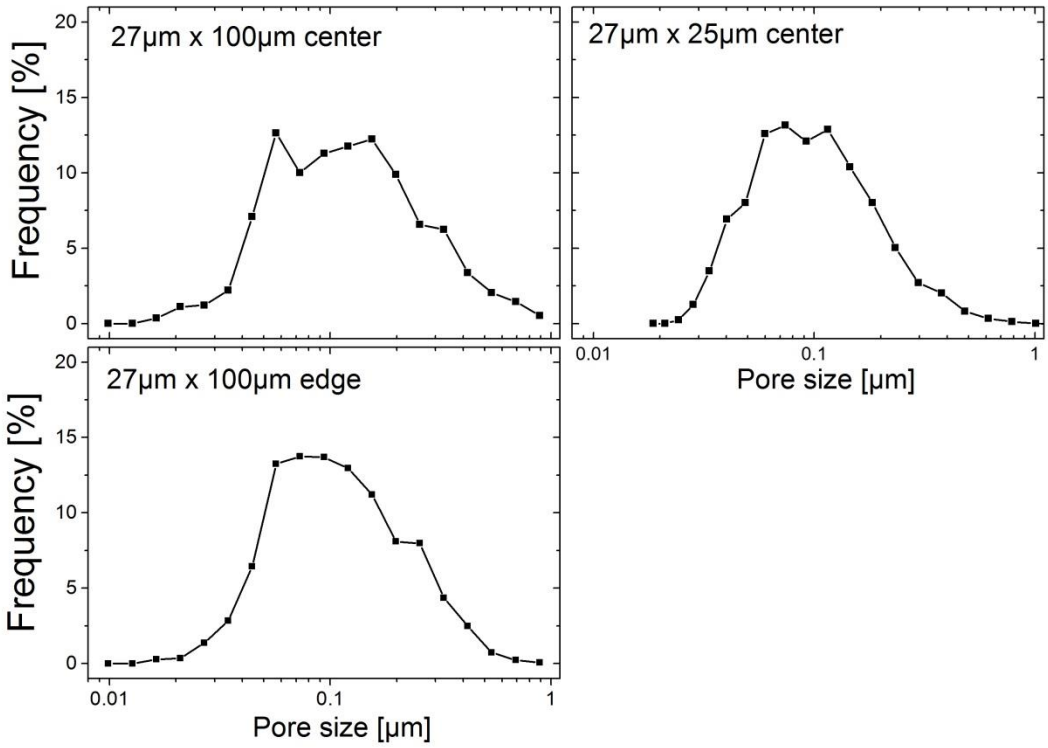

Figure 4-12. Pore size distribution in the 27µm system.

At the edge, pore orientation is always smaller than one; this means that again orientation parallel to the substrate is predominant. Thus, wide stripes are more prone to develop the characteristic microstructural features of constrained films then narrow stripes or delaminated stripe areas.

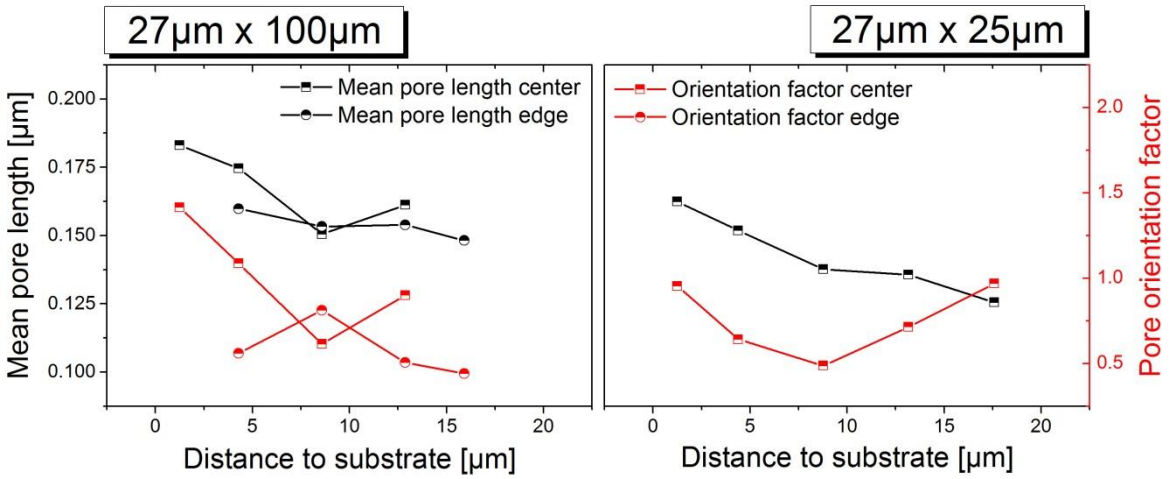

Figure 4-13. Mean pore length (black curves) and pore orientation factor (red curves) measured in the stripe center and at the edge as a function of distance to the substrate. Left: 27µm x 100µm, right: 27µm x 25µm.

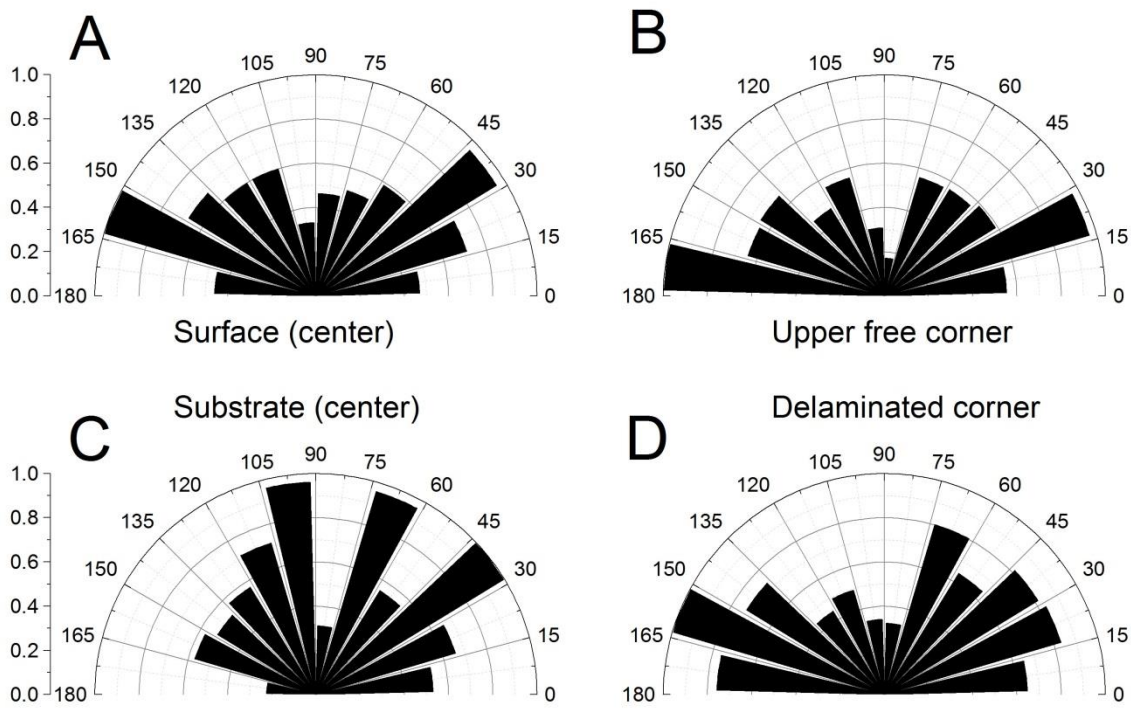

Figure 4-14. Angular distribution of pore orientation with respect to the substrate in the 27µm x 100µm system at different locations in the stripe. A: Central stripe surface, B: Upper edge, C: Central substrate, D: Delaminated corner. Note that delamination angle is 15°; 0° refers to the substrate plane.

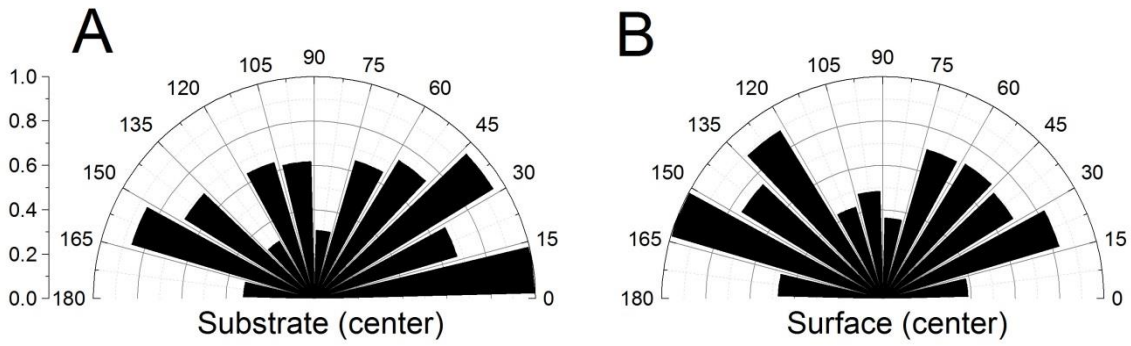

Figure 4-15. Angular distribution of pore orientation with respect to the substrate in the 27µm x 25µm system at different locations in the stripe. A: Central substrate, B: Central surface.

Pore orientation expressed via the angular distribution of the cumulated weighted length of the Feret's diameter is presented in Figure 4-14 for 27µm x 100µm stripes. A preferential pore orientation parallel to the substrate reminiscent of freely sintered laminates deposited by tape casting [34] is found both in the upper and the delaminated corner of the 27µm x 100µm stripe as well as near the surface in the stripe center. Pores in the stripe center at the substrate are more likely to be oriented at angles between 60° and 120° with respect to the substrate. Thus, at all free surfaces of the film, pores are preferentially

oriented in the substrate plane whereas vertically elongated pores are only found in the constrained center. In case of the narrow 27µm x 25µm stripe, angular plots of pore orientation in Figure 4-15 reveal a slightly preferential pore orientation parallel to the substrate everywhere in the stripe, even directly at the substrate.

Alumina stripes on platinum coated sapphire

Alumina stripes on platinum coated substrates show the same trend in density as a function of distance to the substrate. Figure 4-16 shows the linear increase in relative density of a 27µm x 100µm wide stripe sintered at 1350°C for 4h on a continuously sputtered platinum interlayer. The total density is 87.0% compared to 83.7% in the 27µm x 100µm on plain sapphire under the same sintering conditions. Thus, the presence of the platinum interlayer results in enhanced densification, but does not alter the thickness dependent microstructural anisotropy.

4.2.3. Constrained shrinkage: Influence of geometry

The different shapes of narrow and wide stripes and the varying percentage of the edge zone compared to the total stripe width lead to the assumption of non-uniform sintering strains that vary with stripe geometry. In the following section, vertical strains obtained in the stripe center as well as lateral strains measured near the surface and at the interface are studied as a function of stripe geometry.

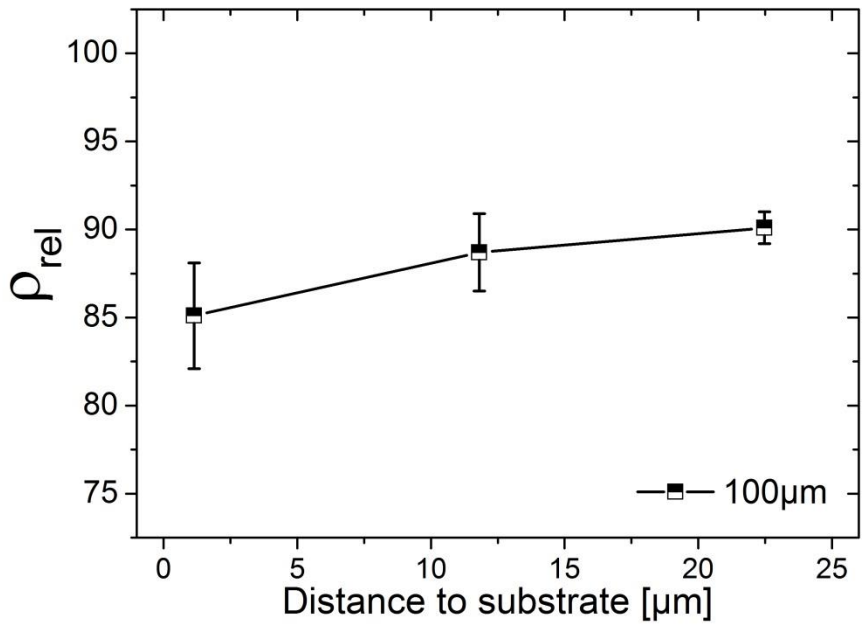

Figure 4-16. Local density in the stripe center measured in the center of a 27µm x 100µm stripe on platinum coated sapphire sintered at 1350°C for 4h.

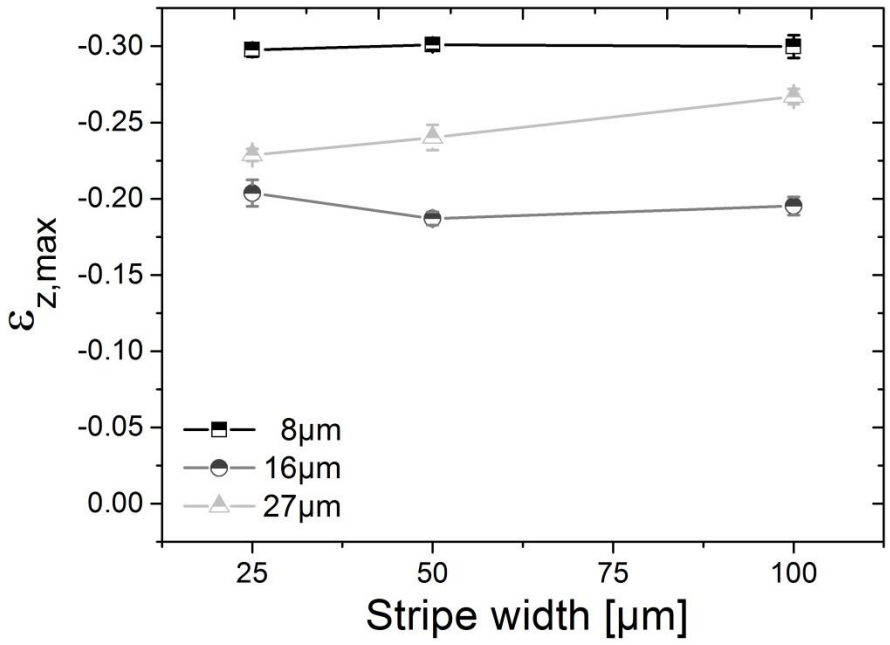

Figure 4-17. True vertical strain as a function of thickness stripe width for three different stripe thicknesses for stripes on smooth sapphire sintered at 1450°C for 4h.

Alumina stripes on plain sapphire

The true vertical strain as a function of stripe width for stripes of different thicknesses is shown in Figure 4-17. Vertical strain remains fairly constant with stripe width for any given thickness; only in the 27µm thick stripes a 0.04 difference between the strain in the narrowest and widest stripes is observed. Stripe thickness, however, has a large influence on the vertical strain, with the thinnest stripes exhibiting the largest values. This effect can be related to thickness dependent drying that results in lower starting densities for the thin stripes.

The behavior of the true lateral strain differs from the vertical strain, showing a negative trend with increasing stripe width for thin films (Figure 4-18) while remaining constant for thick films. Furthermore, the lateral strain at the film surface is higher than the strain measured at the film-substrate interface for all stripes. The difference between the two curves decreases with increasing stripe width in the 8µm system but remains constant in the 27µm system. All of these trends are valid for alumina stripes on smooth as well as rough substrates. However, lateral strain on the rough substrates is lower in all systems consistent with the reduced delamination observed before.

The explanation for the width dependence of the lateral strain is found in the edge displacement. The enhanced inclination of the film edges in wide stripes shown in Figure 4-3 suggests a width dependent increase of the edge displacement.

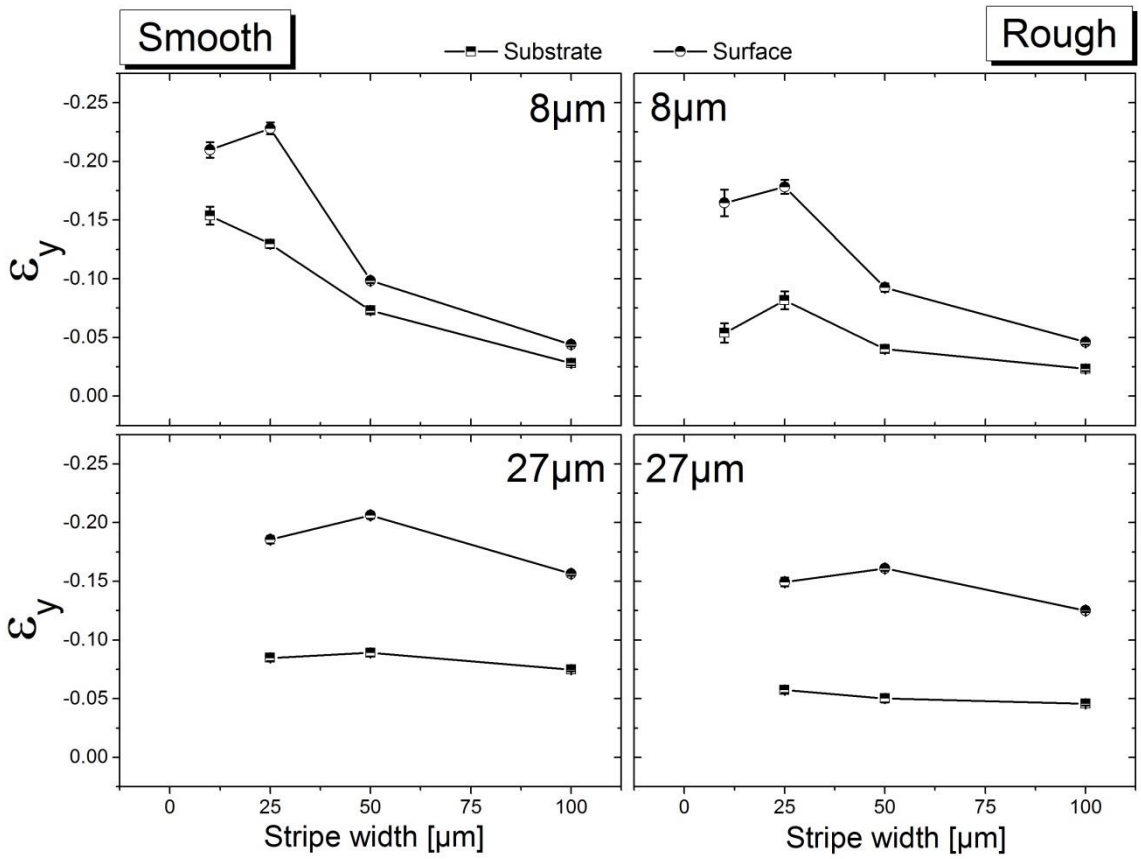

Figure 4-18. True lateral strain measured at the substrate (rectangles) and at the surface (circles) for thin and thick films in smooth and rough substrates.

In Figure 4-19, edge displacement determined as half the difference between green and sintered width is shown for different film thicknesses ranging from 8µm to 32µm. The displacement values at low widths up to 25µm are similar for all thicknesses; however, at 50µm the curves start to deviate. The 32µm x 100µm stripe reaches a displacement of 7.5µm, three times the value of the 8µm x 100µm system. Consequently, an increase of displacement with width is at first observed in both thin and thick films that is consistent with the shape of the cross sections. This increase is followed by a plateau in the all systems up to 27µm thickness. In the 8µm thick system this plateau starts from a width of 25µm, while in case of the 16µm and 27µm thick films the plateau is only reached at 100µm. This is consistent with the observation that the extension of the edge zone is constant in thin films and makes up an increasingly large portion of the decreasing stripe width. This also accounts for the width dependence of the lateral strain. The 32µm system does not show a plateau at all up to a width of 250µm, but the curve is expected to saturate for even wider stripes.

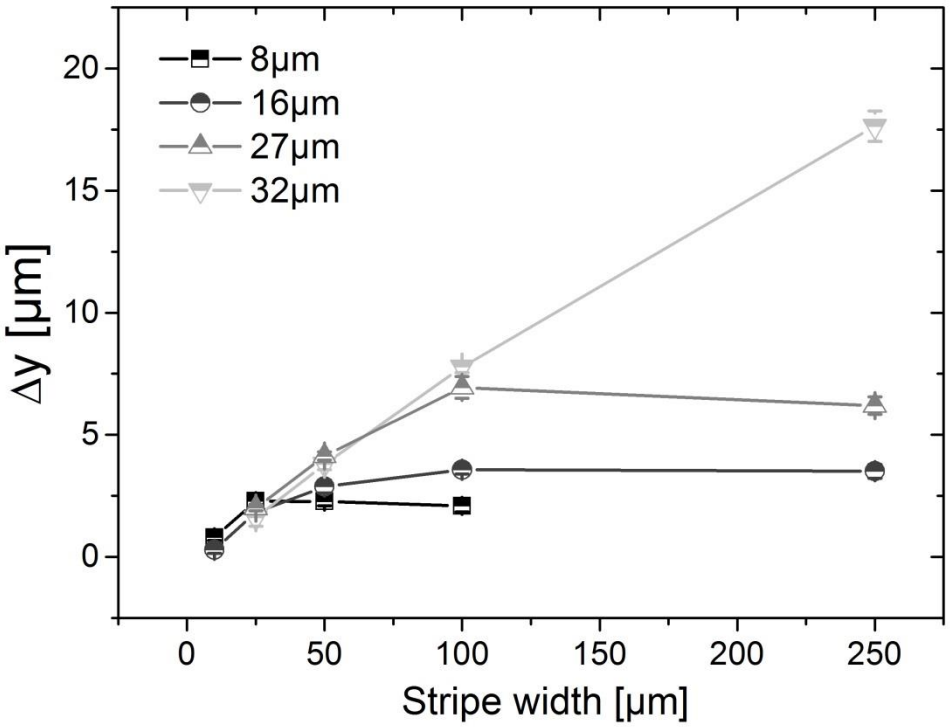

Figure 4-19. Width dependent displacement of the upper film edge for different film thicknesses. 32µm system has been obtained according to drying condition II.

Alumina stripes on platinum coated sapphire

When a platinum interlayer is present, the same geometry dependence of the strain components is observed as in smooth sapphire. The vertical strain decreases with increasing stripe thickness due to the green density gradient, but remains fairly constant over the entire width range as shown in Figure 4-20. The absolute vertical strain values are the same as in smooth sapphire subjected to the same sintering cycle.

In Figure 4-21, width dependent true lateral strain curves for 8µm and 27µm on smooth sapphire and continuously sputtered platinum are contrasted. Lateral strain decreases with increasing stripe width as in the other systems; however, the difference between the strain values measured at the surface and near the interface is smaller when a platinum interlayer is present than in uncoated sapphire specimens. For the 8µm thick films, the difference becomes zero, which means that the lower particle layers are dragged along by the free upper corners. The absolute strain values are higher in case of the platinum substrates, the difference being more pronounced for the low aspect ratio stripes in the 8µm system. Here, the 8µm x 10µm systems on both substrates exhibit a similar surface strain of -0.12 and -0.13, but the corresponding strain near the interface is more than twice as high in the platinum coated specimens. In wide stripes, both surface and interface strain are twice as high when the interlayer is present. This means that the presence of the platinum interlayer affects narrow stripes consisting of

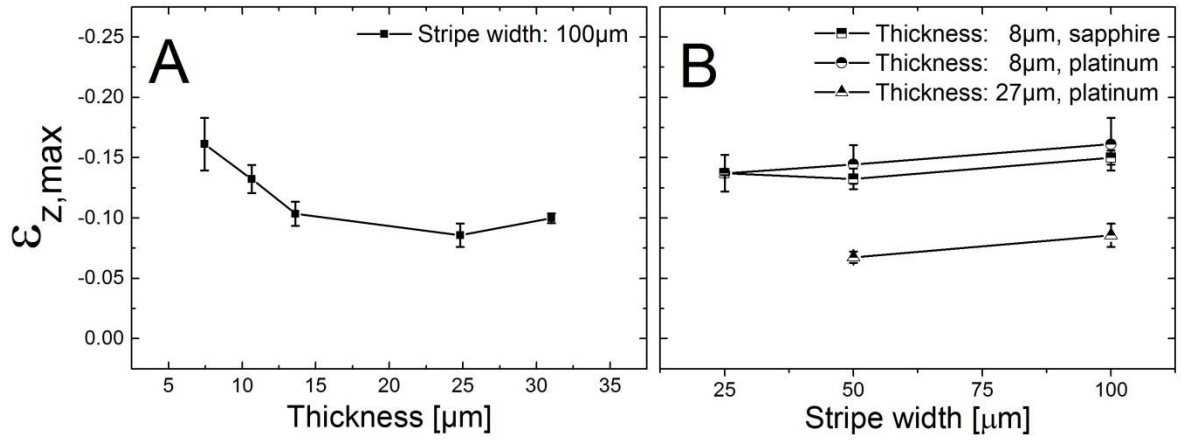

Figure 4-20. True vertical strain as a function of stripe thickness (A) and width (B) for stripes on continuously sputtered platinum layers sintered at 1350°C for 4h.

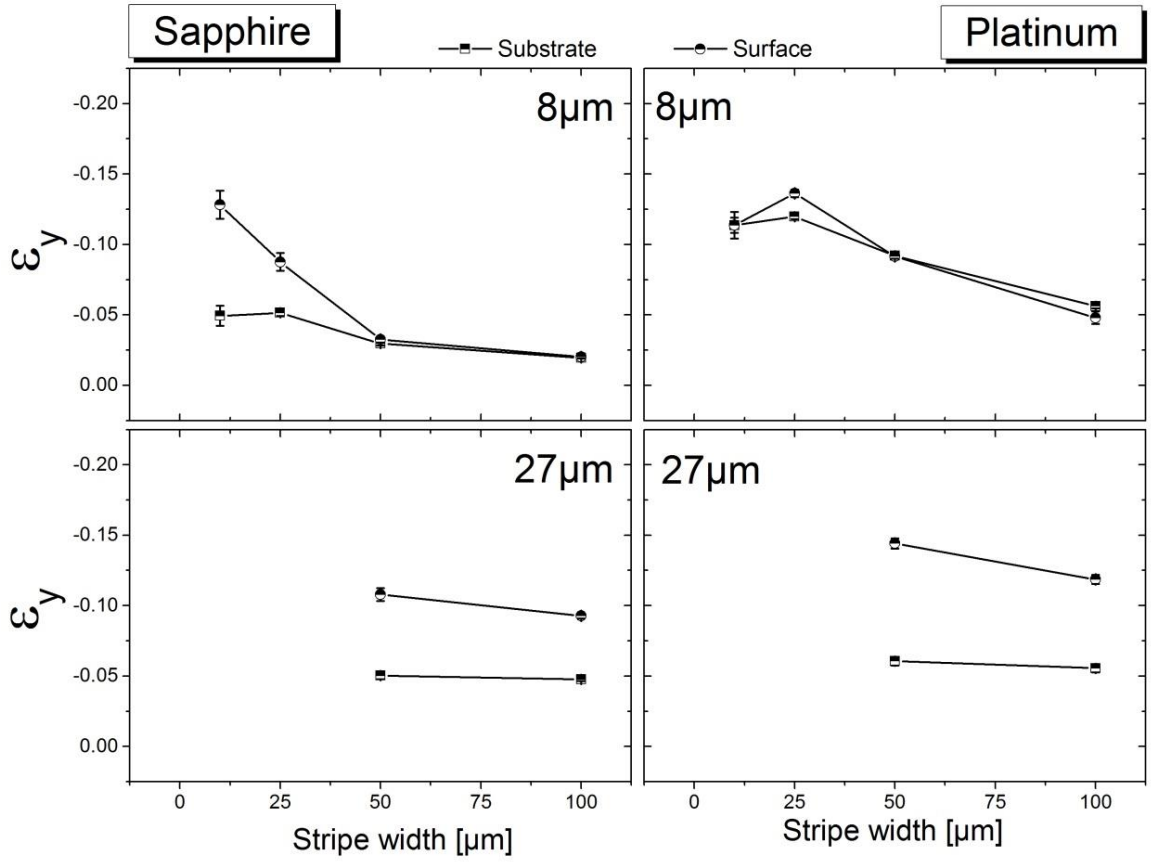

Figure 4-21. Lateral strain measured at the surface (circles) and the substrate (rectangles) on thin and thick films deposited on plain and platinum coated sapphire sintered at 1350°C for 4h.

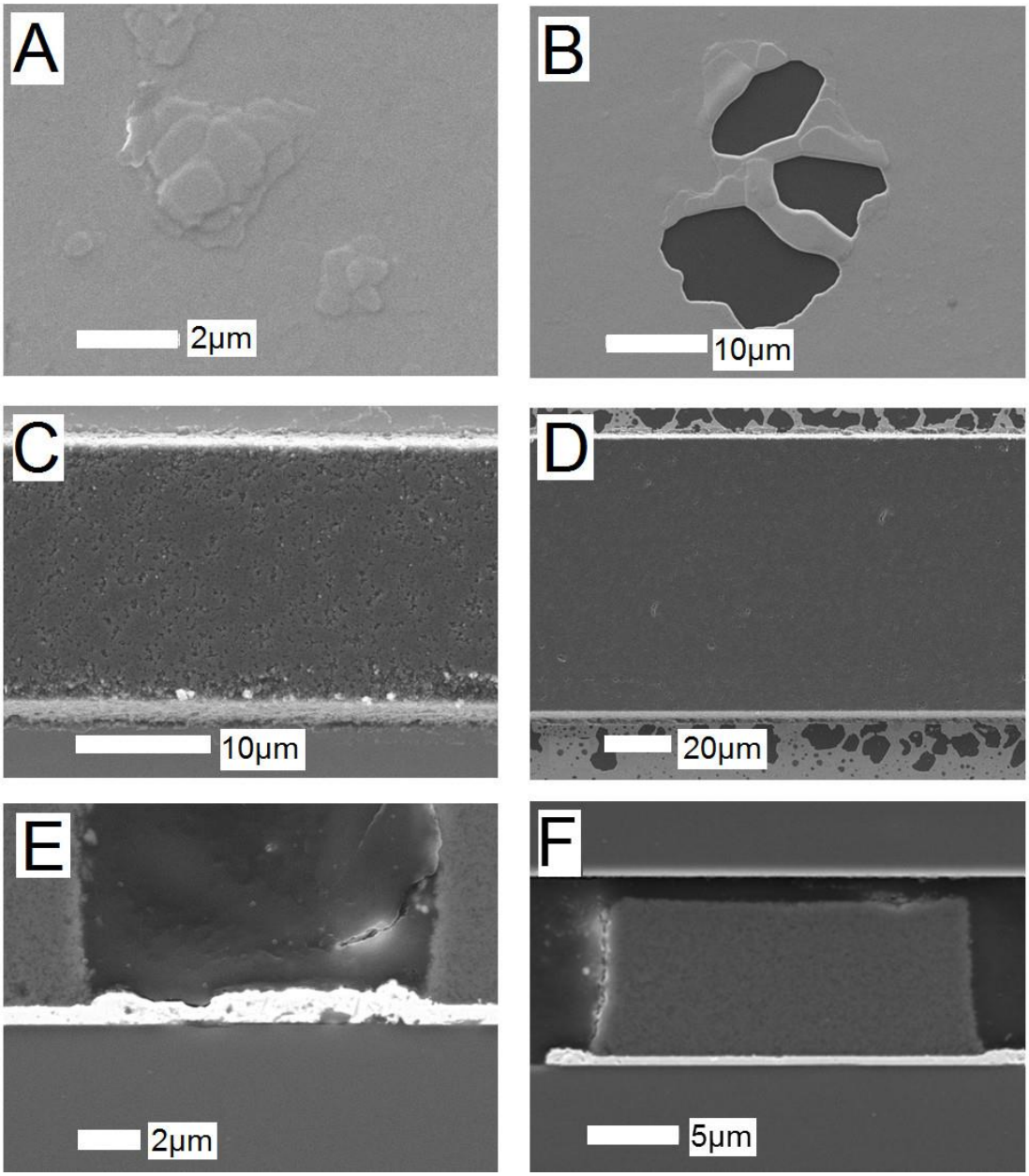

Figure 4-22. Morphology of the platinum interlayer. A: Hillocks and B: Holes in continuously sputtered platinum layer after sintering at 1350°C for 4h. C: Absence of hole formation near 16µm x 25µm stripe and D: Increased hole formation near 16µm x 100µm stripe. E: Increased thickness of platinum layer between stripes, F: Undamaged platinum layer underneath stripe.

overlapping edges less since the latter experience high densification regardless of the interface properties.

In order to understand the enhanced lateral strain in the platinum system, the morphological changes in the platinum interlayer are investigated. Continuously sputter deposited platinum layers remained attached to the sapphire surface for 4h at 1350°C. Higher temperatures could not be studied as complete evaporation of the platinum layer was observed when heated to 1400°C for 30min.

However, even in the samples heated to 1350°C the platinum surface layers deposited onto the sapphire substrates underwent morphological changes during sintering. Hillock and hole formation were observed as shown Figure 4-22 A and B. This phenomenon has also been reported by other researchers [102] in thin platinum films on zirconia single crystal substrates and was attributed to the relaxation of strain energy due to the lattice mismatch. Another possibility is film breakup due to Rayleigh instability, leading to droplet shaped islands [108].

However, hillock and hole formation are not uniform throughout the film. The density of hillocks and holes was lowest far away from the ceramic stripes. A large number of holes is observed along the stripe edges, but only in case of stripes with low aspect ratio that exhibit the highest edge displacement. This is shown in Figure 4-22 B and C, where SEM top view pictures of sintered 16µm x 25µm and 16µm x 100µm stripes are presented. Along the edge of the 16µm x 25µm stripe, no holes are found, whereas the platinum interlayer is almost completely disrupted in case of the 16µm x 100µm stripe edge. In Table 4-2, the observation of hole formation is summarized for the different stripe systems. As a general rule, hillocks and holes are not observed next to the narrowest stripes of any given thickness (10µm and 25µm in width). At 50µm width, occasional to frequent hole formation is observed while rupture of the platinum interlayer takes place in some 100µm and 250µm stripes.

In addition, the platinum interlayer increases in thickness both underneath and next to the alumina stripes, with the increase being larger next to the stripes. This is shown in polished SEM cross sections in Figure 4-22 E and F that reveal the platinum interlayer between as well as underneath two 11µm x 10µm stripes sintered at 1350°C for 4h. Here, island formation at the expense of local grooving is clearly visible between the stripes, whereas beneath the stripe the interlayer has a uniform thickness.

Table 4-2. Hole formation in the platinum interlayer next to stripes of different geometries.

Stripe thickness [µm]	Stripe width [µm]	Hole formation along edge
8	10	None
8	25	Occasional
8	50	Frequent
8	100	Frequent
11	10	None
11	25	None
11	50	Occasional
11	100	Frequent (local rupture)
16	25	None
16	50	Occasional
16	100	Frequent (local rupture)
27	50	None
27	100	Occasional
27	250	Rupture

In Table 4-3, platinum film thicknesses at different locations are listed and compared to the thickness of as-deposited platinum layers as well as an uncoated platinum layer sintered under the same conditions as the platinum layers covered by the alumina stripes. When studying uncoated platinum layers, it is noteworthy that continuously sputtered layers only show a 10% increase in thickness after heat treatment that is not significant considering the accuracy of the measurement. In contrast, discontinuously sputtered layers are more than twice as thick after heat treatment due to higher in-built stresses that lead to more severe hillock formation. In both systems, the thickness of the platinum layer next to the alumina stripe edges has undergone a larger increase than the heat treated, uncoated layer. The area underneath the stripe is slightly thicker than the heat treated, uncoated layer in case of continuously sputtered platinum but thinner in the discontinuously sputtered film. In summary, the increase in platinum layer thickness is more drastic at the uncovered locations than beneath the stripes.

4.2.4. Strain and densification curves

Alumina stripes on plain sapphire

The evolution of strain anisotropy with sintering time is shown Figure 4-23, where the vertical and lateral strain curves of narrow and wide stripes with different thickness are contrasted for rough and smooth substrates. In case of the narrow 27µm x 25µm stripe on smooth sapphire, the vertical and surface lateral strains are equal throughout most of the sintering cycle. Both vertical and surface lateral strain exceed the lateral strain at the substrate. Its counterpart on rough sapphire shows slightly lower vertical and lateral strain with the former overtaking the latter at 60min after the beginning of densification. This indicates that the reduction in lateral strain as observed before does not occur right

Table 4-3. Platinum layer thicknesses and their increase during sintering.

	Type of platinum layer	**Treatment**	**t [µm]**	**Thickness ratio t/t_1**	**Thickness ratio t/t_2**
Continuously sputtered platinum					
t_1	Uncoated	as-deposited	0.36 ± 0.01	---	---
t_2	Uncoated, sintered	1350°C, 4h	0.41 ± 0.04	1.1 ± 0.1	---
t_3	Coated (beneath stripe)	1350°C, 4h	0.60 ± 0.10	1.7 ± 0.3	1.5 ± 0.3
t_4	Coated (next to stripe)	1350°C, 4h	0.95 ± 0.18	2.6 ± 0.5	2.3 ± 0.5
Discontinuously sputtered platinum					
t_1	Uncoated	as-annealed	0.30 ± 0.02	---	---
t_2	Uncoated, sintered	1250°C, 4h	0.76 ± 0.04	2.5 ± 0.2	---
t_3	Coated (beneath stripe)	1250°C, 4h	0.47 ± 0.05	1.6 ± 0.2	0.6 ± 0.1
t_4	Coated (next to stripe)	1250°C, 4h	1.06 ± 0.17	3.5 ± 0.6	1.4 ± 0.2

from the start, but develops in the course of densification. The wider 27µm x 100µm stripes, however, experience enhanced vertical strains throughout the sintering cycle. Here, the surface lateral strain is in the same order of magnitude than the strain of a freely sintering sample with the same starting density sintered to 100% final density (-0.16 in the film vs. -0.13 in the free sample). The out-of-plane strain equals twice the free strain, while the interface lateral strain is reduced.

When comparing the different substrates, increasing lateral strains throughout the sintering cycle are observed on smooth substrates, whereas the curves start at a similar lateral strain level (surface lateral strain of -0.07 after 34min for both substrates) but flatten out after an hour in case of the rough substrate. This means that as in case of the narrow stripes the effect of the substrate roughness manifests itself after a certain amount of densification.

A similar effect is observed in case of the thin, low density stripes of the 8µm thick system. In Figure 4-24, a large difference in vertical to lateral strain is shown from the start of the sintering cycle. It is obvious that the effect is more pronounced for wide 8µm x 100µm stripes. Vertical strains are enhanced compared to the free strain (-0.30 vs. -0.19). The surface lateral strain is reduced in the wide stripe and equal to the free strain in the narrow stripe.

The geometric densification curves of 27µm x 100µm and 27µm x 25µm stripes on smooth and rough sapphire substrates are plotted in Figure 4-25. Here, density was calculated according to eq. 46 taking into account the size of the stripe cross section at every step of the sintering cycle. Since the minimum length detailed in section 3.3.1. was maintained for every sample, shrinkage along the length of the stripe is always smaller than 1% and therefore neglected. Free densification curves obtained by DEM simulations starting from a slightly lower green density (65% vs. 67.1%) have been provided by other researchers for comparison. Densification is severely retarded for all stripe geometries and substrates and the final density is reduced to values between 85% and 95%. The effect is stronger for the wide 27µm x 100µm stripe. In both geometries, the densification curve of the stripe on rough sapphire has a similar shape than its counterpart on smooth substrates, but the curve is shifted towards lower densities with an offset that increases from ca. 2% to 5% in case of the wide stripe and 8% in case of the narrow stripe. This growing difference in density may be caused by the steady increase in lateral strain due to the progressing delamination on smooth substrates over the entire sintering cycle, after crack arrest at an obstacle in the rough substrate has occurred.

Densification curves of 8µm thick stripes are given in Figure 4-26. Here, the curves of narrow and wide stripes coincide at first. Towards the end of the holding time, density of the narrow stripe increases further and exceeds the density of the wide stripe by 8%. Here, again, the increase in density mimics the growth of lateral strain while the vertical strain has flattened.

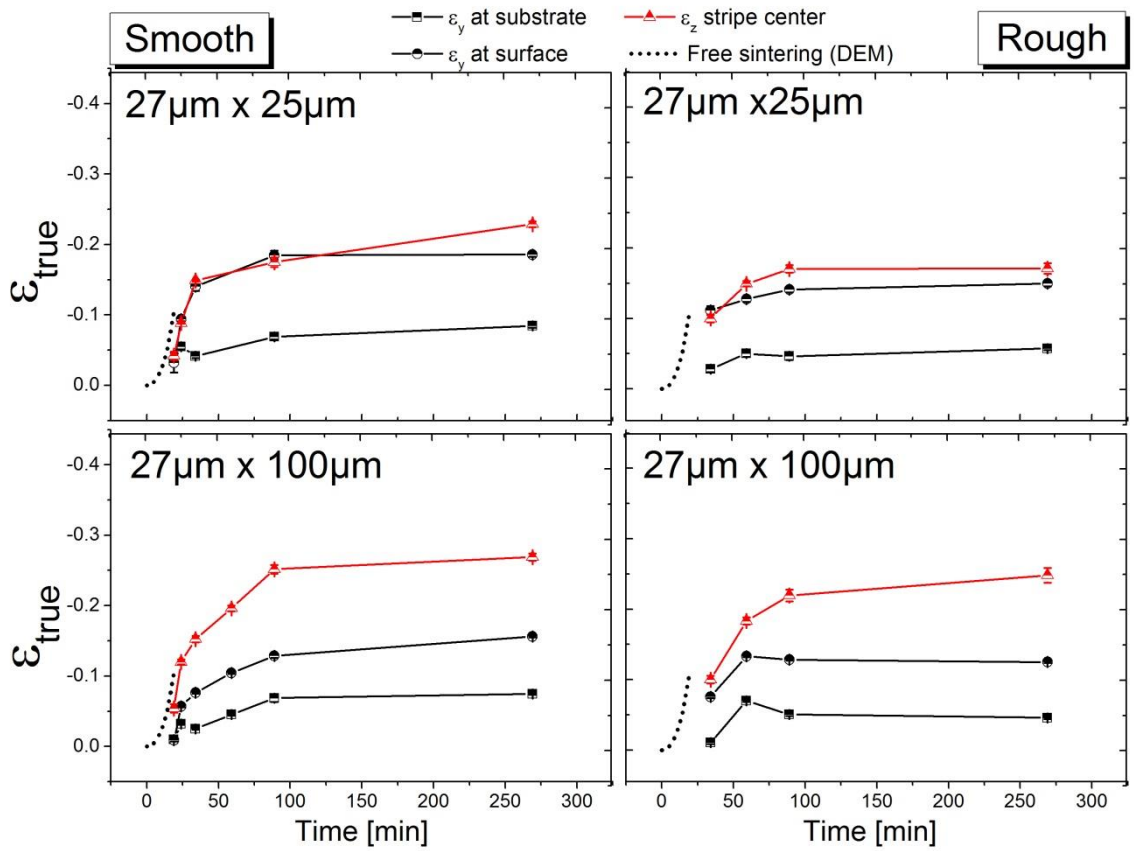

Figure 4-23. Vertical (red) and lateral strain curves (black) measured on narrow stripes of the system 27µm x 25m (top row) and wide 27µm x 100µm stripes (bottom row) on smooth (left column) and rough sapphire substrates (right column). Free sintering data provided by Tobias Rasp from [122].

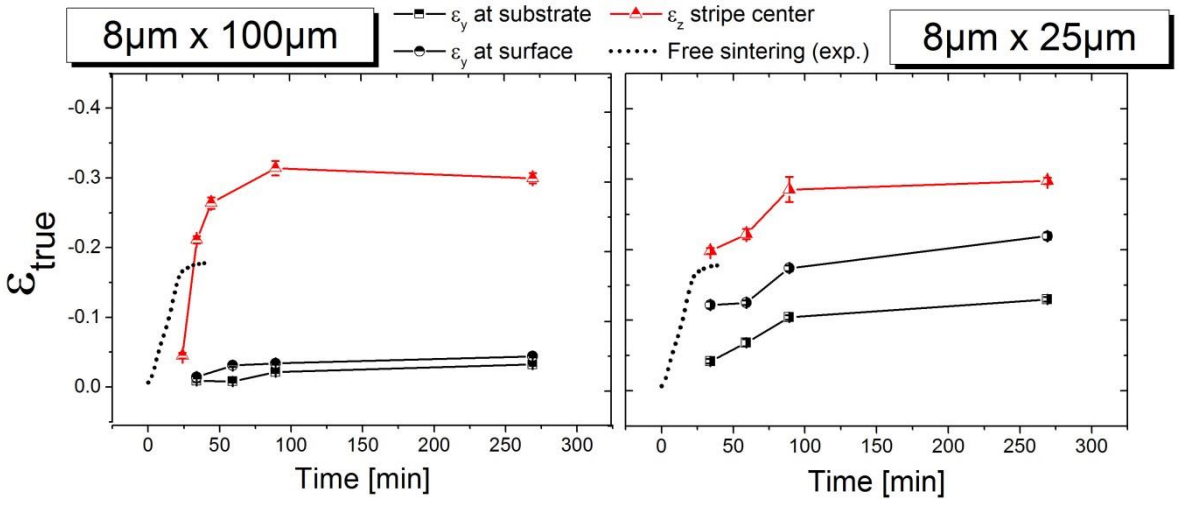

Figure 4-24. Vertical (red) and lateral strain curves (black) measured on stripes of the system 8µm x 100m (left) and wide 8µm x 25µm stripes (right) on smooth sapphire.

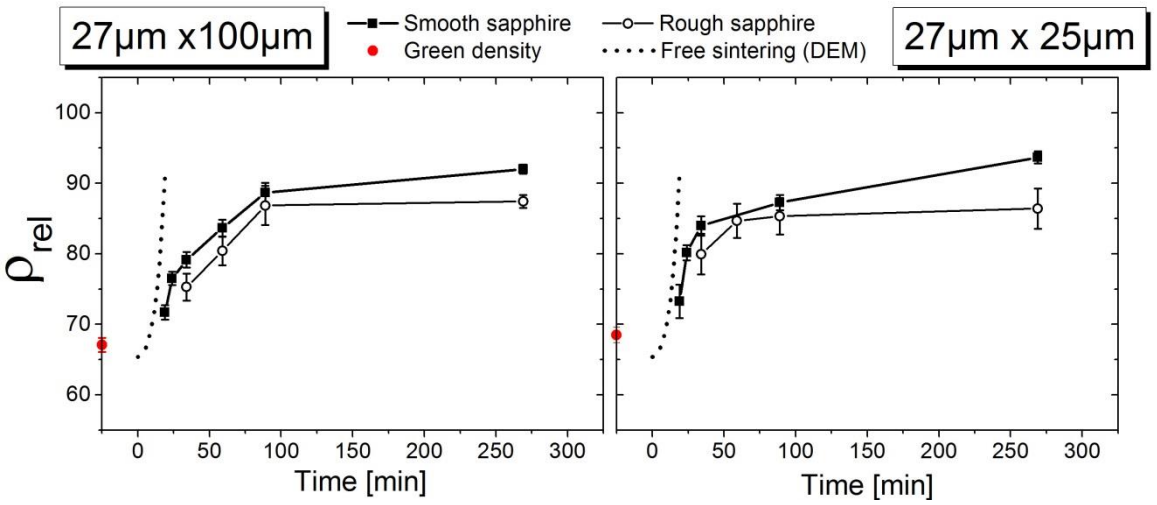

Figure 4-25. Relative geometric density for stripes on smooth (filled symbols) and rough substrates (open symbols) contrasted with free sintering curves obtained by DEM simulations for different stipe geometries. Free sintering data provided by Tobias Rasp [122].

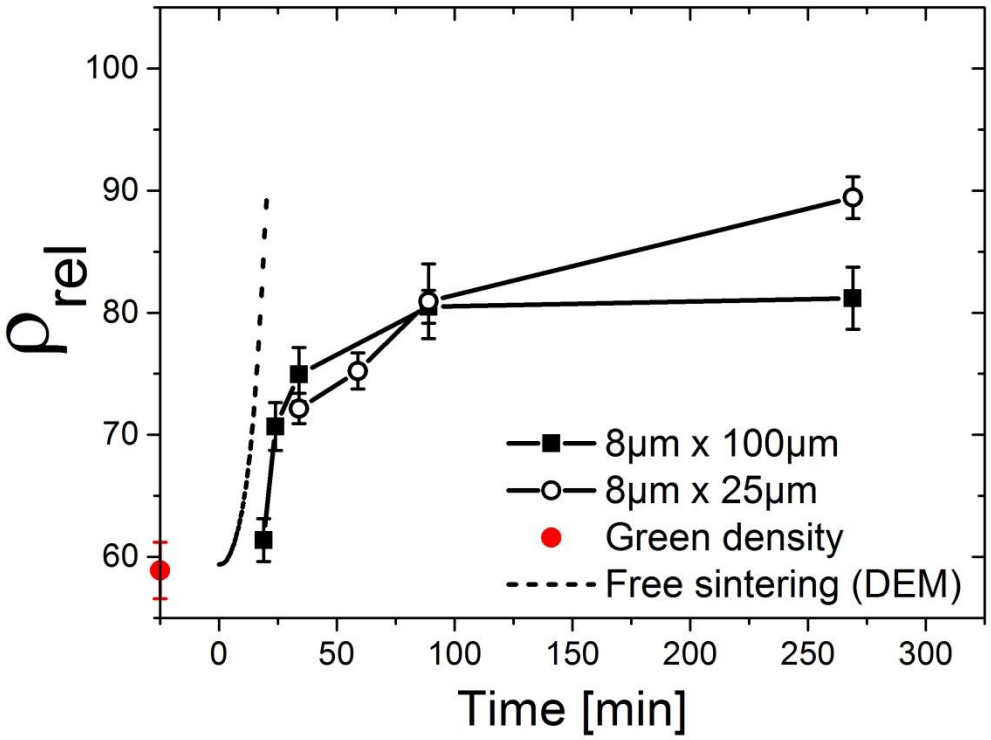

Figure 4-26. Relative geometric density for stripes on smooth substrates contrasted with free sintering curves obtained by DEM simulations for different stipe geometries. Free sintering data provided by Tobias Rasp [122].

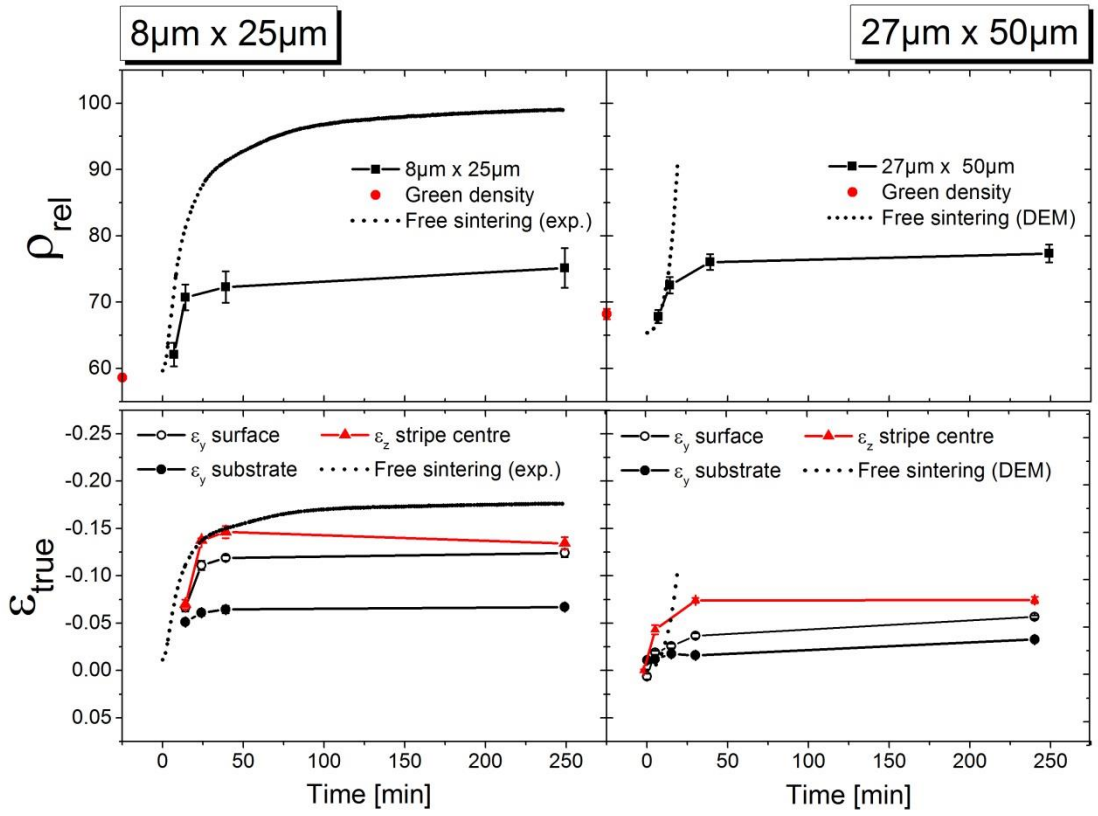

Figure 4-27. Densification (top row) and strain curves (bottom row) of stripes on platinum coated sapphire substrates. Left column: 8µm x 25µm, right column: 27µm x 50µm. DEM data provided by Tobias Rasp from [122].

Alumina stripes on platinum coated sapphire

Strain and densification curves of stripes on platinum coated sapphire are presented in Figure 4-27. Again, density is calculated according to eq. 46 and the in-plane strain parallel to the edge is <1% and thus neglected. As on plain sapphire, densification (top row) is reduced for the stripes compared to the free sintering curves. The main difference in the strain curves (bottom row) caused by the platinum interlayer is the fact that the vertical strain of 8µm x 25µm thick stripes is no longer enhanced compared to free sintering. Furthermore, the vertical strain and surface lateral strain almost equal in the 8µm x 25µm system. In short, thin films on platinum coatings show a similar behavior than thick films on plain sapphire.

4.3. Liquid phase sintering

4.3.1. Microstructure and interface morphology

Cross sections of liquid phase sintered alumina stripes as depicted in Figure 4-28 show alumina grains surrounded by glass pockets as well as large, unfilled pores. At the beginning of the isothermal time,

the substrate has grown into the film over a thickness of up to ca. 2µm. However, growth of the substrate is not observed in every stripe. If present, the effect is most pronounced at the stripe edges. This is a significant difference compared to the pure alumina stripes, where substrate growth into the stripes was observed only occasionally and usually over a lesser distance.

4.3.2. Geometry dependence of strain

In the liquid phase sintered system, the geometry dependence of the lateral and vertical strains show the same effects as in pure alumina stripes. As shown in the left graph in Figure 4-29, the surface lateral strain exceeds the strain at the interface by a factor of two for all stripe geometries. In addition, a decrease in both lateral strain curve with increasing width is observed. When stripe thickness is increased at constant width, both surface and interface lateral strain increase and their difference increases from zero (thin stripes) to a factor of 3. Vertical strain again decreases with thickness; this indicates that a green density is geometry dependent in the liquid phase sintering system as well, with thin stripes exhibiting lower green densities due to constrained drying.

Strain curves of a thin and a thick stripe are presented in Figure 4-30. In case of the 8µm thick stripe, a linear increase in vertical strain is observed throughout the sintering cycle up to values of -0.58, whereas the lateral strain saturates early on at levels around -0.05. The difference in lateral and vertical strains is severely enhanced compared to the pure alumina stripe of the same geometry; this is due to the fact that the lateral strains are similar in magnitude for both materials whereas the vertical strain is larger in the glass-doped stripes due to their lower green density. The 27µm x 100µm stripe shows quasi-free sintering behavior since the vertical and surface lateral strain curves coincide.

This is another difference compared to the pure alumina stripe of the same geometry, whose vertical strain is enhanced throughout the sintering cycle, as shown previously in Figure 4-23. In the liquid

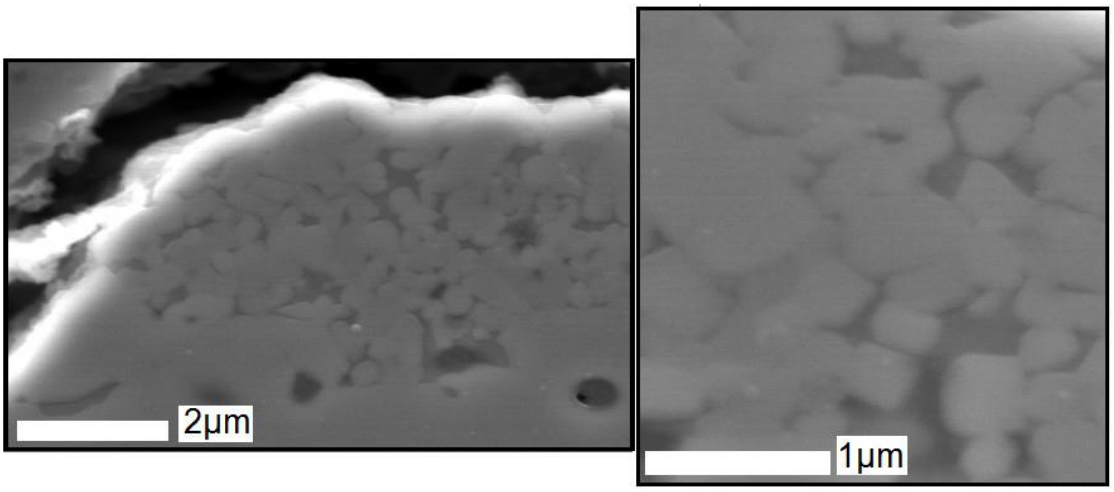

Figure 4-28. SEM micrographs of 8µm x 100µm stripe cross sections. edge (left) and center (right).

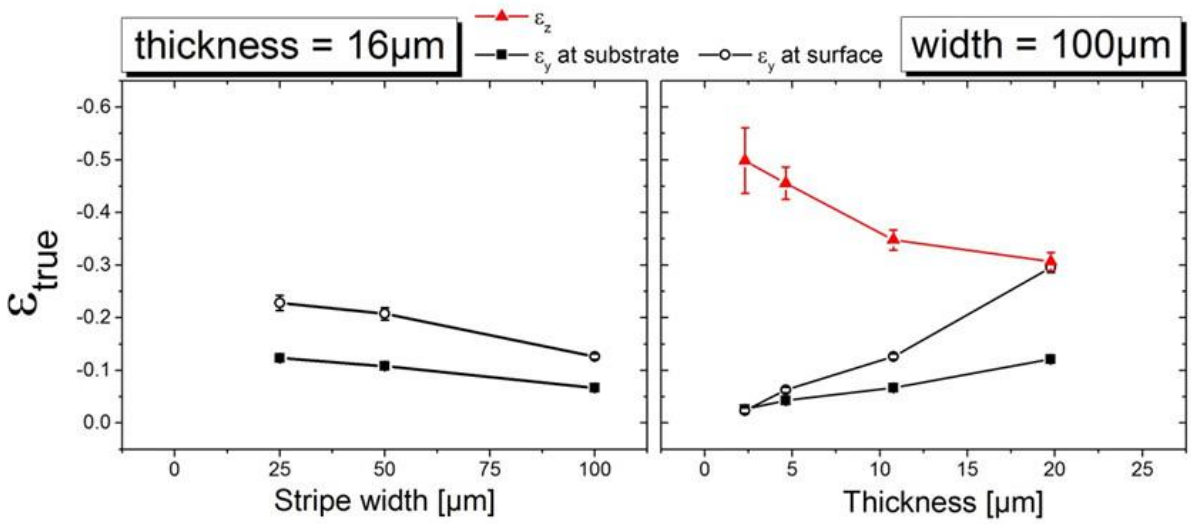

Figure 4-29. True vertical strain (red curve) and lateral strains (black curves) as function of stripe geometry. Left: Width-dependent lateral strain of the liquid phase sintered 16µm thick stripes; right: thickness dependent strains of 100µm wide stripes.

phase sintered system, the surface lateral strain is three times as large as the strain measured at the interface; this factor is two in case of the pure alumina. Thus, the presence of a liquid phase reduces the effect of the substrate constraint, allowing a steeper increase in lateral strain with distance to the substrate as well as quasi-free sintering at thickness-to-width ratios well below unity (0.27 in the present case).

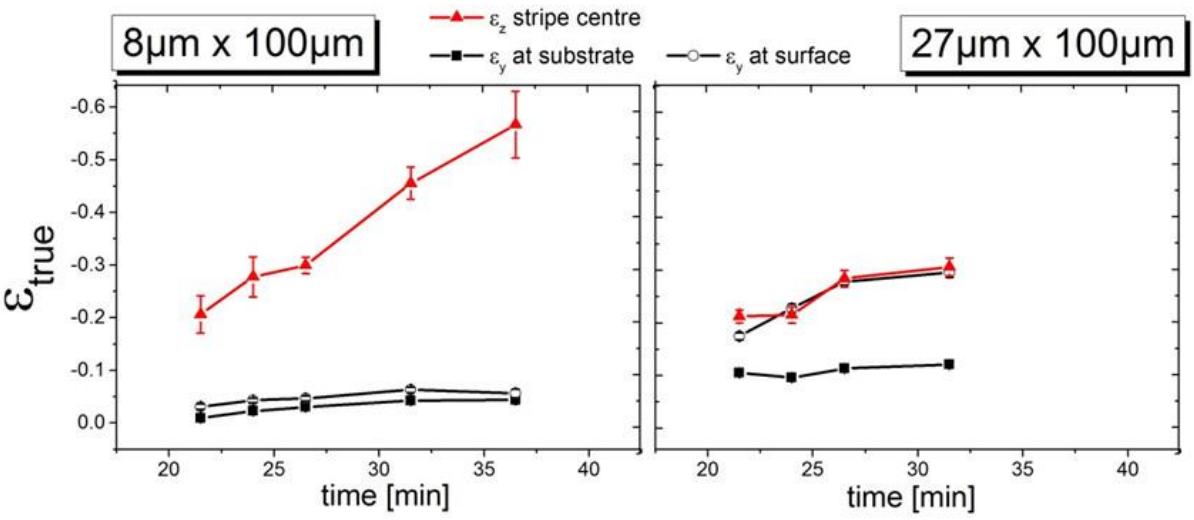

Figure 4-30. Strain curves of the systems 8µm x 100µm and 27µm x 100µm.

4.4. Sintering of cavities and ring structures

4.4.1. Cracking around circular stress concentrators

Sintering of stripes with round cavities is found to promote deformation and cracking. Six different effects were observed depending on the stripe geometry, cavity radius, sintering conditions and substrate material:

1. Opening of the hole
2. Elliptical skewing of the hole
3. Deformation of the stripe edge
4. Random radial cracking
5. Oriented cracking
6. Stripe rupture

In Figure 4-31, examples for the different configurations are given. Picture A shows a C100-20 cavity in an 8µm thick stripe after sintering. Here, the circular cavity has not undergone any changes except for a small increase of its diameter. The C50-10 cavity in picture B, also in an 8µm thick stripe, is elliptically distorted, exhibiting an increase in diameter parallel to the stripe edge and a reduction in diameter perpendicular to it. In some cases, diffuse damage can be found near the endpoints of the minor ellipse axis in type B cavities that precedes the onset of cracking. Type C edge deformation can result in narrow stripes where the edge is close to the cavity, such as the C100-50 cavity in a 27µm thick stripe. Here, the outer edge of the stripe becomes rounded near a large cavity, mimicking its curvature.

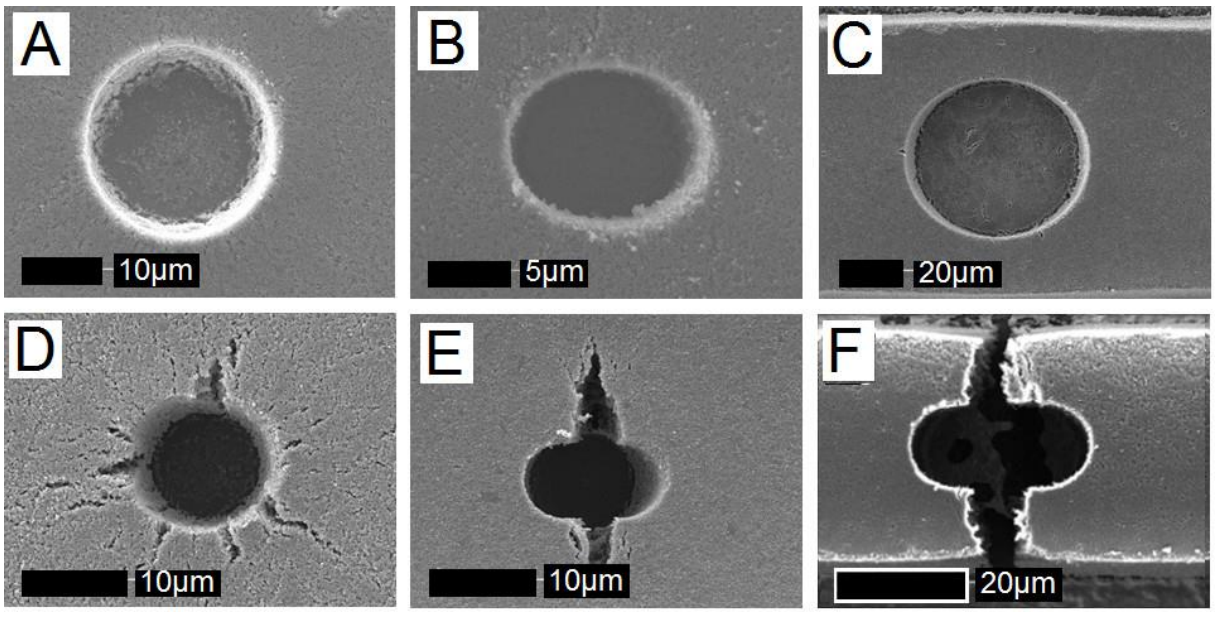

Figure 4-31. Summary of cavity deformation and crack patterns. A: Hole growth, B: Elliptical skewing, C: Edge deformation, D: Random radial cracking, E: Oriented cracking, F: Stripe rupture.

Cracking can occur in different patterns that depend on the stripe geometry and cavity radius. Cavities in wide stripes tend to experience random radial cracking, if at all. This behavior characterizes the C100-5 cavity in picture D. A C50-10 cavity of the 32µm system is shown in picture E. In this case, cracks are oriented perpendicular to the stripe edges. This is usually accompanied by elliptical skewing of the hole and can lead to complete rupture of the stripe followed by lateral shrinkage of the newly formed free surfaces (see picture F). Defects that show this behavior are large compared to the stripe width and are typically located in thick stripes.

In the following section, the influence of the different parameters on cracking and deformation in pure alumina films on smooth sapphire substrates are discussed in detail.

Influence of stripe geometry

According to linear elastic fracture mechanics, **layer thickness** is known to influence the cracking of continuous films [123]. In this study, an additional influence of stripe width has been found. As in continuous films, there is a critical thickness above which cracking occurs. Here, this critical thickness is determined as a function of the stripe width and defect size. Sintered specimens of different thicknesses with cavities of 20µm in diameter and the resulting cracks are presented in in Figure 4-32.

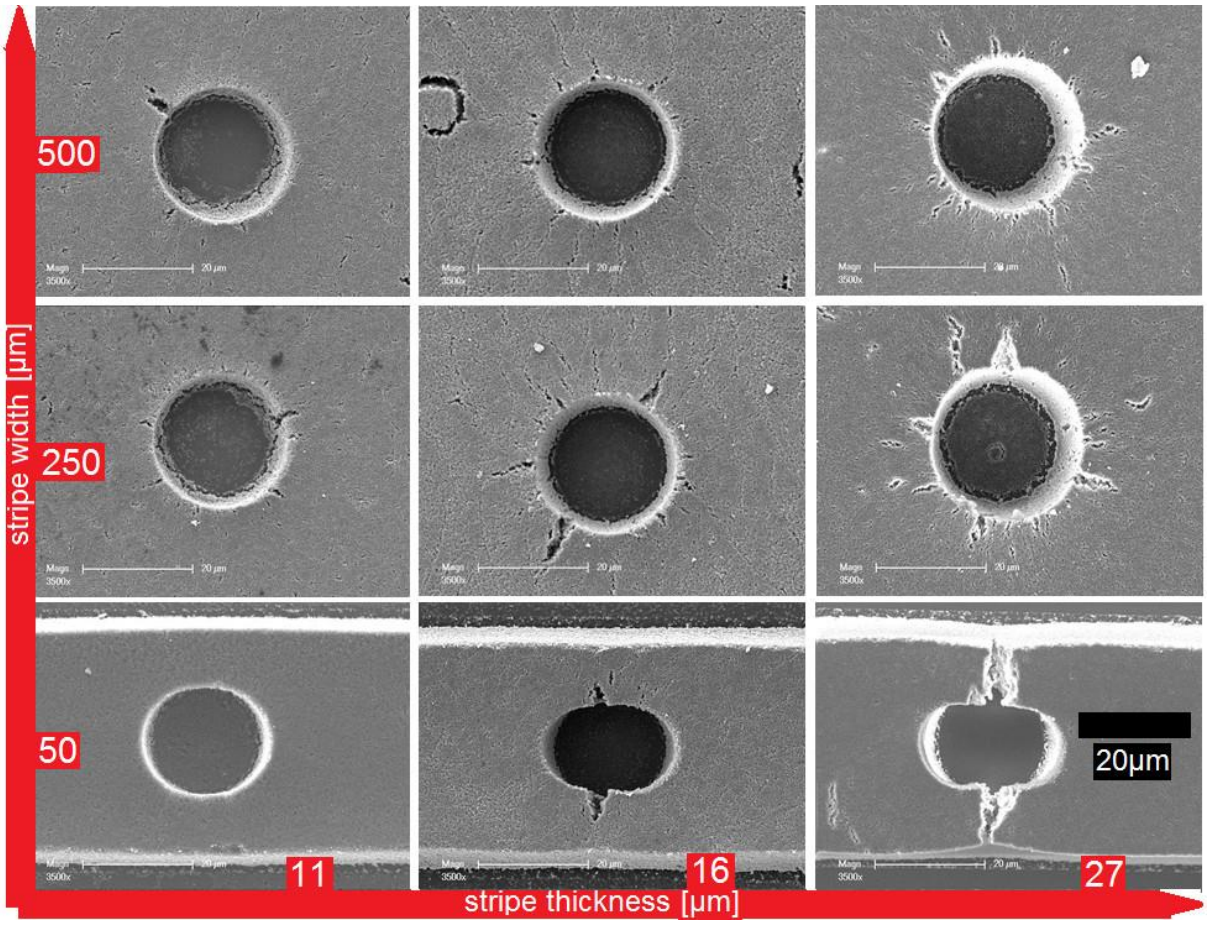

Figure 4-32. Cavity with diameter of 20µm in stripes of varying geometry.

As shown in the lowermost series of micrographs, cracking around C50-20 cavities does occur in the 16µm thick film, but not in 11µm. In the 27µm stripes, cracks propagate to the stripe edges, causing complete rupture of the upper film layers. In addition, elliptical skewing becomes more pronounced with increasing stripe thickness. Thus, the critical thickness for oriented cracking is >11µm, but <11µm for random cracking.

The influence of stripe width on the critical thickness becomes obvious by contrasting the C50-20 cavities with the C250-20 cavities, as shown in the bottom and middle rows in Figure 4-32. The latter show cracking in all stripes of all thicknesses, while the C50-20 cavities in the thinnest stripes do not crack. Thus, large stripe widths promote cracking. Stripe width also determines the crack pattern: Cavities of 20µm in diameter with increasing stripe width (as shown in Figure 4-32 from bottom to top) show a transition between random radial cracks and oriented cracks. The former are present in the C500-20 cavities of thicknesses above 11µm. In stripes of half the width, as in case of the C250-20 cavity, random radial cracking is still observed; however, cracks oriented perpendicular to the edge

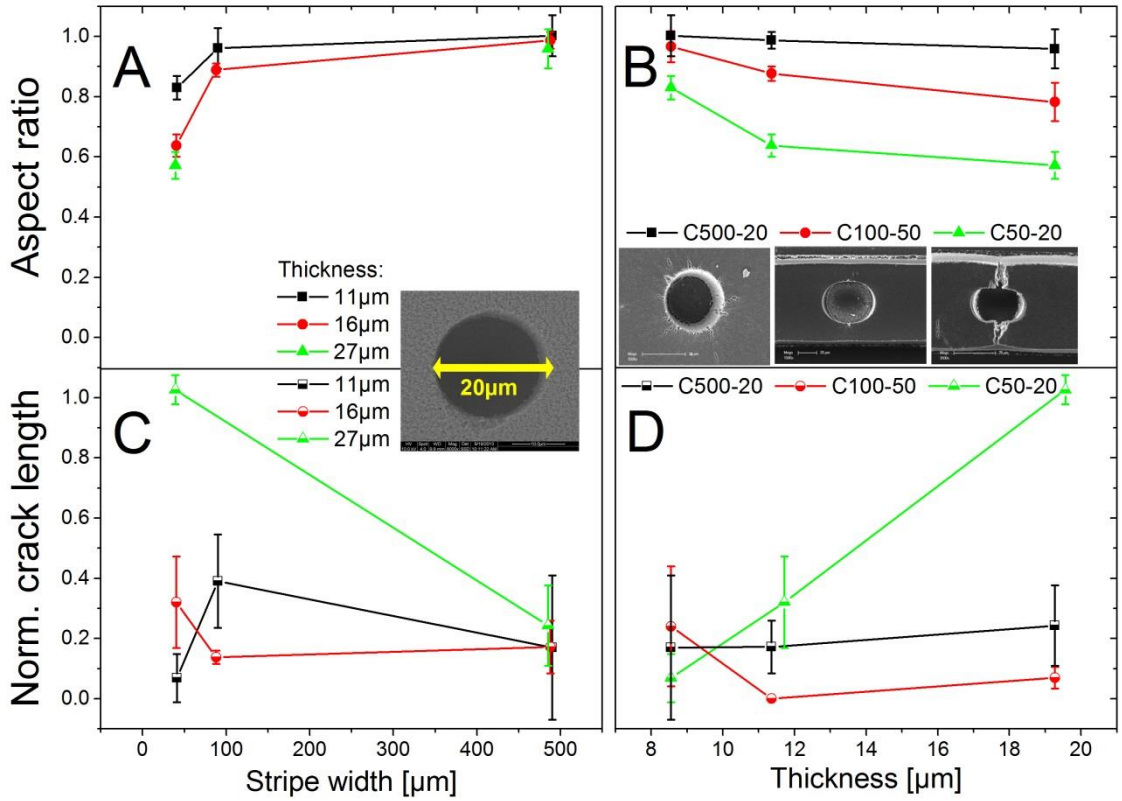

Figure 4-33. Normalized crack length and ellipse aspect ratio as a function of film thickness for systems C50-20, C100-50 and C500-20 on smooth sapphire. A: Width dependent aspect ratio for C50-20, B: Thickness dependent aspect ratio, C: Width dependent crack length for C50-20, D: Thickness dependent crack length.

have a larger opening displacement compared to the other cracks, indicating a beginning tendency to orientation. When the distance to the edge becomes smaller than the hole diameter (system C50-20), only oriented cracks form.

In Figure 4-33, normalized crack length and ellipse aspect ratio are plotted as a function of stripe width and thickness for C50-20 (oriented cracking), C100-50 (deformation with almost no cracking) and C500-20 (random cracking). Here, a strong dependency of both aspect ratio and crack length on stripe width is observed. A 20µm cavity tends to develop elliptical skewing only in narrow stripes (Figure 4-33A); with increasing stripe width the aspect ratio approaches unity. In Figure 4-33 C, crack length normalized by the cavity diameter remains constant with varying stripe width in thin films, but decreases drastically with increasing width in the thickest film. Both elliptical skewing and cracking are therefore influenced by the proximity of the edge; in narrow stripes, a stress buildup due to the finite lateral dimensions causes both skewing and enhanced cracking. This will be discussed in further detail in chapter 5.

When comparing systems with oriented and random cracking, it is obvious that elliptical skewing and oriented cracking always appear together. As shown in Figure 4-33, aspect ratio does not depend on stripe thickness in the system C500-20 that displays random cracking. The systems that undergo oriented cracking, C50-20 and C100-50, show increased elliptical skewing with increasing stripe thickness and the effect is less severe in C100-50 where the absolute distance between cavity and edge is almost twice as large as in C50-20. Crack length is zero for the large C100-50 cavity and constant at 0.2 for the random cracks in C500-20. A positive trend of crack length with stripe thickness is only observed in the case of oriented cracking in C50-20.

Reduction of the **cavity diameter** results in a lower critical thickness for systems that undergo oriented cracking. In Figure 4-34, cavities of different diameters located in stripes of varying thickness and constant width and the resulting cracks are presented. In case of the 5µm cavities, cracks formed in all specimens. Their orientation, however, strongly depends on film thickness; cracking is random in the 11µm thick films and oriented for all higher thicknesses. With increasing diameter of the cavity, both orientation and crack length decrease until there is practically no cracking at all at a diameter of 50µm. This is unexpected since large preexisting flaws have a stronger tendency to grow during sintering than small ones (see critical flaw size described in section 2.6.5.). However, the curvature in small defects is higher and may promote cracking; in addition, stress relaxation by outward curvature of the stripe edge is only possible in large defects since small ones are located at too great a distance

Finally, deformation of the edge in systems that show no or negligible cracking is found to be independent of film thickness. Large cavities in narrow stripes, with a radius equaling the distance between defect and edge (as in 27µm x 100µm in Figure 4-33) cause stress relaxation by outward curvature of the stripe edge. When there is cracking, however, the edge curvature is reduced at the crack tip and sometimes even changes sign, resulting in an inward curvature. This necking effect is observed in the system C50-20 in 27µm stripes (Figure 4-32 C bottom right).

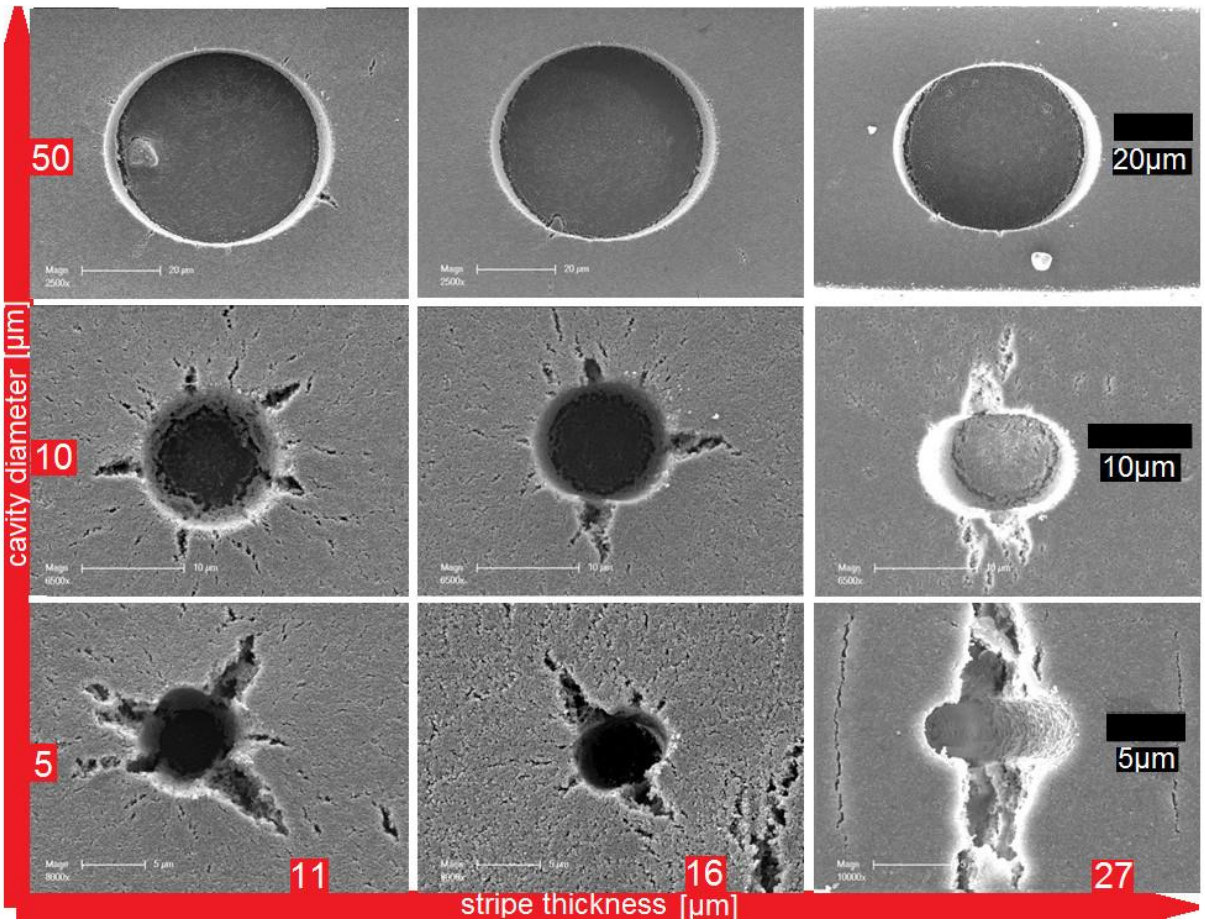

Figure 4-34. Cavities in 100µm wide stripes of different thicknesses with increasing diameter from left to right. Left column: 11µm, middle column: 16µm, bottom column: 27µm

Influence of the substrate

In case of the platinum coated substrates, the same cracking configurations are observed as in the case of plain sapphire. Their dependence on thickness and width also shows a similar trend, as shown in Figure 4-35. As plotted in picture A, cavity aspect ratio increases with stripe width, indicating that cavities in wide stripes retain their original shape whereas in narrow stripes they are skewed by the approaching stripe edges. Again, the effect is most pronounced in thick stripes consistent with the higher edge displacement in these systems. The length of oriented cracks is enhanced by the proximity of the edge (Figure 4-35 C).

Aspect ratio decreases with thickness for cavities that show no or oriented cracking. Cavities that experience random cracking always remain circular. Thick films develop longer cracks only in case of oriented cracking; in all other systems thickness dependence of crack length is negligible. Both aspect ratio and crack length values are in the same range as the values for plain sapphire despite the fact that the sintering temperature was 100°C lower in case of platinum.

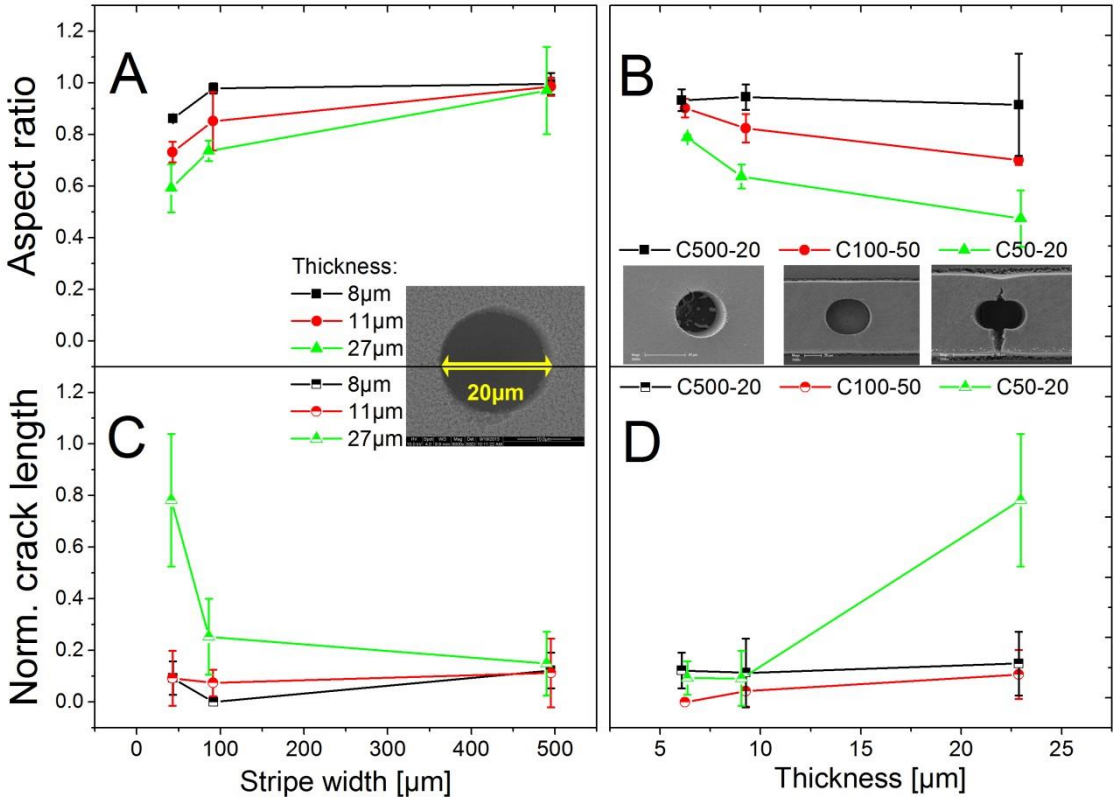

Figure 4-35. Normalized crack length and ellipse aspect ratio as a function of film thickness for systems C50-20, C100-50 and C500-20 on platinum coated sapphire. A: Width dependent aspect ratio for C50-20, B: Thickness dependent aspect ratio, C: Width dependent crack length for C50-20, D: Thickness dependent crack length.

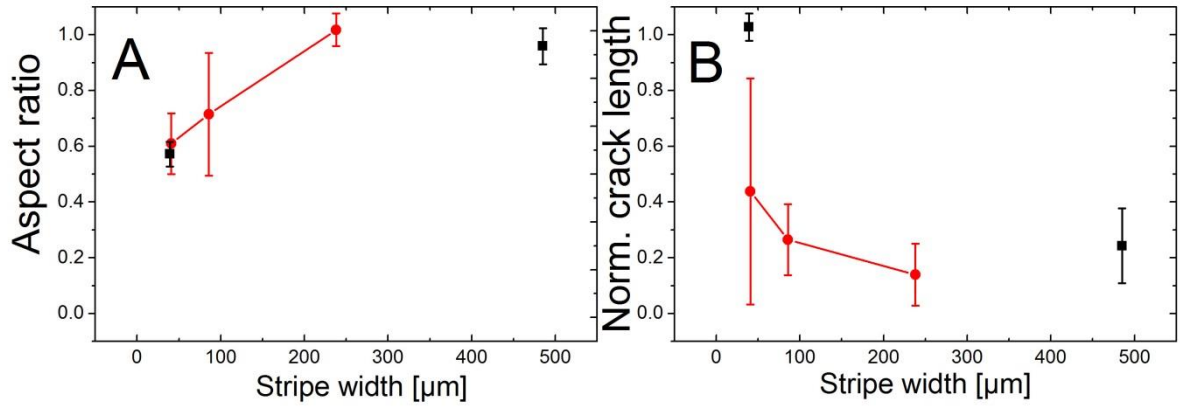

Figure 4-36. Aspect ratio (A) and crack length normalized by cavity diameter (B) as a function of stripe width for a cavity of 20µm in diameter in 27µm thick stripes. Black squares: smooth sapphire, red curves: rough sapphire

On rough sapphire, random cracking around circular cavities is again observed in wide stripes and oriented cracking around elliptically skewed cavities in narrow stripes (see Figure 4-36). Aspect ratio of cavities in 27µm thick stripes is the same on smooth and rough sapphire, while crack length is shorter on rough substrates.

Crack initiation and growth around circular cavities

In-situ environmental scanning electron microscopy (ESEM) gives insight into the cracking mechanisms leading to the effects described above. For instance, it reveals the onset of cracking at temperature just above 1000°C for oriented and 1100°C for random cracking. Crack growth also occurs differently for random and oriented cracks. To elucidate this, in-situ ESEM micrographs of a C250-20 cavity that experiences random radial cracking and a C50-20 cavity prone to oriented cracking are shown in Figure 4-37 to Figure 4-40.

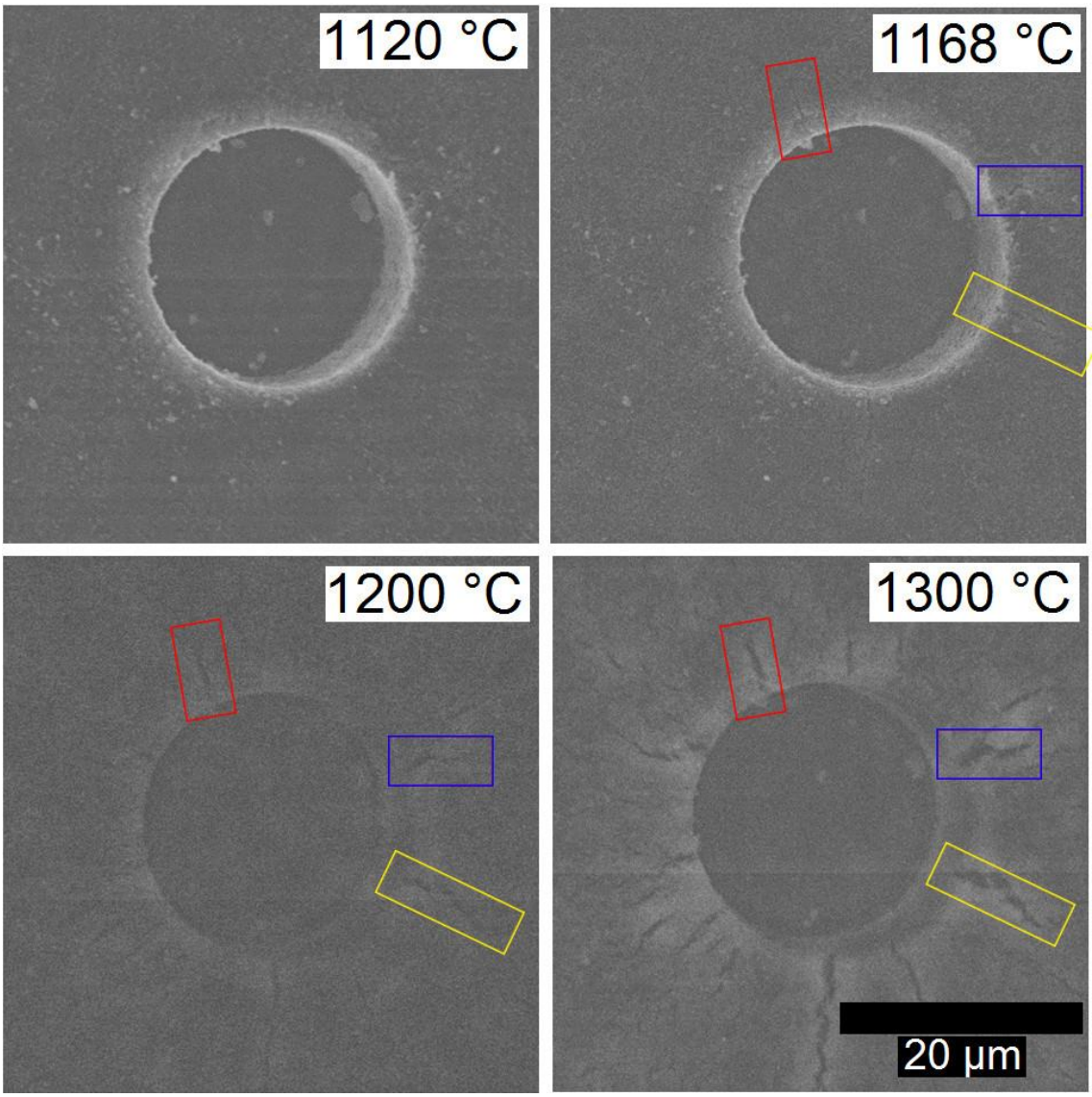

Figure 4-37. Propagation of random radial cracks during sintering of a C250-20 cavity.

In the C250-20 system shown in Figure 4-37, the first fine surface cracks appear at 1120°C. Their position is random and seems to be determined by local porosity fluctuations. Up to 1200°C, their number increases and the existing cracks begin to open. At temperatures between 1200°C and 1300°C, diffuse damage appears around the cavity and cracks seem to propagate by coalescence of microvoids ahead of their tips. Throughout the sintering cycle, a total of nine cracks appear. Their time dependent lengths are plotted in Figure 4-38 and it is shown that a plateau is reached quickly in the case of most cracks.

In case of oriented cracking (Figure 4-39), the crack growth mechanism of microcrack coalescence becomes quite obvious. The first cracks appear at 1004°C at the both points of the cavity edge that are closest to the stripe edges. In case of the lower crack, a microcrack ahead of the crack tip is instantly formed. After the coalescence of both cracks, the resulting crack propagates further until its arrest at a distance of 3µm to the edge. During the remainder of the sintering cycle, crack opening without further prolongation occurs in the film plane as well as through the thickness, increasing the elliptical skewing of the hole. The film edge at the crack tip develops an inward curvature, thus further reducing the space between edge and crack tip.

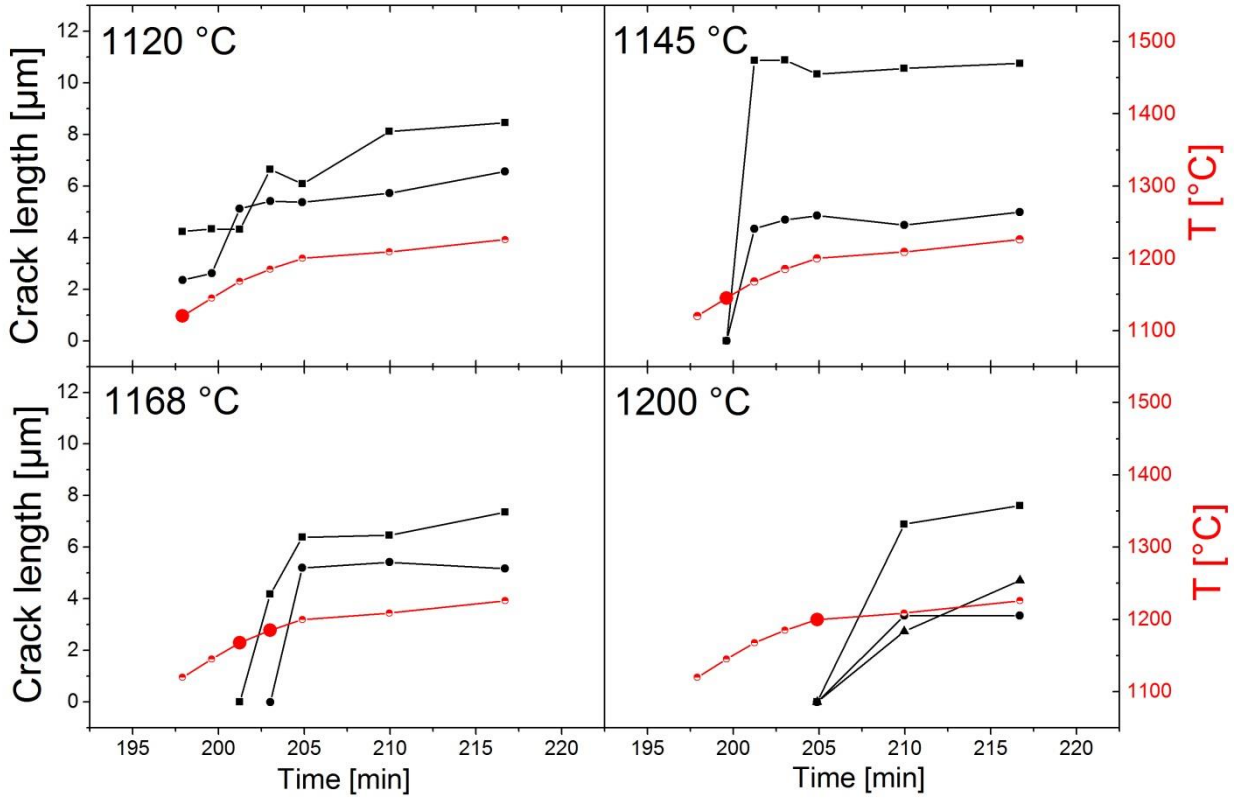

Figure 4-38. Length of cracks initiated at the C250-20 specimen shown in Fig. 4-37 at different stages of the heating schedule as a function of time in the C250-20 cavity with stripe thickness of 27µm on plain sapphire. Each black curve represents one crack in Fig. 4-37. Sintering schedule as shown in Figure 3-11.

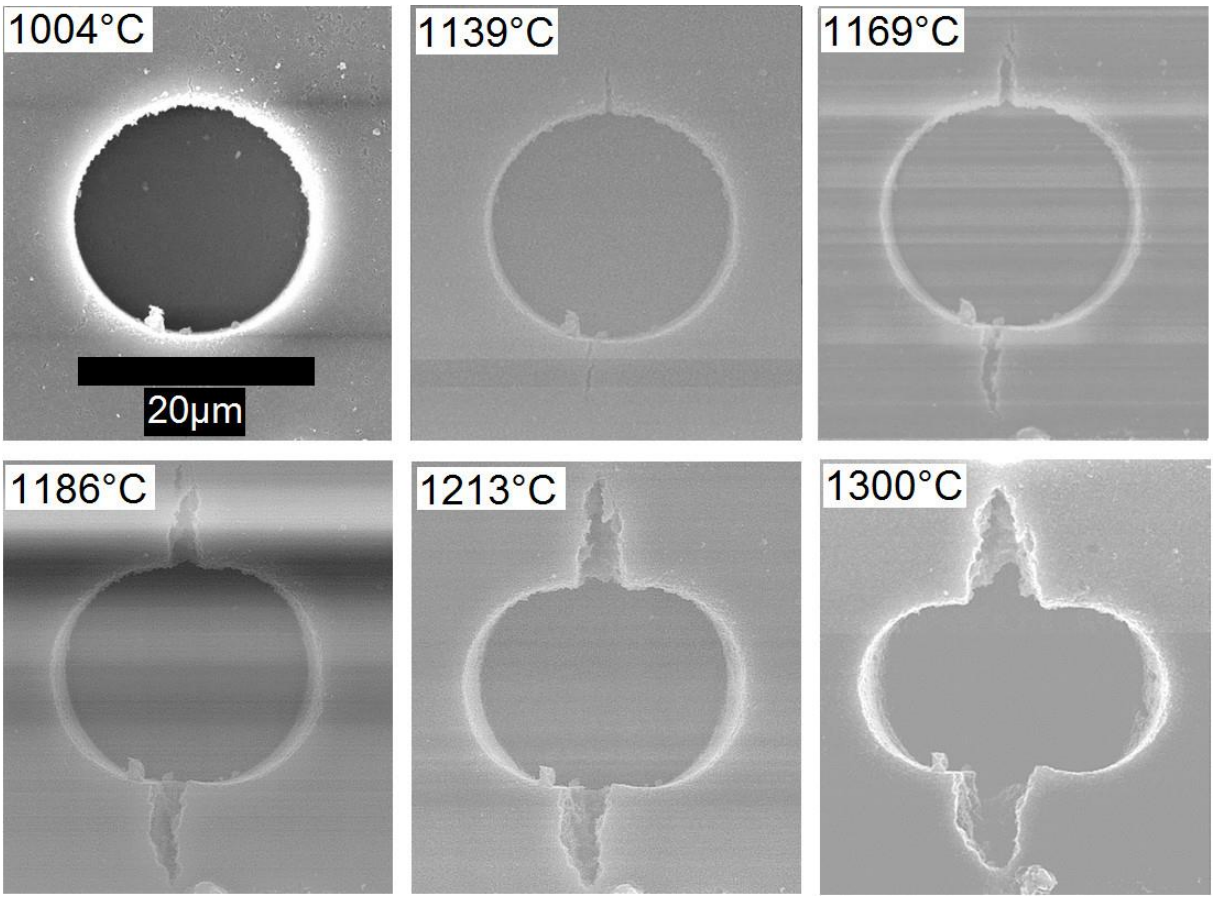

Figure 4-39. Oriented crack propagation at a C50-20 cavity in the 27µm system during sintering.

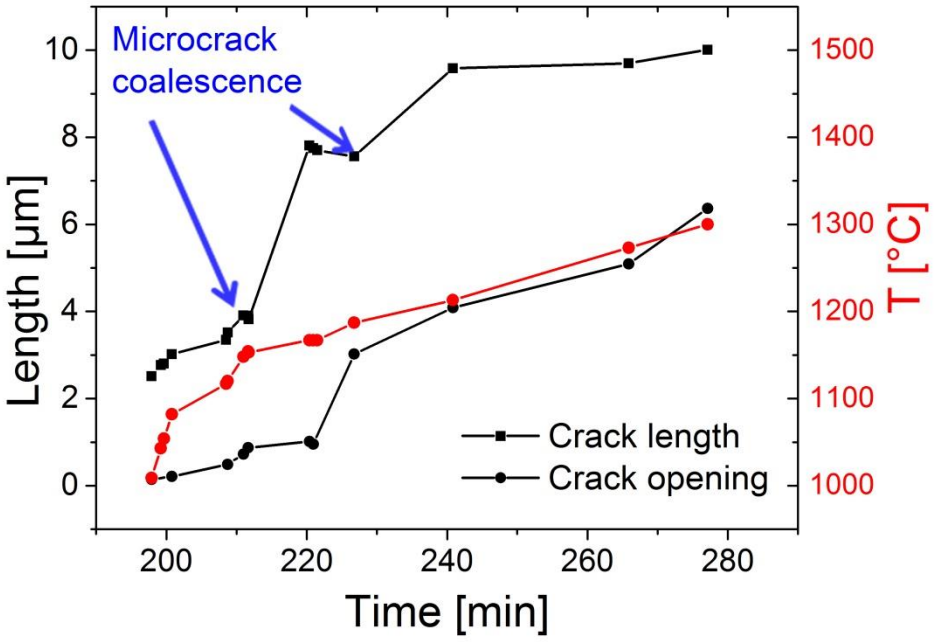

Figure 4-40. Length and opening (measured directly at cavity) of upper crack in the C50-20 system in a 27µm thick stripe on plain sapphire shown in Figure 4-39 subjected to ESEM heating schedule (Figure 3-11) as a function of time.

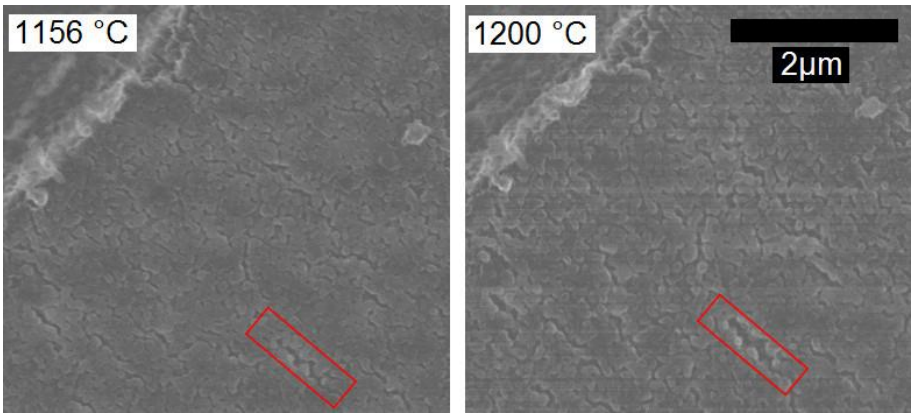

Figure 4-41. Pore orientation and anisometry around a C500-20 cavity in the 16µm system.

In Figure 4-40, the length and opening of the upper crack in the C50-20 system is plotted as a function of sintering time with the blue arrows indicating microcrack coalescence. It is shown that the main crack reaches a local plateau within ten minutes of its formation. After this plateau, a jump in crack length from 4µm to 8µm takes place that coincides with the annexation of two microcracks ahead of the crack tip. The process is repeated twice over until crack arrest. Crack opening is negligible at temperatures below 1100°C which corresponds to the onset of sintering in bulk specimens of the same material. Then a rapid increase takes place after 1100°C have been reached; after this, the crack opening increases linearly with time.

In case of a C500-20 cavity in a thinner film (thickness 16µm), no crack growth is observed during in-situ ESEM. However, pores around the cavity become elliptically elongated and tend to be oriented parallel to the cavity radius. This is shown in Figure 4-41. During sintering, pores grow into microvoids. This pore orientation and growth seems to be the precursor of the microcrack formation observed in the thick stripes shown above.

4.4.2. Cracking around elliptical defects

Elliptical defects have a strong tendency to crack even before any thermal treatment. In the 16µm and 27µm systems, ellipses with a main axis longer or equal 250µm invariably cracked during drying. In the 8µm system, no cracks were found in the as-deposited films; the analysis of the substrate influence on cracking was therefore restricted to this system.

Four different crack configurations were observed (Figure 4-42):

1. Deformation of the stripe edges with no or little cracking
2. Two cracks per endpoint tilted by 30° with respect to the major axis
3. One crack per endpoint oriented parallel to the major axis
4. One crack per endpoint tilted by 30° with respect to the major axis

As in case of the round cavities, crack patterns depend strongly on stripe geometry, cavity size and substrate material. The influence of the individual parameters is discussed in the following section.

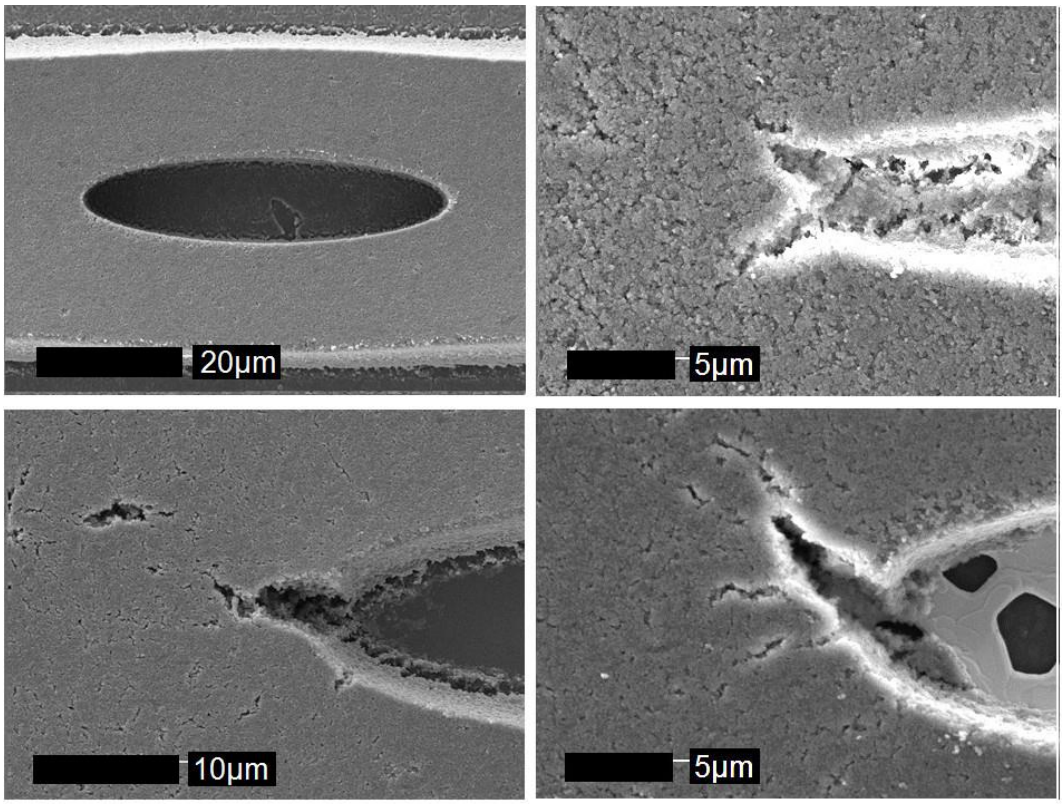

Figure 4-42. Crack patterns observed at elliptical cavities. A: Edge deformation without cracking, B: Double tilted crack formation, C: Single straight crack, D: Single tilted crack.

Influence of stripe geometry

Stripe geometry determines whether or not cracking occurs at the ellipse endpoints. While double crack formation at 30° is due to the two sharp corners near the major axis endpoints, stripe geometry determines whether or not cracking takes place at all.

Edge deformation with no or negligible cracking at the ellipse endpoints is present in high aspect ratio stripes where the distance between the cavity and the stripe edge is small. Here, stress buildup due to the finite stripe dimensions occurs at the endpoints of the minor axis since the latter are closest to the stripe edge. This is the case for elliptical cavities in narrow stripes of 50µm and 100µm width for thicknesses greater or equal 16µm. Since ellipses elliptical cavities in thick wide stripes experienced cracking during drying, study of crack formation was restricted to the 8µm thick stripes.

In an infinite stripe, stresses are expected to be highest at the endpoint of the major axis, since curvature is maximal at this point. This is consistent with the fact that all ellipses in wide stripes (250µm and 500µm) undergo cracking at the major axis endpoints. In the 8µm thick films, ellipses in all stripes undergo such cracking.

Crack length as a function of major axis length and ellipse ratio is plotted in Figure 4-43. It is shown that crack length ranges from 2µm to 8µm for all systems; within the accuracy of the measurement neither an influence of cavity length nor aspect ratio is found.

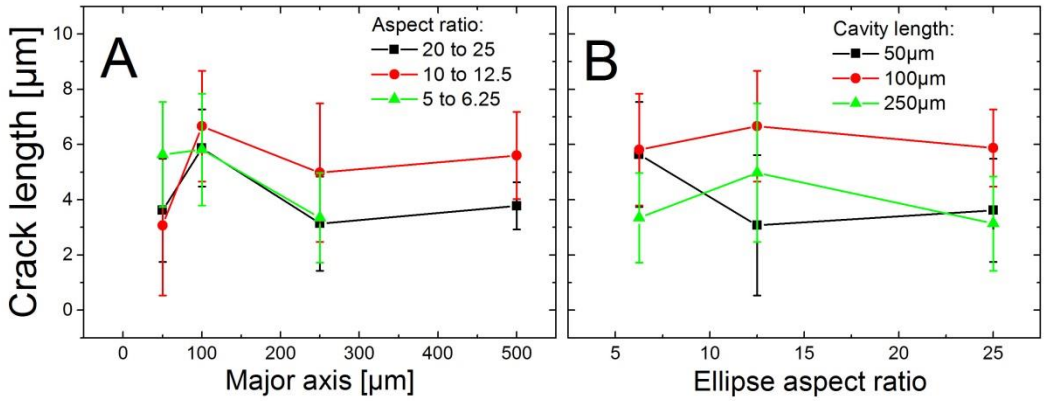

Figure 4-43. Cracking at elliptical cavities in the 8µm system on plain sapphire sintered at 1450°C for 5min. A: Crack length as a function of cavity length for different aspect ratios. B: Crack length as a function of cavity aspect ratio for different major axis lengths.

Crack initiation and growth around elliptical cavities

Cracking around elliptical cavities occurs in a similar fashion as around circular cavities. In the 8µm system, ellipses whose major axis equals 50µm and 100µm with aspect ratios between 0.1 and 0.2 all experience cracking when slowly heated to 1300°C. The first cracks appear at 1119°C as in case of the the randomly cracked cavities and grow by microcrack coalescence to a final length of up to 5µm. In Figure 4-44 (left), the time dependent crack lengths are shown for all ellipses studied in the 8µm system.

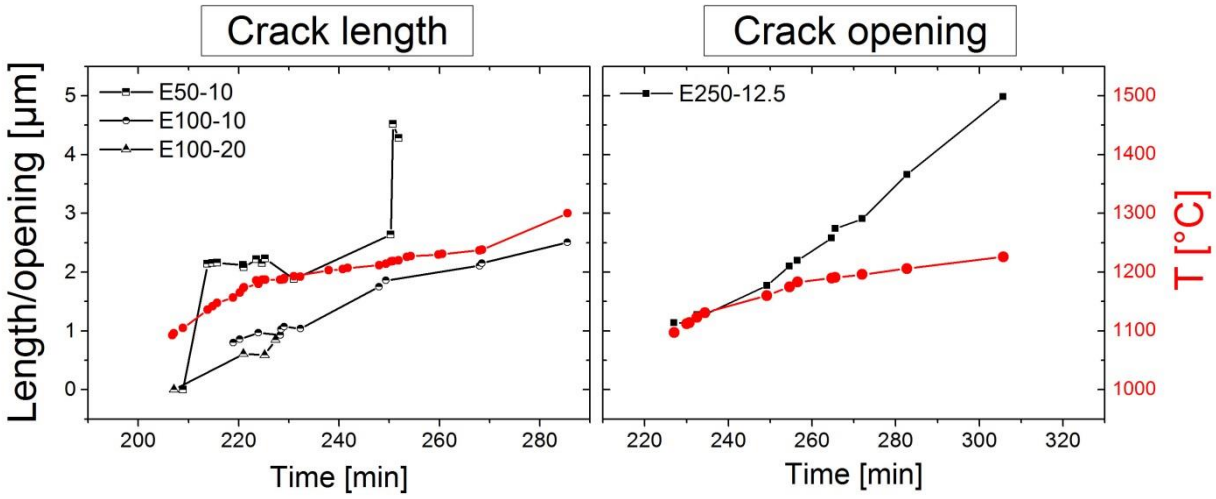

Figure 4-44. Left: Crack length as a function of time for the E100-20, E100-10 and E50-10 ellipses in 8µm thick stripes. Right: Crack opening in the E250-12.5 systems. All systems are on smooth sapphire and have been subjected to the ESEM heating schedule (Figure 3-11).

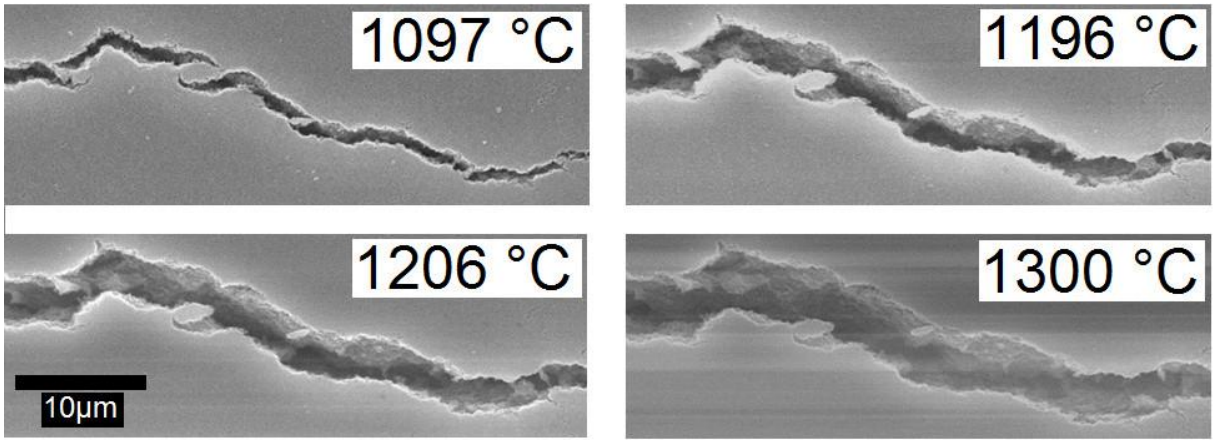

Figure 4-45. In-situ ESEM observation of drying crack in the E250-12.5 ellipse in the 27µm system.

The onset of cracking occurs at roughly the same point during the sintering cycle (1150°C). Crack propagation occurs in a similar fashion for systems E100-10 and E100-20 as both exhibit a linear dependency of crack length on sintering time. The shortest ellipse (system E50-10), however, shows a sharp increase in crack length during the first five minutes followed by a plateau during 40min. At the end of the plateau, a second sharp increase is observed due to the coalescence with a microcrack. Surprisingly, the shortest cavity develops the longest crack, while ellipse aspect ratio was not found to influence the cracking.

When heating an E250-12.5 ellipse of the 27µm system, one observes coalescence and opening of the cracks introduced during drying and preheating. In Figure 4-45, micrographs of a preexisting crack are shown at different stages of the heating schedule. The overall length of the crack hardly changes, whereas crack opening is quite severe as shown in the right hand graph in Figure 4-44. Crack opening is shown to increase linearly time throughout the sintering cycle.

Multiple stress concentrators

Crack initiation in multiple configurations of elongated cavities strongly depends on the stripe thickness. In case of the single cavities, stripes of the 8µm x 100µm system develop longer cracks at the major axis endpoints than their 27µm x 100µm counterparts, consistent with the stress concentration effects perpendicular to the stripe edge in high aspect ratio stripes discussed above. For the double cavities, as shown in Figure 4-46, the effect is reversed; the cracks in the thin 8µm system are almost equal to those of the corresponding single cavity while in the 27µm system, cracks propagate throughout the stripe segment between the two cavities. The cracks at the outer endpoints of both cavities, however, are not longer than those of the single stress concentrator. This indicates that the stress state at neighboring axis end points differs from the stress at the outer endpoints in the 27µm system only, while the distance of the two cavities in the thin 8µm system is sufficient to avoid any interference.

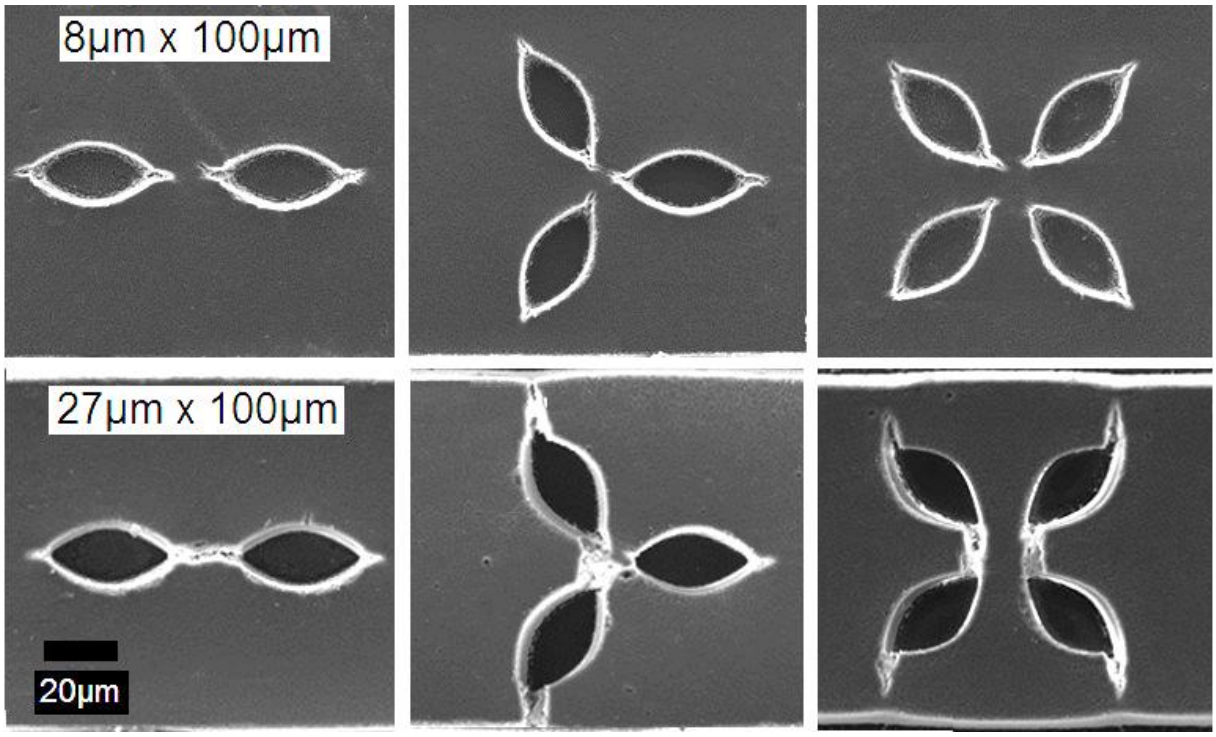

Figure 4-46. Multiple cavity patterns on sapphire substrates after sintering at 1450°C for 5min. Top row: 8µm system, bottom row: 27µm system.

Cracking around triple and quadruple cavities in the 8µm system occurs in the same fashion as in the corresponding single ellipse. Straight cracks originate from the endpoints that act as a prolongation of the main axis. The stress state seems to be the same at all of the endpoints with no interference of the stress fields around the individual ellipses. Crack length in the 27µm system, however, strongly depends on the location of the ellipse endpoint within the pattern. The vicinity of the stripe edge or a second ellipse enhances crack growth leading to propagation of the crack to the next free surface in both cases. Furthermore, the inward edge displacement make ellipses oriented perpendicular to the edge move closer, thus favoring crack propagation between their neighboring major axis endpoints.

4.4.3. Sintering of ring structures

In order to study the sintering of ring structures, knowledge of the interface friction coefficient is required. In Figure 4-47, the regular and normalized friction parameters are presented as a function of film thickness (left) for 100µm wide stripes as well as the square root of film thickness (right) in order to characterize the nature of the interface. Both pure alumina and CAS-alumina stripes exhibit a linear increase of the upper edge displacement, as expected for stiff interfaces. The regular friction coefficient, however, does not decrease linearly up to the maximum thickness, but reaches a plateau at 10µm. In case of platinum coated sapphire, the same phenomena are observed with the distinction that here, the upper edge displacement scales with the inverse of the square root of the film thickness

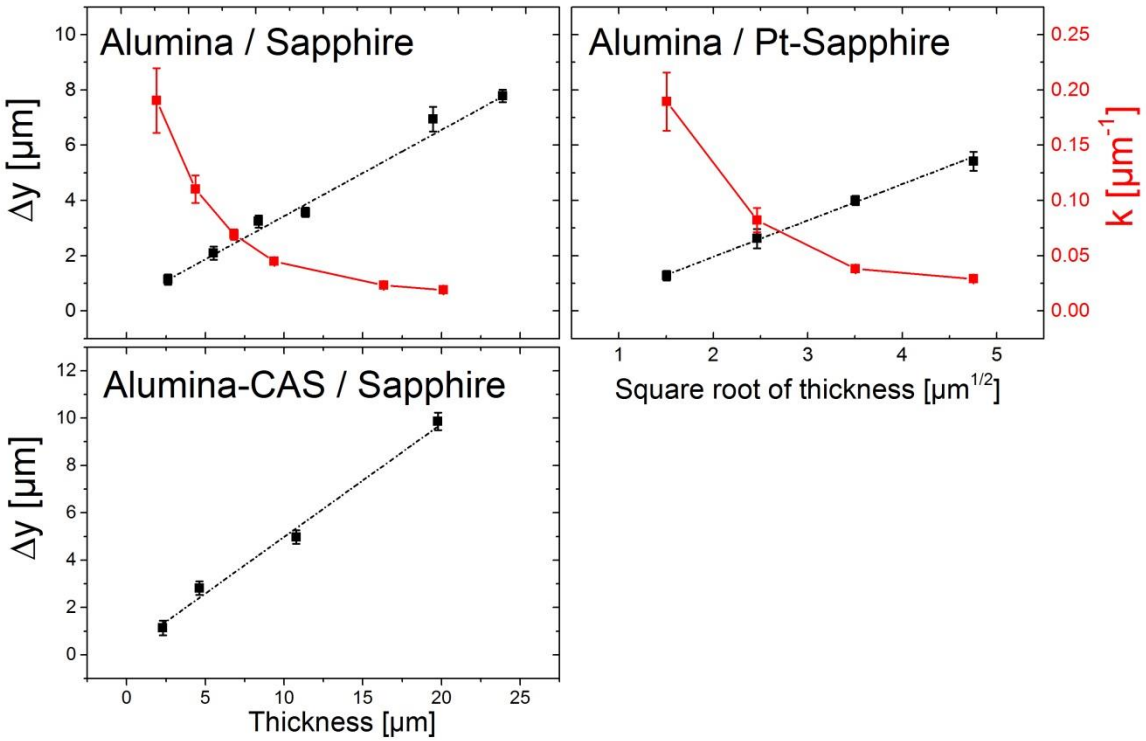

Figure 4-47. Edge displacement (black curves) and friction coefficient (red curves) for 100µm wide stripes of all material systems studied. Left: Stiff interfaces, Right: Compliant interfaces

consistent with the behavior of a compliant interface. Here, too, the regular friction coefficient according to eq. 40 reaches a plateau after a certain thickness. Thus, a threshold thickness-to-width ratio seems to exist that limits the applicability of Jagota's model to real film systems.

In all studied rings, shrinkage of the outer ring radius *b* is observed during sintering. A negative edge displacement is found for all interfaces, its extent being dependent on interface stiffness as observed in case of the stripes. The behavior of the inner ring radius *a* is found to depend on stripe thickness, as thick films experience hole closure, while the outer ring shrinks. The inner hole in thin films, however, grows. A closer look on the interface properties reveals a correlation between hole opening or closure and the product of the friction coefficient times the inner hole radius, as shown in Figure 4-48. For the system with a ring aspect ratio of 0.1 there is qualitative agreement of our observations with Jagota's prediction (Figure 2-15 left) [111].

The trend in the velocity predicted by Jagota resembles the trend of ΔD in our experiments. Firstly, the outer ring shrinks throughout the entire range of ka, but to a lesser degree with increasing friction. Secondly, the displacement of the inner free surface is negative for very compliant interfaces, resulting closure of the hole by the inward pressure of the retreating outer free surfaces. At intermediate values

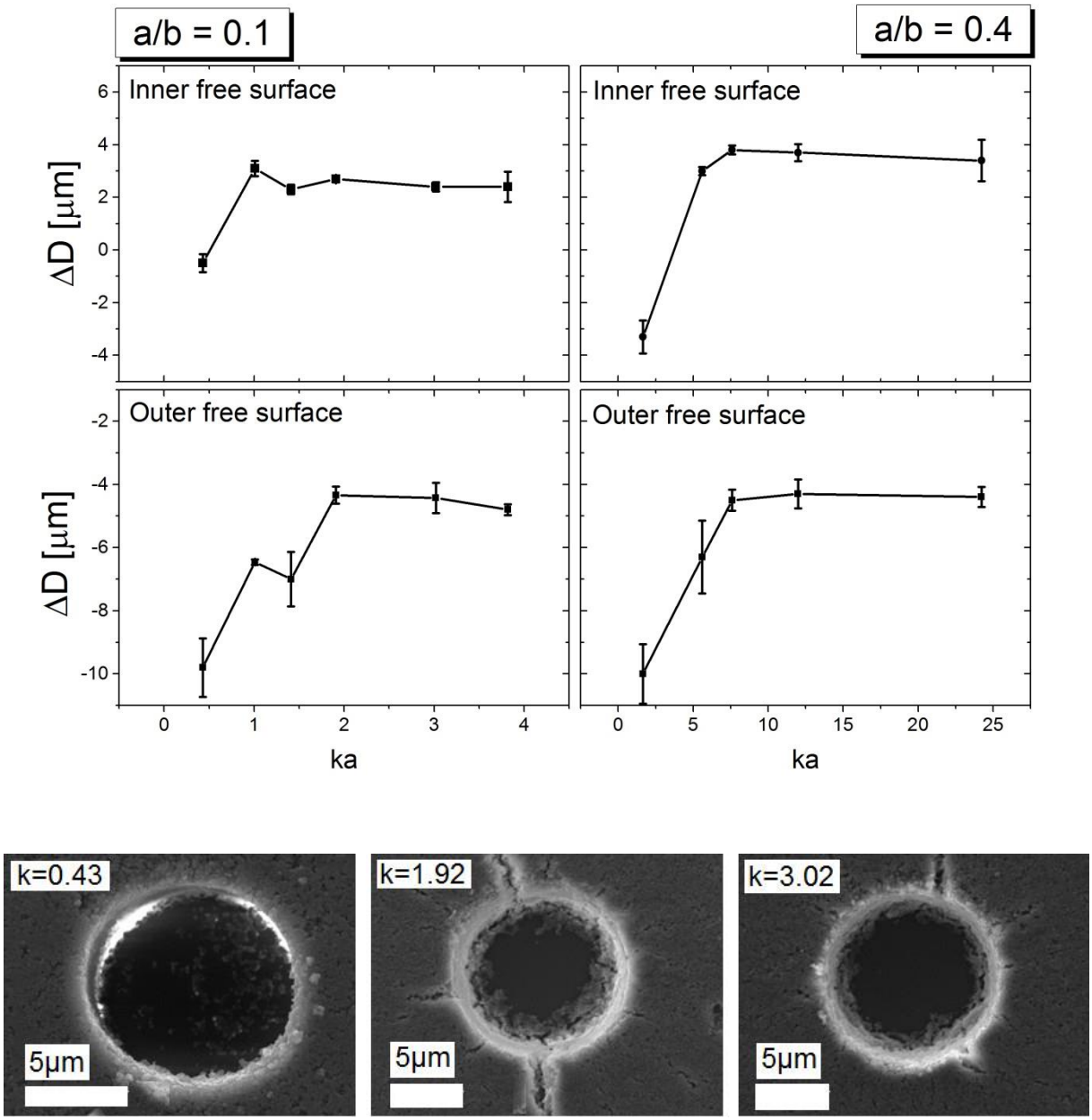

Figure 4-48. Displacement of the inner (top row) and outer free surfaces (middle row) in ring system with radius ratio of 0.1 (left) and 0.4 (right). Bottom row: Micrographs of cracks formed at the inner ring in the 0.1 system on plain sapphire: Left: 27μm, right: 8μm, right: 8μm.

starting at $ka = 1.0$, hole opening occurs and quickly reaches a maximum value before attaining a plateau at $ka = 1.4$.

The same trend is observed for the rings with a radius ratio of 0.4. Here, the transition from negative to positive displacement is even more pronounced. In both systems, the plateau value of the inner edge displacement is between 3μm and 4μm, whereas the displacement of the outer edge reaches 10μm. The outer edge displacement curves are similar for both systems, whereas the inner edge displacement

curve starts from a significantly lower value in case of the 0.4 system. The latter, thinner ring thus experiences stronger closure of the hole.

Furthermore, random radial cracking was observed at the inner hole in some of the ring configurations. Examples of inner holes of the system R50-0.10 for low, intermediate and high ka are given in Figure 4-48. Cracking is not observed in the system that undergoes hole closure at the lowest value of ka. In the intermediate range, however, severe random radial cracking similar to the crack pattern observed in small round cavities in wide stripes is observed. At the highest values of ka, cracking also occurs, but to a lesser degree than in the intermediate range. At the outer ring, cracking does not occur at all. These observations are consistent with Jagota's predictions on the evolution of tangential stresses throughout the ka range. As in case of the round cavities in wide stripes, holes with a high diameter do not undergo cracking. For instance, in the system R100-0.40, cracking is never observed.

5. Discussion

5.1. Constrained drying

The effects of constrained drying inside an elastomer stamp found in this work are summarized as follows: slurry inside thin stamps up to 11µm thickness dries without rupture of the channels from the reservoir and without backflow of slurry into the latter. In thicker stamps, the connections between stripes and reservoir are disrupted and in-plane shrinkage along the stripe length takes place. As a consequence, green densities in the 16µm and 27µm systems are in the range of 67%-70% compared to 57%-59% in case of the thin specimens. This difference is attributed to the additional in-plane strain component in thick films, since the out-of-plane strains are equal at equal stripe thickness-to-width-ratio. This latter effect is attributed to the preferential wetting observed at the channel edges during the MIMIMC process, since curvature is maximal there. Detachment of the slurry from the channel roof occurs in the center while the slurry at the corners is still attached [12]. Thus, trough formation is more severe in wide stripes and makes up a larger percentage of the total stripe thickness in thin stripes. Hence, low thickness-to-width-ratios lead to high vertical drying strains.

The enhanced density in thick stripes is due to the rupture of the stripes from the reservoir that occurs at the point in the pattern where 90° angles are present (see Figure 3-1). This effect is only found in thick stripes since lateral drying shrinkage perpendicular to the stripe edges scales with stripe thickness. For instance, stripes in the 8µm x 100µm system have an as-dried stripe width of 97µm compared to 96µm in the 27µm x 100µm system. Thus, higher stresses are expected at the corners at the conjunction of stripes and reservoir in the thick specimens.

5.2. Solid state sintering of alumina stripes

5.2.1. Shape distortion

Edge inclination and non-uniform stripe thickness have been observed in sintered wide stripes (see Figure 4-3 and Figure 4-4) as predicted by FEM simulations in the literature [81] [82]. Since this deviation from the initial rectangular shape cannot be explained solely by distortion effects due to the MIMIC process, anisotropic lateral and vertical sintering strains are identified as the cause. The height maximum encountered near the edge is in part due to the liftoff of the delaminated edge. However, in the narrow stripes such as 27µm x 50µm, the decrease in height extends beyond the delaminated area. Furthermore, edge inclination stems from the higher lateral strain near the surface due to the reduced in-plane stress at large distances from the substrate. In case of the 27µm stripes, the difference in strain near substrate and surface grow throughout the sintering cycle. The torque created here ultimately results in a delamination crack that grows throughout the isothermal holding time. As a consequence, a shear stress component develops that has been corroborated using FEM simulations provided by Torsten Kraft [124] based on the FEM method described in section 2.3.4. This shear stress is identified as the cause of the shape distortion.

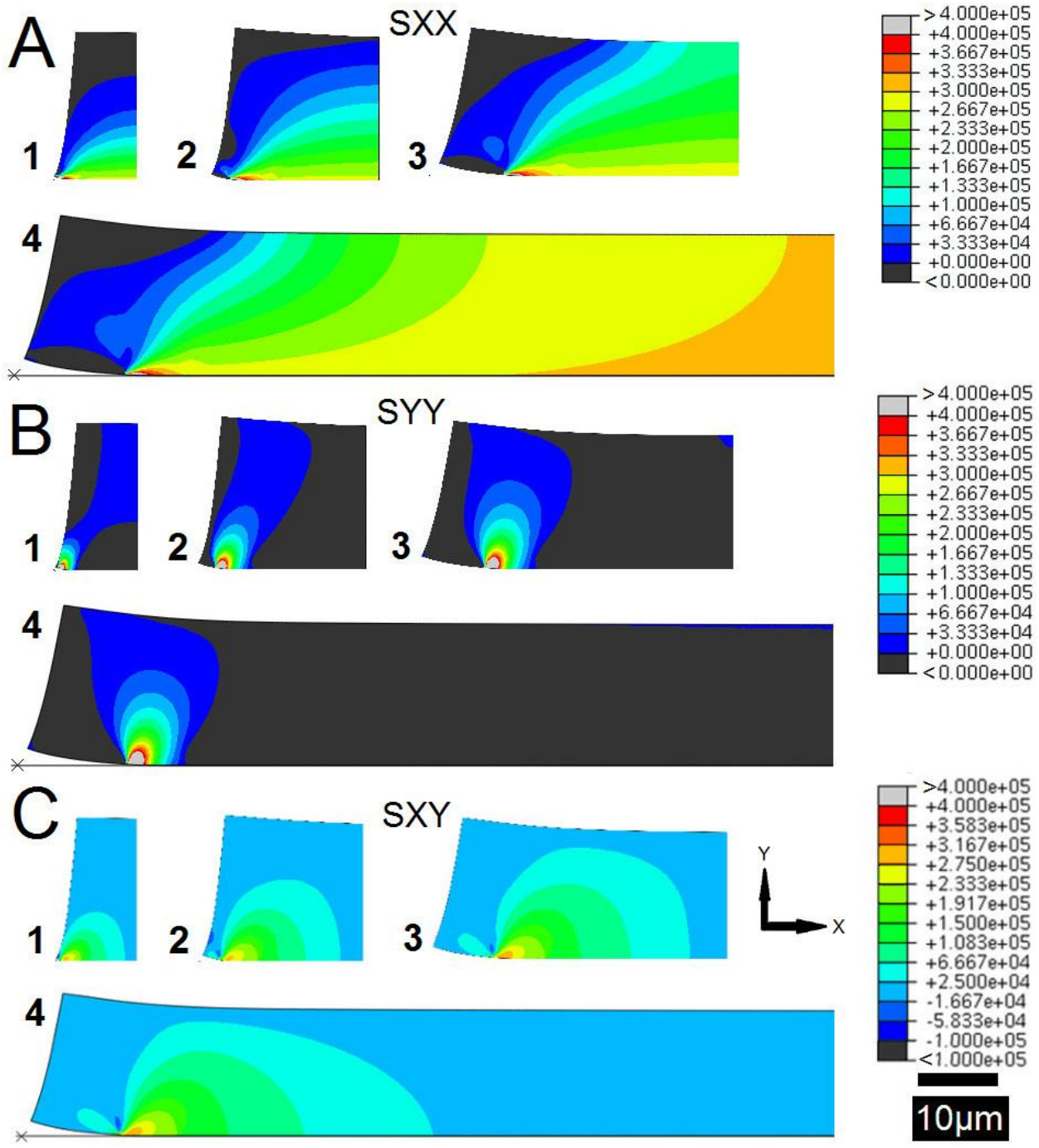

Figure 5-1. FEM simulations of the distribution of stresses (all values in Pa). (A) in-plane stress perpendicular to the edge, (B) out-of-plane stress, and (C) shear stress. 1) 27µm x 25µm, 2) 27µm x 50µm, 3) 27µm x 100µm, 4), 27µm x 500µm. Data and pictures provided by Dr. Torsten Kraft [124].

Simulations fitted to our experimental parameters are carried out based on the method of Svoboda et al. described in [61]. The exact approach for this set of simulations has been published in [84].

In Figure 5-1, the distribution of the stress components is described in detail. Distributions of in-plane (A), out-of-plane (B) and shear stresses (C) are given. The stress is the sum of the sintering stress and the stresses generated by the substrate constraint according to eq. 20. Negative values indicate tensile stresses; this means that the geometric constraint dominates the stress balance in this direction. Positive values correspond to compressive stresses indicating shrinkage in the film that may still be reduced compared to an unconstrained sample.

As shown in Figure 5-1 A, the simulations result in both a vertical and lateral **in-plane stress** gradient with significant differences depending on stripe width. In the narrow 27m x 25µm stripe, a lateral stress gradient is found at all positions. Tensile stresses are maximal near the substrate and decrease with increasing height to reach zero in mid thickness. Directly at the edge, the decrease in stress happens more quickly. Overall, stresses remain rather low compared to the wider stripes. This is consistent with the high overall density and vertical density gradients found in the 27µm x 25µm stripes. In the 27µm x 50µm stripe, the stress distribution in the stripe center is similar to the 27µm x 25µm system. At the edge, however, the beginning delamination results in zero stresses at all free surfaces with both a lateral and vertical gradient. Stress increases from the edge toward the center and from the substrate to the surface, consistent with the skin effect observed in the local density distribution in Figure 4-10. In case of the 27µm x 100µm stripe, the area above the delamination crack is characterized by compressive or zero lateral stresses and lateral and vertical gradients are observed. However, not the entire free surface is characterized by zero or compressive stresses as in case of the 27µm x 50µm stripe. A lateral stress gradient is observed both near the substrate and below the surface, with lower maximum stress below the central surface than at the central substrate. Here, again, a good match with the density gradient in the experiments is found. Finally, the 27µm x500µm stripe edge presents a similar stress distribution as the 27µm x 100µm edge. But since the stripe center is further away from the edge, tensile stress increases to a higher level when approaching the center. This explains the lower central density 27µm x 500µm stripes. Furthermore, no significant vertical stress gradient can be observed in the center; stresses remain high throughout the entire mid-section, thus corroborating the low density in this system.

In Figure 5-1 C, the distribution of the **shear stress** component exerted on the plane parallel to the edge resulting in out-of-plane shear is plotted for different stripe widths. The lift-off of the delaminated corner obviously results in a positive shear stress directed away from the substrate starting from the endpoint of the delamination crack. This region of positive shear stress extends throughout most of the stripe width in narrow stripes; only in the widest stripe a central area with low to near-zero shear is observed.

Hence, the bending of the stripes due to delamination results in a triaxial stress state. A **local out-of-plane stress** develops near the edge that is tensile in nature and that accounts for the reduced vertical shrinkage at this location. In Figure 5-1 B, the resulting distributions of the vertical stress shown for stripes of 27µm thickness with different widths. It is shown that in wide stripes, the areas of out-of-

plane tensile stresses are confined to the edges and are similar in width in all stripes except the narrowest. In the 27µm x 25µm stripe, out-of-plane tensile stresses act throughout the entire width.
In summary, shape distortion is due to the triaxial stress state at the stripe edge which in turn is a direct consequence of delamination. The lift-off of the delaminated edge and its subsequent free shrinkage creates the above mentioned area of shear stress whose extent scales with the length of the delamination crack. Thus, tensile out-of-plane stresses develop near the edges that counteract vertical shrinkage and result in localized thickness maxima. The latter extend throughout the entire stripe in the narrow 27µm x 25µm system since areas of tensile stress near both edges overlap. In wide stripes, the areas of tensile stress are separated by the mid-section that is either unstressed or compression and thus experiences vertical shrinkage, resulting in enhanced surface tapering.

5.2.2. Microstructural anisotropy

Microstructural gradients in the vertical direction in continuous films on rigid substrates are well described in the literature. The finite films in this work showed an additional lateral anisotropy in microstructure. As Figure 4-10 to Figure 4-15 show, density and pore orientation gradients in the vertical and lateral direction are detected in all substrates studied. These gradients are present in all stripe geometries, but the overall density distribution is different for narrow and **wide stripes**. In case of the latter, two delaminated high-density edges are separated by a low density stripe center. This is consistent with predictions obtained from FEM simulations [81] [82]. In a simplistic view, the edge zones are viewed as freely sintering regions while the central part acts as a perfectly constrained film. The edge zones exhibit the following characteristics reminiscent of freely sintered alumina: First, high density (95% to 96% of theoretical) close to the 99% commonly found in unconstrained bulk samples subjected to the same sintering cycle; second, the lack of a vertical density gradient; third, pore orientation predominantly parallel to the substrate (in the direction of slurry flow) as in freely sintered, tape cast alumina laminates [34] that does not change with increasing distance to the substrate.
By contrast, the microstructure in the stripe center exhibits some of the phenomena found in continuous, constrained films: To start with, density increases with increasing distance from the substrate (Figure 4-10 A). Furthermore, pores are oriented perpendicular to the substrate with a vertical gradient in pore orientation factor (Figure 4-13). In the literature, this behavior is ascribed to the loss of in-plane particle contacts due to the tensile stresses imposed by the substrate [78]. However, the nature of this gradient differs from the one found in the continuous films [34]. Pore orientation factor and size decrease with increasing film thickness up to ca. 10µm and then increase again slightly while in continuous films, elongated, oriented pores develop starting from 3µm above the substrate, with increasing orientation factor up to ca. 20µm thickness and a decreasing orientation factor further up. The reason for this deviation may again be found in the distribution of lateral stress in Figure 5-1 A. Since tensile in-plane stresses in finite films are highest near the substrate and

decrease with increasing distance from the substrate, pore elongation is maximal directly at the substrate and deceases further on. For continuous stripes, however, the lateral stresses at a great distance from the edge do not decrease with increasing thickness, as shown in the 27µm x 500µm stripe in Figure 5-1 A. Thus, the modified stress distribution resulting from the proximity of the edge alters the thickness evolution of pore geometry.

Despite the fact that the green microstructure was inaccessible to direct observation due to the difficulty in preparing polished cross sections, these edge zone effects are not believed to be caused by green density gradients. Since vertical drying strains are larger in the stripe center than at the edge consistent with [12] and lateral drying strains perpendicular to the edge were small, a possible green density gradient is likely to result in higher values in the center and thus have a converse tendency than the sintered density.

In **narrow stripes**, no separation into zones is observed. By contrast, characteristics of constrained and free sintering are found at the same time throughout the entire cross section. Despite the fact that a small region of lower density (92%) at the central substrate is enclosed by a high density skin at the free surfaces, density remains rather high throughout the entire stripe. Pore size decreases in the vertical direction while their orientation is predominantly in-plane in mid-thickness. Near the substrate and the free surface, no preferential orientation is observed. Again, good agreement with the lateral stress distribution is found since stresses are low throughout the entire cross section.

Starting from a critical width, no increase in edge zone extension was observed. Thus, the larger the stripe width, the more dominant the central region becomes until the edge effect becomes negligible. When stripe width becomes small enough, the edge zones come closer to each other until superposition is observed. Thus, narrow stripes are viewed as two overlapping free edges with mixed free and constrained characteristics. This again corresponds to the stress distributions in Figure 5-1 since no stress component reaches a plateau throughout the entire stripe thickness.

Vertical microstructural gradients are commonly attributed to the in-plane tangential stresses resulting from friction or drag between sintering particles and the substrate and its limited propagation through the stripe thickness [34] [78]. Thus, in order to explain the additional lateral anisotropy in finite films, a relaxation of the in-plane stresses near the free film edges caused by delamination is postulated, allowing lateral particle movement over a certain length. This local relaxation then leads to a lateral gradient in the in-plane stress dependent on the distance from the substrate. Directly at the substrate, stresses are expected to rise over a shorter distance from the edge than near the surface, thus accounting for the low densification. This again matches the FEM simulations displayed in Figure 5-1.

5.2.3. Geometry dependence of strain components

Vertical strains remain roughly constant with stripe width, but show a strong dependence on thickness. The latter effect is due to the differing starting densities due to the constrained drying, which results in

low densities for thin stripes. Thus, thin stripes experience larger vertical strains when subjected to the same sintering conditions as their thick counterparts. Films of different thicknesses with identical starting densities made of the same powder, however, exhibit similar vertical strains [34]. The lateral strains are dependent on both thickness and width. The geometry dependence of the surface lateral strain of the smooth sapphire system can be expressed in terms of the stripe thickness-to-width ratio, as shown in Figure 5-2. At thickness-to-width-ratios of 0.5 to 1.25, a plateau in lateral strain is found. When moving to smaller aspect ratios, lateral strains drop significantly and approach zero. This can be explained in terms of the width dependent edge zone. Since lateral particle displacement only takes place in the edge zone whose width is constant above a critical stripe width, the lateral particle displacement will make up an ever smaller portion of the stripe width and vanish for quasi-continuous films.

Thick films are found to experience larger strains both near the surface and at the substrate. Here, the reason is believed to be the interface friction and the resulting drag imposed on the particles near the substrate. Since the propagation of the interface friction through the thickness is limited, particles in large distances from the substrate are free to undergo lateral movement to some extent. This height dependent lateral strain is believed to be the cause for the enhanced edge zone density in thick films. In order to validate this assumption, the experimental findings are compared to DEM simulations of lateral particle movement in a 6µm x 100µm from [13] and a 27µm x 100µm stripe that is based on the DEM simulations provided by Tobias Rasp in [122].

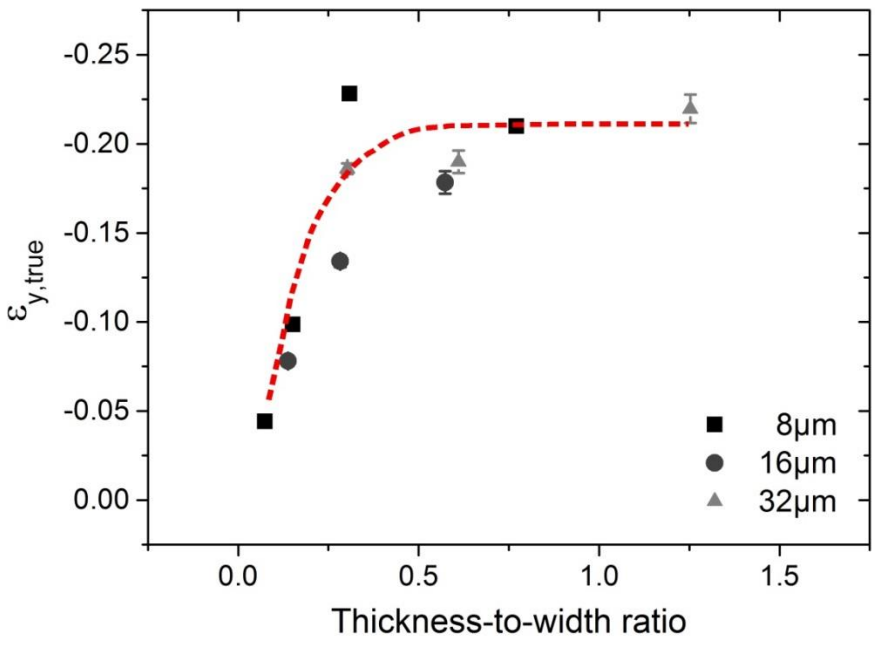

Figure 5-2. Surface lateral strain on films on smooth sapphire sintered at 1450°C for 4h as a function of thickness-to-width-ratio. Dashed line is a guide for the eyes only, not a model.

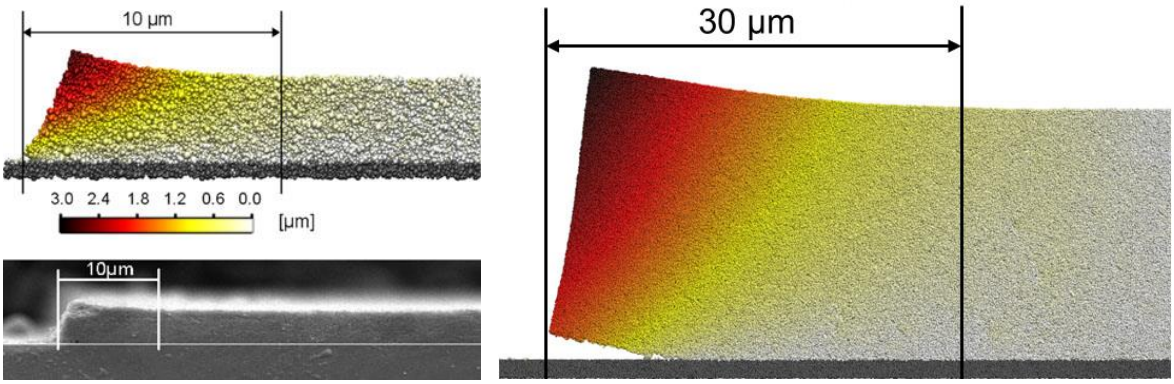

Figure 5-3. DEM simulation of lateral particle displacement during sintering in a 6µm x 100µm stripe [13] (left) and a 27µm x 100µm stripe [122] (right).

The simulation parameters have been fitted to our experiments in terms of particle size, sintering cycle, and stripe geometry. The DEM results of the 6µm x 100µm stripe (Figure 5-3 left) clearly show that lateral particle movement is inhibited directly at the substrate but allowed to some extent above it. The lateral displacement of the particles increases with increasing height. The resulting edge zone with non-zero lateral shrinkage is ca. 10µm in length and therefore in good agreement with the experimental findings in this work (see Figure 4-6 C). In the 27µm x 100µm stripe in Figure 5-3, the delaminated corner experiences lateral particle displacement similar to the free corner since the substrate constraint no longer holds. Above this region, the area of non-zero displacement extends further towards the stripe center to create an edge zone three times the size of the one in the thin stripe consistent with the larger lateral strains near the film surface in thick films. Since there is lateral particle displacement from both edges, it is likely that in a 27µm x 50µm stripe, both edge zones are in contact and the stripe lacks a fully constrained mid-section contrary to the findings in the 6µm x 100µm stripe.

This also explains the dependence of the edge zone length on stripe width shown in Figure 4-5, since at a certain stripe width the interaction of the opposing edges vanishes. When stripe width is increased beyond this threshold, the edges remain constant in size but are separated by a growing mid-section. Also the thickness dependence of delamination length can be attributed to the enlarged lateral strains with increasing distance from the substrate, since a larger difference in surface and substrate-near strains results in larger torque and thus a higher tendency to delaminate.

Apart from its thickness dependence, the lateral strain has also been found to depend strongly on stripe width. This seems to be in contrast to the findings of Martin et al. [78] . According to their DEM simulations on the constrained sintering of micro-pillar geometries, the lateral strain was found to increase with stripe thickness as in our work, but no significant influence of pillar width was found. However, the thickness-to-width ratios of their pillar structures ranged only from 1.11 to 0.37. In this

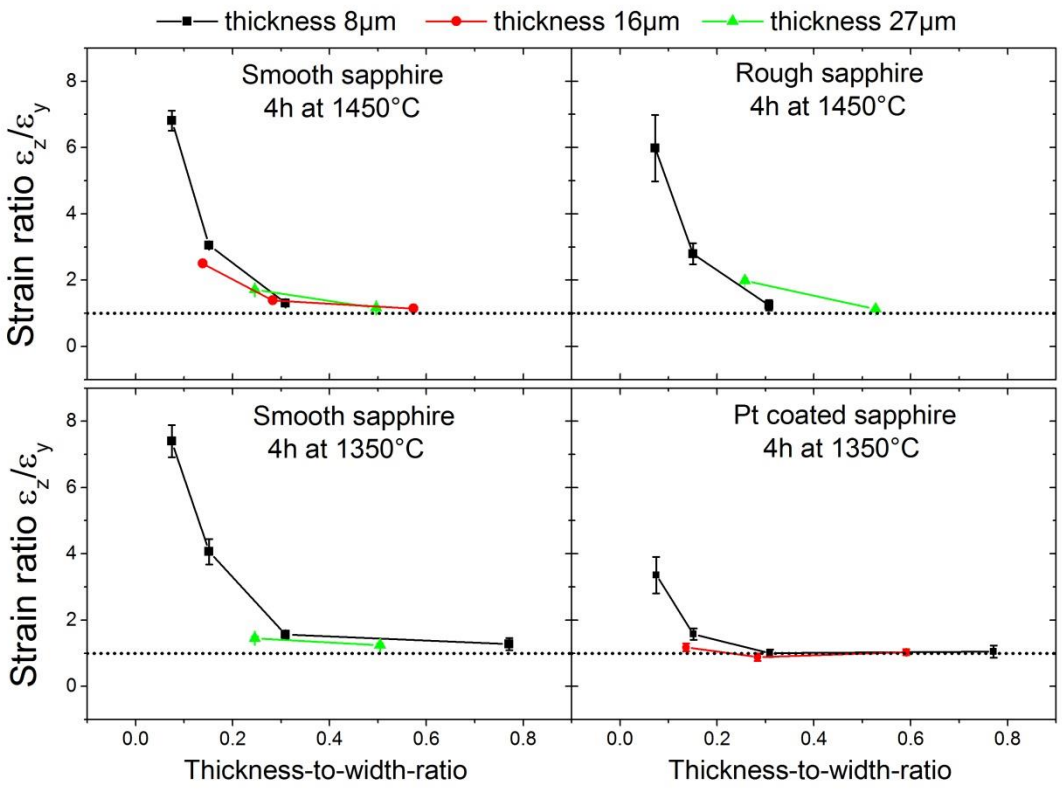

Figure 5-4. Ratio of vertical to surface lateral strain vs. thickness-to-width ratio as a measure of the degree of constraint for all substrates studied. Top row: Smooth sapphire vs. rough sapphire, bottom row: Plain vs. platinum coated sapphire.

range our experiments also yielded similar overall lateral strain values (*e.g.* by comparing the systems 8µm x 10µm and 8µm x 25µm that show similar lateral true strains, or 27µm x 25µm and 27µm x 50µm, in Figure 4-18). The anisotropy of vertical and surface lateral strain components is quantified by the strain ratio shown in Figure 5-4. Again the high aspect ratio stripes exhibit properties reminiscent of free sintering with strain ratios close to unity. Since shrinkage is still constrained in the direction parallel to the stripe edge, the term **partial constraint** is coined to describe the behavior of narrow stripes.

The substrate material influences the degree of constraint. When sintering a platinum coated substrate, the strain ratio reaches unity at aspect ratios of 0.13 (Figure 5-4 bottom right), whereas strain ratios of its plain sapphire counterpart do not flatten out until thickness to width ratios of 0.23 (bottom left). When comparing smooth and rough substrates (Figure 5-4 top row), reduced lateral shrinkage in the rough substrate results in a small increase in strain ratio. The reason for this behavior is believed to be reduced delamination due to crack arrest and will be addressed later.

5.2.4. Substrate variation

Platinum coated sapphire

When using platinum coated substrates instead of plain sapphire, the following changes are observed: The lateral strain increases especially in wide stripes, while the difference between strains at the substrate and at the surface becomes smaller in thin stripes (Figure 4-21). Furthermore, a slight increase in density is observed (Figure 4-16) and delamination length is reduced (Figure 4-9). The vertical strains, however, are unaffected and exhibit the same magnitude as on plain sapphire (Figure 4-20).

Two possible explanations for these phenomena are (I) accommodation of lateral film strain by creep deformation of the platinum interlayer or (II) a reduction in interface friction between the alumina and platinum layers. If creep does occur in the platinum interlayer, the following conditions must be met:

1. At a given stress level and temperature, the magnitude of the creep strain rate must have the same order of magnitude as the free sintering rate.
2. The platinum interlayer must adhere better to the alumina stripe than to the sapphire substrate.
3. The platinum interlayer must rupture or become significantly thinner just outside the stripe edges to allow the platinum layer underneath the stripe to be dragged along during shrinkage.
4. Since creep deformation must conserve the total volume of the platinum, the platinum layer beneath the alumina stripe must become thicker at the expense of the interlayer that is not covered by alumina.

The first condition is evaluated by calculation of the strain rate induced in platinum by the uniaxial sintering stress at a given sintering temperature as provided in [54] [57] and compared to the free strain rate in the same reference. In Figure 5-5, the resulting creep strain rate is contrasted with the free strain rate of TM-DAR alumina. The strain rate ratio ranges from 1.5% to ca. 19% at 1250°C within the density interval of 70% and 80% that has is achieved in stripes sintered at 1250°C for 4h. Thus, according to this estimate, creep deformation plays but a minor role at 1250°C and the reduction of stripe adhesion by the platinum interlayer is deemed to be the dominant factor.

At 1350°C, densities up to 87% have been obtained in thick films on platinum coated substrates (Figure 4-16). At this density, a stress in the magnitude of the uniaxial sintering stress would induce a creep response that is about 45% of the free strain rate of alumina. Thus, at elevated temperatures, the influence of creep deformation in the platinum interlayer on the densification of alumina stripes may become more substantial. However, at low densities as in the beginning of the sintering cycle a far smaller portion of the free sintering strain can be accommodated. This may explain the fact that delamination of thick stripes is merely reduced by a platinum interlayer, not suppressed, since the onset of delamination occurs during the early sintering stages.

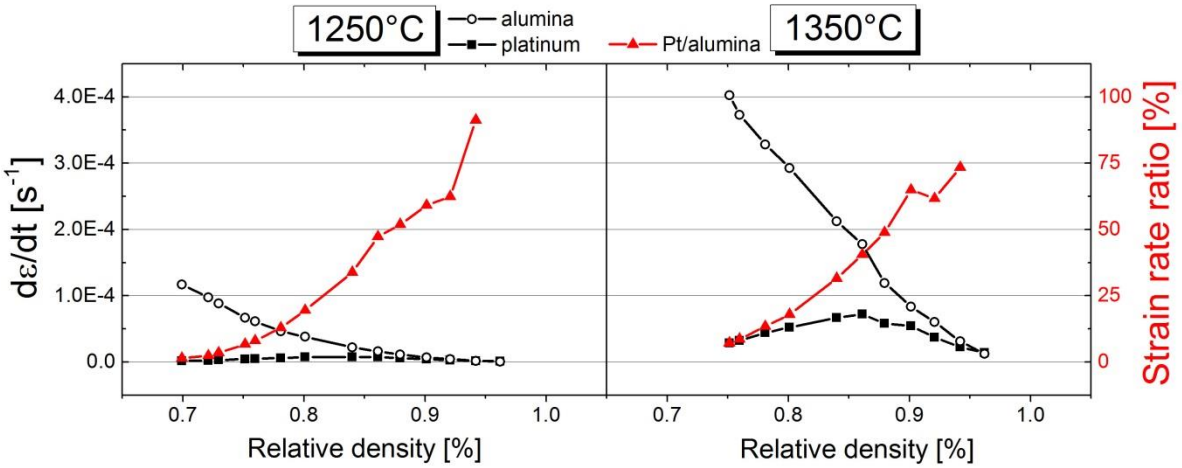

Figure 5-5. Creep strain rate of platinum (black rectangles) and free strain rate of TM-DAR alumina (black circles) as well as strain rate ratio (red circles) at 1250°C (A) and 1350°C (B).

The second condition is expected to be valid in our system since studies of platinum films to alumina substrates of different grain sizes have shown that roughness increases adhesion [103] [104]. Thus, platinum is expected to adhere preferentially to the particulate film.

The third condition is met in wide stripes on continuously sputtered platinum at a sintering temperature of 1350°C. In 8µm, 11µm and 16µm thick stripes, occasional hole formation is observed next to stripes of 50µm width (see Figure 4-22) but not at smaller widths. At 100µm width, most stripes show near-complete rupture of the platinum layer while no damage is observed in 25µm wide stripes. This is consistent with the fact that narrow stripes on platinum do not show enhanced lateral strains compared to their counterparts on plain sapphire, while wide stripes on platinum show up to twice the lateral strain. In discontinuously sputtered films platinum films sintered at 1250°C, occasional hole formation is also observed, but does not seem to occur more frequently next to the stripe edges than further away. Therefore, lateral stress in the alumina films at this temperature seems to be insufficient to induce a significant creep strain rate in the platinum to accommodate the lateral strains in the stripe.

The fourth condition is difficult to validate due to the concurring effects of volatile oxide formation, hillock/hole formation and agglomeration on the morphology of the platinum film. The latter two effects result in an increased thickness of the platinum islands that counteracts the thickness loss by evaporation. Thus, in order to prove that the platinum layer underneath the stripe holds a constant mass, the thickness of the platinum layer at both points must be compared to a platinum layer that is not covered by an alumina stripe and that has been exposed to the same thermal treatment. In the continuously sputter-coated samples, the platinum layer underneath the stripe has increased in thickness compared to the as-deposited or as-annealed platinum layer (Table 4-3). This occurs despite the effect of volatile PtO_2 formation at elevated temperatures that can result in thickness reduction as

high as 0.1µm/h at 1250°C and 0.14µm/h at 1350°C [110] . Thus, the net thickness increase despite volatile oxide formation must be due to strain relaxation phenomena in the platinum layer such as hillock formation and agglomeration. Furthermore, the platinum is ca. twice as thick next to the stripe edges as underneath (Figure 4-22). It is believed that this is due to the alumina stripe which acts as a capping layer. Capping layers have been found to increase the lifetime of platinum films by reducing agglomeration phenomena [107].

Furthermore, the platinum layer next to the stripe is up to twice as thick as an uncoated platinum layer subjected to the same heat treatment. This indicates that the additional strain imposed on the platinum layer next to the stripe by the shrinking edge has been relaxed by local island formation, not by mass flow towards the stripe center. Thus, mass flow of platinum from next to underneath the stripe, cannot be detected.

In summary, at 1350°C creep strain rates of up to 45% of the free sintering rate of alumina can be achieved in theory. However, no evidence of mass flow in the platinum layer from the edges towards the region underneath the stripe center has been detected within the accuracy of the measurement. Therefore, it is assumed that creep in the platinum layer occurs only between the alumina stripes where the lateral stresses of the stripes are relaxed by island formation. Below the stripes, some relaxation of the compatibility strains between platinum and sapphire occurs that results in a smaller increase of increase of stripe thickness. However, no conclusive proof of creep being the only reason for the enhanced lateral strain is found.

Rough substrates

The use of rough substrates instead of polished ones causes three major differences in the sintering behavior of constrained alumina stripes: First, sintered density as shown in Figure 4-11 is by 4% lower in 27µm x 100µm wide stripes and local density minima inside substrate grooves have been observed. Second, delamination length on average is reduced and becomes strongly dependent on the local substrate properties (Figure 4-7). Three types of delamination have observed: Short delamination cracks that are arrested at grooves or hills in the substrate and long cracks at locally smooth parts of the substrate. Finally, the lateral strains are up to 25% lower (Figure 4-18).

The fact that density is minimal inside the substrate grooves seems logical since the contact area between substrate and film is maximal unless in the few cases where internal delamination occurs. In addition, a substrate area with its sinusoidal relief structure can be viewed in terms of a sintering matrix with an array of large rigid inclusions. This simplified view is elucidated in Figure 5-6. The amplitude of the sinusoidal profile is about 3µm and therefore 20 times larger than the alumina particle size, hence the assumption of a continuous matrix around large inclusion underlying the composite sphere model as described in section 2.3.5. is reasonable.

The composite sphere model predicts a compressive hydrostatic stress in the rigid inclusions while the surrounding matrix experiences a tensile radial stress that reduces densification and tangential hoop

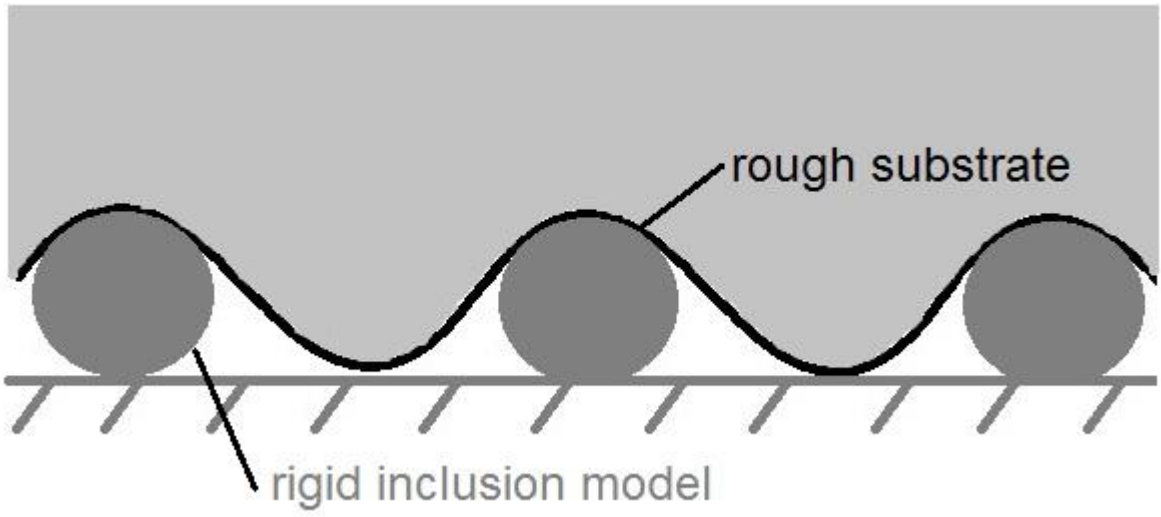

Figure 5-6. Schematic of rough substrate as an array of rigid inclusions on a smooth substrate.

stresses that can lead to cracking, consistent with the observations of reduced density inside the grooves compared to locally flat parts of the substrate as well as occasional detachment of the alumina film from the substrate along a slope.

In order to validate the assumption of enhanced tensile stresses inside the grooves, DEM simulations provided by Tobias Rasp of a TM-DAR film with the dimensions of 27µm x 100µm on a rough substrate are available [122]. The substrate roughness is approximated using a sinusoidal surface with a groove depth of 3.2µm. In Figure 5-7, a contour plot of the local density on rough and smooth substrates is shown. The simulation results match the experimental observation of lower density inside the grooves; however, the effect is limited to the occurrence of a few large pores, shown as blue areas inside the grooves. In addition, internal delamination is observed much more frequently than in experiments. Comparison to the density distribution of the same stripe on a smooth substrate (Figure 5-7 A) reveals a slightly more pronounced skin effect, but no higher overall density in the smooth substrate as observed in the experiments. This is most likely caused by the internal delamination that allows for local free densification. Internal delamination is rarely observed in experiments.

Distributions of the vertical stresses are given in Figure 5-7 B. Stresses are zero near the stripe surface as expected for a shrinking film. Inside the grooves, the vertical stress is clearly tensile as marked by the blue areas, thus accounting for the lower density and the tendency to delaminate inside the grooves. However, the localized stresses inside the grooves are very slight and their propagation throughout the

film thickness is limited. Thus, this reduced density beneath the stripe surface compared to stripes on smooth sapphire (89% on rough vs. 92% on smooth sapphire, Figure 4-10 and 4-11) must have other reasons as well. Here, the reduced delamination length comes into play. In Figure 4-7, the three different crack configurations observed for rough substrates are presented and it has been shown that

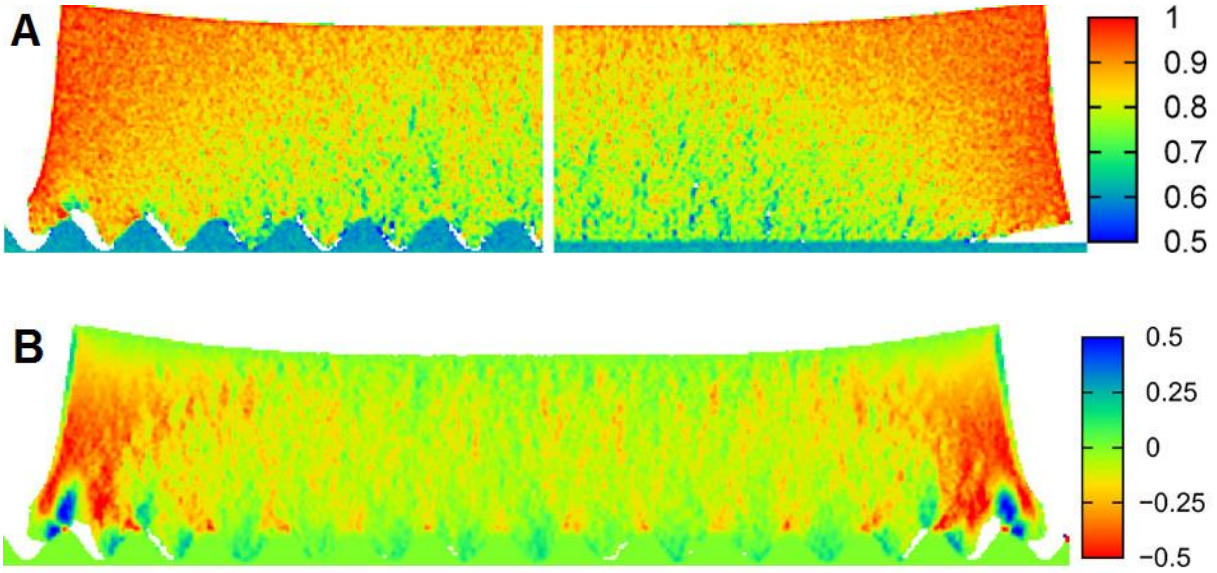

Figure 5-7. Local density and stress distribution in a 27µm x 100µm alumina stripe on a rough sapphire substrates obtained by DEM simulations [122]. A: Density distribution on rough and smooth substrate, Bottom: Out-of-plane stress in MPa [122].

local variations in slope, both from negative to positive and vice versa, result in crack arrest at half the delamination length commonly found in smooth substrates. In order to understand the implications of the reduced crack length on densification and strain, the stress distribution obtained by FEM simulations are again helpful. As shown in the top pictures of Figure 5-1, zero or compressive lateral stresses are observed above the delaminated area. Close to the surface, these regions of compressive stress extend beyond the delaminated length resulting in enhanced density near the surface. It is assumed that if the delamination crack is stopped early in the sintering cycle due to the presence of a hillock, the part of the stripe edge subjected to compressive surface lateral stresses will be smaller since the free surface area is reduced in case of short delamination cracks. Thus, the tensile lateral stress will show a stronger increase from the delamination crack endpoint towards the center, resulting in a lower central density. The lateral strains are then reduced for the same reason.

5.3. Strain and densification curves

Figure 4-23 and Figure 4-24 revealed the following facts about constrained densification on **plain sapphire** substrates: Narrow stripes achieve higher densities than wide ones throughout the sintering cycle. Here, vertical strains are only enhanced for wide stripes whereas they are equal to surface lateral strains right from the start in narrow systems. The difference between surface lateral and interface lateral strains increases throughout the sintering cycle.

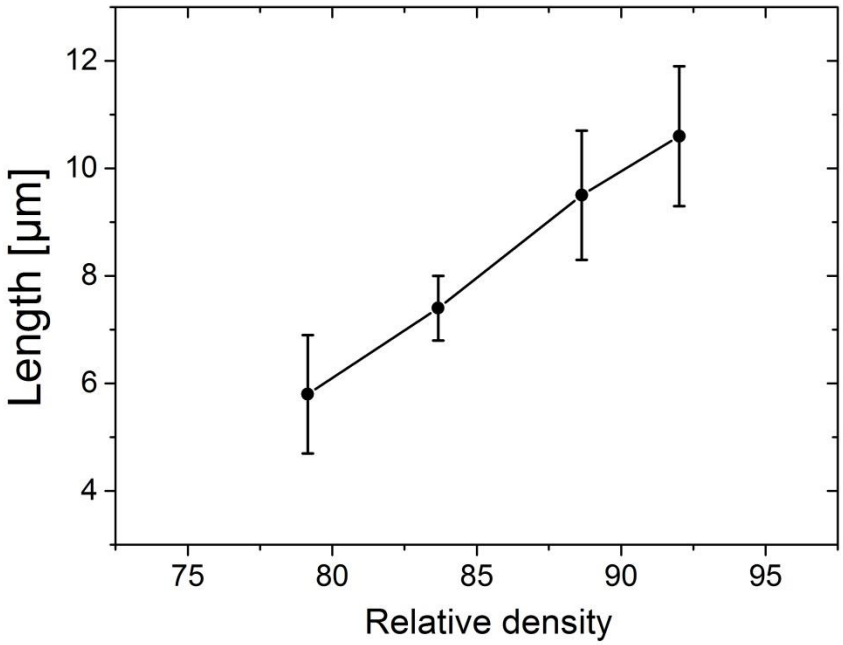

Figure 5-8. Evolution of the delamination crack in a 27µm x 100µm stripe on smooth sapphire throughout the sintering cycle.

The difference in density between smooth and rough substrates increases during the sintering cycle; this increase is driven by the lateral strain that grows throughout the sintering cycle in smooth sapphire whereas it reaches a plateau on rough sapphire. Furthermore, the threshold width for enhanced vertical strain is lower than on smooth sapphire.

The geometry dependence on the strain development during sintering is consistent with the assumption that lateral strain is not inhibited in the edge areas, as validated by the DEM simulations presented before in Figure 5-3. Thus the densification curves of narrow stripes share the above mentioned characteristics with free sintering curves. The fact that **rough substrates** induce reduced lateral strains in such narrow stripes is a consequence of the reduced delamination length. As stated above, shorter delamination cracks lead to smaller areas of compressive lateral stress and thus stronger tension in the stripe center. The degree of constraint imposed by rough substrates is therefore higher. The faster saturation of the lateral strains in stripes on rough substrates is also explained by the development of the delamination crack throughout the sintering cycle. In Figure 5-8, delamination length in the 27µm x 100µm system on smooth sapphire is plotted as a function of density. At low densities at the beginning of the isothermal holding time, crack length already exceeds the 5µm found in rough substrates at the end of the sintering cycle. Thus, if we assume that crack propagation in rough substrates occurs in the same fashion as in smooth substrates before the first obstacle is

encountered, this means that cracks form and grow during the heating ramp and are stopped at densities below around 75% in rough substrates but keep propagating until the final density is achieved. This matches the development of the interface lateral strain on rough substrates since it reaches a plateau at 80%, shortly after the crack arrest has occurred. Thus, the influence of substrate roughness on strain and densification is likely to be a consequence of delamination crack arrest early in the sintering cycle. This effect is considered to be more important than the influence of porous pockets inside substrate grooves on overall densification since the substrate under most stripes has only a few 3µm deep pockets (typically 1-3 pockets per 100µm stripe).

When a **platinum interlayer** is applied, strain and densification curves (Figure 4-27) change and become more similar to free sintering curves. For instance, an 8µm x 25µm stripe on platinum does not show enhancement of the vertical strain compared to the free sintering strain whereas both strain components differ by a factor of 1.5 on smooth sapphire. The reason for this behavior is the enhanced lateral shrinkage due to a combination of reduced interface friction and the possibility of creep strain relaxation via creep in the platinum layer. Thus, the degree of constraint is reduced when a metallic interlayer is applied.

5.4. Liquid phase sintering

Liquid phase sintered stripes share many characteristics of pure alumina stripes, such as constrained drying, anisotropic and geometry dependent strain components, delamination as well as a varying degree of constraint for different stripe aspect ratios. Some of the effects of constrained sintering appear to be alleviated by a liquid phase. For example, higher surface lateral strains are achieved and quasi-free sintering with equal surface lateral and vertical strains occurs in wider stripes when a liquid phase sintering aid is added, as shown in Figure 4-29. This is consistent with the assumption that a liquid phase reduces both the interparticle friction and the drag imposed on the particles by the substrate. Thus, despite the fact that lateral strains at the interface are around -0.1 in both pure and doped alumina, the surface lateral strains are smaller in the pure system (-0.18 vs. -0.3 for 27µm x 100µm on smooth sapphire). Hence, the influence of the substrate constraint propagates through the film thickness to a lesser extent in the liquid phase sintering material due to the greater ability of the particles to rearrange. The fact that the interface lateral strains are not smaller in the pure system is thought to be due to the influence of delamination. Here, a comparison is difficult due to the different starting densities of pure and doped alumina stripes; however, delamination values of both materials are contrasted at the end of the sintering cycles after the substrate lateral strain has reached a plateau based on the assumption that at this point crack arrest has occurred. In the solid state sintering system, the delamination crack length at the end of the sintering cycle reaches 10µm in the 27µm x 100µm system, but only 5µm in liquid phase sintering stripes of the same geometry. Thus, the two components that add up to the total lateral strain near the interface – sliding of the stripe edge along

the interface before and free densification of the edge after delamination – take different values for pure and doped alumina, free densification being dominant in pure and sliding in glass-added alumina.

5.5. Cracking around cavities

Around **circular cavities**, cracking and elliptical skewing was observed. A critical cavity diameter was observed above which no cracking occurred. Thicker stripes show an enhanced tendency to crack and deform. Furthermore, finite stripe dimensions resulted in oriented cracking. Crack growth occurred via formation of by microcrack formation ahead of the crack tip at temperatures below the onset of sintering and coalescence with the main crack.

Elliptical cavities whose main axis is oriented parallel to the stripe edges were affected by the proximity of the edge in a similar fashion than the round cavities. Ellipses located at large distances from the stripe edges cracked at the major axis endpoints since curvature is maximal there. The precrack faces moved apart during sintering, increasing the aspect ratio. Near the edge, cracking was inhibited and the precrack faces were pushed inward by the receding stripe edges. Crack growth also occurred by microcrack coalescence.

In **multiple elongated cavities**, cracking occurred at the cavity endpoints in thin films no matter what the configuration; in thick films, cracks grew preferentially towards the edge or towards the other cavities in the immediate vicinity.

The proximity of the edge to an intentionally introduced **circular cavtiy** results in oriented cracking perpendicular to the edge (see Figure 4-32), thus leading to the assumption that localized tensile stresses appear at the points of the void that are closest to the edge. This is reminiscent of the stress concentration in cracked plates of finite lateral dimensions described in linear elastic fracture mechanics (Figure 2-14). Both during constrained drying and sintering tensile in-plane stresses are imposed by the substrate. Since stripe dimensions are finite only in the direction perpendicular to the edge, localized stress buildup occurs. In thick films, a significant stress development already takes place during drying since cracking in 27µm thick films is observed just above 1000°C which is below the onset of free sintering of TM-DAR alumina. This assumption is supported by the fact that localized cracking is already observed around some C50-20 cavities after drying in uncontrolled atmosphere. During drying, tensile in-plane stresses occur parallel to the edge while stresses are relaxed by slip perpendicular to it. Since as-dried films are already under stress, a small additional stress buildup, *e. g.* due to a thermal expansion mismatch between substrate and film, may be sufficient to induce cracking at the cavity. Furthermore, the phenomenon of oriented cracking resembles the results of Martin et al. [89] who found that in a prenotched sample constrained by two opposing rigid plates defect opening occurs in the constrained direction while cracking took place perpendicular to the free edge whenever particle rearrangement was inhibited. Since their constraining conditions mimic those of narrow ceramic stripes where the free edge may recede, but the material is

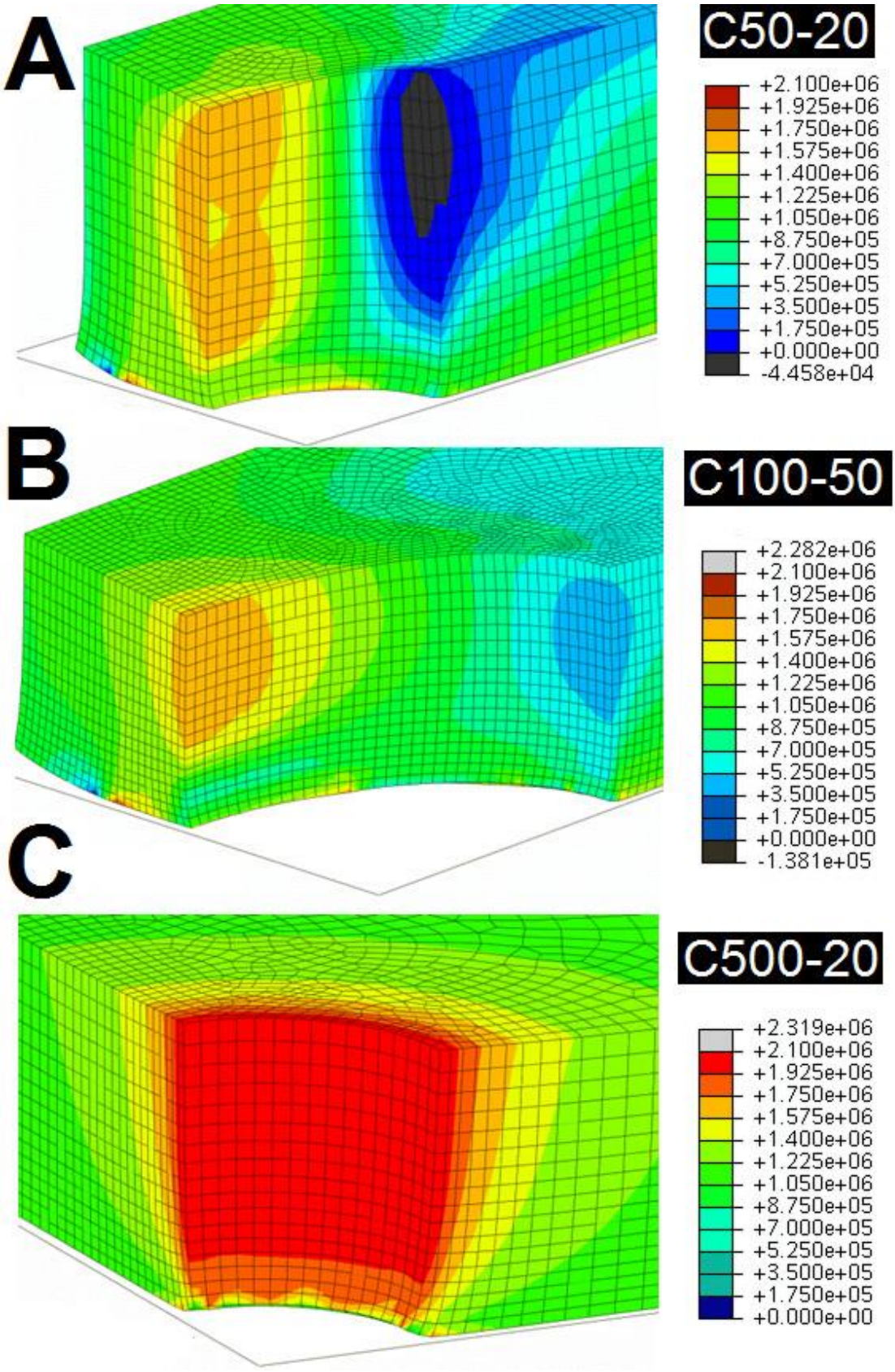

Figure 5-9. FEM simulation of maximum principal stress in Pa during densification of stripes with round cavities. A: C50-20, B: C100-50, C: C500-20. Picture and data courtesy of Torsten Kraft [124].

held in place perpendicular to the edge. Since particle rearrangement is also limited due to the substrate constraint, their findings are consistent with skewing and cracking found in this work. Their explanation for the notch opening is as follows: Densification in the constrained direction occurred above and below the notch since constraint is released at the free edges. Since the free edges move closer to the predefect during lateral shrinkage, its radius in the unconstrained direction is reduced. The combination of both effects results in the elliptical skewing and ultimately in breakup of contacts perpendicular to the edge.

However, this does not account for the enhanced tendency for localized cracking in thick films compared to thin ones since particle rearrangement is expected to be less inhibited far away from the substrate. Here, rearrangement is thought to be reduced due to the larger green density of the 27µm thick specimens that results in a higher coordination number of the ceramic particles.

Random cracking around cavities in quasi-continuous films occurs in agreement with the findings on cracking around metal vias in ceramic dielectrics [7]. Since the edge is located at a great distance from the defect (a/W = 0.04), the finite width correction factor for the stress concentration factor according to eq. 37 is unity and no stress concentration perpendicular to the edge occurs. The absolute values of the tensile stresses seem to be higher in the case of random cracking since in the 11µm thick system C500-20 cavities experience random cracking while C50-20 cavities do not crack at all.

In Figure 5-9, FEM simulations of maximum principal stresses around three different round cavities in the 27µm thick system provided by Dr. Torsten Kraft [124] are shown. The data confirm the assumption of stress localization being responsible for the oriented cracking. Consistent with our findings, high tensile stresses develop at the part of the cavity that is closest to the edge in C50-20 and C100-50. In C50-20, these high tensile stresses extend throughout the stripe thickness, consistent with the through-thickness cracks observed in experiments. In C100-50, the stress maximum is confined to the upper half of the stripe consistent with the short superficial cracks found in real specimens of this geometry.

In comparison, tensile stresses are high at all points of the C500-20 cavity that has been shown to undergo random radial cracking in our experiments. The absolute values of the tensile stresses in the randomly cracking system exceed those in the oriented systems. In addition, elliptical skewing is reproduced in the simulations for the C50-20 and C100-50 systems.

The width and thickness dependence of skewing and cracking observed in all substrate systems (Figure 4-33, Figure 4-35 and Figure 4-36) can be reduced to the influence of strain as the controlling parameter. It has been shown before that lateral strain is controlled by the thickness-to-width ratio of the stripes (see Figure 5-2). When plotting aspect ratio and normalized crack length as a function of surface lateral strain for systems with oriented cracking as shown in Figure 5-10, it is found that aspect ratio decreases and crack length increases with lateral shrinkage. This also accounts for the influence of the different substrates, since increased roughness or the application of a platinum interlayer modifies the lateral shrinkage.

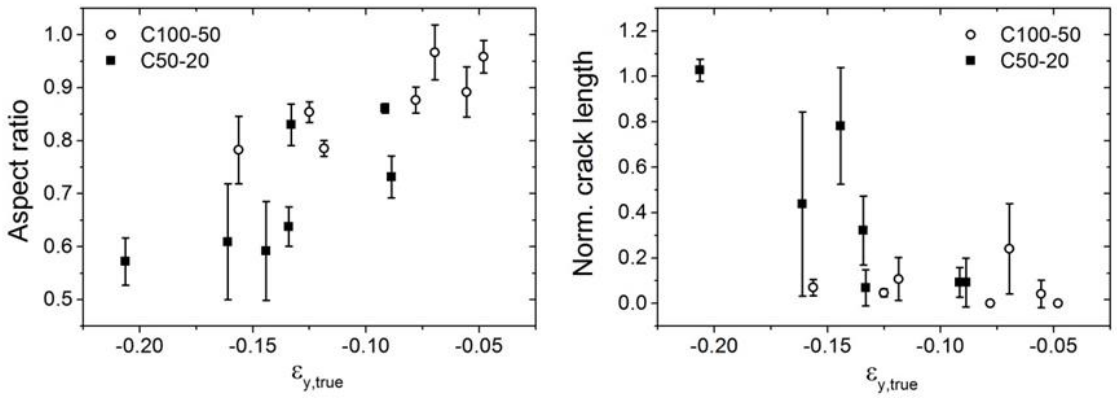

Figure 5-10. Aspect ratio of initially round cavity (left) and crack length normalized by the initial cavity diameter (right) as a function of surface lateral strain for the systems C100-50 and C50-20 for all substrates.

The influence of lateral strain on the elliptical deformation of the C50-20 cavity in the 27µm thick stripe can be visualized as follows: At 1000°C, the first surface cracks appear at the cavity perpendicular to the edge. With the onset of lateral shrinkage at 1100°C, the two opposing points of the cavity that are closest to the edges begin to move closer to each other, pushed inward by the receding free edges. In contrast, the two opposing points of the cavity radius located farthest from the stripe edge are dragged apart since lateral shrinkage also occurs at the new free surface created by the oriented cracks. This means that lateral shrinkage now occurs parallel and perpendicular to the stripe edge, thus reducing the former radius of the cavity and expanding the latter. The final aspect ratio is lowest in the C50-20 cavity of 27µm thickness, since it is located entirely in the edge zone of the stripe where lateral shrinkage takes place.

Skewing is less pronounced in the C100-50 system in Figure 5-9 B despite the similar distance to the edge since here the lateral stress is relaxed by deformation of the stripe edge. Here, the area between the defect and the edge can be viewed as a 25µm wide stripe that has a lower edge displacement than a 100µm wide stripe.

Crack growth occurs in creeping mode in cavities with oriented cracks. Bordia and Jagota [113] have ascribed crack growth ahead of elliptical flaws in alumina films to the angular shape of the particles that results in a variety of contact areas. Thus, the contact right ahead of the tip is not necessarily the strongest one and fracture occurs where the local stress intensity factor is maximal. In addition, variations in the dihedral angle determine local instability. In finite films with cavities near the edge, another factor contributes to the time-dependent cracking: The opening of oriented cracks is enhanced by the opening of the hole during sintering since the newly formed free surfaces are bound to undergo

displacement. Consequently, the stress intensity factor is enhanced and crack growth takes place. In random cracking systems such as C500-20, by contrast, the absence of elliptical skewing means that virtually no growth of the instantaneously formed crack openings occurs.

Stress distributions around **elliptical cavities** are not available; however, it is assumed that a similar stress buildup takes place. Far away from the edge, stresses are maximal at the ellipse endpoints which are located at maximum distance to the edge. Thus, the proximity of the edge reduces the stresses at the major axis endpoints but does not result in high enough tensile stresses to induce cracking at the minor axis endpoints. The increased opening of drying cracks located at the ellipse endpoints in thick films in Figure 4-45 is consistent with the findings of Wang et al. [6] who reported crack opening during constrained sintering without prolongation in preexisting cracks that exceeded a certain length. Here, again, the newly formed free edges recede due to their capability to undergo lateral shrinkage.

5.6. Interface friction coefficient

100µm wide alumina stripes on sapphire substrates were found to present a stiff interface since the friction parameter scales inversely with film thickness. This is consistent with the results previously obtained by Bordia et al. [113] on continuous alumina films on sapphire. The absolute values of the inverse edge displacement they measured on continuous films, however, is lower than in case of the patterned films in this work (see Table 2-2) by a factor of 2.7. This deviation is ascribed to the difference in alumina particle size and sintering schedule applied in both works that lead to differences in the densification behavior. The inverse edge displacement is therefore not suited to compare different material systems.

In case of a compliant interface as in alumina films on platinum substrates, a linear increase of the edge displacement with the inverse of the square of the film thickness has been found both in patterned films in this work and in continuous films by Bordia et al., thus validating the predictions made by Jagota's model [111]. The friction coefficient calculated according to eq. 40, however, decreases with increasing film thickness only up to thicknesses of ca. 10µm above which a plateau is found (Figure 4-47 left). In the plateau region, the influence of the increasing edge displacement in the denominator is counteracted by the increasing viscous Poisson's coefficient. The reason for this deviation is the stronger densification of thick stripes aided by delamination, since this effect is not included in the model. As delamination leads to higher total densities, the numerator in eq. 40 is no longer constant since the viscous Poisson's ratio increases with increasing sintered density. As stated above, delamination length is dependent on stripe thickness; thus, there is a thickness limit up to which the friction coefficient can be correctly calculated. In case of the 100µm wide stripes in pure alumina stripes on smooth substrates in Figure 4-47 (left); the limit is found at a sintered thickness of ca. 11µm corresponding to the 16µm x 100µm system. This system shows a delamination length of 2-3µm, with

a negligible influence on the overall stripe cross section, while in the 27µm x 100µm system, the delamination cracks make up more than 20% of the stripe width.

In the continuous films of Bordia et al., investigation of the densities of the stripes has not been carried out. However, the declining portion of the stripe cross section dominated by edge effects with increasing stripe width found in this work leads to the assumption that the normalized friction coefficient is a suitable approximation for continuous films since their overall stripe density should not be affected by edge effects.

Sintering of ring structures

The behavior of ring structures during sintering was found to be consistent with the prediction made by Jagota et al. [111]. Several aspects were confirmed: Firstly, a transition from hole closure in low friction systems to hole opening in high friction systems was observed both in narrow rings of the 0.4 system and wide rings of the 0.1 system. The shape of the displacement curves obtained in this work is in very good agreement with the normalized velocity predicted in the model. However, the absolute friction value of the curve maximum is twice as high in the experiment (ka =1.0 vs. 0.5). This deviation may be due to the fact that the model predictions were made for viscous sintering films.

Hole closure was stronger in the narrow ring. This is supposed to be caused by the interference of the lateral stress fields that originate from both edges similar to the effects observed in narrow stripes. A section through an R100-40 ring of 27µm thickness is comparable to a 30µm wide stripe whose cross section is entirely made up of two overlapping edge zones. Thus, narrow ring systems show quasi-free sintering behavior with non-zero lateral strains throughout their entire cross section (for comparison, see right hand picture in Figure 5-3). This is consistent with the distribution of radial stresses over the ring cross section shown in Figure 2-16. Stresses at the outer and inner free surface are zero and rise quickly in high friction systems ($ka \geq 2$) to a constant interior value. This matches the behavior of wide stripes with their separation in constrained mid-section and freely shrinking edge zones, as presented in the FEM stress distributions in Figure 5-1. The fact that the plateau values of the inner and outer edge displacement are similar in narrow and wide stripes leads to the assumption that as soon as there is no more interference between outer and inner edge, the edge zones are equivalent and merely separated by an increasingly large mid-section. Thus, hole opening can occur. Again, this is consistent with the behavior observed in sintering stripes.

Jagota's prediction on tangential hoop stress distribution is also confirmed qualitatively by the present experiments. According to the model, tangential stresses are maximal at the inner free surface and partially relaxed at the outer ring surface. The absolute value of the maximum stress scales with ka. In our experiments, evidence for high tangential stresses at the inner ring was found in the high ka systems in the form of radial cracking. In the system with the lowest friction, no such cracks formed.

The effect of the substrate material on the friction coefficient is consistent with the differing degree of constraint observed in the stripes. The lowest friction was observed in the thickest system (27μm). Then followed the 8μm rings on platinum. The highest friction was found in 8μm rings on sapphire.

6. Summary and outlook

6.1. Summary

In the present work, the influence of finite lateral dimensions on the constrained sintering of patterned films has been studied with special focus on the stripe geometry and the film-substrate interface. In the first part, shrinkage of stripe patterns with different geometries was studied. The dominance of the freely shrinking edge as a consequence of delamination and the resulting non-negligible lateral strains at low feature widths is established as the main consequence. At subcritical feature widths, three basic assumptions commonly underlying the mathematical modelling of constrained sintering are no longer valid: Firstly, the in-plane strain component along the finite direction is no longer negligible. Secondly, the vertical strain is no longer enhanced compared to the free sintering. Thirdly, perfect film adhesion to the substrate is not guaranteed. In short, the simplified two-dimensional stress state with zero stress along the vertical directions assumed in models is not found in narrow stripe systems; by contrast, a triaxial stress state is present. The critical width below which these deviations begin was found to be dependent on stripe thickness as well as the nature of the interface. Patterned films therefore represent an intermediate state between free and constrained sintering.

Several microscopic and macroscopic phenomena are caused by this stress state: Wide stripes were found to deviate from their original rectangular geometry after sintering due to a separation in delaminated, high-density edges and an undeformed, perfectly constrained mid-section. This result confirms preexisting FEM results on shape distortion in wide stripes as well as custom FEM and DEM simulations provided by other researchers for this work. In narrow stripes, no such deviation from the original shape occurred. Differential lateral shrinkage in thick stripes lead to delamination that was found to scale both with stripe thickness and with. Lateral strains were higher at the film surface as predicted by DEM simulations in the literature.

Lateral strains were found be maximal in narrow stripes and decrease with decreasing thickness-to-width ratio. The reason for this behavior was found to be the edge zone, since the latter is the only part of the film that allows lateral particle movement. Since the percentage of the edge zone of the entire stripe width decreases width increasing width, the above mentioned strain development is found. In narrow stripes, lateral strains reached the same order of magnitude as the vertical strains. This phenomenon is referred to as quasi-free sintering. A material dependent threshold value of thickness-to-width ratio was established above which this behavior occurs.

In addition, microstructural gradients both in the vertical and lateral dimension were observed in cross section. Density was found to be minimal at the substrate and to increase when moving upward, while pore orientation and elongation decreases with increasing distance to the substrate. This is consistent with the literature results on continuous films. However, additional lateral gradients were found that resulted in high density near the edge that decreases when approaching the center. Pore orientation

near the edges was equivalent to the results on freely sintering laminates. The density distribution resulted in a skin effect in narrow stripes whose average density was higher than in wide stripes.

Enhancement of the substrate roughness caused a reduction in delamination length due to crack arrest at local barriers as well as a reduction in density inside substrate grooves. The first phenomenon is responsible for the reduced lateral strains in rough substrates. Both phenomena contribute to the reduction of the overall density in rough stripe systems. Custom DEM simulations provided by other researchers revealed tensile vertical stresses inside the substrate grooves as a cause. However, the influence of reduced delamination was identified as the dominant factor since reduced densification compared to smooth substrates only asserted itself after crack arrest.

Addition of a platinum interlayer caused an increase in lateral strains despite a reduction in delamination length as well as an increase in sintered density, while lowering the threshold value of thickness-to-width ratio for quasi-free sintering. An unambiguous identification of a sole underlying mechanism for this behavior is difficult; however, the morphology of the platinum layer after sintering allows the assumption that creep deformation of the platinum interlayer accommodates some of the lateral stress imposed on the substrate as the platinum layer is dragged along by the shrinking edges.

Densification curves have been measured for smooth, rough and platinum coated substrates. Here, quasi-free sintering was observed in high aspect stripes on smooth substrates. Throughout the sintering cycle, delamination increased in a linear fashion with density, allowing the lateral strains to rise until the end of the heating schedule. In the case of rough substrates, lateral strains reached a plateau whose onset is thought to correspond to crack arrest. Thus, the reduced density and lateral strains in stripes on smooth substrates were related to the reduced densification.

Densification curves in low aspect ratio stripes presented matching characteristics of continuous stripes studied by other researchers. Here, lateral strains were in the range of -0.05 and were exceeded sixfold by the vertical strains. When a platinum interlayer was present, quasi-free sintering occurred in thin films such as the 8µm x 25µm system that shows no such behavior on plain sapphire. A liquid phase sintering aid had a similar effect on constrained densification; here, too, quasi-free sintering with identical vertical and surface lateral strains took place in systems that act as constrained films in the pure alumina system. The effect of the substrate constraint was found to propagate throughout the stripe thickness to a lesser degree that without the sintering aid; 27µm x 100mm stripes of pure and doped alumina showed similar interface lateral strains, but the surface lateral strain of the doped system exceeded the pure system by a factor of 1.7. This effect was ascribed to the decreased interparticle friction in the presence of liquid phase.

In the second part, cracking around intentionally introduced cavities was studied. Again, the proximity of the edge to the cavity had a major effect on crack patterns. While random radial cracks appeared around round cavities in wide stripes, narrow stripes developed two cracks perpendicular to the stripe edges that in the thickest specimens caused complete rupture of the stripe. In addition, the lateral movement of the edges resulted in elliptical skewing of the defects. These effects were observed in all

substrates and scaled with the lateral strain measured in stripes with the same aspect ratio but without predefects. Crack propagation occurred in a creeping mode via microcrack coalescence in case of the oriented cracks; random radial cracks appeared instantaneously and did not grow further through the sintering cycle. Small defects were found to be more likely to crack since large holes acted as free, non-curved inner surfaces that underwent shrinkage analogous to the outer stripe edges.

Similar edge effects were observed in the case of elliptical defects. Here, cracking at the endpoints occurred only if the distance between edge and defect was big enough. When several elliptical holes were present, cracks had a tendency to grow into neighboring holes independent of their orientation with respect to the original crack plane.

Calculation of the interface friction coefficient was carried out. Its thickness dependence was found to match the model predictions for compliant platinum interfaces and stiff ceramic-ceramic interfaces. Addition of a liquid phase sintering aid did not alter the nature of the interface. However, due to the high delamination narrow stripes, a limiting film thickness was established above which the model can be no longer applied. This is the case whenever interference between the two opposing stripe edges causes the overall stripe properties to be dominated by edge effects. With the help of the friction coefficient, the sintering of ring structures was studied. A friction dependent transition of hole closure to hole opening was found that is in very good agreement with model predictions.

6.2. Outlook

This thesis provides an in-depth analysis of the influence of finite feature size on the constrained sintering behavior. However, several aspects of this work are eligible for further investigation. Since traditional ceramic processing for the direct measurement of green density is challanging, more advanced techniques such as in- or ex-situ x-ray tomography can be applied to generate densification curves and evaluate the local microstructure development. Furthermore, sequential focused ion beam treatment may further enhance the quality of the polished cross sections.

The sample fabrication process used in this work could be further improved by applying different drying conditions or slurry solid contents to specimens of different thicknesses. Like this, samples of different thicknesses but identical green densities may be produced.

In addition, conclusive proof that creep deformation in the platinum layer is the reason for the enhanced lateral strain is still missing. A set of experiments to settle this matter could be designed in the following way: Interlayers of a variety of metals with different creep behavior but similar adhesion properties to alumina could be used to repeat the sintering experiments. If the lateral strain response is found to scale with the creep strain rate at a given temperature and stress, this would prove the existence of creep induced strain enhancement.

Another relevant question is the validity of the present findings for other film materials. In practical applications, conductive vias made of metallic pastes are a one of the most widespread film systems with finite dimensions that may suffer degradation from delamination or cracking. Threshold thickness-to-width ratios for quasi-free sintering may be established *e. g*. for silver or copper pastes.

7. List of tables

8. List of figures

9. References

1. Wilson, S.A., R.P.J. Jourdain, Q. Zhang, R.A. Dorey, C.R. Bowen, M. Willander, Q.U. Wahab, M. Willander, S.M. Al-hilli, O. Nur, E. Quandt, C. Johansson, E. Pagounis, M. Kohl, J. Matovic, B. Samel, W. van der Wijngaart, E.W.H. Jager, D. Carlsson, Z. Djinovic, M. Wegener, C. Moldovan, R. Iosub, E. Abad, M. Wendlandt, C. Rusu, and K. Persson, *New materials for micro-scale sensors and actuators: An engineering review.* Materials Science and Engineering: R: Reports, 2007. **56**(1–6): p. 1-129.

2. Lee, H.-J., T.-H. Yoon, J.-H. Park, J. Perumal, and D.-P. Kim, *Characterization and fabrication of polyvinylsilazane glass microfluidic channels via soft lithographic technique.* Journal of Industrial and Engineering Chemistry, 2008. **14**(1): p. 45-51.

3. Fudouzi, H. and Y. Sakka, *Micro Gas Sensor Assembly of Tin Oxide Nano-Particles by a Capillary Micromolding Process.* Journal of the Ceramic Society of Japan, 2010. **118**(3): p. 202-205.

4. Heule, M. and L.J. Gauckler, *Miniaturised arrays of tin oxide gas sensors on single microhotplate substrates fabricated by micromolding in capillaries.* Sensors and Actuators B 93, 2003. **93**: p. 100-106.

5. Tiggelaar, R.M., P.W.H. Loeters, P. van Male, R.E. Oosterbroek, J.G.E. Gardeniers, M.H.J.M. de Croon, J.C. Schouten, M.C. Elwenspoek, and A. van den Berg, *Thermal and mechanical analysis of a microreactor for high temperature catalytic gas phase reactions.* Sensors and Actuators A: Physical, 2004. **112**(2–3): p. 267-277.

6. Wang, X., Z. Chen, and A. Atkinson, *Crack formation in ceramic films used in solid oxide fuel cells.* Journal of the European Ceramic Society, 2013. **33**(13–14): p. 2539-2547.

7. Green, D.J., O. Guillon, and J. Rödel, *Constrained sintering: A delicate balance of scales.* Journal of the European Ceramic Society, 2008. **28**(7): p. 1451-1466.

8. Geissler, M. and Y. Xia, *Patterning: Principles and Some New Developments.* Advanced Materials, 2004. **16**(15): p. 1249-1269.

9. Xia, Y. and G.M. Whitesides, *Soft lithography.* Angewandte Chemie International Edition, 1998. **37**: p. 550-575.

10. Holthaus, M.G., L. Treccani, and K. Rezwan, *Comparison of micropatterning methods for ceramic surfaces.* Journal of the European Ceramic Society, 2011. **31**(15): p. 2809-2817.

11. *Nanoterra Corporate Homepage*. 2014 2014-01-31]; Available from: http://www.nanoterra.com/soft_lithography.asp.

12. Martin, C.R. and I.A. Aksay, *Topographical Evolution of Lead Zirconate Titanate (PZT) Thin Films Patterned by Micromolding in Capillaries.* Journal of Physical Chemistry B, 2003. **107**: p. 4261-4268.

13. Rasp, T., C. Jamin, A. Wonisch, T. Kraft, and O. Guillon, *Shape Distortion and Delamination During Constrained Sintering of Ceramic Stripes: Discrete Element Simulations and Experiments.* Journal of the American Ceramic Society, 2012. **95**(2): p. 586-592.

14. ten Elshof, J.E., S.U. Khan, and O.F. Göbel, *Micrometer and nanometer-scale parallel patterning of ceramic and organic–inorganic hybrid materials.* Journal of the European Ceramic Society, 2010. **30**(7): p. 1555-1577.

15. Kim, E., Y. Xia, and G.M. Whitesides, *Micromolding in Capillaries: Applications in Materials Science.* Journal of the American Chemical Society, 1996. **118**(24).

16. Beh, W.S., Y. Xia, and Q. Dong, *Formation of patterned microstructures of polycrystalline ceramics from precursor polymers using micromolding in capillaries.* Journal of Materials Research, 1999. **14**(11): p. 3994-4003.

17. Heule, M., J. Schell, and L.J. Gauckler, *Powder-Based Tin Oxide Microcomponents on Silicon Substrates Fabricated by Micromolding in Capillaries.* Journal of the American Ceramic Society, 2003. **86**(3): p. 407-12.

18. Rosqvist, T. and S. Johansson, *Soft micromolding and lamination of piezoceramic thick films.* Sensors and Actuators A: Physical, 2002. **97–98**(0): p. 512-519.

19. Vartuli, J.S., M. Özenbas, C.-M. Chun, M. Trau, and I.A. Aksay, *Micropatterned lead zirconium titanate thin films.* Journal of Materials Research, 2003. **18**(5): p. 1259-1265.

20. Jang, J.-S., M. Jank, V. Maier, K. Durst, N. Travitzky, and Z. C., *SiC ceramic micropatterns from polycarbosilanes.* Journal of the European Ceramic Society, 2010. **30**: p. 2773–2779.

21. Lee, D.-H., K.-H. Park, L.-Y. Hong, and D.-P. Kim, *SiCN ceramic patterns fabricated by soft lithography techniques.* Sensors and Actuators A: Physical, 2007. **135**(2): p. 895-901.

22. Straue, N., M. Rauscher, S. Walther, H. Faber, and A. Roosen, *Preparation and soft lithographic printing of nano-sized ITO-dispersions for the manufacture of electrodes for TFTs.* Journal of Materials Science, 2009. **44**: p. 6011-6019.

23. Seils, S., R. Baraki, C. Jamin, and O. Guillon, *Free-Standing Patterned Ceramic Structures Obtained by Soft Micromolding.* Advanced Engineering Materials, 2011. **13**(6): p. 502-508.

24. Dobrovinskaya, E., L.A. Lytvynov, and V. Pishchik, *Sapphire: Material, Manufacturing, Applications*. Micro- and Optoelectronic Materials, Structures, and Systems. 2009: Springer Science+Business Media, LLC.

25. Zhang, D., B. Su., and T. W. Button, *Preparation of concentrated aqueous alumina suspensions for soft-molding microfabrication.* Journal of the European Ceramic Society 24 2004. **24**(231-237).

26. Ahn, S.-J., J.-H. Min, J. Kim, and J. Moon, *Process Mechanism for Vacuum-AssistedMicrofluidic Lithography with Ceramic Colloidal Suspensions.* Journal of the American Ceramic Society, 2008. **91**(7): p. 2143-2149.

27. Imasu, J., H. Fudouzi, and Y. Sakka, *Micro-Scale Patterning of Ceramic Colloidal Suspension by Micro Molding in Capillaries (MIMIC) with Assistance of Highly Infiltrating Liquid.* Journal of the Ceramic Society of Japan. **114**(1332): p. 725-728.

28. Guillon, O., C. Jamin, and R.K. Bordia, *Effect of drying conditions on patterned ceramic films processed by soft micromolding.* Journal of the Ceramic Society of Japan, 2010. **118**(1376): p. 321-325.

29. Wang, X., L. Ge, J. Lu, X. Li, K. Qiu, Y. Tian, S. Fu, and Z. Cui, *Fabrication of enclosed nanofluidic channels by UV cured imprinting and optimized thermal bonding of SU-8 photoresist.* Microelectronic Engineering, 2009. **86**(4–6): p. 1347-1349.

30. Huang, Y.-Y., W.-X. Zhou, K.J. Hsia, E. Menard, J.-U. Park, J.A. Rogers, and A.G. Alleyne, *Stamp Collapse in Soft Lithography.* Langmuir, 2005. **21**: p. 8058-8068.

31. Gentry, S.P. and J.W. Halloran, *Depth and width of cured lines in photopolymerizable ceramic suspensions.* Journal of the European Ceramic Society, 2013. **33**(10): p. 1981-1988.

32. Rahaman, M.N., *Ceramic Processing and Sintering*. 2003, New York: M Dekker, Inc.

33. Raj, P.M., A. Odulena, and W.R. Cannon, *Anisotropic shrinkage during sintering of particle-oriented systems—numerical simulation and experimental studies.* Acta Materialia, 2002. **50**(10): p. 2559-2570.

34. Guillon, O., S. Krauß, and J. Rödel, *Influence of thickness on the constrained sintering of alumina films.* Journal of the European Ceramic Society, 2007. **27**(7): p. 2623-2627.

35. Wakai, F., *Modeling and Simulation of Elementary Processes in Ideal Sintering.* Journal of the American Ceramic Society, 2006. **89**(5): p. 1471-1484.

36. Kang, S.-J.L. Sintering. 2005, Oxford: Butterworth-Heinemann.

37. Raj, R., *Analysis of the Sintering Pressure.* Journal of the American Ceramic Society, 1987. **70**(9): p. C-210-C-211.

38. German, R.M., *Sintering theory and practice*, ed. K.H.J. Buschow, et al. 2001, Oxford: Elsevier.

39. Ollagnier, J.B., *Constraint and Anisotropy During Sintering of a LTCC Material*, *PhD thesis in Materials Science*. 2008, TU Darmstadt.

40. Ostrowski, T., A. Ziegler, R.K. Bordia, and J. Rödel, *Evolution of Young's Modulus, Strength, and Microstructure during Liquid-Phase Sintering.* Journal of the American Ceramic Society, 1998. **81**(7): p. 1852-1860.

41. Leite, E.R., M.A.L. Nobre, E. Longo, and J.A. Varela, *Microstructural development of ZnO varistor during reactive liquid phase sintering.* Journal of Materials Science, 1996. **31**(20): p. 5391-5398.

42. Park, H.-H., S.-J. Cho, and D. Yoon, *Pore filling process in liquid phase sintering.* Metallurgical Transactions A, 1984. **15**(6): p. 1075-1080.

43. Lee, S.-M. and S.-J.L. Kang, *Theoretical analysis of liquid-phase sintering: Pore filling theory.* Acta Materialia, 1998. **46**(9): p. 3191-3202.

44. Dong, W., H. Jain, and M.P. Harmer, *Liquid Phase Sintering of Alumina, I. Microstructure Evolution and Densification.* Journal of the American Ceramic Society, 2005. **88**(7): p. 1702-1707.

45. Dong, W., H. Jain, and M.P. Harmer, *Liquid Phase Sintering of Alumina, II. Penetration of Liquid Phase into Model Microstructures.* Journal of the American Ceramic Society, 2005. **88**(7): p. 1708-1713.

46. Dong, W., H. Jain, and M.P. Harmer, *Liquid Phase Sintering of Alumina, III. Effect of Trapped Gases in Pores on Densification.* Journal of the American Ceramic Society, 2005. **88**(7): p. 1714-1719.

47. Olevsky, E.A., *Theory of sintering: from discrete to continuum.* Materials Science and Engineering: R: Reports, 1998. **23**(2): p. 41-100.

48. Reed, J.R., *Priciples of Ceramic Processing*. 1995: Wiley VCH.

49. Bordia, R.K. and G.W. Scherer, *On constrained sintering—I. Constitutive model for a sintering body.* Acta Metallurgica, 1988. **36**(9): p. 2393-2397.

50. Bordia, R.K. and G.W. Scherer, *On constrained sintering—II. Comparison of constitutive models.* Acta Metallurgica, 1988. **36**(9): p. 2399-2409.

51. Christensen, R.M., *Theory of Viscoelasticity*. 1982: Academic Press.

52. Garino, T.J. and H.K. Bowen, *Kinetics of Constrained-Film Sintering.* Journal of the American Ceramic Society, 1990. **73**(2): p. 251-257.

53. Zuo, R., E. Aulbach, and J. Rödel, *Viscous Poisson's coefficient determined by discontinuous hot forging.* J. Mater. Res., 2003. **18**(9): p. 2170 - 2176.

54. Zuo, R., E. Aulbach, and J. Rödel, *Experimental determination of sintering stresses and sintering viscosities.* Acta Materialia, 2003. **51**(15): p. 4563-4574.

55. Cai, P.Z., G.L. Messing, and D.J. Green, *Determination of the Mechanical Response of Sintering Compacts by Cyclic Loading Dilatometry*. Journal of the American Ceramic Society, 1997. **80**(2): p. 445-452.

56. Lee, S.-H., G.L. Messing, and D.J. Green, *Bending Creep Test to Measure the Viscosity of Porous Materials during Sintering.* Journal of the American Ceramic Society, 2003. **86**(6): p. 877-882.

57. Zuo, R. and J. Rödel, *Temperature dependence of constitutive behaviour for solid-state sintering of alumina.* Acta Materialia, 2004. **52**(10): p. 3059-3067.

58. Zuo, R., E. Aulbach, and J. Rödel, *Viscous Poisson's coefficient determined by discontinuous hot forging.* J. Mater. Res., 2003. **18**(9): p. 2170 - 2176.

59. Wakai, F., Y. Shinoda, and T. Akatsu, *Methods to calculate sintering stress of porous materials in equilibrium.* Acta Materialia, 2004. **52**(19): p. 5621-5631.

60. Ashby, M.F., *A first report on sintering diagrams.* Acta Metallurgica, 1974. **22**(3): p. 275-289.

61. Svoboda, J., H. Riedel, and H. Zipse, *Equilibrium pore surfaces, sintering stresses and constitutive equations for the intermediate and late stages of sintering—I. computation of equilibrium surfaces.* Acta Metallurgica et Materialia, 1994. **42**(2): p. 435-443.

62. Riedel, H., H. Zipse, and J. Svoboda, *Equilibrium pore surfaces, sintering stresses and constitutive equations for the intermediate and late stages of sintering—II. Diffusional densification and creep.* Acta Metallurgica et Materialia, 1994. **42**(2): p. 445-452.

63. Chang, J., O. Guillon, J. Rödel, and S.-J.L. Kang, *Uniaxial viscosity of gadolinium-doped ceria determined by discontinuous sinter forging.* Journal of the European Ceramic Society, 2007. **27**(10): p. 3127-3133.

64. Mohanram, A., S.-H. Lee, G.L. Messing, and D.J. Green, *A novel use of constrained sintering to determine the viscous Poisson's ratio of densifying materials.* Acta Materialia, 2005. **53**(8): p. 2413-2418.

65. Petersson, A. and J. Ågren, *Constitutive behaviour of WC–Co materials with different grain size sintered under load.* Acta Materialia, 2004. **52**(7): p. 1847-1858.

66. Gillia, O., C. Josserond, and D. Bouvard, *Viscosity of WC–Co compacts during sintering.* Acta Materialia, 2001. **49**(8): p. 1413-1420.

67. McMeeking, R.M. and L.T. Kuhn, *A diffusional creep law for powder compacts.* Acta Metallurgica et Materialia, 1992. **40**(5): p. 961-969.

68. Du, Z.Z. and A.C.F. Cocks, *Constitutive models for the sintering of ceramic components—I. Material models.* Acta Metallurgica et Materialia, 1992. **40**(8): p. 1969-1979.

69. Venkatachari, K.R. and R. Raj, *Shear Deformation and Densification of Powder Compacts*. Journal of the American Ceramic Society, 1986. **69**(6): p. 499-506.

70. Wang, X., J.-S. Kim, and A. Atkinson, *Constrained sintering of 8 mol% Y_2O_3 stabilised zirconia films.* Journal of the European Ceramic Society, 2012. **32**(16): p. 4121-4128.

71. Cocks, A.C.F. and N.A. Fleck, *Constrained sintering of an air-plasma-sprayed thermal barrier coating.* Acta Materialia, 2010. **58**(12): p. 4233-4244.

72. Li, F., J. Pan, O. Guillon, and A. Cocks, *Predicting sintering deformation of ceramic film constrained by rigid substrate using anisotropic constitutive law.* Acta Materialia, 2010. **58**(18): p. 5980-5988.

73. Scherer, G.W. and T. Garino, *Viscous Sintering on a Rigid Substrate.* Journal of the American Ceramic Society, 1985. **68**(4): p. 216-220.

74. Guillon, O., E. Aulbach, J. Rödel, and R.K. Bordia, *Constrained Sintering of Alumina Thin Films: Comparison Between Experiment and Modeling.* Journal of the American Ceramic Society, 2007. **90**(6): p. 1733-1737.

75. Kim, J.-S., R.A. Rudkin, X. Wang, and A. Atkinson, *Constrained sintering kinetics of 3YSZ films.* Journal of the European Ceramic Society, 2011. **31**(13): p. 2231-2239.

76. Guillon, O., L. Weiler, and J. Rödel, *Anisotropic Microstructural Development During the Constrained Sintering of Dip-Coated Alumina Thin Films.* Journal of the American Ceramic Society, 2007. **90**(5): p. 1394-1400.

77. Wang, X. and A. Atkinson, *Microstructure evolution in thin zirconia films: Experimental observation and modelling.* Acta Materialia, 2011. **59**(6): p. 2514-2525.

78. Martin, C.L. and R.K. Bordia, *The effect of a substrate on the sintering of constrained films.* Acta Materialia, 2009. **57**(2): p. 549-558.

79. Wonisch, A., O. Guillon, T. Kraft, M. Moseler, H. Riedel, and J. Rödel, *Stress-induced anisotropy of sintering alumina: Discrete element modelling and experiments.* Acta Materialia, 2007. **55**(15): p. 5187-5199.

80. Bordia, R.K., R. Zuo, O. Guillon, S.M. Salamone, and J. Rödel, *Anisotropic constitutive laws for sintering bodies.* Acta Materialia, 2006. **54**(1): p. 111-118.

81. Zhao, Y. and L.R. Dharani, *Theoretical model for the analysis of a ceramic thin film sintering on a non-sintering substrate.* Thin Solid Films, 1994. **245**(1–2): p. 109-114.

82. Olevsky, E.A., V. Tikare, and T. Garino, *Multi-Scale Study of Sintering: A Review.* Journal of the American Ceramic Society, 2006. **89**(6): p. 1914-1922.

83. Kraft, T. and H. Riedel, *Numerical simulation of solid state sintering; model and application.* Journal of the European Ceramic Society, 2004. **24**(2): p. 345-361.

84. Jamin, C., T. Rasp, T. Kraft, and O. Guillon, *Constrained sintering of alumina stripe patterns on rigid substrates: Effect of stripe geometry.* Journal of the European Ceramic Society, 2013. **33**(15–16): p. 3221-3230.

85. Cundall, P.A. and O.D.L. Strack, *A discrete numerical model for granular assemblies.* Geotechnique, 1979. **29**(1): p. 47-65.

86. Henrich, B., A. Wonisch, T. Kraft, M. Moseler, and H. Riedel, *Simulations of the influence of rearrangement during sintering.* Acta Materialia, 2007. **55**(2): p. 753-762.

87. Svoboda, J. and H. Riedel, *New solutions describing the formation of interparticle necks in solid-state sintering.* Acta Metallurgica et Materialia, 1995. **43**(1): p. 1-10.

88. Bouvard, D. and R.M. McMeeking, *Deformation of Interparticle Necks by Diffusion-Controlled Creep.* Journal of the American Ceramic Society, 1996. **79**(3): p. 666-672.

89. Martin, C.L., H. Camacho-Montes, L. Olmos, D. Bouvard, and R.K. Bordia, *Evolution of Defects During Sintering: Discrete Element Simulations.* Journal of the American Ceramic Society, 2009. **92**(7): p. 1435-1441.

90. Jauffrès, D., C.L. Martin, A. Lichtner, and R.K. Bordia, *Simulation of the toughness of partially sintered ceramics with realistic microstructures.* Acta Materialia, 2012. **60**(12): p. 4685-4694.

91. Rasp, T., T. Kraft, and H. Riedel, *Discrete element study on the influence of initial coordination numbers on sintering behaviour.* Scripta Materialia, 2013. **69**(11–12): p. 805-808.

92. Raj, R. and R.K. Bordia, *Sintering behavior of bi-modal powder compacts.* Acta Metallurgica, 1984. **32**(7): p. 1003-1019.

93. Hsueh, C.H., A.G. Evans, R.M. Cannon, and R.J. Brook, *Viscoelastic stresses and sintering damage in heterogeneous powder compacts.* Acta Metallurgica, 1986. **34**(5): p. 927-936.

94. Scherer, G.W., *Sintering with rigid inclusions.* Journal of the American Ceramic Society, 1987. **70**(10): p. 719-725.

95. Lange, F.F., *Constrained network model for predicting densification behavior of composite powders.* Journal of Materials Research, 1987. **2**(01): p. 59-65.

96. Anderson, T.L., *Fracture Mechanics - fundamentals and applications*. 1991, Boca Raton, Florida: CRC press, Inc.

97. Riedel, H., *Fracture at high temperatures*. 1987: Springer-Verlag Berlin Heidelberg 1987 418

98. Dörre, E. and H. Hübner, *Alumina: Processing, properties and applications*. 1984, Berlin New York Springer-Verlag.

99. Kendall, K., *Adhesion: Molecules and Mechanics.* Science, 1994. **263**(5154): p. 1720-1725.

100. Rödel, J. and A.M. Glaeser, *Pore Drag and Pore-Boundary Separation in Alumina.* Journal of the American Ceramic Society, 1990. **73**(11): p. 3302-3312.

101. Karbasi, A., A. Hadjikhani, R. Hrubiak, A. Durygin, and K. Jones, *High Temperature Interactions in Platinum/Alumina System*, in *Processing and Properties of Advanced Ceramics and Composites V*. 2013, John Wiley & Sons, Inc. p. 45-53.

102. Galinski, H., T. Ryll, L. Schlagenhauf, L.J. Gauckler, P. Stender, and G. Schmitz, *Hillock formation of Pt thin films on single-crystal yttria-stabilized zirconia.* Physical Review B, 2012. **85**(12): p. 125408.

103. Floyd, R., Bulletin of the American Ceramic Society, 1963. **42**: p. 65.

104. Belič, L.I., M. Stipanov, and P. Pavli, *The influence of ceramic microstructure on metal-ceramic seal formation.* Vacuum, 1990. **40**(1–2): p. 55-57.

105. Tiggelaar, R.M., R.G.P. Sanders, A.W. Groenland, and J.G.E. Gardeniers, *Stability of thin platinum films implemented in high-temperature microdevices.* Sensors and Actuators A: Physical, 2009. **152**(1): p. 39-47.

106. Gruber, W., S. Chakravarty, C. Baehtz, W. Leitenberger, M. Bruns, A. Kobler, C. Kübel, and H. Schmidt, *Strain Relaxation and Vacancy Creation in Thin Platinum Films.* Physical Review Letters, 2011. **107**(26): p. 265501.

107. Firebaugh, S.L., K.F. Jensen, and M.-A. Schmidt, *Investigation of high-temperature degradation of platinum thin films with an in situ resistance measurement apparatus.* Journal of Microelectromechanical Systems, 1998. **7**(1): p. 128-135.

108. Strobel, S., C. Kirkendall, J.-B. Chang, and K.K. Berggren, *Sub-10 nm structures on silicon by thermal dewetting of platinum.* Nanotechnology, 2010. **21**: p. 505301.

109. Chaston, J.C., *Reactions of Oxygen with the Platinum Metals.* Platinum Metals Review, 1964. **8**: p. 50-54.

110. Wrbanek, J.D. and K.L.H. Later, *Preparation and Analysis of PlatinumThin Films for High Temperature Sensor Applications*, in *NASA/TM—2005-213433*. 2005, NASA Center for Aerospace Information.

111. Jagota, A. and C.Y. Hui, *Mechanics of sintering thin films — I. Formulation and analytical results.* Mechanics of Materials, 1990. **9**(2): p. 107-119.

112. Jagota, A. and C.Y. Hui, *Mechanics of sintering thin films — II. Cracking due to self-stress.* Mechanics of Materials, 1991. **11**(3): p. 221-234.

113. Bordia, R.K. and A. Jagota, *Crack Growth and Damage in Constrained Sintering Films.* Journal of the American Ceramic Society, 1993. **76**(10): p. 2475-2485.

114. Frame, D., *Microstructure Development and Crack Growth in Constrained Electrolytes*, in *University of Washington*. 2006.

115. Bordia, R.K. and R. Raj, *Sintering Behavior of Ceramic Films Constrained by a Rigid Substrate.* Journal of the American Ceramic Society, 1985. **68**(6): p. 287-292.

116. Brydson, R., S.-C. Chen, F.L. Riley, S.J. Milne, X. Pan, and M. Rühle, *Microstructure and Chemistry of Intergranular Glassy Films in Liquid-Phase-Sintered Alumina.* Journal of the American Ceramic Society, 1998. **81**(2): p. 369-379.

117. Dash, S., M. Kamruddin, P.K. Ajikumar, A.K. Tyagi, and B. Raj, *Nanocrystalline and metastable phase formation in vacuum thermal decomposition of calcium carbonate.* Thermochimica Acta, 2000. **363**(1–2): p. 129-135.

118. Ferrari, B., R. Moreno, J.L. Rodriguez, and E. Rojas, *Conformado por via coloidal de recubrimientos en la cara de un tubo de acero.* Boletin de la Sociedad de Cerámica y Vidrio, 2004. **43**(2): p. 501-505.

119. Grimm, F., *Sintern strukturierter Aluminiumoxidschichten auf steifen Substraten mit einer Glasphase, Bachelor thesis in Materials Science*. 2013, TU Darmstadt.

120. Keil, P., *Einfluss des Substratmaterials und der Substratrauheit auf das Sinterverhalten strukturierter Aluminiumoxidschichten, Bachelor thesis in Materials Science*. 2013, TU Darmstadt.

121. Zuo, R., E. Aulbach, R.K. Bordia, and J. Rödel, *Critical evaluation of hot forging experiment: case study in alumina*. Journal of the American Ceramic Society, 2003. **86**: p. 1099-1105.

122. Rasp, T., *Modellierung von Anisotropieentwicklung und Rissausbreitung beim Sintern dünner keramischer Schichten, PhD thesis*. in progress, Karlsruhe Institute of Technology, 2014.

123. Xia, Z.C. and J.W. Hutchinson, *Crack patterns in thin films.* Journal of the Mechanics and Physics of Solids, 2000. **48**(6–7): p. 1107-1131.

124. Kraft, T., *private communication*. 2013: Fraunhofer Institut für Werkstoffmechanik, Freiburg.

Curriculum Vitae

Data

Christine Jamin
Alexanderstr. 9
64732 Bad König
ccjamin@gmx.de
born July 18th 1984 in Speyer, Germany

Education and Career

July 2011 – Jan. 2014	Technische Universität Darmstadt, PhD student
Feb. 2011 – June 2011	Maternity leave
Jan. 2011	Universidade de Aveiro, visiting researcher
Aug. 2010 – Dec. 2010	Maternity leave
Apr. 2011 – June 2011	Universidade de Aveiro, visiting researcher
Nov. 2009 – Aug. 2010	Technische Universität Darmstadt, PhD student
Mar. 2007 – Apr. 2007	Penn State University, Pennsylvania, USA, student intern
Sept. 2006 – Feb. 2007	Universidad Complutense de Madrid, Spain, Erasmus student
Feb. 2005 – Apr. 2005	Internship at W. C. Heraeus, Hanau
Sept. 2003 – Oct. 2008	Technische Universität Darmstadt, degree in Materials Science
June – Aug. 2003	Internship at BASF S.A., Tarragona
Mar 2003	High school diploma at Hannah Arendt High School in Haßloch

Publication list

1. Papers in refereed journals

Jamin, Christine; Rasp, Tobias; Kraft, Torsten; Guillon, Olivier:
Constrained sintering of alumina stripe patterns on rigid substrates: Effect of stripe geometry
Journal of the European Ceramic Society (2013), 33 (15) pp. 3221-3230

Amaral, Luis; Jamin, Christine; Senos, Ana M. R.; Vilarinho, Paula M.; Guillon, Olivier:
Constrained sintering of $BaLa_4Ti_4O_{15}$ thick films: Pore and grain anisotropy.
Journal of the European Ceramic Society (2013), 33 (10) pp. 1801-1808

Amaral, Luis; Jamin, Christine; Senos, Ana M. R.; Vilarinho, Paula M.; Guillon, Olivier:
Effect of the Substrate on the Constrained Sintering of $BaLa_4Ti_4O_{15}$Thick Films.
Journal of the American Ceramic Society (2012), 95 (12) pp. 3781-3787

Rasp, Tobias; Jamin, Christine; Wonisch, Andreas; Kraft, Torsten; Guillon, Olivier:
Shape Distortion and Delamination During Constrained Sintering of Ceramic Stripes: Discrete Element Simulations and Experiments.
Journal of the American Ceramic Society (2012), 95 (2) pp. 586-592.

Seils, Sascha; Baraki, Raschid; Jamin, Christine; Guillon, Olivier:
Free-Standing Patterned Ceramic Structures Obtained by Soft Micromolding.
Advanced Engineering Materials (2011), 13 (6) pp. 502-508.

Guillon, Olivier; Jamin, Christine; Bordia, Rajendra K.:
Effect of drying conditions on patterned ceramic films processed by soft micromolding.
Journal of the Ceramic Society of Japan (2010), 118 (1376) pp. 321-325.

2. Conference talks and posters

Jamin, Christine, Guillon, Olivier:
Sintering of patterned ceramic layers.
Conference poster, ICCPS-11, 2010, Zurich, Switzerland.

Jamin, Christine, Guillon, Olivier:
Sintering of patterned alumina films.
Oral presentation, Sintering 2011, Jeju Island, Korea

Jamin, Christine; Seils, Sascha; Baraki, Raschid; Guillon, Olivier:
Sintering of free standing ceramic structures produced by soft micromolding in capillaries.
Oral presentation, Symposium Hochleistungskeramik, 2011, Karlsruhe, Germany.

Jamin, Christine, Guillon, Olivier:
Sintering of patterned alumina films.
Oral presentation, CMCEE 2012, Dresden, Germany.

Amaral, Luis; Senos, Ana M. R.; Jamin, Christine; Guillon, Olivier; Vilarinho, Paula M:
Stress assisted grain growth and dielectric properties of BaLa 4Ti4O15 thick films.
Conference proceeding, CICMT-8 2012, Erfurt, Germany.

Jamin, Christine, Guillon, Olivier:
Influence of the substrate on the constrained sintering of alumina patterned films.
Oral presentation, Euromat 2013, Sevilla, Spain.

Eidesstattliche Erklärung

Christine Jamin
Alexanderstr. 9
64732 Bad König

Hiermit erkläre ich an Eides statt, dass ich die vorliegende Dissertation selbständig und nur mit den angegebenen Hilfsmitteln angefertigt habe. Von mir wurde weder an der Technischen Universität Darmstadt noch an einer anderen Hochschule ein Promotionsversuch unternommen.

_____

Bad König, den 24.3.2014